EPFL

Thèse n° 9917

# Precipitation, Characterization, Kinetic, and Thermodynamic Modelling of Synthetic C-S-H Systems (C-S-H, CASH, CSH+$)

Présentée le 25 août 2022

Faculté des sciences et techniques de l'ingénieur
Laboratoire des matériaux de construction
Programme doctoral en science et génie des matériaux

pour l'obtention du grade de Docteur ès Sciences

par

**Maya Nicole HARRIS**

Acceptée sur proposition du jury

Dr Y. Leterrier, président du jury
Prof. P. Bowen, Prof. K. Scrivener, directeurs de thèse
Dr M. Zajac, rapporteur
Dr D. Kulik, rapporteur
Dr A. Testino, rapporteur

École polytechnique fédérale de Lausanne

2022

# Abstract

This thesis investigates the effects of aluminates, sulfates, and heterogeneous substrates on the nucleation and growth of synthetic calcium-silicate-hydrates (C-S-H) produced by dropwise precipitation. The use of synthetic C-S-H, separate from other cementitious phases, allows formation mechanisms and kinetics effects to be investigated in a simplified system. The addition of other ions and substrates then allows an approach to the more complicated, multi-phase system of cement and concrete. The first goal of this thesis was to reproducibly synthesize single-phase C-S-H with Ca:Si from 1 to 2. Guidelines were described for collection, drying, and handling of the precipitates to prevent the formation of $Ca(OH)_2$ during synthesis and minimize carbonation. Interlayer spacing in precipitates was studied by transmission XRD to compare the effects of Ca:Si, relative humidity, and time, using the 14Å tobermorite structure as a baseline for synthetic C-S-H. This showed that with minimal drying, the interlayer space approaches 14Å, higher than previously studied in the dried, synthetic C-S-H system. Investigations on the effect of production method between synthesis in a batch reactor and in a continuous segmented flow tubular reactor (SFTR), showed that samples produced in the SFTR generally had higher water contents and higher interlayer spacings.

The growth and nucleation kinetics of C-S-H were then investigated with the combined thermodynamic and population balance equation model (PBEM). First, the model was expanded to include a larger thermodynamic database which allowed for the incorporation of aluminates and sulfates into equilibrium calculations. Additionally, a basic user-interface was added to allow the user to change between C-S-H systems previously restricted to Ca:Si of 2. The expanded model can calculate growth and nucleation outputs with or without collected kinetic data, and inputs can be modified in an excel spreadsheet. Saturation indices of C-S-H and portlandite were calculated for the full range of Ca:Si molar ratios and, and all showed $Ca(OH)_2$ to be undersaturated at Ca:Si from 1 to 2, confirming previous experimental data for the production of phase pure synthetic C-S-H. The five “unknown” parameters in the PBEM (interfacial

tension, cohesion energy, growth rate constant, the shape factor, and the kinetic order of growth) were then recalculated for C-S-H and C-S-H + sulfates ($) with Ca:Si molar ratio = 1.75. Reasonable values were obtained for interfacial tension and cohesion energy, although the possibility of $Ca^{2+}$ adsorption on the surface of precipitates may decrease the accuracy of these estimations. The pure-phase Ca:Si 1.75 sample exhibited a recalculated growth rate constant on the order of $10^{-10}$ $m^3/g^2$*mol*s, while the addition of sulfates resulted in a constant on the order of $10^{-8}$ $m^3/g^2$*mol*s. Comparison of supersaturation indices of CSH + $ at Ca:Si > 1.5 showed the simultaneous precipitation of $Ca(OH)_2$ with C-S-H, confirmed by XRD results, reducing the accuracy of the PBEM. As a result, the model needs further development for 2 phase systems. Kinetic data collection for calcium-aluminum-silicate hydrates (C-A-S-H) showed strong interference with the $Ca^{2+}$ ion selective electrode and secondary salt formation before reaction.

The surface characteristics of C-S-H, C-A-S-H, and C-S-H + $ were investigated by acoustophoresis to compare the effects of Ca:Si, washing, and dispersion media on zeta potential measurements. Results showed the necessity of full characterization of both solutions and precipitates in order to understand and compare acoustophoresis results. Zeta potential was observed to increase with increasing pH and Ca:Si when dispersed in both filtered supernatants and NaOH solution at a pH of 12. $Ca^{2+}$ desorption was indicated upon dispersing in NaOH solution rather than in filtered supernatant. C-S-H samples washed and re-dispersed in NaOH pH 12 solution were titrated with calcium solution and exhibited a partial reversibility of $Ca^{2+}$ adsorption. Potentials of C-A-S-H and C-S-H + $ were lower than measured on the C-S-H samples. To better understand how the surfaces change in response to such experimental modifications, the data will be evaluated in the light of recent atomistic simulations on C-S-H surfaces.

In the final section of the thesis C-S-H, C-A-S-H, and C-S-H + $ were grown on the surface of heterogeneous substrates, quartz and calcite, to approach C-S-H growth in real systems. Quartz exhibited slow dissolution, and small amounts of hydrates were observed on the surfaces of the substrate. C-A-S-H, produced by dropwise precipitation in the presence of quartz, exhibited denser nanofoils while

C-S-H + $ formed denser aggregates in comparison to the samples without quartz. Calcite dissolved partially in solution, allowing C-S-H and C-S-H + $ with fibrillar and ribbon morphologies with lengths of~1μm – 2μm after a month in solution. Calcite, placed in a silicate and aluminum solution exhibited the slow probable formation of C-A-S-H. In the first days, natrolite ($Na_2Al_2Si_3O_{10} * 2H_2O$) initially formed, and after a month calcium slowly incorporated into the structure, forming nanoglobules. After three months in solution, the sample exhibited a dense nanofoil morphology with a homogeneous distribution of Ca, Si, Al, O in STEM-EDX analysis.

Overall, the results from this thesis provided helpful information on synthetic C-S-H, C-A-S-H, and C-S-H + $ at the full range of Ca:Si molar ratios, particularly ratios above 1.5, as observed in Portland cement. As we get closer to understanding and controlling C-S-H in real systems, this work will help provide insight as to how heterogenous substrates and aluminates introduced by SCMs, in addition to sulfates, commonly added to cement via gypsum, affect the early age strength and kinetics of C-S-H formation.

## Keywords

Calcium silicate hydrate; synthetic C-S-H; dropwise precipitation; nucleation and growth; sulfates; aluminates; population balance equation model; heterogeneous substrates; calcite; quartz; SCMs; sustainability

# Résumé

Cette thèse étudie les effets des aluminates, des sulfates et des substrats hétérogènes sur la nucléation et le développement des hydrates de silicate de calcium synthétiques (C-S-H) produits par précipitation goutte à goutte. L'utilisation de C-S-H synthétique, séparé des autres phases cimentaires, permet des études des mécanismes de formation et les effets cinétiques dans un système simplifié. L'ajout d'autres ions et substrats permet alors une approche du système multiphase plus compliqué du ciment et du béton. Le premier objectif de cette thèse était de synthétiser de manière reproductible C-S-H monophasé avec Ca:Si de 1 à 2. Des directives ont été décrites pour la collecte, le séchage et la manipulation des précipitants afin d'empêcher la formation de $Ca(OH)_2$ pendant la synthèse et de minimiser la carbonatation. L'espacement entre les couches dans les précipitants a été étudié par DRX en transmission pour comparer les effets de Ca:Si, de l'humidité relative et du temps, en utilisant la structure de la tobermorite 14Å comme référence pour le C-S-H synthétique. Cela a montré qu'avec un séchage minimal, l'espace intercouche approche 14 Å, plus élevé que celui étudié précédemment dans le système C-S-H synthétique séché. Des études sur l'effet de la méthode de production entre la synthèse dans un réacteur discontinu et dans un réacteur tubulaire à flux segmenté continu (SFTR) ont montré que les échantillons produits dans le SFTR avaient généralement des teneurs en eau plus élevées et des espacements intercouches plus élevés.

La cinétique de croissance et de nucléation de C-S-H a ensuite été étudiée avec le modèle combiné d'équation thermodynamique et d'équilibre de population (PBEM). Tout d'abord, le modèle a été élargi pour inclure une plus grande base de données thermodynamique qui a permis l'incorporation d'aluminates et de sulfates dans les calculs d'équilibre. De plus, une interface utilisateur de base a été ajoutée pour permettre à l'utilisateur de changer entre les systèmes C-S-H auparavant limités à Ca:Si de 2. Le modèle étendu peut calculer les sorties de croissance et de nucléation avec ou sans données cinétiques collectées, et les entrées peuvent être modifiées dans un tableur excel. Les indices de saturation de C-S-H et de portlandite ont été calculés pour toute la gamme des rapports molaires Ca:Si et, et tous ont montré que $Ca(OH)_2$ était sous-saturé à Ca:Si de 1

à 2, confirmant les données expérimentales précédentes pour la production de phase pure C-S-H synthétique. Les cinq paramètres "inconnus" du PBEM (tension interfaciale, énergie de cohésion, constante de vitesse de croissance, facteur de forme et ordre cinétique de croissance) ont ensuite été recalculés pour C-S-H et C-S-H + sulfates ($) avec un rapport molaire Ca:Si = 1,75. Des valeurs raisonnables ont été obtenues pour la tension interfaciale et l'énergie de cohésion, bien que la possibilité d'adsorption de $Ca^{2+}$ à la surface des précipitants puisse diminuer la précision de ces estimations. L'échantillon de Ca:Si 1,75 en phase pure a présenté une constante de vitesse de croissance recalculée de l'ordre de $10^{-10}$ $m^3/g^2$*mol*s, tandis que l'ajout de sulfates a entraîné une constante de l'ordre de $10^{-8}$ $m^3/g^2$* mol*s. La comparaison des indices de sursaturation de C-S-H + $ à Ca: Si > 1, 5 a montré la précipitation simultanée de $Ca(OH)_2$ avec C-S-H, confirmée par les résultats DRX, réduisant la précision du PBEM. En conséquence, le modèle doit être développé davantage pour les systèmes à 2 phases. La collecte de données cinétiques pour les hydrates de calcium-aluminium-silicate (C-A-S-H) a montré une forte interférence avec l'électrode sélective d'ions $Ca^{2+}$ et la formation de sel secondaire avant la réaction.

Les caractéristiques de surface de C-S-H, C-A-S-H et C-S-H + $ ont été étudiées par acoustophorèse pour comparer les effets de Ca:Si, du lavage et des milieux de dispersion sur les mesures du potentiel zêta. Les résultats ont montré la nécessité d'une caractérisation complète des solutions et des précipitants afin de comprendre et de comparer les résultats d'acoustophorèse. On a observé que le potentiel zêta augmentait avec l'augmentation du pH et du Ca:Si lorsqu'il était dispersé dans les surnageants filtrés et la solution de NaOH à un pH de 12. La désorption de $Ca^{2+}$ était indiquée lors de la dispersion dans la solution de NaOH plutôt que dans le surnageant filtré. Les échantillons de C-S-H lavés et redispersés dans une solution de NaOH de pH 12 ont été titrés avec une solution de calcium et ont montré une réversibilité partielle de l'adsorption de $Ca^{2+}$. Les potentiels de C-A-S-H et C-S-H + $ étaient inférieurs à ceux mesurés sur les échantillons de C-S-H. Pour mieux comprendre comment les surfaces changent en réponse à de telles modifications expérimentales, les données seront

évaluées à la lumière de simulations atomistiques récentes sur des surfaces C-S-H.

Dans la dernière section de la thèse, C-S-H, C-A-S-H et C-S-H + $ ont été cultivés à la surface de substrats hétérogènes, quartz et calcite, pour approcher la croissance de C-S-H dans des systèmes réels. Le quartz a présenté une dissolution lente et de petites quantités d'hydrates ont été observées sur les surfaces du substrat. C-A-S-H, produit par précipitation goutte à goutte en présence de quartz, présentait des nanofeuilles plus denses tandis que C-S-H + $ formait des agrégats plus denses par rapport aux échantillons sans quartz. La calcite s'est dissoute partiellement en solution, permettant C-S-H et C-S-H + $ avec des morphologies fibrillaires et en ruban avec des longueurs de ~ 1 µm - 2 µm après un mois en solution. La calcite, placée dans une solution de silicate et d'aluminium a montré la lente formation probable de C-A-S-H. Dans les premiers jours, la natrolite ($Na_2Al_2Si_3O_{10} * 2H_2O$) s'est initialement formée, et après un mois, le calcium s'est lentement incorporé dans la structure, formant des nanoglobules. Après trois mois en solution, l'échantillon présentait une morphologie de nanofeuille dense avec une distribution homogène de Ca, Si, Al, O dans l'analyse STEM-EDX.

Dans l'ensemble, les résultats de cette thèse ont fourni des informations utiles sur les phases synthétiques C-S-H, C-A-S-H et C-S-H + $ à toute la gamme des rapports molaires Ca:Si, en particulier les rapports supérieurs à 1,5, comme observé dans le ciment Portland. Au fur et à mesure que nous nous rapprochons de la compréhension et du contrôle du C-S-H dans les systèmes réels, ce travail aidera à mieux comprendre comment les substrats hétérogènes et les aluminates introduits par les SCM, en plus des sulfates, généralement ajoutés au ciment via le gypse, affectent la résistance au jeune âge et la cinétique de formation de C-S-H.

## Mots-clés

Silicate de calcium hydraté; C-S-H synthétique, précipitation goutte à goutte ; nucléation et croissance ; sulfates ; aluminates ; modèle d'équilibre de population ; substrats hétérogènes ; calcite ; quartz, SCMs, durabilité

# Table of Contents

# List of Figures

# List of Tables

# Glossary

Notation of relevant oxide compounds

| | | |
|---|---|---|
| C | $CaO$ | Calcium oxide |
| S | $SiO_2$ | Silicon dioxide |
| H | $H_2O$ | Water |
| A | $Al_2O_3$ | Aluminum oxide |
| $ | $SO_3$ | Sulfate |
| F | $Fe_2O_3$ | Iron oxide |

Notation of relevant main anhydrous and hydrated phases of cement:

| | | |
|---|---|---|
| C-S-H | $CaO\text{-}SiO_2\text{-}H_2O$ | Calcium silicate hydrate |
| C-A-S-H | $CaO\text{-}Al_2O_3\text{-}SiO_2\text{-}H_2O$ | Calcium aluminum silicate hydrates |
| CH | $Ca(OH)_2$ | Calcium hydroxide or portlandite |
| Cc | $CaCO_3$ | Calcium carbonate |
| $C_3S$ | $3CaO{\cdot}SiO_2$ | Tricalcium silicate |
| $C_2S$ | $2CaO{\cdot}SiO_2$ | Dicalcium silicate |
| C3A | $3CaO{\cdot}Al_2O_3$ | Tricalcium aluminate |
| C4AF | $4CaO{\cdot}Al_2O_3{\cdot}Fe_2O_3$ | Tetracalcium aluminoferrite |

Notation of methods:

| | |
|---|---|
| XRD | X-ray diffraction |
| TGA | Thermogravimetric analysis |
| XRF | X-ray fluorescence |
| TEM | Transmission electron microscopy |
| ICP-OES | Inductively-coupled plasma spectrometry |
| Ca:Si | Calcium to silicon molar ratio |
| SCM | Supplementary cementitious material |
| SFTR | Segmented flow tubular reactor |
| PBEM | Population balance equation model |

# Chapter 1. Introduction

## 1.1 Background of cement

Cement and concrete are the highest produced man-made materials in the world. Concrete has been made since before the time of the Romans, and is composed of cement, aggregates, water, and air. Given the availability of raw materials, concrete and cement are produced worldwide, increasing 20% from 2010-2020 with demand from developing countries [1]. In 2015, cement generated 7-8% of global $CO_2$ emissions [2]. The main source of $CO_2$ emissions is the production of clinker in which raw materials, primarily limestone and clay, are heated to ~1450℃, or calcined, and then ground. Gypsum in small quantities is often added during this stage to control the setting of the cement [3]. During the calcination process, limestone (mainly $CaCO_3$) breaks down into CaO and $CO_2$.

To decrease $CO_2$ emissions, supplementary cementitious materials, SCMs, like fly ash and slag, are substituted for clinker in what are called blended cements. However, the addition of SCMs changes the chemistry of cement after hydration as studies have shown that reactivity and strength decrease with increasing SCM content [4].

This thesis is a part of the Engineered Calcim-Silicate-Hydrates for Applications (ERICA) project, funded by the European Union under the Horizon 2020 Marie Sklodowska-Curie Innovative Training Network Program (Grant Agreement No. 764691).

### 1.1.1 Cement hydration

Today, over 99% of cement is based on Portland cement [5]. There are four main anhydrous phases in Portland cement clinker. Alite (an impure $C_3S$) composes more than 50% by weight, followed by belite (an impure $C_2S$), tricalcium aluminate ($C_3A$), and tetracalcium aluminoferrite ($C_4AF$). In many cases, small amounts of gypsum are added into this mix to control reactivity. When water is added to cement, the following hydration products are formed via a dissolution precipitation process: calcium silicate hydrate (C-S-H), portlandite ($Ca(OH)_2$), ettringite, monosulfate aluminate hydrate, and aluminum hydroxides.

In the hydration of the primary anhydrous constituents of cement, alite and belite, calcium silicate hydrate, or C-S-H, is the main product formed. As a result, C-S-H makes up 50% - 60% of the solid volume of hardened cement paste, and is primarily responsible for the early age strength of cement [6]. Due to its higher reactivity, alite reacts with water before belite and produces the C-S-H that contributes to the early strength of cement after 2 hours to 14 days of hydration [6].

$$(C_3S, C_2S) + water \rightarrow C - S - H + portlandite + heat$$

The hydration of cement can be divided into six stages, displayed in Figure 1.1.1 which shows the heat released via calorimetry measurements and calcium concentration in the ensuing solution as a function of time [7], [8]. Upon the addition of water (stage 0), there is a rapid heat release in minutes which then, in the first stage, slows down rapidly. The second stage, or the induction period, shows a very low heat release for a couple of hours. The third stage is the acceleration period in which heat is released as $Ca(OH)_2$ and C-S-H grow rapidly, lasting 3 to 24 hours. This is then followed by stage four, the deceleration period, where $C_3S$ and $C_3A$ continue hydration but at a slower rate [9]. Finally, the hydration of $C_2S$ and $C_4AF$ primarily occurs, during the fifth stage in a slower hydration process.

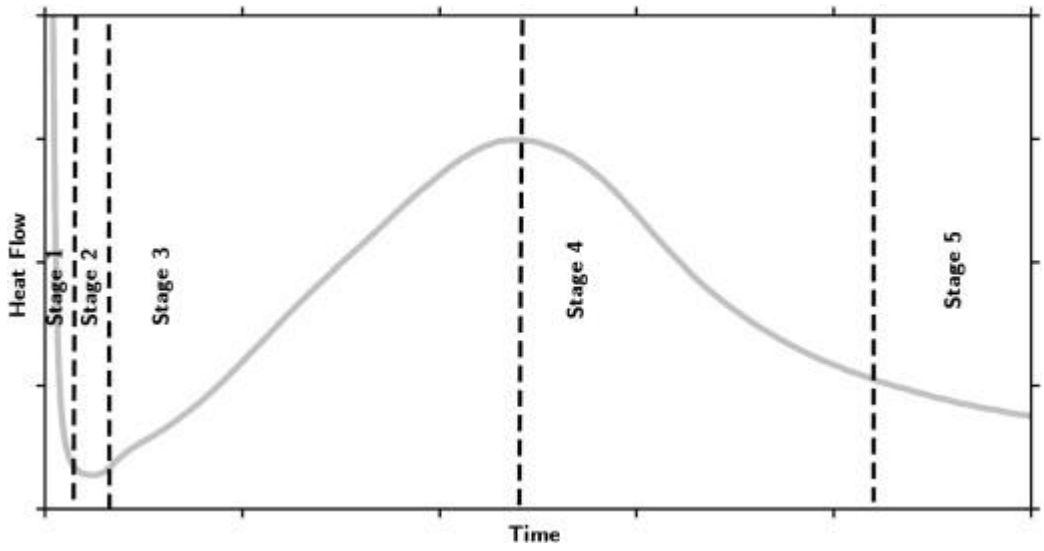


Figure 1.1.1 Schematic representation of heat flow evolution during the hydration of cement[7].

### 1.1.2 Calcium-silicate-hydrate (C-S-H)

C-S-H is the main hydration phase of ordinary Portland cement and is known to have a variable Ca:Si and water content. The Ca:Si (in cements) can range from 1.2 to 2.1 depending on the ions in the surrounding pore solution[10]. In hydrated cement pastes, the Ca:Si ratios most commonly observed tend to be between 1.5-2, averaging 1.7-1.8 in early age hydrated Portland cement pastes[10]. Water content in C-S-H has been difficult to characterize as drying and pore solution both affect the H:Si molar ratio, with a wide range from ~0.7-3.3[11]–[16].

On an atomic scale, the structure of C-S-H is similar to a defective 14Å tobermorite, composed of a double layer of Ca-O between drierketten silicate chains, separated by interlayers of water, hydroxyl groups, and calcium ions[14], [17], [18]. As C-S-H is poorly crystalline and difficult to characterize in among the other cementitious phases, researcher have used synthetic C-S-H to study the main hydration phase under more controlled conditions. To determine the structure of C-S-H, $^{29}$Si nuclear magnetic resonance (NMR) has been used to study the location of silicates in C-S-H and consequently the structure[19]. Figure 1.1.2 compares the atomistic structures of the 14Å tobermorite and the defective C-S-H with shorter drierketten chains, separated by calcium in the bridging site, denoted as $Q^{2b}$ in the figure[11], [17], [20], [21]. Using the 14Å tobermorite with a Ca:Si of 0.83 as a basis, researchers introduced defects into the mineral phase to reach ratios observed in cementitious systems[17], [22].

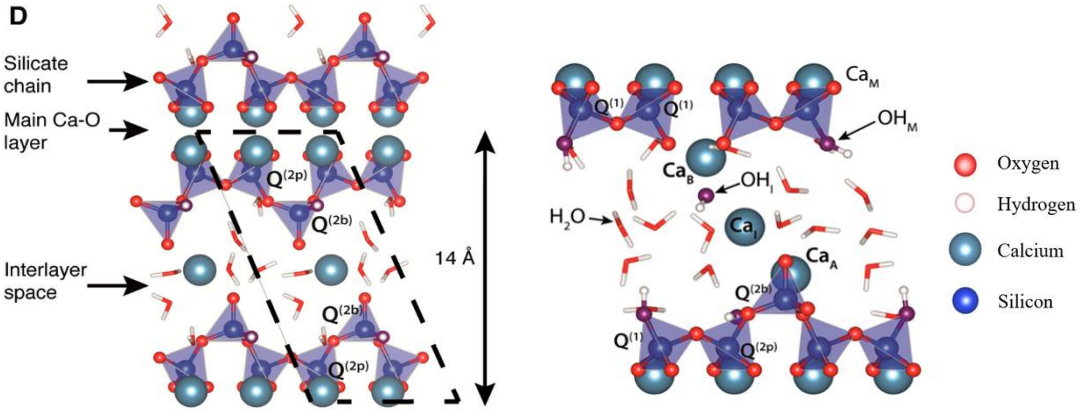


Figure 1.1.2 Atomic structure of (a) 14Å tobermorite and (b) C-S-H with defective drierketten chains[17] $Q^{(2b)}$ structures refer to bridging-type silicate tetrahedron surrounded on either side by $Q^{(2p)}$ pairing-type silicate tetrahedrons, $Q^{(1)}$ refers to silicate species terminating the chains

Over the past two decades, C-S-H has been synthesized separately from other cementitious phases to study strength, structure, and solubility of the main hydration phase[23]–[29]. Most commonly, synthetic C-S-H has been produced by combining CaO or $Ca(OH)_2$ with a reactive silica. However, at initial Ca:Si molar ratios of 1.5 and above, the C-S-H samples produced by this method form conjunctively with $Ca(OH)_2$, and the resulting C-S-H has a Ca:Si < 1.5. The C-S-H synthesized in this thesis is produced by the dropwise precipitation method in which reaction kinetics are controlled to avoid the supersaturation of portlandite[17], [30]–[32].

In applied systems, C-S-H is observed to have a fibrillar or needle-like morphology as it grows from cement grains[10], [33]. Synthetic C-S-H typically exhibits nanoglobule or nanofoil morphologies[17].

As the stoichiometric composition of C-S-H changes, and as sulfates and aluminate-rich SCMs are added into cements, the chemical properties of C-S-H change. Some of the underlying questions that need to be answered for more proper use of SCMs are: How do elements in SCMs, such as aluminates, affect the growth and nucleation of C-S-H? And on a smaller scale, how might the bulk and surface composition of C-S-H change? How does the homogeneous nucleation of synthetic C-S-H differ from heterogeneous nucleation in applied cements—is morphology modified, and could this modify mechanical properties on a larger scale? There are still many fundamental questions to be answered in regards to C-S-H in order to understand how the main hydration phase of cement nucleates and grows under different solution conditions.

## 1.2 Motivation & objectives

The main objective of this thesis is to investigate synthetic C-S-H with a broad range of Ca:Si molar ratios (1 to 2) with different solution compositions to slowly approach the complexity of applied systems. The precipitation of synthetic C-S-H in the presence of sulfates and aluminates is investigated. To approach the heterogeneous nucleation observed in applied systems, C-S-H is synthesized in the presence of quartz and calcite, which are substrates commonly found in modern blended cements. Water content, the kinetics of nucleation and growth, surface characteristics, and morphology are studied with the goal of better understanding C-S-H systems and how it acts in application.

In this thesis, C-S-H was produced using the dropwise precipitation method in which supersaturation is controlled by careful addition and mixing of reactants to achieve a homogeneous product[17], [32]. The effect of sulfates, aluminates, and Ca:Si on the growth and nucleation of synthetic C-S-H was investigated by the population balance equation model[30], [31]. C-S-H was also synthesized in a segmented flow tubular reactor (SFTR) to increase amount produced[34]. Samples were characterized and analyzed by wide-angle and transmission XRD, TGA, ICP-OES, XRF, TEM, STEM-EDX, and acoustophoresis. Thermodynamic modelling with GEMS and PhreeqC software was done to calculate aqueous speciation and supersaturation ratios at equilibrium to better understand results[35]–[37].

In summary, the purpose of this thesis is to contribute to bridging the gap between synthetic C-S-H and C-S-H in real systems. Sulfates and aluminates are commonly present in the main hydration phase, and C-S-H is known to grow heterogeneously. These factors are added to the synthetic C-S-H system in this thesis with the goal of shedding light on how the structure, morphology, aqueous speciation, growth and nucleation changes as studies approach more applied systems.

## 1.3 Organization of thesis

This dissertation is composed of eight chapters. A brief overview of cementitious materials and cement hydration is given in Chapter 1. In Chapter 2, characterization and analysis methods used extensively through this thesis are explained. Chapters 3-6 each describe different studies in this thesis, and specific literature reviews are given in the introduction of each section.

This thesis is organized as follows:

**Chapter 1**

Introduction – This chapter introduces the topic of the thesis in addition to a brief introduction on sulfates and aluminates in cementitious systems

**Chapter 2**

Materials and methodology – This chapter explains the characterization methods used including XRD, TGA, ICP-OES, XRF, TEM, and STEM-EDX

**Chapter 3**

Synthesis of C-S-H, scale-up & preliminary studies of interlayer water – This chapter presents a reproducible method to synthesize single-phase C-S-H at Ca:Si molar ratios from 1 to 2. Also, interlayer water spacing in synthetic C-S-H is studied under different production and drying methods.

**Chapter 4**

Kinetics of C-S-H – This chapter investigates the growth and nucleation of C-S-H at a fuller range of Ca:Si molar ratios, than previously attempted, by population balance equation modelling. Early studies on applying the model to C-S-H with the addition of sulfates and aluminates are also presented.

**Chapter 5**

Surface characteristics of synthetic C-S-H systems – This chapter analyses zeta potential measurements on C-S-H systems as Ca:Si, washing conditions, and dispersing media change to investigate how the surface of C-S-H terminates under different conditions.

**Chapter 6**

Heterogeneous substrates and synthetic C-S-H morphology – This chapter investigates the effects of calcite and quartz on the morphology of synthetic C-S-H with the goal of both emulating and understanding the morphologies observed in applied cementitious systems.

**Chapter 7**

Summary and conclusions of the thesis – This chapter summarizes these studies done on synthetic C-S-H and how this work can be continued based on the findings of this thesis to further benefit the cement community.

**Chapter 8**

Appendix

# Chapter 2. Materials & methodology

In this chapter, the preparation of synthetic C-S-H by dropwise precipitation in both a batch reactor and a segmented flow tubular reactor is described. Batch reactor synthesis is further detailed in Chapter 3. The preparation of synthetic C-S-H with the addition of sulfates, aluminates, and heterogeneous substrates is described in the relevant chapters. Many of the characterization methods including XRD, TGA, TEM, and ICP, used throughout this thesis are described in this chapter.

## 2.1 Thermodynamic Modelling, GEMS & PhreeqC

Thermodynamic modelling was done using the PhreeqC v.3 software and the Gibbs free energy minimization software, GEM-Selektor v.3 (GEMS)[35]–[37]. PhreeqC was developed by the U.S. Geological Survey for aqueous geochemical modelling. GEMS was developed at PSI, Viligen and EMPA, Dubendorf to compute chemical speciation and phase assemblage at equilibrium. In this thesis, these programs were used to predict speciation, phase assemblage, and reaction conditions for the synthetic C-S-H system. Databases used in this work are Cemdata 18.1, PSI Nagra, and the LLNL database[38]–[40]. Further details on solid solutions and C-S-H models used are given in Appendix I.

## 2.2 Sample synthesis

### 2.2.1 Dropwise precipitation

To prepare samples by dropwise precipitation, sodium metasilicate solution (100-200 mL) was placed into a reactor with 10M NaOH in different amounts, required to change the pH and control the resulting Ca:Si molar ratio. This solution was purged under 10mL/min of nitrogen flow for 30 minutes. Calcium nitrate solution (100 – 200 mL) was added at rates up to 2mL/min to the reactor at a temperature 19℃, and high mixing is maintained: 700 rpm for the first 30 minutes, and at 1100 rpm until collection. Throughout the reaction, pH (InLab Expert Pro-ISM-IP67, Mettler Toledo), and $Ca^{2+}$ concentration (perfectION$^{TM}$, Mettler Toledo) can be monitored[41]. After three hours, the sample was taken out of the reactor and stored in suspension. To prepare a wet sample, the solution was filtered and washed with 60 mL of a 1:1 decarbonated water and ethanol solution. To dry, a filtered and washed sample was placed in a -80℃ freezer for 24 hours and freeze dried for an additional 24-48 hours in an Alpha 1-2 LDplus freeze dryer operating at -50℃ and 0.01mbar.

### 2.2.2 Scaled-up synthesis, Segmented Flow Tubular Reactor (SFTR)

Samples were synthesized in a segmented flow tubular reactor (SFTR, Figure 2.2.1) [34]. The SFTR, pictured in Figure 2.2.2, consists of 40 meter long tube with an internal diameter of 4mm.

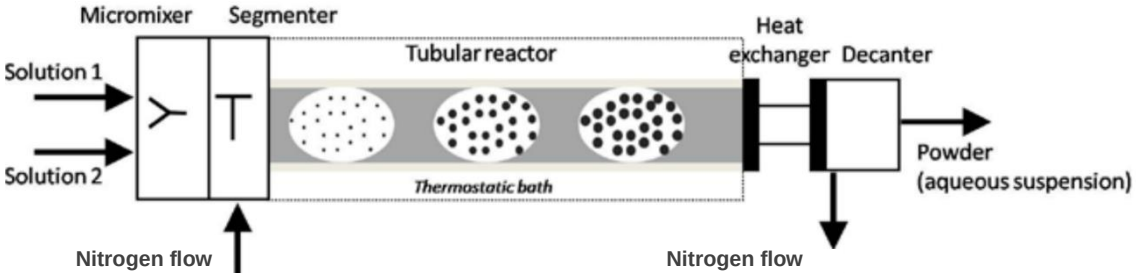


Figure 2.2.1 Diagram of Segmented Flow Tubular Reactor (SFTR)[34]

Calcium nitrate solution and sodium metasilicate solution with NaOH to control the pH and Ca:Si were simultaneously pumped into the SFTR. Reactants were pumped at a rate of 10mL/min and were mixed together with a passive micromixer which increased the effectiveness of mixing. The stream was then segmented inside of the reactor by a nitrogen flow. The volume of each segmented reactor was between 0.12-0.25 $cm^3$. After mixing in the SFTR, samples were collected at the end of the tube and allowed to mix with a magnetic stirrer for at least an additional 3 hours. Temperature was maintained at 19°C inside the reactor, and the reaction was kept at the control temperature during mixing.

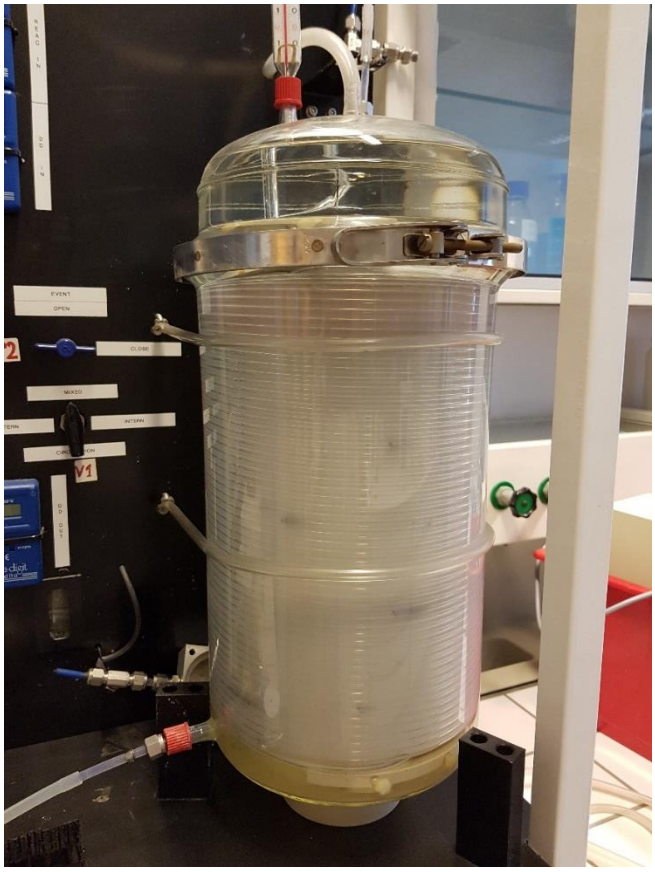

Figure 2.2.2 Picture of segmented flow tubular reactor

## 2.3 Characterization methods

### 2.3.1 X-ray diffraction (XRD)

Diffractograms of C-S-H were measured using CuKα-source XRD (PANanalytical) at a wavelength of 1.54Å with a fixed divergence slit. Both wide-angle X-ray (Bragg-Brentano) diffraction and transmission x-ray (Debye-Scherrer) diffraction was done.

*Wide-angle x-ray diffraction*

A fixed angle divergence slit size of ½ was used for XRD measurements. Both freeze-dried and filtered, wet samples were measured with this technique. Samples were prepared by the backloading process in which samples are loaded from behind to prevent ordering at the surface of measurement. Patterns were collected between 5° and 70° at 2Θ. The resulting XRD pattern was recorded by the X'PERT Data Collector software.

*Transmission x-ray diffraction*

A fixed angle divergence slit of ¼ was used for XRD measurements. Freeze-dried samples were analyzed using this technique. Samples were prepared in a 1mm outer diameter glass capillary with a 0.01mm wall thickness. Patterns were collected between 5° and 65° at 2Θ and the resulting XRD pattern was recorded by the X'PERT Data Collector software.

### 2.3.2 Thermogravimetric analysis (TGA)

TGA was performed on a Mettler Toledo AG (TGA/SDTA851e). Freeze-dried samples were heated at a rate of 10°C/min from 30°C to 1000°C under a flow of nitrogen at 10 mL/min.

### 2.3.3 Acoustophoresis

Zeta potential was measured with electroacoustics by the AcoustoSizer II supplied by Colloidal Dynamics, pH was also monitored. The equipment was calibrated with potassium silicotungstate (KSiW). Details of sample dispersion are given in the later chapters.

### 2.3.4 Transmission electron microscopy (TEM)

TEM samples were prepared on a carbon film 300 mesh grid, supplied by Electron Microscopy Sciences. The transmission electron microscope used for these studies was the Tecnai Osiris TEM, supplied with FEI. The microscope was operated at 200 kV in the TEM mode for diffraction analysis.

### 2.3.5 Inductively-coupled plasma spectrometry – optical electron spectroscopy (ICP-OES)

To measure elemental composition of samples, ICP-OES analyses were done. Freshly prepared filtered samples and supernatants were dissolved in 65% nitric acid, placed in an ultrasonic bath, and in a 50°C oven for 24 hours before being sent to the lab. Quantities and dilutions are specified in the relevant chapters. ICP was carried out on an ICPE-9000 Shimadzu instrument in optical emission spectroscopy.

### 2.3.6 X-ray fluorescence (XRF)

X-ray fluorescence spectroscopy was done on an Optim'X 9900 Ceram XRF model. 20 g of freeze-dried sample was further dried at 105°C for 24 hours and ignited at 950°C for 1 hour. 7.7 g of lithium tetraborate ($Li_2B_4O_7$) were added to the 0.7 g of the calcined sample to make a fused bead.

# Chapter 3. Synthesis of C-S-H, scale-up & preliminary studies of interlayer water

This chapter presents the developed protocol for the synthesis of C-S-H in the batch and segmented flow tubular reactors using the dropwise precipitation method. Thermodynamic modelling (GEMS, Cemdata 18.1) was used to predict how pH, temperature, and dilution effect the resulting Ca:Si of synthetic C-S-H. Additionally, preliminary studies of the interlayer were carried out with transmission XRD to understand the effects of Ca:Si and relative humidity on interlayer spacing.

## 3.1 A method for the reliable and reproducible precipitation of phase pure high Ca/Si ratio (>1.5) synthetic calcium silicate hydrates (C-S-H)

This section is based on a paper published in Cement and Concrete Research in 2022[32].

### 3.1.1 Abstract

Various methods have been developed to synthesize C-S-H; however, these methods have only allowed for the successful production of pure-phase C-S-H with Ca:Si of 1.5 or less. Attempts to form higher Ca:Si ratios by these methods gives C-S-H (Ca:Si 1.5 or less) in the presence of $Ca(OH)_2$. This paper focuses on a reliable method to produce single-phase C-S-H with Ca:Si molar ratios between 1 and 2. Reactant concentrations, temperature, pH, and mixing conditions are carefully controlled to ensure homogeneous precipitation of C-S-H. Guidelines on collection, drying, storage, and handling are also described.

## 3.1.2 Introduction

Calcium silicate hydrate, $CaO\text{-}SiO_2\text{-}H_2O$, or C-S-H, is the glue of Portland cement. Formed during the hydration of alite and belite, which together make up about 70-80% of Portland cement, C-S-H is the chief contributor to early-age strength and comprises around 50% of the solid volume of hardened cement paste[42]. With its strength and high specific surface area, applications of C-S-H range from construction to more biological applications[27], [43], [44].

C-S-H has a variable stoichiometry and water content. At early ages, the C-S-H in hydrated Portland cements has Ca:Si molar ratios between 1.7 and 2. It is possible to obtain C-S-H at a wide range of Ca:Si molar ratios from 0.7 to over 2, which is related to concentrations of Ca and Si in solution and the local pH[11], [17], [24].

Preparation of synthetic, single-phase C-S-H allows characterization of the main hydration phase without the presence of additional minerals. In work done over the past two decades, C-S-H has been synthesized in different ways to study solubility[23], structure and morphology[24]–[26], compressive strength[27], bioactivity, and setting[28], [29]. Most commonly, C-S-H has been synthesized by combining CaO or $Ca(OH)_2$ with a reactive silica and reacting for three to ten months[14], [16], [23], [25], [27], [45]–[49]. However, this synthesis route has been shown to only, reliably, produce single-phase C-S-H at Ca:Si molar ratios of 1.5 or below. Double decomposition of sodium silicate with a calcium salt has also been used to make synthetic C-S-H at a wide range of Ca:Si molar ratios, described in work done by Chen et al. and Lodeiro et al.[23], [50]. Samples with nominal Ca:Si of up to 1.9 were synthesized, but the samples were reported to have formed in conjunction with portlandite, and corrected Ca:Si ratios were not reported.

Kumar et al. succeeded in producing pure, single-phase C-S-H at a Ca:Si of 2 using a method which combines direct double decomposition and dropwise precipitation[17]. The experimental data obtained from this high Ca:Si C-S-H allowed an atomistic level model to be constructed that accounts for the full range of Ca:Si molar ratios. However, this synthesis method has proven to be difficult to replicate, and much like the other methods, targeting higher Ca:Si ratios has often resulted in producing C-S-H in conjunction with $Ca(OH)_2$ (portlandite), and/or $CaCO_3$ (carbonates).

Thermodynamic and kinetic modelling indicates that the Ca:Si of C-S-H produced in the method of Kumar et al. depends on the pH of the environment, and from kinetic modelling portlandite is never oversaturated in the media as long as care is taken to maintain proper mixing throughout the synthesis[30]. Despite this, we find in practice that portlandite and carbonates may form.

Much like any family recipe, there are one or two minor ingredients or tricks that make all the difference between high-quality, pure C-S-H and a mixed, poor-quality C-S-H.  In this work, we describe a reproducible protocol for pure, single-phase, synthetic C-S-H with Ca:Si molar ratios from 1 to 2 based on the dropwise precipitation method and GEMS thermodynamic modelling with the Cemdata 18.1 database[35], [36], [38]. The samples were characterized with X-ray diffraction (XRD), thermogravimetric analysis (TGA), x-ray fluorescence (XRF), and inductively coupled plasma spectrometry (ICP-OES) with the goal of defining the steps needed to produce pure C-S-H and determining which parameters affect the formation of secondary phases. To prevent the formation of impurities during collection, drying, storage, and handling; additional guidelines are provided.

### 3.1.3 Characterization methods

*X-ray Diffraction*

X-ray powder diffraction was carried out by a PANalytical X'pert X-ray diffractometer with an X'celerator detector with double bounced monochromatic CuK$\alpha_{1,2}$ radiation. Wet and dry C-S-H samples were prepared through the back-loading process, in which the sample holder is loaded from the rear, and placed on a rotating sample stage. The patterns were recorded between 5°-70° (2θ) with a fixed divergence slit of ½ and a step size of 0.017° for 30 minutes. XRD was used to observe the intrinsic C-S-H peaks at 29.4, 32.1, and 50.1 ± 0.1°[51], as well as any secondary phases.

*Thermogravimetric analysis*

To analyze samples by TGA, dried C-S-H was heated at a rate of 10℃/min from 30°C to 1000°C under a flow of nitrogen at 10 mL/min. The weight losses in relation to time and temperature were recorded on a Mettler Toledo AG (TGA/SDTA851e). Portlandite and calcium carbonate amounts were analyzed using the tangent method at temperatures between 400°C - 480°C and 600°C - 710°C, respectively, as described by Lothenbach et al.[52]. The tangent method reduces overestimation due to the continuation of water loss in C-S-H at higher temperatures.

*Inductively coupled plasma–optical emission spectrometry (ICP-OES)*

To prepare C-S-H samples for ICP analysis, 0.013 grams of freshly prepared, wet C-S-H was dissolved in 1 mL of 65% nitric acid and placed in an ultrasonic bath for 30 minutes. 9mL of 0.1M diluted aqua regia was added to each sample. The solution was placed in the ultrasonic bath for an additional 15 minutes, and then placed in a 50°C oven for 24 hours. Desired dilutions were prepared with decarbonated water. Acidified precipitate samples exhibited maximum concentrations of Ca, Si, and Na at 200, 100, and 100 mg/L, respectively.

To prepare a reaction supernatant sample for ICP, 2mL of supernatant were acidified in 3mL of 65% nitric acid. The solution was placed in an ultrasonic bath for 30 minutes. 4-fold, 10-fold, and 20-fold dilutions were made using decarbonated water. Acidified supernatant samples exhibited maximum concentrations of Ca, Si, and Na at 70, 5, and 2000 mg/L, respectively.

All diluted samples were stored in 15 mL polypropylene tubes and sent to Heidelberg Cement for analysis. ICP was carried out on an ICPE-9000 Shimadzu instrument in optical emission spectroscopy mode (ICP-OES).

*X-ray fluorescence spectroscopy (XRF)*

To cross check the ICP results, the C-S-H samples were analyzed using X-Ray fluorescence spectroscopy (Optim'X 9900 Ceram XRF model). 20 grams of hydrated sample were dried at 105°C for 24 hours and ignited at 950°C for 1 hour. 7.7 grams of lithium tetraborate ($Li_2B_4O_7$) were added to the 0.7 grams of the calcined sample to make a fused bead.

### 3.1.4 Reactor setup & operation

*Batch reactor*

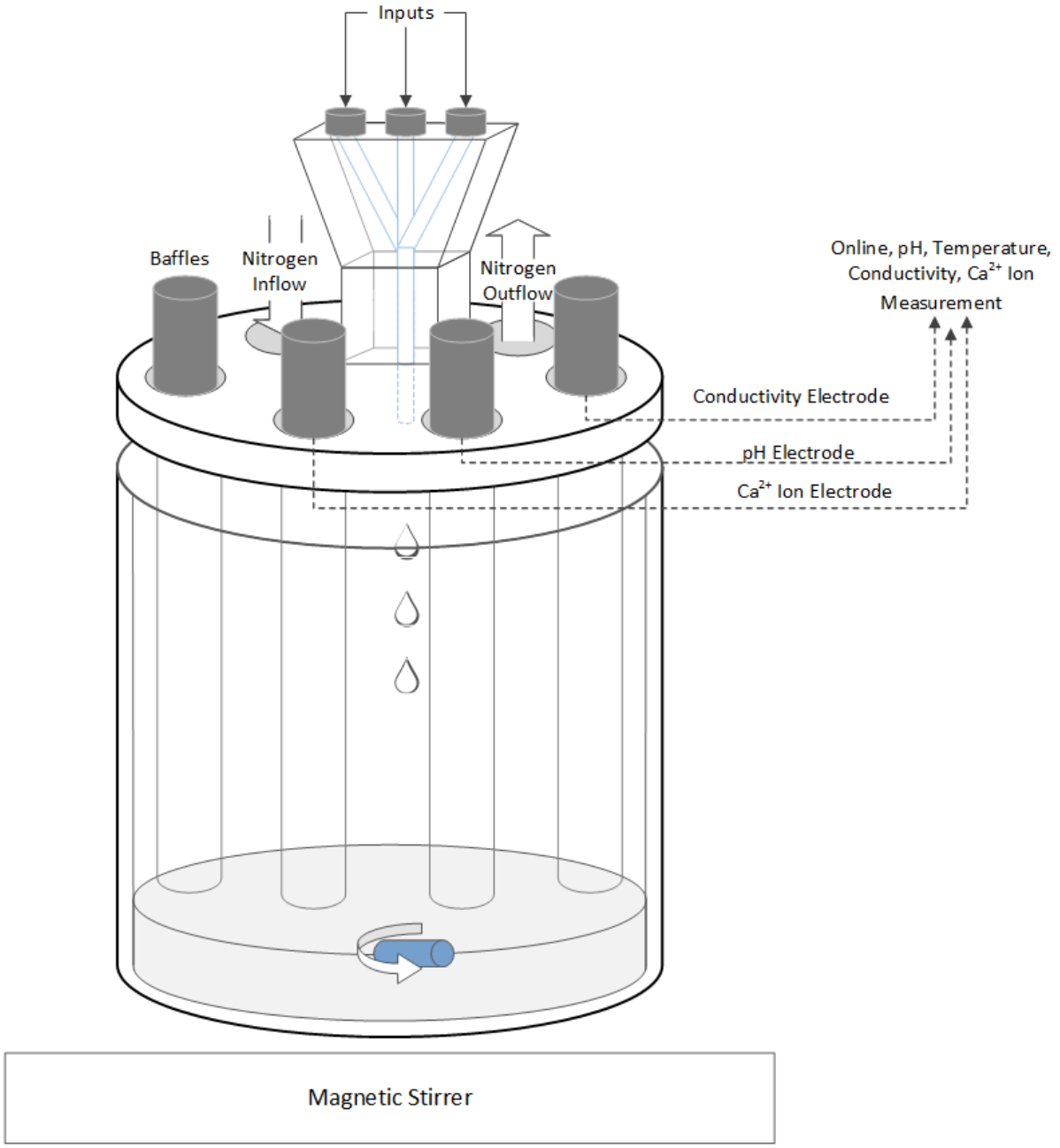


Figure 3.1.1 Schematic of batch reactor setup for dropwise precipitation of C-S-H[17], with slots in the lid for nitrogen purging and in-situ measurements.

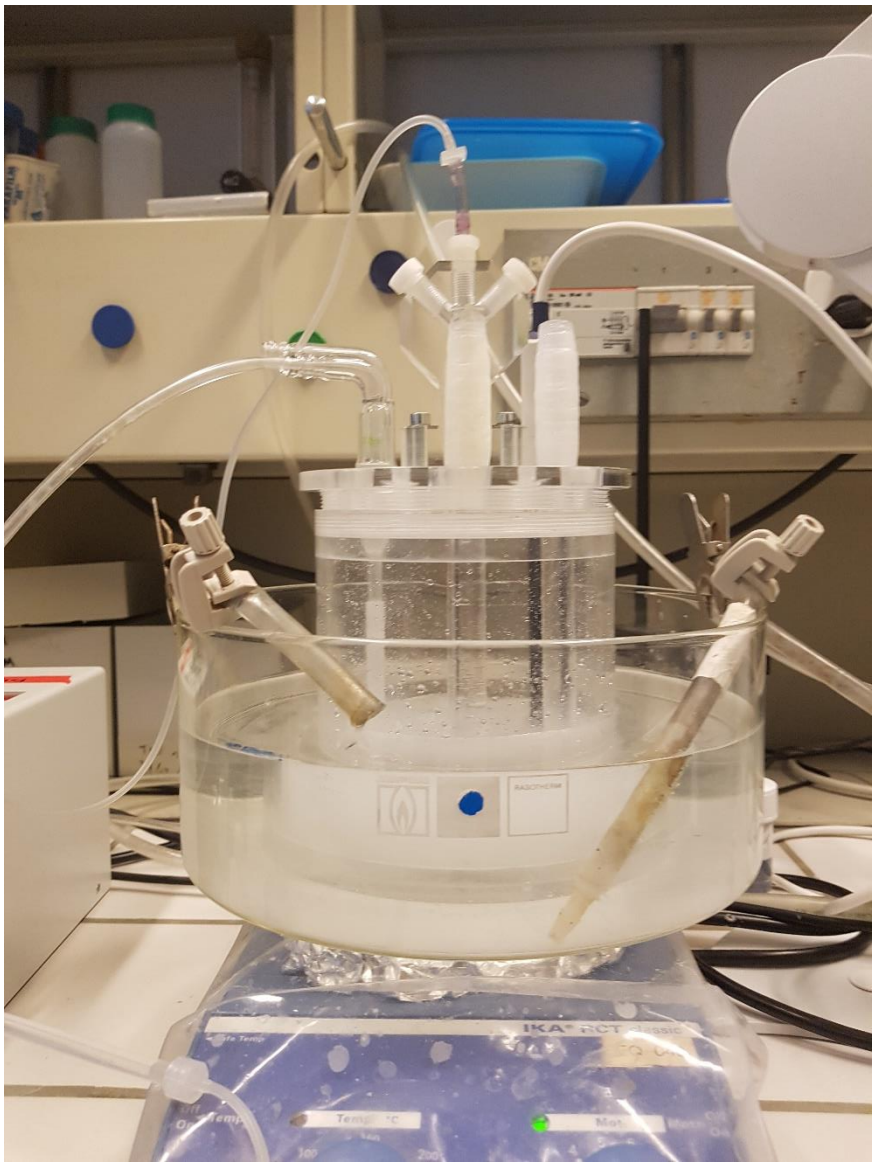

Figure 3.1.2 Picture of batch reactor, water bath, and magnetic stirrer for synthetic C-S-H synthesis

The C-S-H was synthesized in a 12cm diameter poly(methyl methacrylate) (PMMA) reactor, based on the setup of Kumar et al.[17] (Figure 3.1.1 and Figure 3.1.2). The reactor lid has six slots for in-situ measurements, PMMA bars to increase turbulence and mixing inside the reactor, and glass inlet and outlet tubes for a gas purge. A polyvinyl chloride (PVC) tube is placed at the bottom of the glass inlet. Additionally, a 3-input y-shaped micromixer system with a spiral static mixer is included.

A Mettler Toledo InLab Expert Pro ISM-P67 pH electrode and a Mettler Toledo perfectION Combination calcium electrode were used for in-situ measurements, collected on Mettler Toledo Easy Direct software. The reactor was placed in a bath and the temperature was regulated by a thermostat at 19°C.

Solutions were introduced to the reactor by an ISMATEC REGLO-CPF Analog piston pump with an RH0.CTC pump head, and after synthesis, the precipitate was collected via a vacuum-filtration system on a 200nm filter paper (Whatman ME 24/21 STL). Calcium nitrate ($Ca(NO_3)_2 * 4H_2O$, CAS: 13477-34-4) and sodium metasilicate ($Na_2SiO_3$, CAS: 6834-92-0) were supplied from Sigma-Aldrich. NaOH pellets were supplied from Acros Organics (CAS: 1310-73-2), and ethanol was supplied from Reactolab S.A.

*Solution preparation*

Before synthesis, all parts of the apparatus were washed with deionized water and dried in a laminar flow hood. Piston pump tubes were purged with a solution of 50% ethanol, 50% pure water, and rinsed with a 50 mL solution of pure water before and after use. Ion electrodes and pH meters were stored in the respective storing solutions, calibrated twice before use, and washed with deionized water.

Solutions of calcium nitrate, sodium metasilicate, and sodium hydroxide were prepared with decarbonated water. During and after preparation, the solutions were covered with a lid to avoid any contamination by dust. The solutions were stored for a maximum of two weeks before use.

### 3.1.5 Synthesis

*Mix design*

The Gibbs Energy Minimization Software or GEMS and the Cemdata 18.1 database were used to simulate the relationship between Ca:Si ratio of synthetic C-S-H and pH as alkalis were added to the system[35], [36], [38]. The CSHQ and CNASH_ss solid solution models were used to make thermodynamic calculations[38]. As the solubility of portlandite is inversely proportional to temperature, it is easier to avoid portlandite precipitation at lower temperatures. As a result, the temperature in all simulations was maintained at 19°C. 100 mL of 0.224M calcium nitrate and 0.1M sodium metasilicate were simulated at equilibrium with varying amounts of pH regulator, NaOH, as shown in Table 1 to achieve the listed target Ca:Si values.

Table 3.1.1 Cemdata 18.1-modelled pH equilibrium values and required 10M NaOH solution volume for target Ca:Si molar ratio in absence of $Ca(OH)_2$ and total reaction volume of 200 mL[35].

| **Target Ca:Si** | **pH** | **10M NaOH solution** |
|---|---|---|
| 1 | 11.4 | 75 µL |
| 1.25 | 11.9 | 675 µL |
| 1.5 | 12.5 | 1.625 mL |
| 1.75 | 12.9 | 3.475 mL |
| 2 | 13.5 | 10 mL |

*Synthesis & drying*

100 mL of 0.1M sodium metasilicate solution was placed in the reactor with the required amount of 10M NaOH solution for each Ca:Si ratio, as listed in Table 3.1.1, and conditions for thermodynamic calculations are further described in Appendix I. The batch reactor was placed in a thermostat-controlled water bath at a temperature of 19°C to reduce the chance of portlandite formation. The reactor was then purged under a flow of nitrogen at 10 mL/min and mixed at 700 RPM for a minimum of 30 minutes to ensure even distribution of alkali. Once the reactor reached the desired temperature, the mixing speed was increased to 1100 RPM, and 100 mL of 0.224M calcium nitrate solution was pumped into the reactor at a rate of 2 mL/min.

After a minimum of three hours of reaction, the precipitate was taken out of the reactor and stored in suspension. To prepare a wet sample for analysis, the suspension was filtered and washed with 60 mL of a 1:1 pure water and ethanol solution. To dry, 25 grams of a filtered and washed sample were placed in a -80°C freezer for 24 hours and freeze dried for an additional 24 hours in an Alpha 1-2 LDplus freeze dryer operating at -50°C and 0.01 mbar, yielding 5-7 grams of dried sample.

## 3.1.6 Results

*Precipitate characterization: pure synthetic C-S-H*

The X-ray diffractograms in Figure 3.1.3 display the characteristic peaks of C-S-H at 29.4, 32.1, and 50.1 ± 0.1° 2θ for all C-S-H samples[51]. The diffractogram of the wet sample, immediately after filtration, exhibits a broad water peak. As C-S-H is poorly crystalline, the C-S-H peaks are still broad after drying, but no secondary phases are observed.

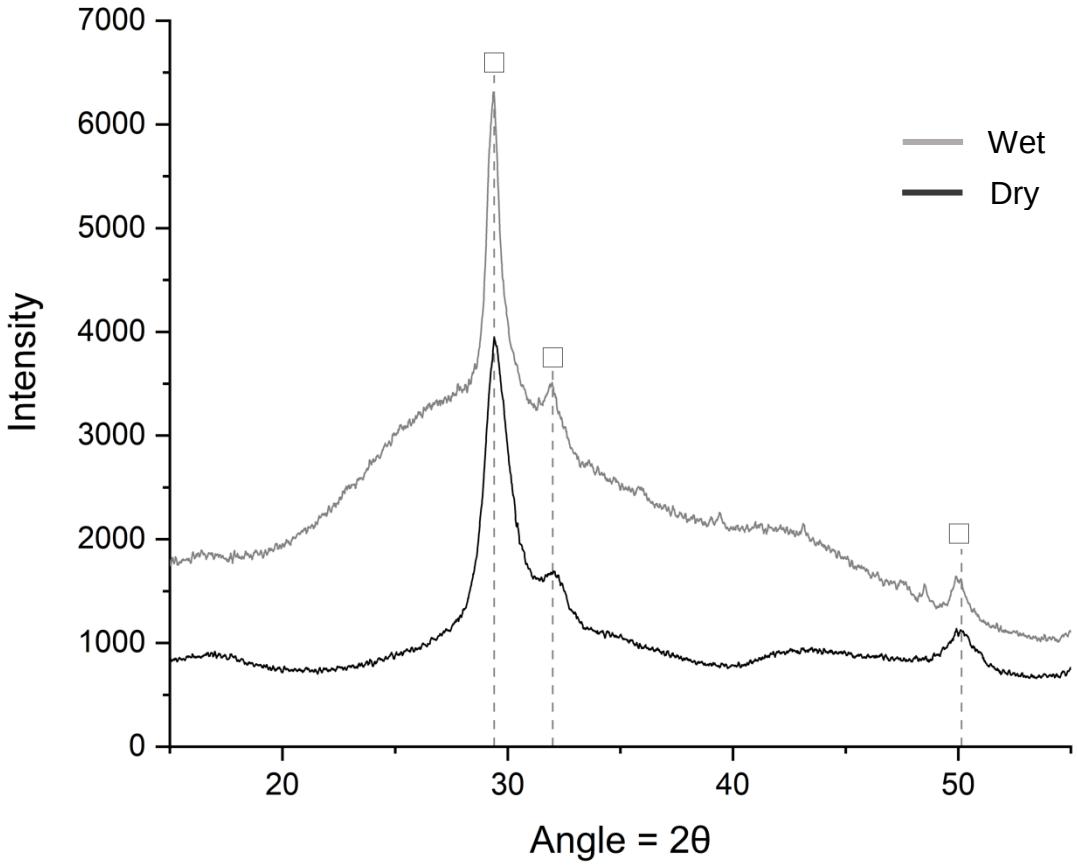


Figure 3.1.3 Filtered wet (gray) and freeze-dried (black) x-ray diffraction patterns of a pure C-S-H sample. C-S-H peaks are marked by, □. Ca:Si = 1.3

All C-S-H, of both high and low Ca:Si, is susceptible to carbonation on exposure to air[17]. Figure 3.1.4 shows the differential thermogravimetric (DTG) analysis of the same Ca:Si = 1.3 sample analyzed above. As for the XRD diffractogram, no portlandite is observed. The sample exhibits some decomposition due to the presence of carbonates, possibly both amorphous and crystalline, represented by the losses between 600 and 800°C. Losses due to carbonation are observed in C-S-H samples both with and without the formation of portlandite, and can also be seen in Figure 3.1.6 and Figure 3.1.7.

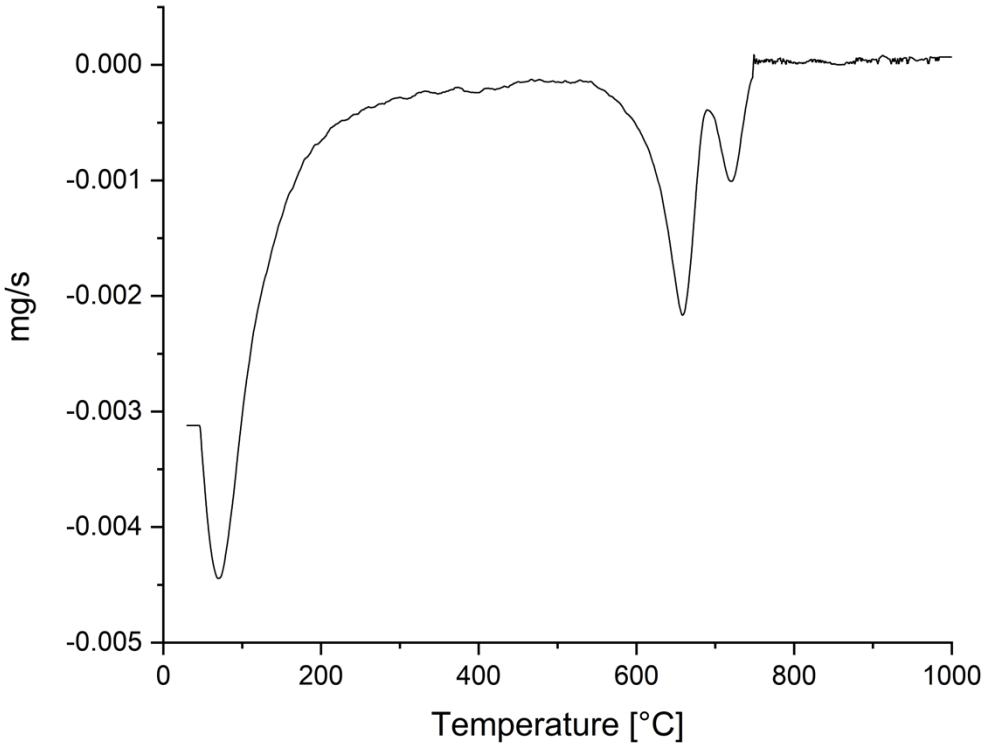


Figure 3.1.4 Differential thermogravimetric analysis (DTG) of pure C-S-H sample exhibiting losses due to both crystalline and amorphous carbonation between 600 and 800°C, Ca:Si = 1.3

*$Ca(OH)_2$ formation in synthetic C-S-H*

High Ca:Si C-S-H gives the same diffraction patterns as its lower Ca:Si counterpart. However, as the Ca:Si exceeds 1.5, portlandite formation is more often observed, affecting the actual Ca:Si of the C-S-H. Figure 3.1.5 shows the diffraction patterns of two dried samples with target Ca:Si of 1.9. In the XRD of the second sample, portlandite peaks are observed.

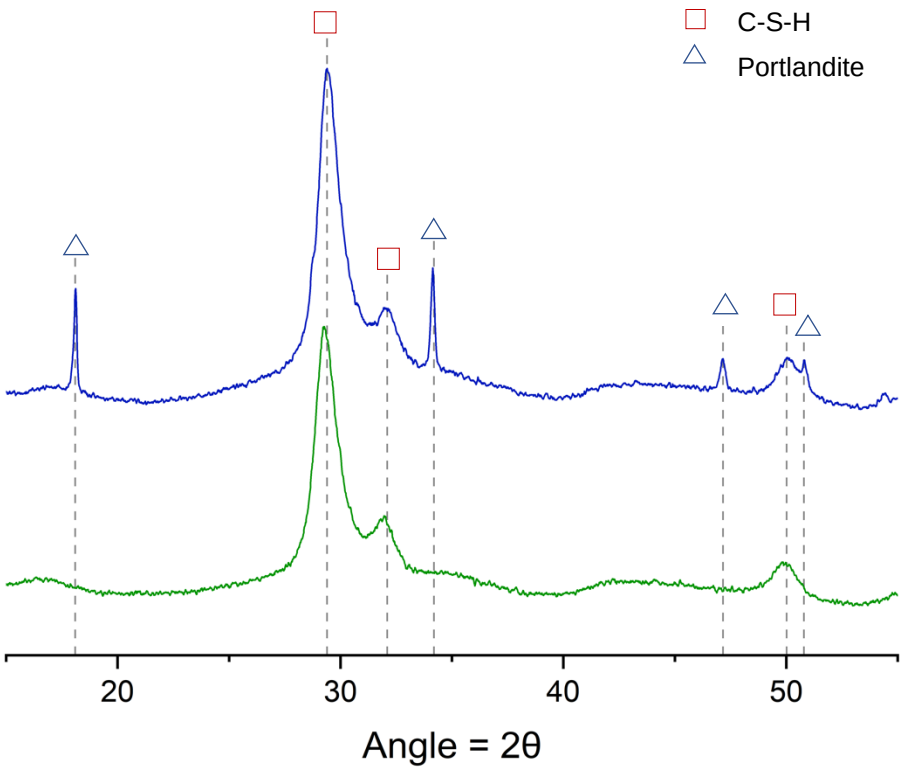


Figure 3.1.5 Pure (green) and impure (blue) C-S-H with nominal Ca:Si = 1.9 .

In Figure 3.1.6, thermogravimetric analysis of a nominal Ca:Si =1.9 sample which exhibited portlandite peaks shows a decomposition from the presence of portlandite at 400°C and carbonation around 600°C. If the amount of portlandite measured by TGA is taken out of the overall mass, the recalculated Ca:Si of the C-S-H is 1.8. If decomposition due to carbonation is also attributed to portlandite, the new adjusted Ca:Si becomes 1.73. ICP-OES analysis for this sample measured a Ca:Si of 1.79, suggesting that the majority of measured carbonation is of C-S-H itself and not of portlandite, and therefore does not affect the calculated Ca:Si of the C-S-H before carbonation. Figure 3.1.7 shows the thermogravimetric analysis of a nominal Ca:Si = 1.9 sample which exhibited only losses due to carbonation.

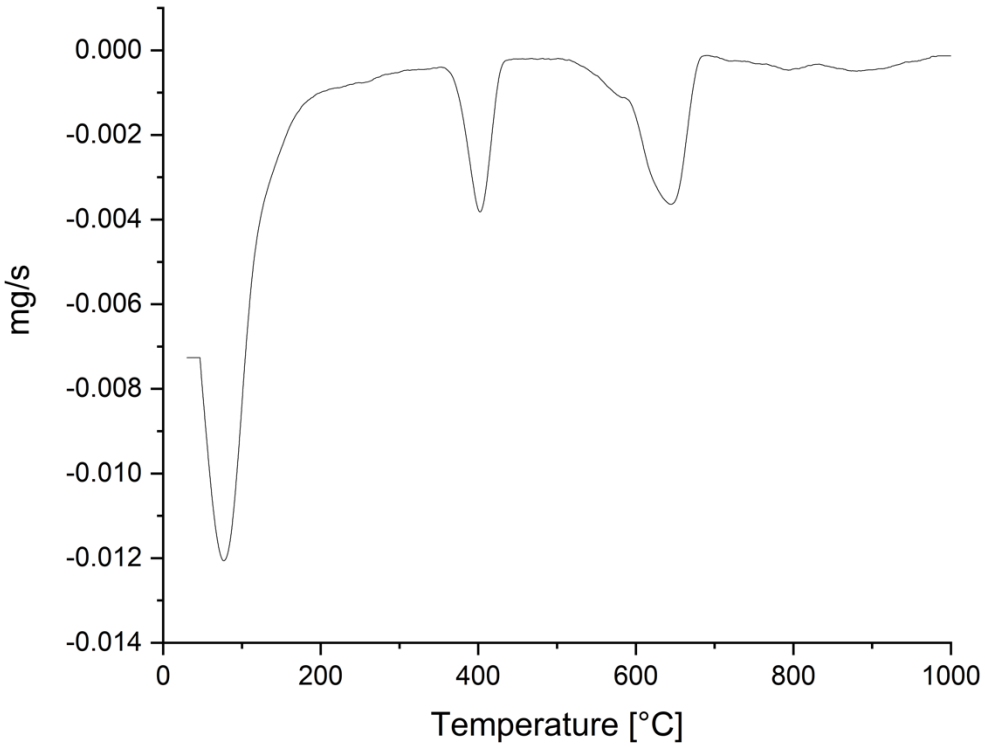


Figure 3.1.6 Differential thermogravimetric analysis (DTG) of impure C-S-H sample exhibiting losses due to the presence of portlandite at 400°C and losses due to both amorphous and crystalline carbonation between 600 and 800℃, Nominal Ca:Si = 1.9

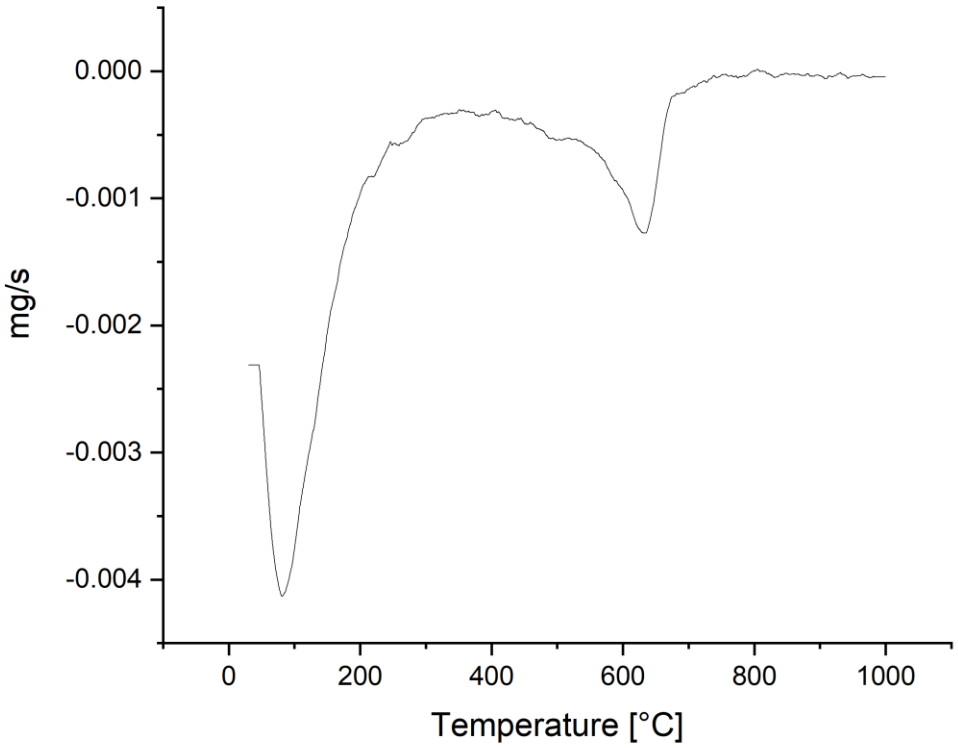


Figure 3.1.7 Differential thermogravimetric analysis (DTG) of impure C-S-H sample exhibiting losses due to carbonation between 600 and 800℃, Nominal Ca:Si = 1.9

*An overview of synthesized samples*

The Ca:Si molar ratios of 46 samples from TGA analysis versus the target ratio are plotted in Figure 3.1.8. The boxes in orange show recalculated Ca:Si values which account for both carbonation and portlandite decomposition peaks as sources of portlandite. The green boxes show the recalculated Ca:Si values, assuming that the portlandite peaks are the only source of portlandite in the samples. C-S-H at both high and low Ca:Si carbonates slightly in the TGA environment. As a result, the most accurate recalculated Ca:Si molar ratios can be represented by the green boxes. Pure, single-phase C-S-H was obtained at all nominal Ca:Si molar ratios, and the maximum pure Ca:Si produced was between 1.93 and 2. Of the samples plotted in Figure 3.1.8, 60% were single-phase C-S-H, 24% of samples formed portlandite and have recalculated ratios within 2% of the nominal value.

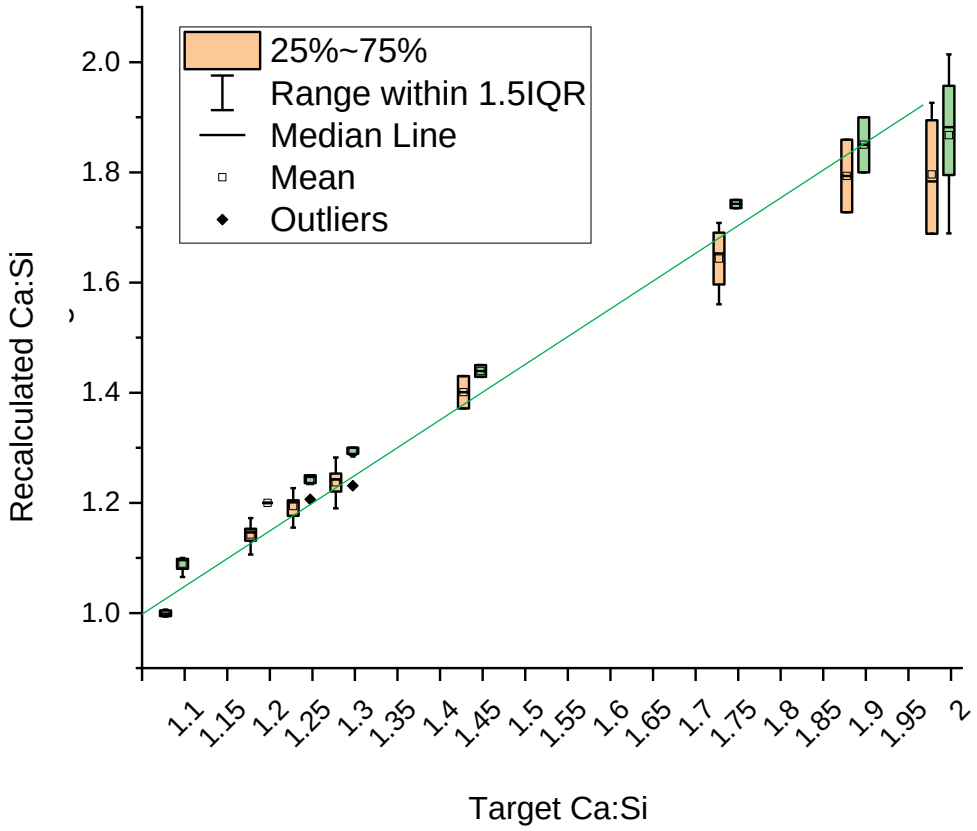


Figure 3.1.8 Plot of target Ca:Si molar ratios vs ratios from TGA analysis for 46 C-S-H samples, based on decomposition due to portlandite only (green), and decomposition from portlandite + carbonated portlandite (orange). Green line represents target Ca:Si. Ranges within 1.5 of the interquartile range (IQR) are shown.

Figure 3.1.9 shows Ca:Si molar ratios, calculated from measurements of calcium and silicon in the precipitates with ICP and XRF. Lower Ca:Si molar ratios display a good correlation with the target ratios; however, at Ca:Si molar ratios of 1.8 and higher, the measured Ca:Si values are higher than the targeted ratios, most notably in samples with target ratios of 1.9 and higher, possibly due to adsorbed calcium at the surfaces that is not accounted for in the stoichiometric reaction as discussed in more detail below.

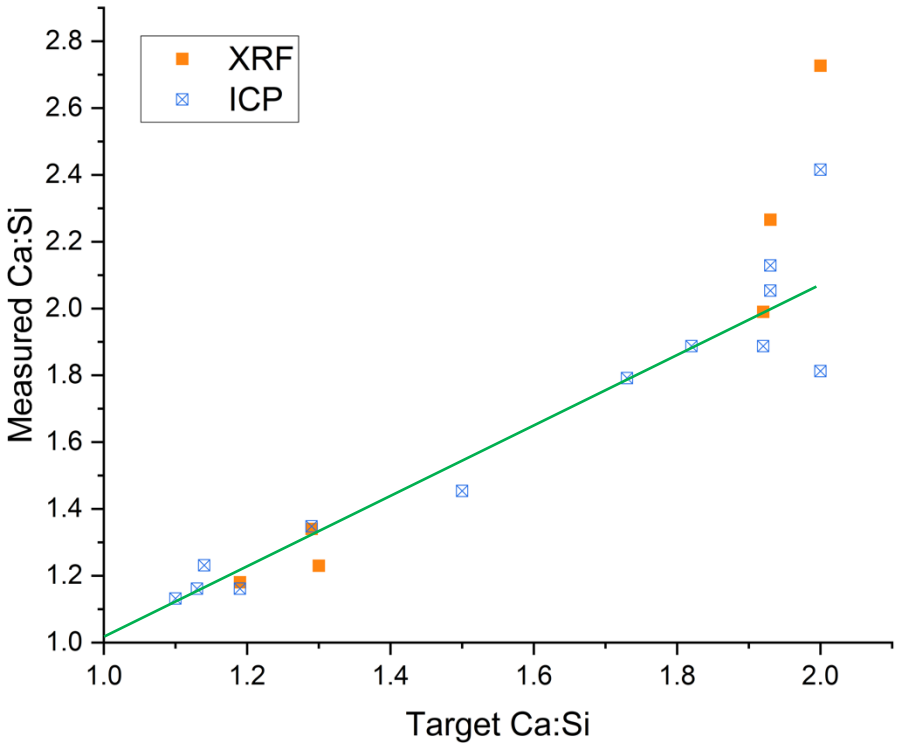


Figure 3.1.9 Nominal Ca:Si molar ratios as measured by X-ray fluorescence (XRF)(orange) and inductively coupled plasma spectrometry (ICP-OES)(blue). Green line represents target Ca:Si.

Three samples which showed no portlandite peaks by XRD, were analyzed by XRF, ICP, and TGA to determine how the experimental Ca:Si ratios compared to the target values. The results are displayed in Table 3.1.2.

Table 3.1.2 Comparison between target Ca:Si molar ratio and Ca:Si molar ratios measured by XRF, ICP, and TGA with portlandite (CH) and carbonates (Cc). An average error of all experimental data with respect to each target ratio is given.

| Target | XRF | ICP | TGA w/ CH | TGA w/ CH & Cc | Avg % Error |
|---|---|---|---|---|---|
| **1.19** | 1.18 | 1.16 | 1.19 | 1.17 | 1.26% |
| **1.35** | 1.34 | 1.34 | 1.35 | 1.33 | 0.74% |
| **1.95** | 1.99 | 2.05 | 1.95 | 1.93 | 2.05% |

The sample with the target Ca:Si of 1.95 exhibited slightly higher measured Ca:Si molar ratios in XRF and ICP while the lower Ca:Si samples show very close correlation with the targeted value. Overall, the results are consistent between the three methods within the expected error of the measurements

*Supernatant analysis*

Comparison of supernatant analysis between thermodynamic modelling and ICP shows that GEMS predicts a higher amount of calcium and sodium in the supernatant than measured empirically. At a nominal Ca:Si of 1.7, GEMS predicts a concentration of 3.8mmol/L while only 0.39mmol/L of calcium is measured. As the Ca:Si ratio increases, the discrepancy between GEMS calculations and measurements increases.

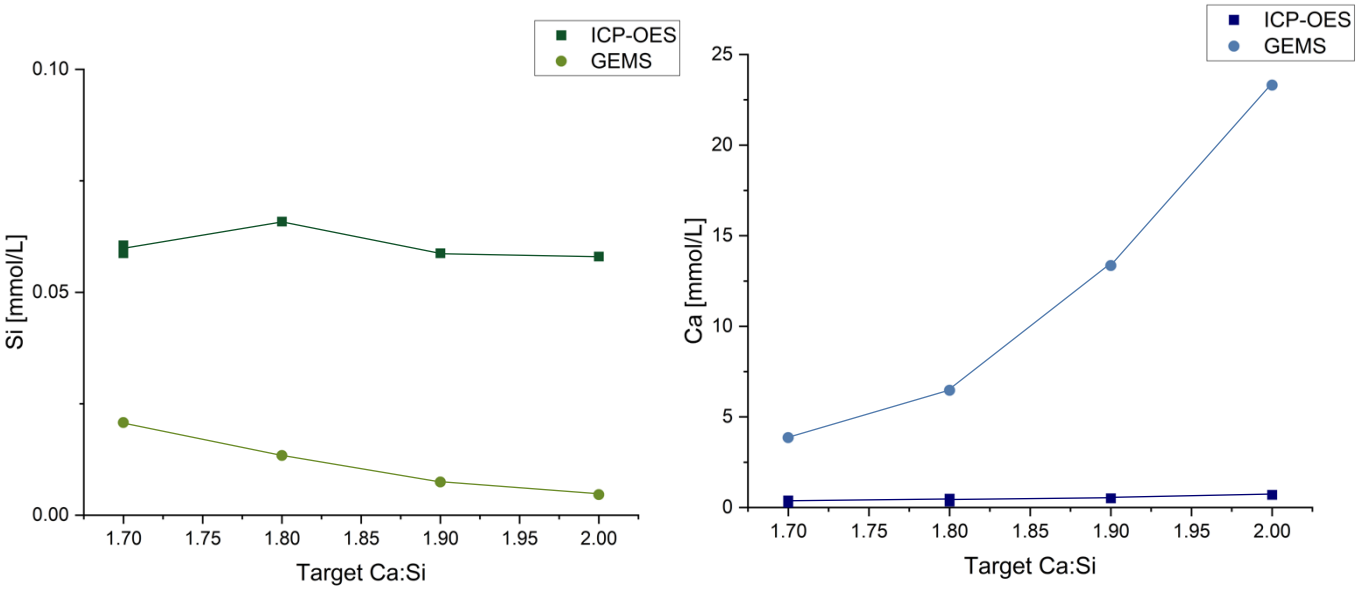


Figure 3.1.10 Silicon (green) and calcium (blue) concentrations in supernatants, Cemdata 18.1-calculated & measured (ICP-OES)

At a nominal Ca:Si of 2.0, thermodynamic modelling predicts a Ca concentration of 23.3mmol/L to be compared with the measured value of 0.69mmol/L. These results suggest that there could be an adsorption of calcium on the surface of the C-S-H, and that the amount of adsorption increases with increasing Ca:Si. This is consistent with the higher Ca:Si ratios observed in the ICP-XRF data in Table 3.1.2 and Figure 3.1.9 and the lower concentrations of calcium measured in the supernatants. The amount of calcium adsorbed seems to be closely related to the Ca/Si ratio.

GEMS predicts a silicon concentration that is significantly lower than the measured value in the supernatant samples over the full range of Ca:Si molar ratios. GEMS calculates silicon concentrations between 0.0005 and 0.02mmol/L. Measured concentrations range between 0.05-0.06mmol/L.

Some discrepancy between GEMS and measured concentrations is expected as GEMS provides equilibrium values and does not factor surface complexation into the calculations[35], [38]. Additionally, the lower amounts of calcium and sodium in the supernatant are coherent with the higher amounts of calcium measured in the precipitates, suggest that as the Ca:Si molar ratio increases, the adsorption of calcium and sodium on the surface of C-S-H also increases. Interfacial concentration profiles such as those predicted by Labbez et al.[53] would be needed to further evaluate this proposed adsorption phenomena, but are outside the scope of this manuscript.

*Supersaturation condition*

The precipitation of C-S-H is a thermodynamically driven process, and the preferential formation of high Ca:Si C-S-H over portlandite can be understood by comparing the saturation indices of the two hydration products as the reaction proceeds.

The saturation index compares the activity products of ions composing a phase at a current state versus the liquid-solid equilibrium state[54]. For a solid phase of composition $A_aB_b$, the stoichiometric solubility product, $K_{sp}$, can be described in the law of mass action as a product of activities, demonstrated in Equation 3.1.

$$K_{sp} = \frac{\{A\}^a\{B\}^b}{\{A_aB_b\}} = \{A\}_{eq}^a\{B\}_{eq}^b \quad (3.1)$$

The denominator of Equation 3.1, $\{A_aB_b\}$ demonstrates that the activity of a pure phase is 1. A $K_{sp}$ above 1 indicates solubility, and below 1 indicates insolubility in media at chemical equilibrium. For a solution out of equilibrium, the ion activity product is described in Equation 3.2.

$$IAP = \{A\}_{actual}^a\{B\}_{actual}^b \quad (3.2)$$

The saturation index, demonstrated in Equation 3.3, is a ratio comparing the IAP and the $K_{sp}$.

$$SI = \frac{IAP}{K_{sp}} \tag{3.3}$$

When the IAP is equal to the $K_{sp}$, the saturation index is at equilibrium, or saturated. When the IAP is below the $K_{sp}$, the SI is below 1 and undersaturated, and when the IAP is above $K_{sp}$, the SI is above 1 and is supersaturated.

Saturation indices of C-S-H and portlandite were calculated for the described synthetic C-S-H recipes with the population balance model of Andalibi et al.[30], [31]. For Ca:Si ratios of 2 and 1.75, the saturation indices of C-S-H are above 1 throughout the reaction. Meanwhile the indices of portlandite are below 1, which remains undersaturated throughout.

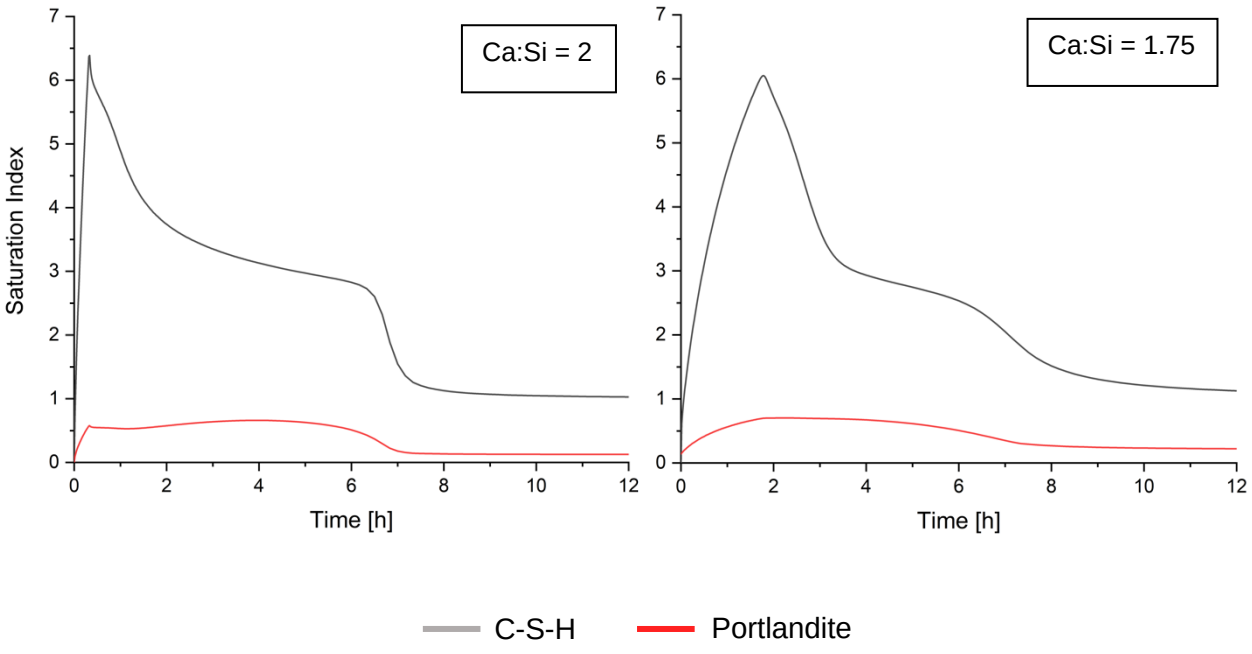


Figure 3.1.11 Saturation indices for synthetic C-S-H (black) and portlandite (red) Ca:Si = 1.75 and 2, calculated with the population balance model

The well-mixed system favors C-S-H precipitation without the precipitation of a second phase. Not only is the C-S-H saturation index 8 to 10 times higher than the saturation index of portlandite, but also the saturation index of portlandite never reaches 1 and portlandite is always preferentially soluble in the media.

In previous experiments to synthesize C-S-H, the Ca:Si ratio plateaus at 1.5 as the solubility of portlandite lowers with increasing pH, and high pH, ~12.4 and above, is required for high ratio C-S-H [11], [17]. As a result, in a poorly mixed system, or in a system in which the calcium solution is added too quickly to the reactor higher concentrations of hydroxide ions may occur locally, increasing the chance for portlandite formation in conjunction with C-S-H.

In a synthetic system in which the initial concentrations are controlled to create supersaturation conditions for C-S-H, and in a system in which the reactants are added at the correct rate and the total reactor volume is small enough and well designed to ensure proper mixing, the preferential precipitation of C-S-H and C-S-H alone can be assured.

### 3.1.7 C-S-H filtering, storage & handling

*Filtering & collection*

After a minimum of three hours of reaction, the precipitate was removed from the reactor and stored in suspension or collected through vacuum filtration. The suspension was filtered until 100mL remains unfiltered. The suspension was then washed with 60 mL 1:1 pure water and ethanol solution, and filtered again until the C-S-H had a wet paste consistency.

To prevent the formation of portlandite during vacuum filtration, enough supernatant was kept in the sample to prevent the compact cracking, effectively keeping the precipitate in an equilibrium. Similarly, when precipitates are not filtered for long enough and form a soupy paste, the C-S-H is more prone to carbonation.

*Storage and handling*

Synthetic C-S-H can be stored both wet and dry. For stability, samples are best kept as sealed suspensions. If precipitated in accordance to the protocol, synthetic C-S-H will not form any additional or undesired phases in equilibrium with the reaction liquor, and will remain in equilibrium.

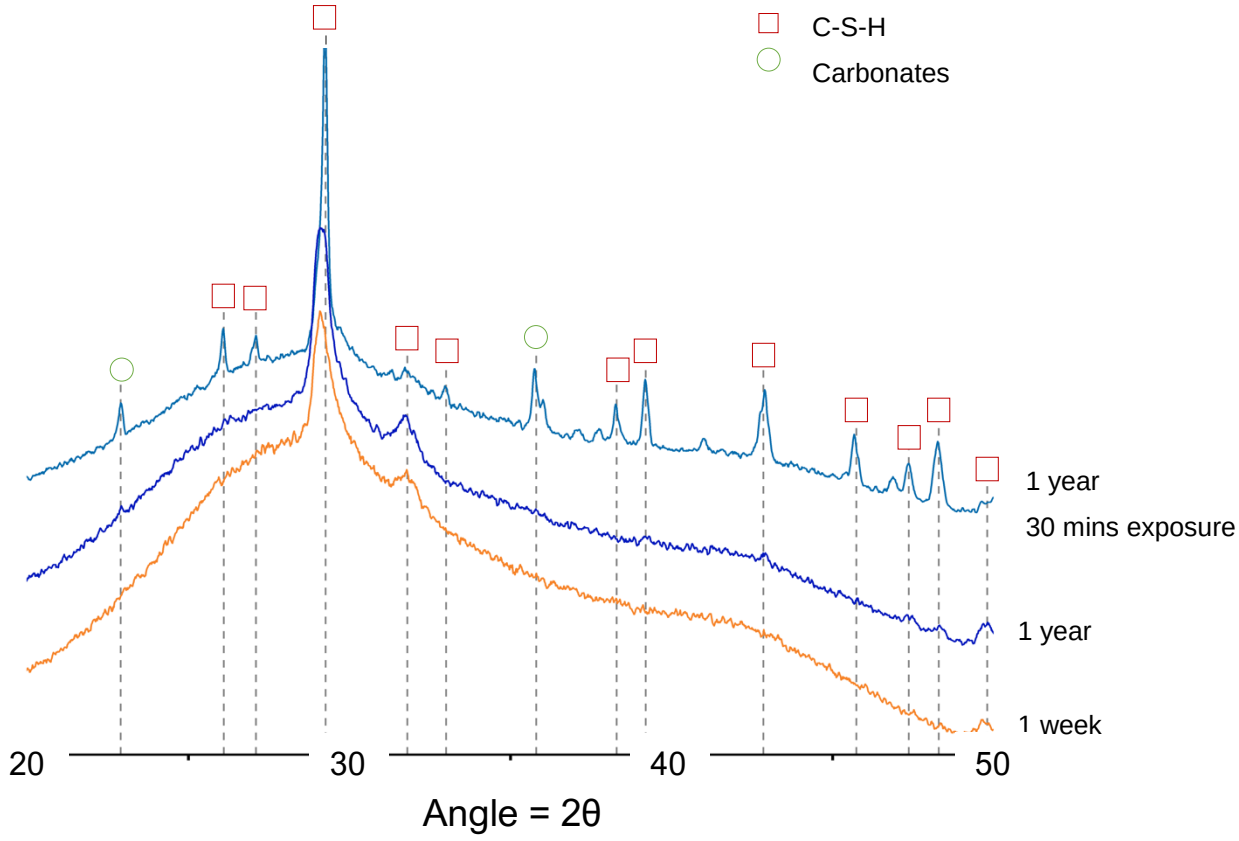


Figure 3.1.12 XRD diffraction patterns for wet C-S-H, Ca:Si = 1.9 at 1 week (orange) 1 year (dark blue), and 1 year after 30 minutes exposure to ambient environment (light blue)

High Ca:Si samples show stability after one year in storage; though samples carbonate when exposed to ambient conditions for only 30 minutes, as seen in Figure 3.1.12.

Drying more than the suggested 25 grams of filtered sample can lead to damp samples, which will carbonate after a shorter period of time in storage. Storage in an airtight container and a sealed bag is most appropriate to prevent carbonation and portlandite formation of dried samples, as seen in Figure 3.1.13.

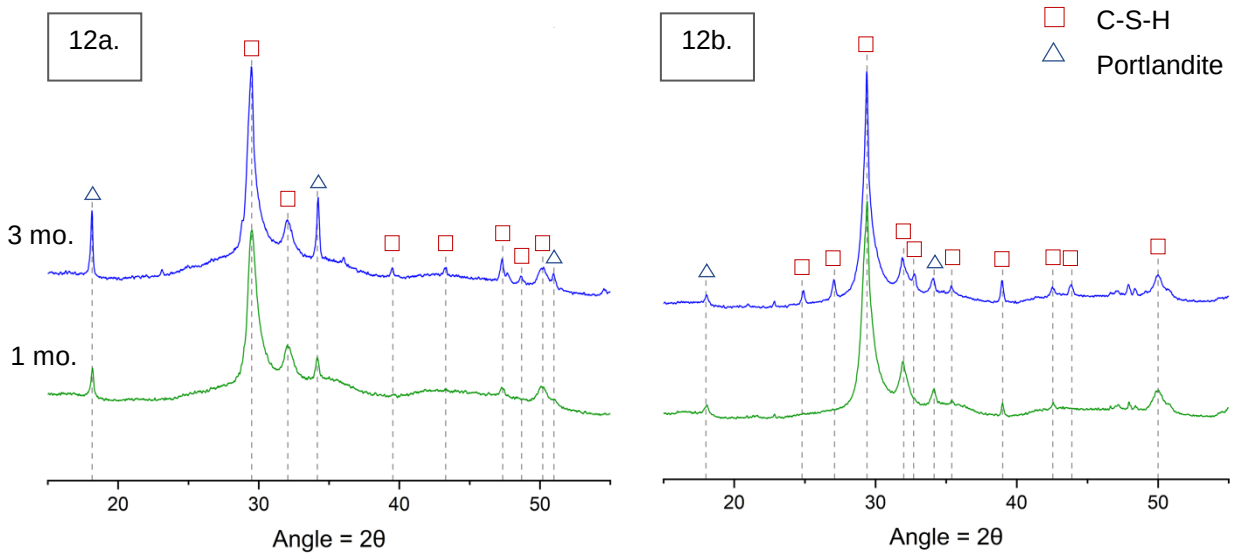


Figure 3.1.13 Longevity analysis of 1 month old (green) and 3-month-old (blue) impure samples with different degrees of sealing. (a) corresponds to a sample exhibiting small amounts of portlandite sealed completely in a Polyethylene tube and bag. (b) corresponds to a sample kept in a polyethylene tube. Both samples show increased carbonation and the non-bagged sample shows increase in portlandite peaks.

Samples that show the presence of portlandite are more susceptible to carbonation and the formation of more portlandite. However, when sealed completely, more portlandite does not form.

### 3.1.8 Conclusions

The objective of this section is to provide guidelines for the synthesis of pure, single-phase C-S-H at both low and high Ca:Si molar ratios that range from 1 to 2. Careful control of temperature and mixing is required to maintain supersaturation conditions for C-S-H while simultaneously suppressing the supersaturation of portlandite, and synthesizing pure, single-phase products. Additionally, thorough cleaning and preparation are imperative to avoid creating sites for nucleation due to dust particles or other impurities.

The synthesis step, however, is not the only factor that must be controlled in producing single-phase C-S-H. Samples may be synthesized without secondary phases, but can form $Ca(OH)_2$ or $CaCO_3$ in the drying, handling, or storage steps.

When comparing the measured concentrations of calcium and silicon in the precipitates and the corresponding supernatants, a significant amount of calcium from the supernatant appears to be adsorbed on the precipitate which may be attributed to surface interactions, particularly on high Ca:Si C-S-H. Further investigation is needed in future work to better understand these phenomena.

In summary, this section provides a reliable method for the production of both low and high Ca:Si ratio synthetic C-S-H. The section highlights where care has to be taken both in the precipitation method and on consequent handling to allow reproducible synthesis of synthetic C-S-H with a desired Ca:Si ratio.

## 3.2 Preliminary investigation of interlayer spacing in synthetic C-S-H

### 3.2.1 Introduction

Water plays a large role in the structure of C-S-H. On the atomistic scale, water can be found as a part of the silanol groups, in the interlayers, and surrounding the material. The structure of C-S-H, as currently understood, is based on the atomistic model of 14Å tobermorite[17], [22], in which C-S-H with Ca:Si molar ratios from 1.25

to 2.0 are accounted for as calcium finds place in the interlayer and in the bridging site on the silicate chain with increasing Ca:Si. An atomistic structure of Ca:Si 1.75 C-S-H is pictured in Figure 3.2.1.

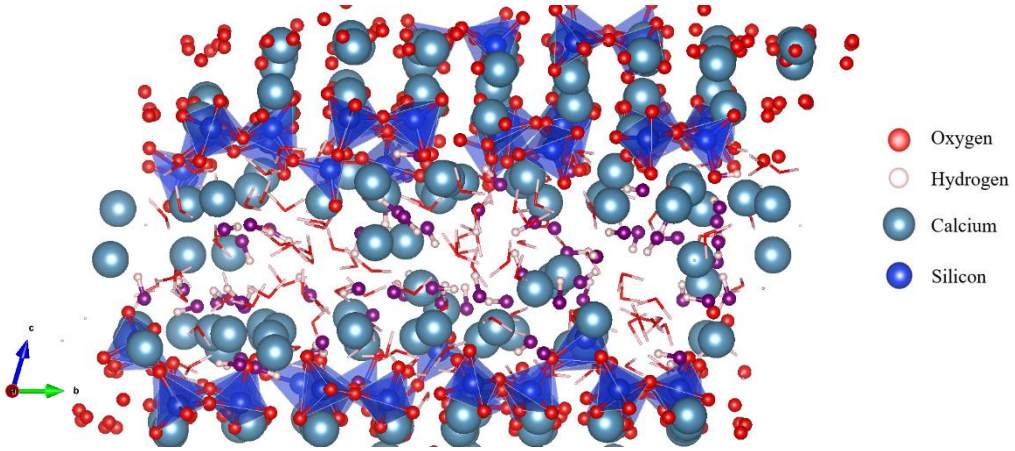


Figure 3.2.1 Atomistic structure of C-S-H, Ca:Si = 1.75, prepared by Ziga Casar (EPFL)

Questions still remain in understanding the interlayer space in C-S-H and how it changes as a function of Ca:Si, drying, and humidity. Previous studies on interlayer spacing in C-S-H give information on the micro- and macroscale properties of C-S-H including studies that gave relations between basal spacing, Ca:Si, and bulk modulus[12], [55]–[61]. On a smaller scale, many different methods have been studied in conjunction. Maruyama observed the effect of relative humidity on water as measured by $^{1}$H NMR relaxometry to see the effect on the water exchange between interlayer water and gel-pore water[62]. In synthetic C-S-H, this exchange was observed to continue after one day, which stops in hydrated cement pastes. In synthetic C-S-H, the exchange between interlayer water and gel-pore water is attributed to the long-range sheet-type morphology which better aids the exchange in comparison to the more fibrillar morphologies observed in a hydrated cement paste, raising a third parameter of interest: time[62].

Roosz et. al's work on synthetic C-S-H produced by the hydration of $Ca(OH)_2$ exhibited interlayer spacings from 9.6Å to 12Å as the sample went from dried to fully hydrated, respectively[63]. However, what is classified as 'fully hydrated' in the study

of Roosz et al. resembles the dried samples presented in chapter 4.1, lending to some questions on classification of ‘wet’ and ‘dry’, in addition to further description of drying processes[63].

The effect of different drying methods on $H_2O$:Si at Ca:Si ranging up to nominal ratios of 2.1 has been compared in a variety of studies[11]. Freeze drying, the drying method used in this thesis, exhibited higher $H_2O$:Si than samples dried at 110°C in experiments done by L’Hopital[12]. However, when comparing the experiments of Richardson, Beaudoin, Cong, and Fuji, both light drying under $N_2$ and solvent extraction leave the C-S-H samples with higher $H_2O$:Si molar ratios[13], [14], [16], [24]. These experiments all universally exhibited an increase in water in the samples as the Ca:Si increases, though these samples at ratios above 1.5 have formed in conjunction with portlandite, and water content in single phase C-S-H at high ratios has yet to be fully studied.

In characterizing cementitious materials, wide-angle X-ray diffraction is often used for both qualitative and quantitative purposes. However, for synthetic C-S-H, a poorly crystalline and poorly ordered material, wide-angle XRD is primarily qualitative, as broad peaks and a hump due to the presence of water make quantifying any additional phases difficult without the aid of other characterization methods. To characterize the interlayer peak, between 6° and 10° at 2Θ, wide angle XRD again is not the ideal method to use as reflection geometry is used, where the detector is on the same side as the sample surface, and is not as accurate at lower angles, particularly below 5° at 2Θ. Transmission X-ray diffraction, used in this section to characterize synthetic C-S-H, allows for higher resolution at lower angles as transmission geometry is used. Additionally, the samples are prepared in capillaries and spin during sample acquisition, minimizing any preferred orientation effects.

In this section, synthetic C-S-H produced by the dropwise precipitation method described in Section 3.1 and by a segmented flow tubular reactor (SFTR) is freeze-dried and characterized with transmission X-ray diffraction to observe the peak between 6° and 10° at 2Θ, representing the interlayer spacing.

As water content plays a large role on the crystallinity and order of C-S-H, experiments were done to determine how this translates to synthetic, high Ca:Si C-

S-H. To better characterize the drying processes, samples were studied in greater detail by thermogravimetric analysis. Additionally, experiments were carried out to characterize the effect of relative humidity, time, and Ca:Si on interlayer spacing.

### 3.2.2 Sample preparation & characterization

*C-S-H synthesis*

Samples studied in this chapter were produced by two methods. Samples produced by batch reactor synthesis were produced in accordance to the method described in greater detail in Section 3.1. Sodium metasilicate solution and NaOH were slowly pumped into calcium nitrate and mixed at 19°C for 3 hours before filtration, collection, and drying.

Samples were also synthesized in a segmented flow tubular reactor (SFTR) [34]. In this method, calcium nitrate and sodium metasilicate were simultaneously pumped into an SFTR, consisting of a 40 meter-long tube with an internal diameter of 4mm. NaOH solution was added to the silicate solution to control the pH and resulting Ca:Si. Reactants were pumped into the SFTR at a rate of 10mL/min, and after being mixed with a micromixer, solutions were segmented in the reactor by nitrogen. The volume of each segmented reactor was between 0.12-0.25 $cm^3$. After being mixed in the SFTR, solutions were collected and allowed to mix for 3 hours. Temperature was maintained at 19°C inside the reactor, and the reaction is kept at the control temperature during mixing.

Calcium nitrate ($Ca(NO_3)_2*4H_2O$, CAS: 13477-34-4), sodium metasilicate ($Na_2SiO_3$, CAS: 6834-92-0), and nitric acid ($HNO_3$, CAS: 7697-37-2) were supplied from Sigma-Aldrich. NaOH pellets were supplied by Acros Organics (CAS: 1310-73-2). Isopropanol and ethanol were supplied by Reactolab S.A.

*Collection & freeze drying*

Samples were vacuum filtered and washed with 60mL of 1:1, decarbonated water:ethanol solution. Samples were then placed in a -80°C freezer for 24 hours and freeze dried for an additional 1-2 days, depending on the experiment, in an Alpha 1-2 LDplus freeze dryer operating at -50°C and 0.01mbar.

*Transmission x-ray diffraction*

To prepare a sample for analysis by transmission XRD, filtered and freeze-dried C-S-H was loaded into a 1mm diameter glass capillary. Samples were loaded into a PANalytical X'pert X-ray diffractometer with an X'celerator detector with double bounced monochromatic CuK$\alpha_{1,2}$ radiation. The patterns were recorded between 4°-65° (2θ) with a fixed divergence slit of ¼ and a step size of 0.017° for 45 minutes. XRD was used to observe the intrinsic C-S-H peaks at 29.4, 32.1, and 50.1 ± 0.1°[51], in addition to the interlayer peak between 6° and 10°, which is of particular interest in this set of experiments. Some measurements were taken in triplicate, and an error of ±0.05° at 2Θ is measured. However, samples exhibited consistent decrease in interlayer spacing between scans, possibly due to change in sample, as described in Section 3.1.7. As a result, first measurements are reported in this section.

*Thermogravimetric analysis*

To analyze samples by TGA, dried C-S-H was heated at a rate of 10℃/min from 30°C to 1000°C under a flow of nitrogen at 10 mL/min. The weight losses in relation to time and temperature were recorded on a Mettler Toledo AG (TGA/SDTA851e). Water was analyzed using the horizonal method at temperatures between 30°C and 300℃. Portlandite and calcium carbonate amounts were analyzed using the tangent method at temperatures between 400°C - 480°C and 600°C - 710°C, respectively, as described by Lothenbach et al.[52]. The horizonal method was used when all loss at the chosen temperature can be attributed to one source. The tangent method reduces overestimation due to the continued loss of water in C-S-H at higher temperatures.

## 3.2.3 Results & discussion

*Relative humidity*

In a first experiment, four samples of batch-produced C-S-H with portlandite and nominal Ca:Si ratios of 1.7 were placed at varying relative humidities ranging from 11% to 97% for eight months. The samples were then characterized by XRD and

TGA to observe the effect on the interlayer peak and the water content in the samples.

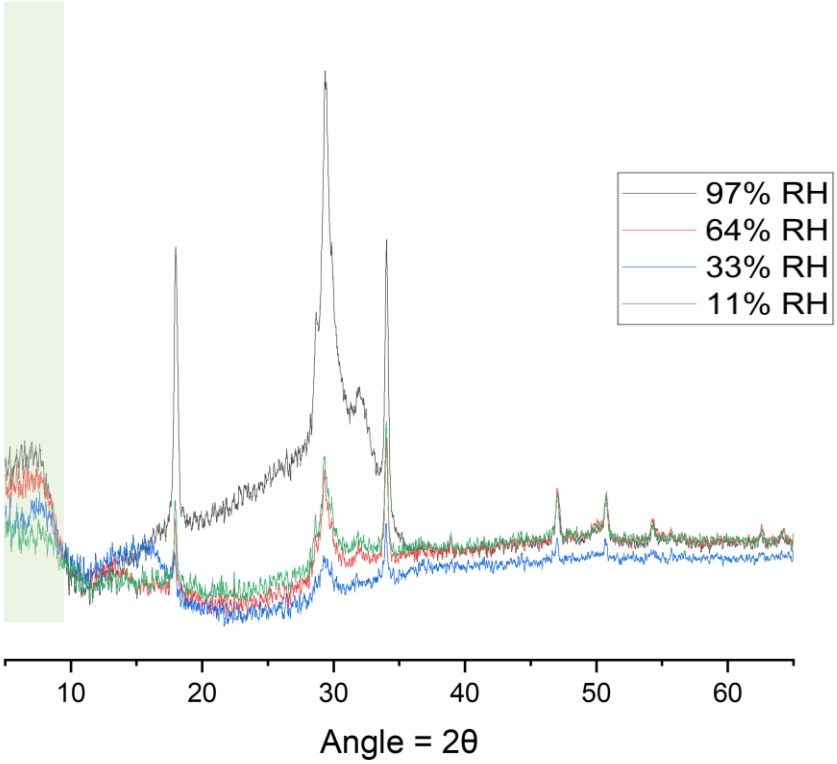


Figure 3.2.2 X-ray diffractogram of freeze-dried, batch-produced C-S-H, nominal Ca:Si = 1.7 at varying relative humidities

TGA results gave a corrected Ca:Si of 1.65 for both samples at relative humidities of 97% and 64%. No correlation between water loss in TGA data and humidity was observed, all samples exhibited water loss by mass between 10% and 15% for samples studied in triplicate. The samples at relative humidities of 33% and 11% both exhibited corrected Ca:Si ratios of 1.68.

XRD diffractogram results proved inconclusive although a clear interlayer peak is observed, noise in samples distorts exact location of interlayer peaks. However, the peaks average an angle of 7.1 ± 0.1 at 2Θ, which corresponds to an interlayer distance of 12.1-12.4Å. Additionally, there appears to be a slight shifting left of peak as the relative humidity increases, indicating an increase in interlayer spacing, which matches the work by Roosz et al[63]. However, the difference between the low and high relative humidity samples is much smaller than seen in previous work.

Additionally, the sample kept at 97% relative humidity, perhaps most similar to the 'fully hydrated' samples by Roosz et al., exhibit a water hump between angles of 15° and 35° at 2Θ[63].

*Drying effects*

To observe the effect of drying and Ca:Si on interlayer spacing, synthetic C-S-H produced in both batch reactor and SFTR was dried and analyzed by XRD.

In Figure 3.2.3, batch-produced C-S-H samples with masses between 20 and 25 grams were dried and studied by transmission XRD. The XRD diffractograms show no consistent trends between Ca:Si and interlayer spacings as the sample with a Ca:Si of 1.25 exhibits a higher spacing of 13.5-13.6Å in comparison to the lower spacings of 12.2-12.3Å for the samples with Ca:Si = 1.5 and 1.0.

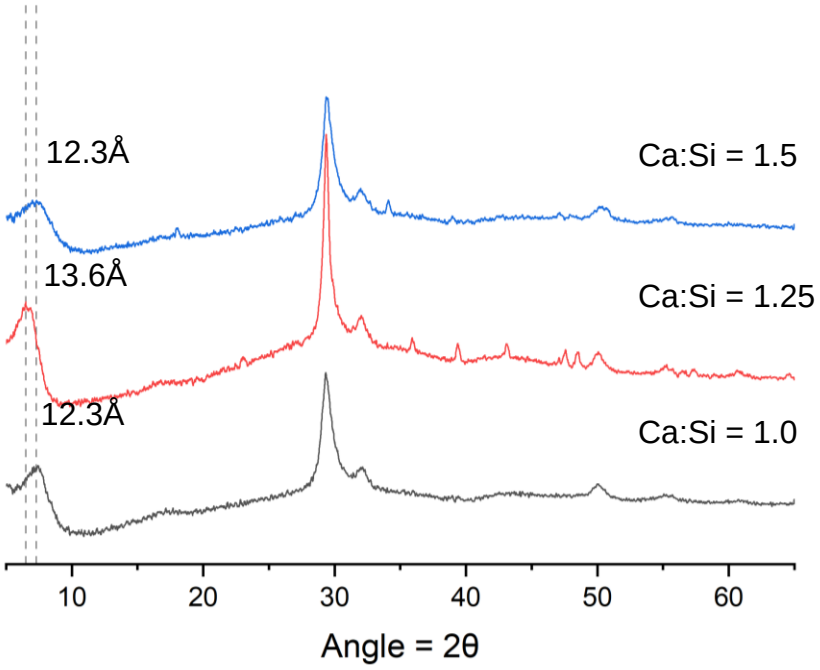


Figure 3.2.3 X-ray diffractogram of batch reactor-produced samples dried in -80°C freezer, and in -50°C freeze dryer at 0.01 mbar for 24 hours each, C-S-H Ca:Si = 1.0 (grey), 1.25 (red), and 1.5 (blue)

In a second analysis, to ensure a more consistent comparison between Ca:Si ratios, exactly 20 grams of C-S-H samples with Ca:Si of 1.25, 1.5 and 1.75 were dried and analyzed by transmission XRD. The diffractograms, this time, exhibited consistently

higher interlayer spacings ranging up to 13.9Å, although, like before no trend between Ca:Si and interlayer spacing is observed as the Ca:Si ratio 1.5 sample exhibits the lowest peak at 6.36° at 2Θ, corresponding to an interlayer spacing of 13.9Å.

The samples placed for 48 hours in the freeze dryer exhibited higher interlayer spacings, though there again is no clear trend between the spacing and the Ca:Si.

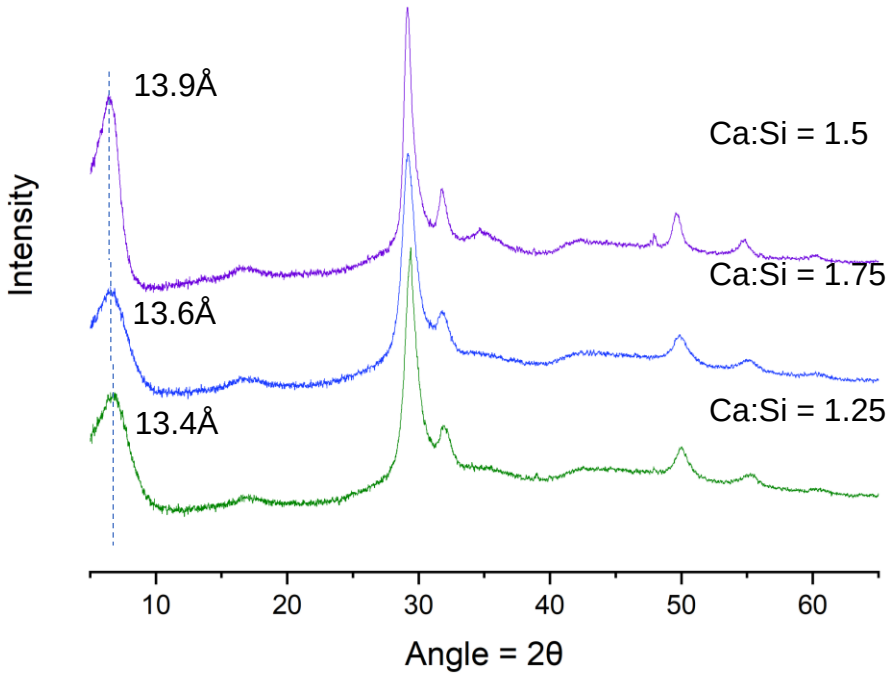


Figure 3.2.4 Comparison of transmission X-ray diffractograms of SFTR-produced samples place in -80°C freezer for 24 hours, and in -50°C freeze dryer at 0.01 mbar for 48 hours C-S-H Ca:Si 1.25 (green), Ca:Si = 1.5 (purple), and Ca:Si = 1.75 (blue) exhibiting interlayer plane spacings between 13.4 - 13.8 Å.

The Ca:Si = 1.5 sample was analyzed again a year later after storage in both a PMMA centrifuge tube and a bag, to observe the change in interlayer spacing, plotted in 0. After a year, XRD analysis on the same sample exhibits a very slight shift to the left, the peak observed at 6.5° at 2Θ, corresponding to an interlayer spacing of 13.6Å .

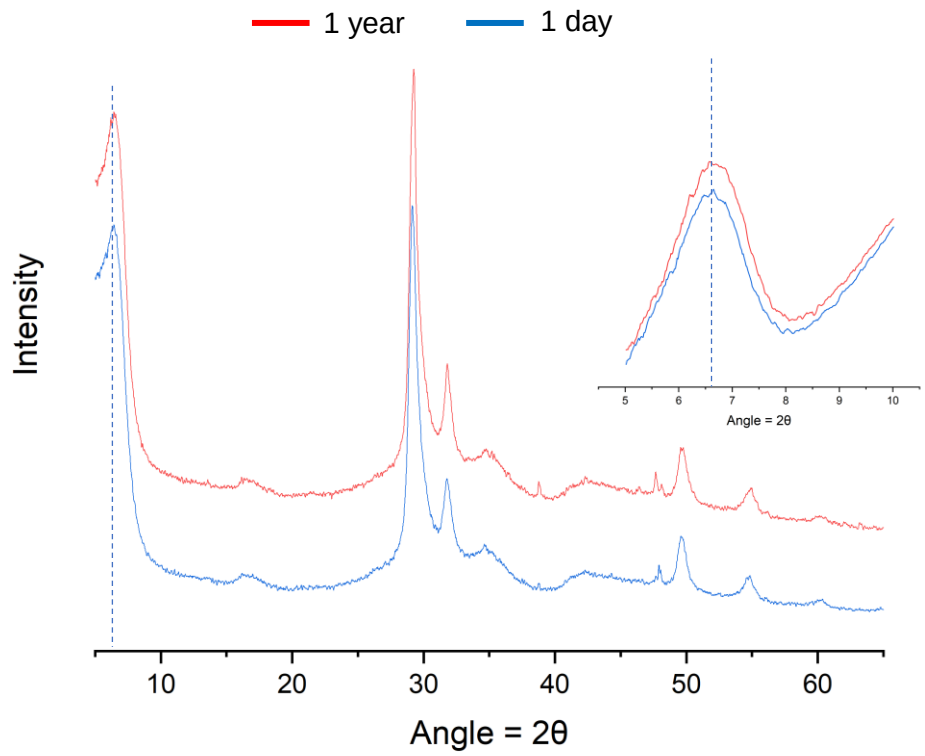


Comparison between XRD diffractograms of SFTR-produced C-S-H Ca:Si = 1.5 at 1 day (blue), and 1 year (red)

### 3.2.4 Water content in synthetic C-S-H

In understanding the effect of water on the interlayer spacing of synthetic C-S-H, it is difficult to separate the effects of filtration and drying on the water content intrinsic to the structure of the C-S-H, particularly given that surplus capillary water is expected in the preparation of synthetic C-S-H.

Differences between synthetic C-S-H produced with the two different reactors were also observed. Density visibly changes as the Ca:Si molar ratio increases, as low ratio C-S-H below Ca:Si molar ratios of 1.5 have more of a gel-like consistency and the higher ratio Ca:Si C-S-H resembles more of a paste. Density changes are also visibly observed between the C-S-H samples produced in the two different reactors. Samples produced in the SFTR visibly resemble more of a gel at higher Ca:Si molar ratios. When dried, SFTR samples appeared to be more homogeneous in size and shape of aggregates, displayed in Figure 3.2.5.

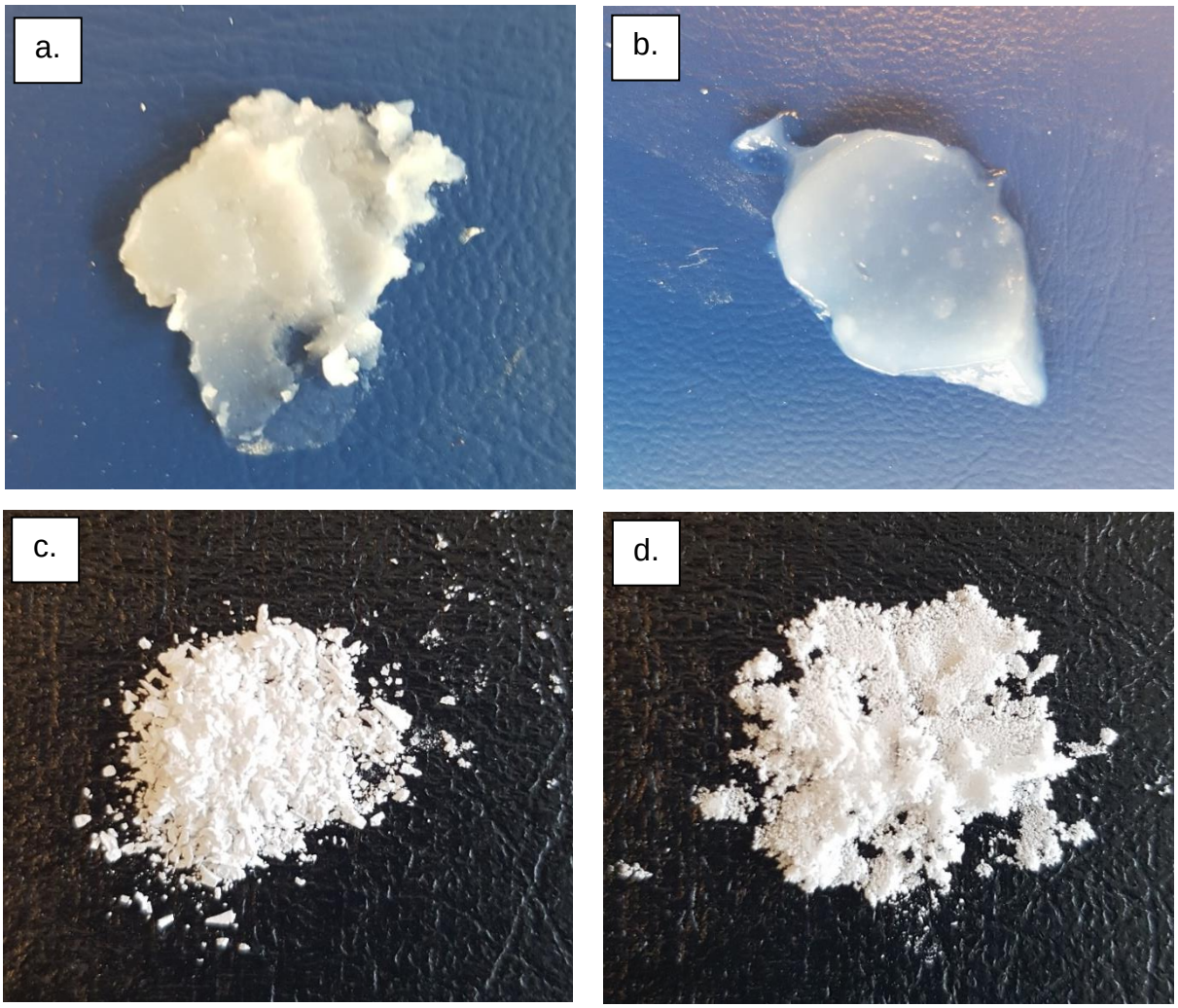


Figure 3.2.5 Synthetic C-S-H produced in a batch reactor (a, c), and in a segmented flow tubular reactor (b, d). Comparison of wet, filtered samples (a, b), and freeze dried samples (c, d), dried in the process decribed in section 3.1.5

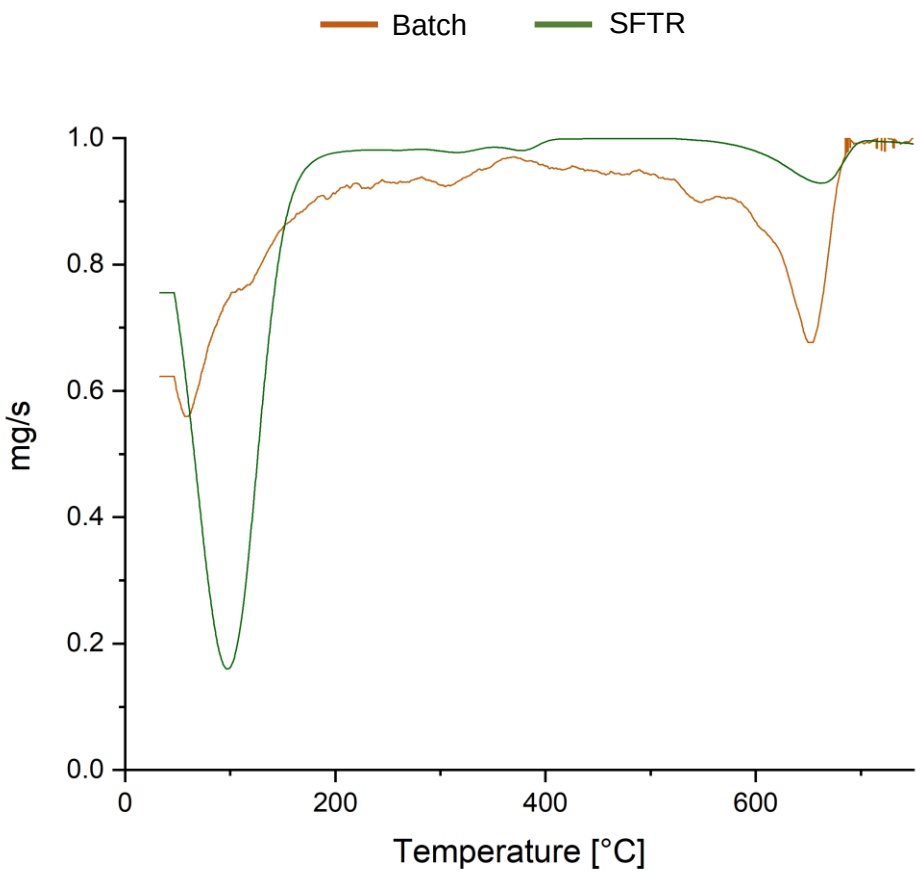


Figure 3.2.6 Differential thermogravimetric analysis (DTG) C-S-H, Ca:Si = 1.75 produced in a batch reactor versus C-S-H produced in a segmented flow tubular reactor (SFTR)

Preparation mode of synthetic C-S-H, shows different effectiveness of drying methods in both visual and differential thermogravimetric analyses between batch reactor and segmented flow tubular reactor (SFTR) preparation (Figure 3.2.6).

In analyzing water loss from thermogravimetric analysis, samples produced by the batch reactor method exhibited on average 16% weight loss due to water in 47 samples. This is in contrast to the 23% loss due to water in 30 SFTR-produced samples. In the studied samples, water loss is considered between temperatures of 30°C to 300°C, and should suitably account for capillary water, though loss due to water in the interlayer or that is perhaps bonded more strongly to the surface may continue to occur until higher temperatures, exhibited by the two DTG plots in Figure 3.2.6. While the SFTR-produced sample has a strong water peak between 0°C and

200℃, the batch-produced sample exhibits water loss which may continue up to 400℃.

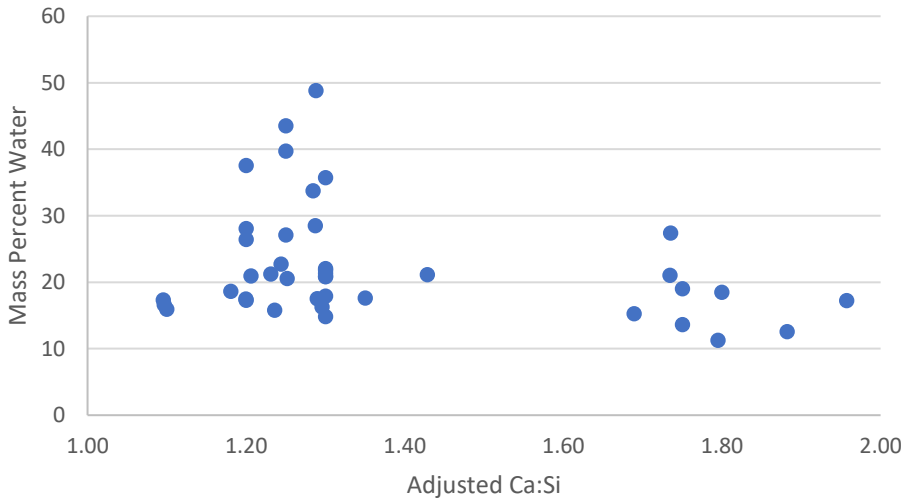


Figure 3.2.7 Mass percent loss of water by thermogravimetric analysis for 50 samples

A comparison between Ca:Si and mass loss due to water is plotted in Figure 3.2.7, though a wide range of values are recorded, higher water content seems to be observed in lower Ca:Si molar ratios, ranging up to 48% water loss and averaging 24% loss due to water between Ca:Si ratios of 1 to 1.5. At ratios of 1.5 and higher, the loss due to water averages 17%.

### 3.2.5 Discussion

There is much more work to be done to understand the effects of Ca:Si, drying, and humidity on the interlayer spacing and water content of synthetic C-S-H. Consistency between sample handling, preparation method, filtration, and drying is key, down to working with exact masses to allow for adequate comparison. Additionally, transparency between these methods is also highly important as the definitions of fully hydrated vs. fully dried C-S-H remain ambiguous.

The relative humidity experiment exhibited only a small change between the high and low RH values, though seemingly a slightly higher spacing is observed at the

higher humidities. Still, this analysis seems inconclusive as the lowest relative humidity sample at 11% is comparable to the ‘fully hydrated’ C-S-H sample of Roosz et al, and the high relative humidity samples in this study exhibit some of the lowest interlayer spacings observed in this section[63]. This lends to the question, what is fully hydrated, and how can we be sure to analyze our synthetic C-S-H at this condition? One could argue that in allowing the samples to equilibrate for eight months, as was done for the samples measured at different relative humidities, it is in fact a slow drying. This is to be compared with the samples which were analyzed within the week of synthesis, and exhibited higher interlayer spacings at 2Ɵ. However, the sample in 0 comparing two samples over a year disproves the hypothesis that time alone contributes the decreasing of interlayer spacing—the year-old sample exhibiting an interlayer spacing, though decreased over the year, is still above 13.5Å.

Although no clear trend between Ca:Si and interlayer spacing is seen, it is observed that interlayer spacings ranging up to 14Å are achievable, which is particularly relevant given that the atomistic model, built with the help of NMR experiments on synthetic C-S-H, was based on a 14Å tobermorite[17], [22]. The question still remains however, how can we consistently produce these higher interlayer spacing C-S-H samples? Why are we observing high spacings in some samples and not in others?

Preparation method appears to play a large role on interlayer spacing as the SFTR-produced samples both consistently exhibit higher interlayer spacing and show, on average, higher amounts of mass loss due to water from TGA analysis. More work, however, must be done to see if this hypothesis is true, and to identify the ideal handling methods to best characterize the interlayer spacing as synthesized.

At this stage, no conclusion can be made as to whether the interlayer spacing of the sample is measured as it was in the sample before drying. Freeze drying of synthetic C-S-H, in comparison to harsh drying conditions at 110℃, has shown to keep more water in the samples. However, previous work in which the $H_2O$:Si molar ratios were measured after solvent extraction, exhibited higher amounts of water in C-S-H than measured in freeze dried samples. As a result, measurements on wet or properly fully hydrated samples would be ideal. Preliminary experiments to prepare fully

hydrated samples for transmission XRD have been attempted, but the size of the capillaries in combination with the strong cohesion properties of C-S-H have made this task a difficult one. Proton-NMR provides another option to gather data about water distribution in synthetic C-S-H samples, and preliminary data was collected for our samples, but was inconclusive. More work needs to be done to properly prepare the samples so that the amount of capillary water is not too high.

## 3.3 Conclusions & future work

In this chapter, the synthesis process for pure, single-phase C-S-H is described in section 3.1 in addition to guidelines on filtration, storage, and handling. By controlling the cleaning process, mixing speeds, and addition rates, supersaturation of C-S-H over portlandite was maintained, allowing for the synthesis of pure-phase, high Ca:Si ratio C-S-H. Thermodynamic modelling was done with the Cemdata 18.1 database and the GEMS software to determine the ideal concentrations of reactants and amount of NaOH needed to modify the pH of the reaction solution and consequently the Ca:Si molar ratio of resulting C-S-H. Samples were characterized by inductively-coupled plasma spectrometry and x-ray fluorescence to validate the produced Ca:Si molar ratios. Additionally, thermogravimetric analysis was used to quantify $Ca(OH)_2$ and $CaCO_3$ in the impure samples. Result showed that pure-phase, high Ca:Si molar ratios above 1.5 were successfully achieved up to a ratio of 2, though purity became more difficult with increasing ratio. Additionally, high ratio C-S-H above a Ca:Si of 1.8 exhibited higher amounts of calcium in the precipitates than expected. This is further explored in Chapter 5.

In section 3.2, C-S-H, produced with both the batch reactor method and in a segmented flow tubular reactor, was studied by transmission x-ray diffraction to observe the effects of Ca:Si, relative humidity, and time on interlayer spacing and free water in the samples. Using the 14Å tobermorite as a baseline for the expected spacing in a non-collapsed synthetic C-S-H sample, experiments were carried out to see if this spacing could be achieved. Results showed that interlayer spacing increased incrementally with increasing relative humidity, exhibiting spacings between 12.1-12.4Å. Higher spacings were observed in samples produced in an

SFTR, the highest spacing at 13.9Å for a Ca:Si = 1.5 sample. However, no correlations between Ca:Si and interlayer spacings were observed.

The effect of production method, between the batch and segmented flow tubular reactor is also observed as XRD results of samples produced in the SFTR show higher interlayer spacings than those produced by batch reactor synthesis. Thermogravimetric analysis also displays this difference between the two production methods as higher amounts of water are often found in the SFTR-produced samples.

In the future, more work will be needed to analyze samples as produced, unaffected by the drying process. Transmission XRD of wet samples and proton-NMR would be helpful in continuing these studies. Additionally, particle size distribution and specific surface area measurements would be helpful in understanding the differences between batch reactor-produced and SFTR-produced samples.

# Chapter 4. Kinetics of C-S-H

## 4.1 Introduction

In cementitious materials, growth and nucleation are based on a dissolution and supersaturation-driven system, as $C_3S$ dissolution gives way to both portlandite formation and calcium-silicate-hydrate precipitation. C-S-H is the main product of cement hydration, composing 50-60% of hardened cement paste. As C-S-H is one of many phases, the growth and nucleation of C-S-H alone is not well understood and difficult to characterize experimentally in the complex mixture of cement and even $C_3S$ hydration alone.

The most popular routes to investigate cement and $C_3S$ hydration kinetics has been by using the Avrami model and models based on the boundary nucleation and growth (BNG) approach[64]. The Avrami model combines nucleation and growth rates into a single value, which is unsatisfactory for this system as the two phenomena should be regarded separately. The BNG models currently used, on the other hand, assume that the nucleation rate per unit area of an exposed particle is constant—this would mean that the nucleation rate is highest at the beginning of mixing reactants, would only decrease as surfaces are covered[64]. Neither of these two models quite follow the classical nucleation theory, most commonly used to describe the kinetics of nucleation and the formation of a new thermodynamic phase, as in both models nucleation and growth are coupled[65]–[67]. Additionally, both the Avrami and BNG models neglect supersaturation.

A population balance model approach has been successful in gaining insights into the nucleation and growth of $CaCO_3$, $BaSO_4$, and $BaTiO_3$, in which supersaturation is regarded as the result of chemical reactions[30], [68]–[70]. A population balance model, developed by Andalibi et al., was applied to synthetic C-S-H precipitation and allows thermodynamics to be considered in conjunction with kinetics, satisfying the supersaturation requirement in describing the C-S-H system.

In this intensive work by Andalibi et al., the precipitation mechanisms of synthetic C-S-H were successfully described using a population balance equation model (PBEM), a model combining mass balances, population size distributions, chemical

speciation, and supersaturation as the thermodynamic driving force to the growth and nucleation of C-S-H[30], [31]. The work by Andalibi et al. albeit groundbreaking in its use of PBEM and incorporating a non-spherical particle shape was restricted to pure-phase C-S-H with a Ca:Si of 2. The goal of this chapter is to further develop the Andalibi model to make it more flexible with respect to Ca:Si and introduce other chemical species such as sulfates and aluminates to start approaching the complex nature of real cement pore solutions. The extended model will then be tested on newly collected kinetic data for the precipitation of synthetic C-S-H—pure phase, and in the presence of sulfates and aluminates. The chapter starts with a brief description of the combined thermodynamic and population balance model before describing the kinetic experiments and model modifications. The newly collected kinetic data is then confronted with the model before summarizing the outcome of the research.

### 4.1.1 Thermodynamic modelling

Equilibrium can be defined as the state of a chemical system at which the Gibbs free energy is minimized given a composition, temperature, and pressure. Systems tend to evolve towards equilibrium, and the thermodynamic modelling software used in this thesis calculates systems at different points of equilibrium; however, this does not provide insight into the rate at which equilibrium is reached or the intermediate steps and phases.

Reaction affinity or supersaturation are fundamental properties which describe the requirements of a system to either dissolve or precipitate, effectively describing systems out of equilibrium. Reaction affinity, $\phi$, can be functionally described as the difference between chemical potential of a phase or component, $\mu$, and chemical potential at equilibrium $\mu_{eq}$ (Eq. 4.1). R is the universal gas constant and T is absolute temperature.

$$\phi = \frac{\mu - \mu_{eq}}{RT} \tag{4.1}$$

$$d\mu_i = RTdlna_i \tag{4.2}$$

Chemical potential can then be related to the activity of the solute (α), describing the thermodynamic concentration of a solute as it is non-ideal (Eq. 4.2). Molar affinity can then be described as a function of molar activity and supersaturation, S, is commonly described as the ratio between the activity of a solution at a given point and at equilibrium.

$$\phi = ln\frac{a}{a_{eq}} \tag{4.3}$$

$$S \equiv \frac{a}{a_{eq}} \tag{4.4}$$

$$S_i = \frac{\alpha_i(T,P_0)}{\alpha_i^*(T,P_0)} \tag{4.5}$$

The saturation index can also be described as a ratio between the ion activity product, IAP, and the $K_{sp}$, defined below where {A} and {B} are the activities of ions in solid $A_aB_b$. The IAP refers to the thermodynamic solubility product at the current state, actual, while the $K_{sp}$ defines the thermodynamic solubility product at equilibrium, eq.

$$SI = \frac{\{A\}^a_{actual}\{B\}^b_{actual}}{\{A\}^a_{eq}\{B\}^b_{eq}} = \frac{IAP}{K_{sp}} \tag{4.6}$$

In the case of C-S-H, supersaturation is the driving force for the precipitation of the new phase, represented by saturation index (Eq. 4.6) which compares state and equilibrium activities of component *i* at temperature, T, and pressure, $P_0$. As a result, the population balance model describing C-S-H accounts for nucleation and growth as separate phenomena which are triggered by the thermodynamics of the solution and supersaturation.

### 4.1.2 Quadrature Method of Moments

The quadrature method of moments (QMOM) method was used by Andalibi et al. to solve the set of population balance equations based on the work by Marchisio and Fox[30], [71].

To setup the population balance model and solve it using the QMOM, Andalibi et al. describes the C-S-H system by a set of internal and external coordinates[30]. Internal coordinates describe intrinsic properties of the particles of interest like size, composition and shape while external coordinates describe the location of the particle. A number density function is then used to describe a population of particles as it relates to time, location, and internal coordinates, n(t, x, L), respectively, normalized over the system volume.

Equation 4.6 describes the baseline mass balance applied to the system to quantify the growth and nucleation of C-S-H[30]. The model assumes a well-mixed precipitation system which is forming only one, uniform-composition phase. The equation states that the rate of change of the number of particles in the reactor n as a function of time, t, and crystallite size, L, plus growth ($G_L$) and the change of the volume, V, of the reactants as the reaction proceeds is equivalent to the sum of inflows and outflows, Q, in the reactor volume and discrete jumps, h, accounting for aggregation, nucleation events, and breakage.

$$\frac{\partial n}{\partial t} + \frac{\partial}{\partial L}(nG_L) + n\frac{d(lnV)}{dt} = -\sum_{j=1}^{F}\frac{Q_j n_j}{V} + h \qquad (4.7)$$

Integrating the equation and multiplying each side by $L_k$ gives the following equation (Eq. 4.7) in which $m_{k,j}$ is the $k_{th}$ moment of the $j_{th}$ flow.

$$\frac{dm_k}{dt} + m_k\frac{d(lnV)}{dt} = k\int_0^{\infty} n(t,L)G_L L^{k-1}dL - \sum_{j=1}^{F}\frac{Q_j m_{k,j}}{V} + \int_0^{\infty} hL^k dL \qquad (4.8)$$

In a system of particles, the first set of moments must be closed, or only containing functions of the moments. To solve the system of equations, QMOM was the chosen method to calculate the integrals that are dependent on n(t,L) by interpolating to get the summation (Eq 4.8) in which $w_\alpha$ and $L_\alpha$ are the weights and nodes. Weight, $w_\alpha$ has the same units of n(t,L)dL as # particles/$m^3$ in suspension.

$$\int n(t,L)\, g(L) dL \;\approx\; \sum_{\alpha}^{N} w_\alpha g(L_\alpha) \tag{4.9}$$

The zeroth and first moments give the total particle number and particle length, and the second and third moments give the total particle surface area and the total particle volume per system volume, respective. The first 2N-1 set of linear systems can be described as follows:

$$m_0 = \sum_{\alpha=1}^{N} w_\alpha$$

$$m_1 = \sum_{\alpha=1}^{N} w_\alpha L_\alpha$$

$$\ldots \tag{4.10}$$

$$m_{2N-1} = \sum_{\alpha=1}^{N} w_\alpha L_\alpha^{2N-1}$$

In the work by Andalibi et al, the Gordon and Wheeler algorithms are used which assume a normal distribution and calculate weight and abscissa values[30], [72]–[74].

### 4.1.3 The Population Balance Model

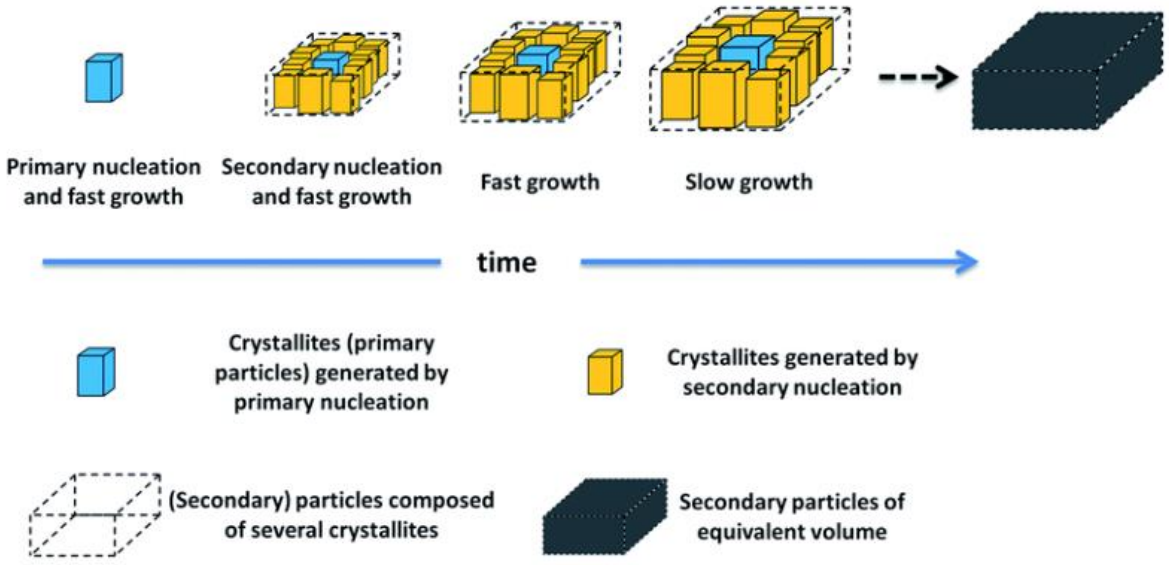


Figure 4.1.1 Processes accounted for in population balance model to describe C-S-H precipitation from[30].

Figure 4.1.1 displays the processes considered in the population balance model of C-S-H[30]. The first step is the formation of primary nuclei, discontinuous and spontaneous as crystallites form. Afterwards, secondary nucleation takes place in which secondary nuclei form only if previous nuclei or crystals are present. As nuclei form and for a period afterwards, the system undergoes fast growth, and as the reactant concentrations in solution are depleted, the system then goes into a slow growth regime before reaching its final state.

In order to quantify the precipitation of C-S-H with thermodynamics as the driving force, the model by Andalibi et al. uses the moment-transformed population balance equation which separately accounts for primary nucleation, secondary nucleation, and molecular growth.

The expanded moment transferred mass balance in Equation 4.11:

$$\frac{dm_k}{dt} = -m_k \frac{Q}{V} + k \sum_{\alpha=1}^{N} w_\alpha(t) \times G\left(L_\alpha(t)\right) \times \left(L_\alpha(t)\right)^{k-1} + L_I^k \times J_I(t) + L_{II}^k \times J_{II}(t) \quad (4.11)$$

Transformed into moments, this equation represents 2N ordinary differential equations in which the discrete jumps, h, have been further separated into $L_I$ and $L_{II}$ for primary and secondary critical nuclei sizes, and $J_I$ and $J_{II}$ are primary and secondary nucleation rates. G is the linear growth rate accounted for by the quadrature weights and nodes, $w_\alpha$ and $L_\alpha$, respectively.

Based on detailed comparison of three simple solubility models of C-S-H, Andalibi et al. calculated C-S-H supersaturation at fixed Ca:Si = 2.0 based on Kersten's model, shown in Equation 4.12.

$$S = \left(\frac{a_{CaOH^+} \times {a_{OH}}^{0.5} \times {a_{H_3SiO_4}}^{0.5}}{K_{sp}^{C-S-H}}\right)^{\frac{1}{v_{Kersten}}} \quad (4.12)$$

The variable, $\alpha$, represents the molal activities of the mentioned species, $K_{sp}$ as the solubility product constant, of $6.0313 \times 10^{-8}$ in all simulations, and v = 2 as the number of ions produced by a solid unit after dissolution. An adjusted $K_{sp}$ value was used, after detailed comparison with experimental measured values at Ca:Si = 2.0.

In the final set of equations, there are five unknown variables, which are iteratively solved for by minimizing calculated free $Ca^{2+}$ to the experimentally measured values. The five unknown parameters are interfacial tension, γ, cohesion energy, σ for secondary nucleation, growth rate constant, $k_r$, kinetic order of growth, g, and the edge length to thickness ratio, $a_r$. The flowrate, Q, can also be slightly corrected.

The linear growth rate, G, used in this model uses the power law approximation of crystal growth and can be represented as follows[75]:

$$G = \frac{k_A k_r}{3 k_v \rho_{solid}} \left[c_{eq}(S-1)\right]^g \quad (4.13)$$

The linear growth rate is a function of the growth rate constant, $k_r$ and the kinetic order of growth, g. $k_A$ and $k_V$ represent the area and volume shape factors, $\rho_{solid}$ is

the molar density of the solid, and $c_{eq}$ representing the solubility of the crystal in solution.

Primary and secondary nucleation, $J_I$ and $J_{II}$, are described below in Equations 4.14 and 4.15. $A_I$ and $A_{II}$ represent the number of crystallites per volume and per area as a function of time, respectively. $\Delta G_{max}$ is the activation free energy at primary and secondary nucleation events, *v* is the sum of ions and cations, and $k_B$ is Boltzmann's constant. The secondary nucleation term also includes $x_A$, available surface area fraction for secondary nucleation, and $A_T$, total formed substrate surface area.

$$J_I = A_I(vlnS)^2 \times exp\left[\frac{-\Delta G_{max,I}}{k_B T}\right] \quad (4.14)$$

$$J_{II} = A_{II}(vlnS)^2 \times exp\left[\frac{-\Delta G_{max,II}}{k_B T}\right] \times x_A A_T \quad (4.15)$$

$A_I$ and $A_{II}$ can be further broken down into the following equations as functions, solved with the Zeldovich formulation[30], [76], [77]:

$$A_I = \frac{D}{L_m^5 v_0}\sqrt{\frac{\left(\frac{k_B T}{\gamma}\right)^3}{3\pi B}} \quad (4.16)$$

$$A_{II} = \frac{D}{L_m^4 v_0}\sqrt{\frac{\left(\frac{k_B T}{\gamma_{eff}}\right)^3}{3\pi B}} \quad (4.17)$$

D is the apparent diffusion coefficient of the solute, v0 is the molecular volume of the solution, approximated as water in this model, Lm is the is the size of a unit cell, and B is the geometric shape factor, a function of $k_A$ and $k_V$. γ and $\gamma_{eff}$ are interfacial energy and effective interfacial energy, which is described as follows:

$$\gamma_{eff} = \gamma - \frac{\sigma}{2(a_r+2)} \quad (4.18)$$

Cohesion energy is σ and edge length to thickness ratio is $a_r$, both parameters to be solved for by the model. The activation free energies at primary and secondary nucleation events can be expanded as follows:

$$\Delta G_{max,I} = \frac{-B\Omega^2\gamma^3}{(k_B T \times vlnS)^2} \quad (4.19)$$

$$\Delta G_{max,II} = \frac{-B\Omega^2\gamma_{eff}^3}{(k_B T \times vlnS)^2} \quad (4.20)$$

Where Ω is the unit particle molar volume. In equations 4.21 and 4.22, the critical size of primary and secondary nuclei is described.

$$L_I = \frac{2k_A\Omega\gamma}{2k_v k_B T \times vlnS} \quad (4.21)$$

$$L_{II} = \frac{2k_A\Omega\gamma_{eff}}{2k_v k_B T \times vlnS} \quad (4.22)$$

Coupled with thermodynamic databases, Cemdata18.1, LNLL, the model replicates the steps taken in the dropwise precipitation method, calculates thermodynamic equilibrium, and solves for the unknown parameters at each time step[30], [31], [35], [37], [39], [40]. In order to both correct and validate the model, the calculated $Ca^{2+}$ evolution is regressed to the measured free $Ca^{2+}$ by changing the unknown parameters within a suitable range.

The objective of the work in this chapter is to apply the population balance model to C-S-H with Ca:Si molar ratios below 2. Additionally, work is done to expand the population balance model to account for the addition of other elements, namely aluminates and sulfates. Kinetic data was collected for C-S-H, C-A-S-H, and C-S-H + $ and analyzed for the changes in both thermodynamics and kinetics from the Ca:Si = 2 system described by Andalibi et al. A small user interface was also added to the population balance model to allow for easier, use, expansions, and modifications of the program.

## 4.2 Materials & methodology

### 4.2.1 Kinetic data collection

To collect kinetic data, 200 mL of 0.022M calcium nitrate solution was placed into the batch reactor. The reactor was placed in a thermostat-controlled water bath at a temperature of 19°C and purged for 30 minutes under a flow of nitrogen at 10 mL/minute and 700 RPM mixing.

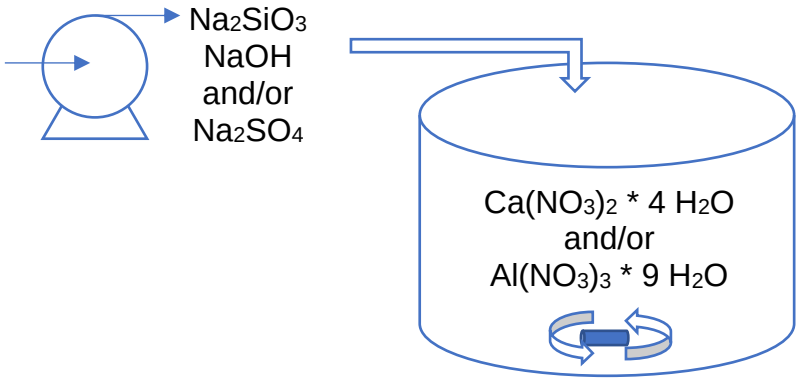


Figure 4.2.1 Schematic for kinetic data collection dropwise precipitation reactor setup

Once the reactor reached the desired temperature, the mixing speed was increased to 1100 RPM, and 200 mL of 0.01M sodium metasilicate solution mixed with NaOH to control the pH and resulting Ca:Si was pumped into the reactor by an ISMATEC REGLO-CPF analog pistol pump with an RH0.CTC pump head at a rate of 1.5 mL/min, kept constant throughout each experiment. Experiments are described in Table 4.2.1. The pH was monitored with a Mettler Toledo InLab Expert Pro ISM-P67 pH electrode[41]. Free $Ca^{2+}$ concentration was measured with a Mettler Toledo perfectION Combination calcium ion selective electrode, collected on the Mettler Toledo Easy Direct software. After twelve hours of data collection every 20 seconds, the precipitate was taken out of the reactor and stored in suspension.

Table 4.2.1 Kinetic Data collection experiments for C-S-H, C-S-H+$, and C-A-S-H at Q = 1.5 mL/min

| | **C-S-H** | **C-S-H + $** | **C-A-S-H** |
|---|---|---|---|
| **Ca:Si** | 1.75 | 1.75 | 1.6 |
| **$Na_2SO_4$** | - | 17.5mM | - |
| **$Al(NO_3)_3$ * 9 $H_2O$** | - | - | 1.5mM |

## 4.2.2 Thermodynamic modelling

Thermodynamic modelling was done using the PhreeqC v.3 software to calculate speciation, phase assemblage, and reaction conditions for the synthetic C-S-H system[37]. PhreeqC was developed by the U.S. Geological Survey for aqueous geochemical modelling. Databases used in this work are Cemdata 18.1, PSI Nagra, and the LLNL database, and are coupled into the population balance model to make equilibrium calculations at each timestep[38]–[40].

## 4.2.3 Population balance model

The population balance model for synthetic C-S-H, developed by Andalibi et al., described the precipitation of C-S-H at a Ca:Si of 2 on the mesoscale level[30], [31].

The first set of codes, given in the supplementary information of the 2017 Andalibi paper, is the initial population balance model for C-S-H at a Ca:Si molar ratio of 2 in which the experimental data is regressed to the calculated calcium concentrations. The second set of codes is separated into functions in which parameters can be manually changed to modify temperatures, starting concentrations, and other values. The first code does not allow for easy change of small parameters while the second set of codes does not regress to experimental data, and so one major goal of this chapter was to combine the two and decrease some of the hard coding to allow the programs to be expanded to allow for calculations on different Ca:Si molar ratios and the addition of different elements to the C-S-H system in an easier, more user-friendly fashion.

## 4.3 Additions to population balance equation model

The population balance models, as published in the 2017 and 2020 papers by Andalibi et al. were expanded to more easily account for the addition of sulfates and aluminates[30], [31]. Additionally, a basic user interface, shown in Figure 4.3.1 was added to the program to allow for changing certain parameters including temperature, Ca:Si, and flowrate.

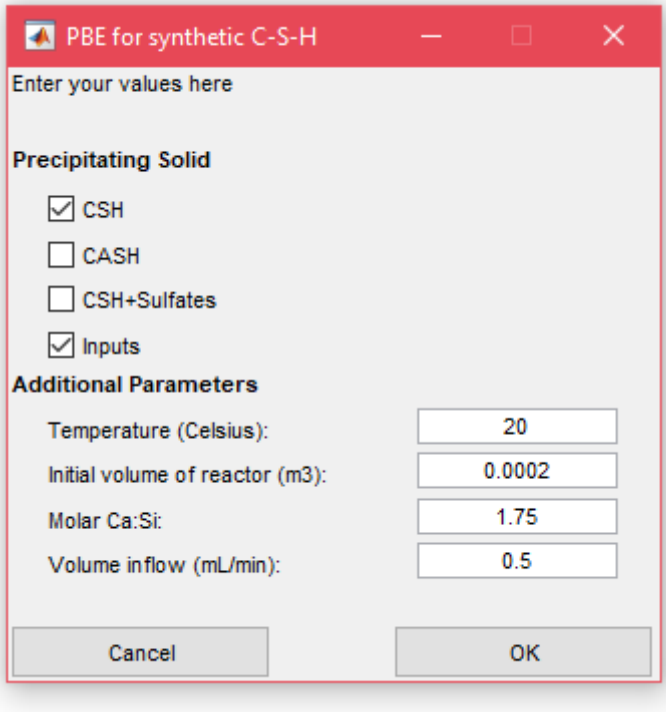


Figure 4.3.1 Simple user interface added to population balance model codes[30], [31]

To increase the effectiveness and flexibility of the model, more kinetic data for C-S-H and C-S-H systems can be collected, and recalculated parameters can be added into the system as a function of the different Ca:Si molar ratios and systems, as begun in the upcoming discussions. Currently, the program allows the user to choose between C-S-H, C-A-S-H and C-S-H + $, and default parameters for molar volume, log K, and the change in enthalpy for the precipitating solid can be input with an excel sheet.

Additionally, an option was added to make thermodynamic calculations in two modes: with the kinetic data input serving as the sole source of $Ca^{2+}$ concentrations

in solution, and with starting concentrations as the only given information for cases without input, displayed in Figure 4.3.2. In the latter mode, the input calcium concentration is reacted fully with the goal of making equilibrium aqueous speciation calculations for a chosen system over time for a system in which there may be no kinetic data. Additionally, the five unknown kinetic parameters can be manually modified as desired.

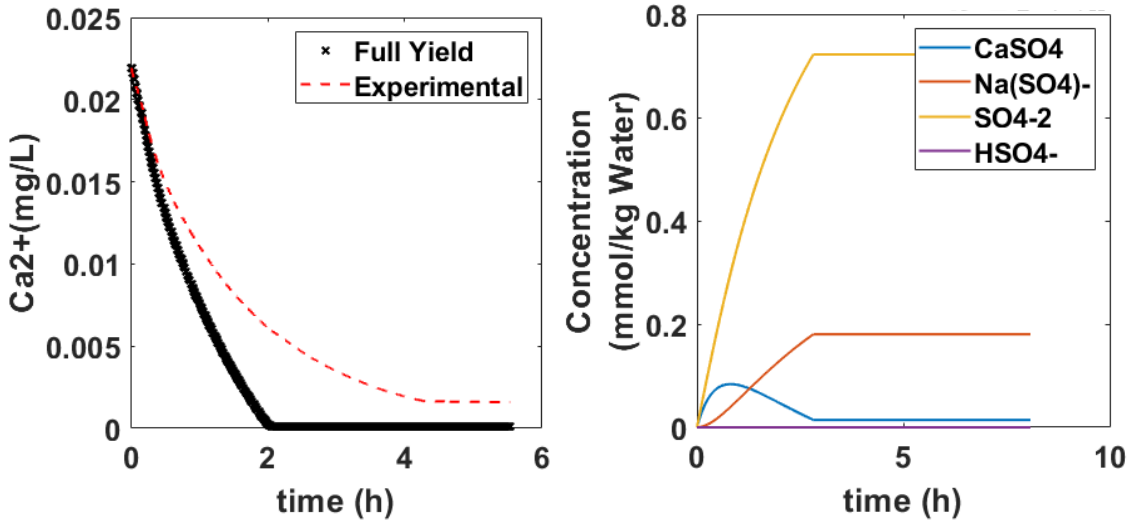


Figure 4.3.2 Outputs of equilibrium calculator for synthetic C-S-H system. (a) Comparison between experimental $Ca^{2+}$ consumption curve at Q = 1.3mL/min, and full yield calculation for C-S-H Ca:Si = 1.75 system. (b) Full yield calculation of aqueous sulfate species in C-S-H + $ system, Q = 1.3 mL/min.

Finally, the objective function from the 2017 Andalibi et al. publication[30] in which difference between experimentally collected $Ca^{2+}$ and the calculated concentrations is minimized was combined with the programs from the 2020 Andalibi et al. publication[31] in which recipes, flowrates, and other parameters could be more easily changed. The following sections are the results from using the updated model.

## 4.4 Pure phase C-S-H

### 4.4.1 Modifying Ca:Si

The population balance model was used to calculate saturation indices for C-S-H and portlandite for Ca:Si molar ratios from 1 to 2, as compared in Figure 4.4.1. The

pHs evolution throughout precipitation is plotted in Figure 4.4.2, and correspond to required pHs for each Ca:Si, given in Section 3.1. C-S-H remains supersaturated throughout the precipitation process. The five unknown “fitted” parameters (γ, σ, $k_r$, g, and $a_r$.) were those identified by Andalibi et al.[30]. For Ca:Si molar ratios of 1.5 and higher C-S-H is quickly supersaturated, faster as the ratio increases, and the SI decreases to ~1 as the reaction proceeds. For Ca:Si molar ratios of 1 and 1.25, the systems are also supersaturated, though not to the same degree as the higher Ca:Si C-S-H. The saturation indices of low ratio C-S-H remain constant after reaching the peak for the time duration modelled here.

Portlandite, for the precipitation of C-S-H at all Ca:Si molar ratios, has a saturation index below 1 for all ratios, indicating the system is undersaturated to portlandite formation and no formation of CH is possible under the described conditions.

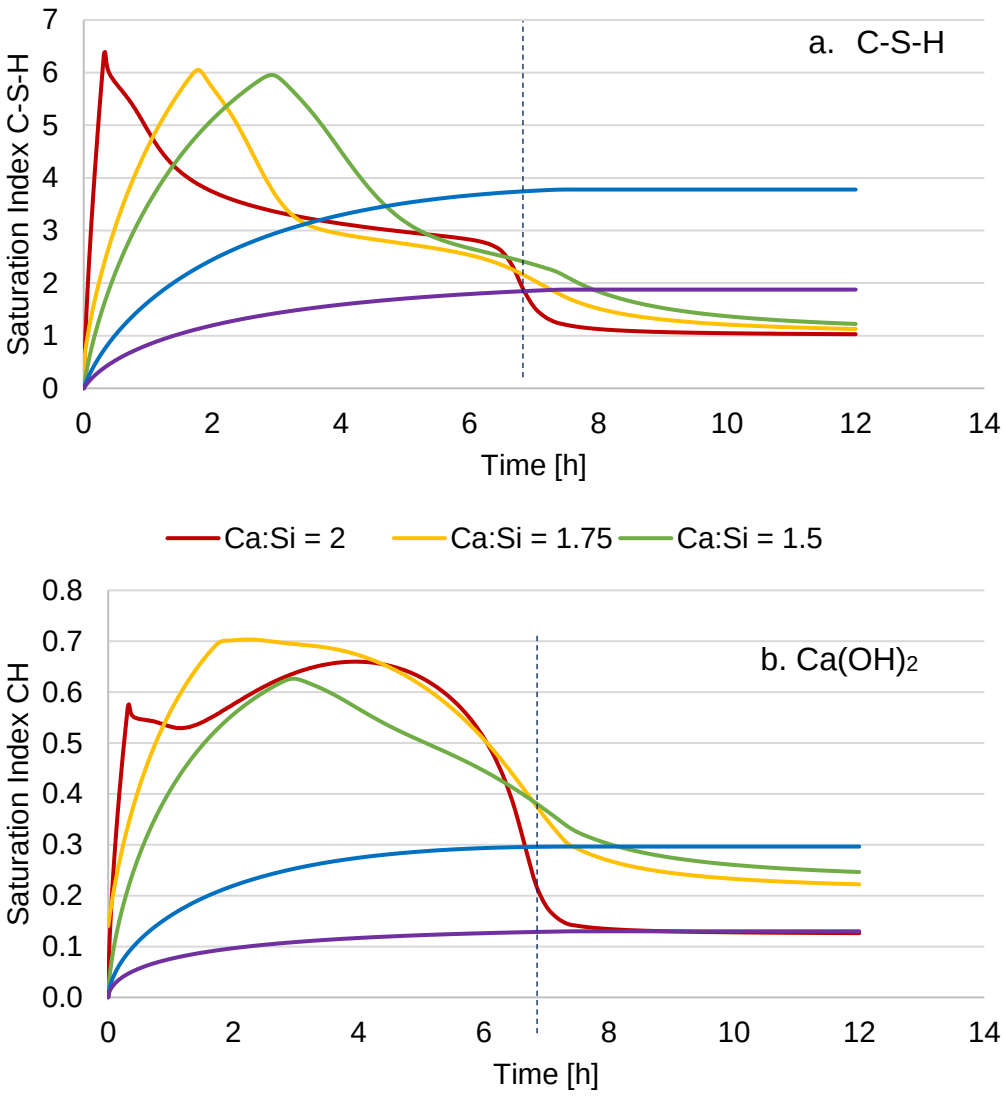

Figure 4.4.1 Comparison between saturation indices of (a) C-S-H and (b) portlandite for C-S-H produced by dropwise precipitation, calculated by population balance model, Q = 0.5 mL/min[30], [31]. Black line indicates the time when the addition of silicate and NaOH solution stops.

The saturation index curves for both C-S-H and portlandite at Ca:Si molar ratios of 1.25 and 1.0 exhibit an increase in saturation index with time, though no changes in profile throughout the consumption of calcium and formation of C-S-H. As calculations were made using the kinetic parameters calculated for the PBE model at a Ca:Si of 2, it is possible that kinetic data must be collected and new parameters must be calculated for Ca:Si ratios on the lower end <1.5 for the model to better predict how saturation index changes with time.

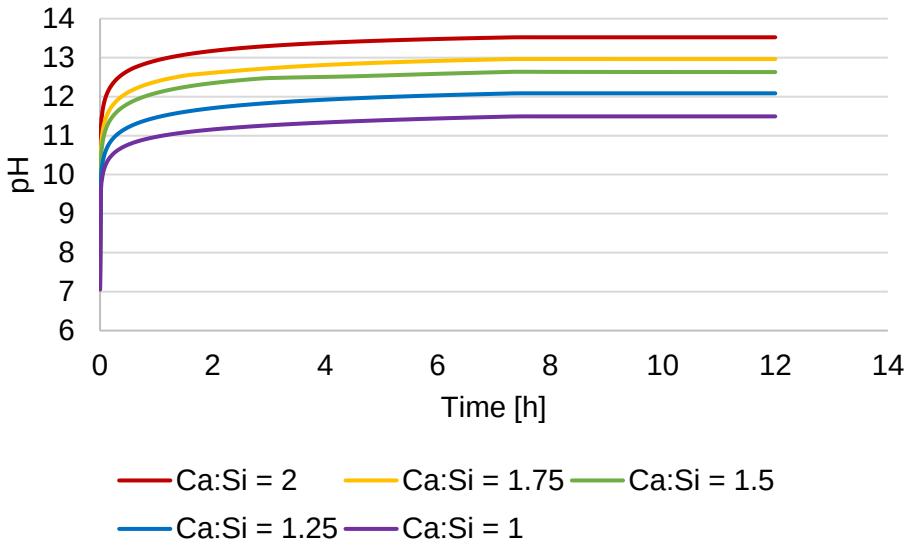


Figure 4.4.2 Comparison between pHs supernatant solution of C-S-H produced by dropwise precipitation method, calculated by population balance model, Q = 0.5 mL/min[30], [31]

## 4.4.2 Recalculation of “unknown” parameters for C-S-H, Ca:Si = 1.75

Two sets of kinetic data were collected for precipitated synthetic C-S-H, Ca:Si = 1.75. Data was entered into the population balance model, and calculated free calcium concentration was minimized to the measured calcium by changing the

values for interfacial tension, cohesion energy, the growth rate coefficient, the kinetic order of growth, and the crystallite edge length to thickness ratio, displayed in Figure 4.4.3.

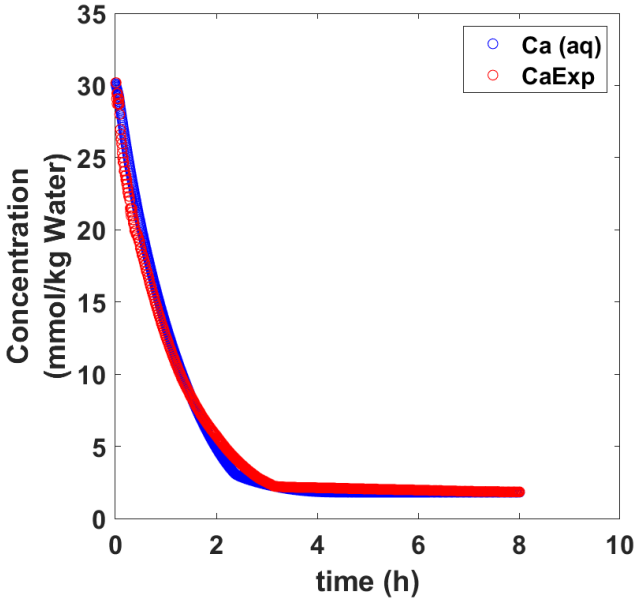


Figure 4.4.3 Comparison between experimentally collected $Ca^{2+}$ concentration and PBEM calculated $Ca^{2+}$, Q = 1.5 mL/min

The population balance model recalculated parameters are listed below in Table 4.4.1. In comparison to the parameters received for the Ca:Si = 2 system determined by Andalibi et al., there is little difference between the interfacial tension, cohesion energy, and the kinetic order of growth[30]. Interfacial tension and cohesion energy are heavily dependent on surface interactions, so for further accuracy of these values, addition of surface-based thermodynamics would improve the estimations, particularly given the possibility of adsorption on the high surface area surfaces of C-S-H at Ca:Si C-S-H > 1.5[32], [78]–[81].

A decrease in the growth rate coefficient is observed in comparison to the higher ratio system, decreasing to $1x10^{-10}$ from $2.25x10^{-9}$. Other estimations of the growth rate coefficient of C-S-H by Bellmann and Scherer calculated values on the order of $10^{-13}$, for C-S-H grown on the surface of calcite, so the recalculated values remain reasonable, although on calcite, there may be lower saturation indices and consequently lower growth rates[82]. The change in the aspect ratio of crystallite

length to thickness is difficult to evaluate as the disordered nature of C-S-H makes this extremely difficult to evaluate experimentally.

Table 4.4.1 Comparison between PBEM calculated parameters for C-S-H at Ca:Si = 2 at Q = 2 mL/min, and 1.75 at Q = 1.5 mL/min

| | **C-S-H Ca:Si = 2[30]** | **C-S-H Ca :Si = 1.75** |
|---|---|---|
| Interfacial tension (mJ/m2) | 55.66 | 55.0 |
| Cohesion energy (mJ/m2) | 47.10 | 47.3 |
| Growth rate coefficient (m3/g2*mol*gs) | 2.25e-9 | 1.00e-10 |
| Kinetic order of growth | 1.80 | 1.68 |
| Edge length/thickness | 0.50 | 1.91 |

Population balance model outputs for amount of C-S-H precipitated, pH, and ionic strengths are plotted in Figure 4.4.4.

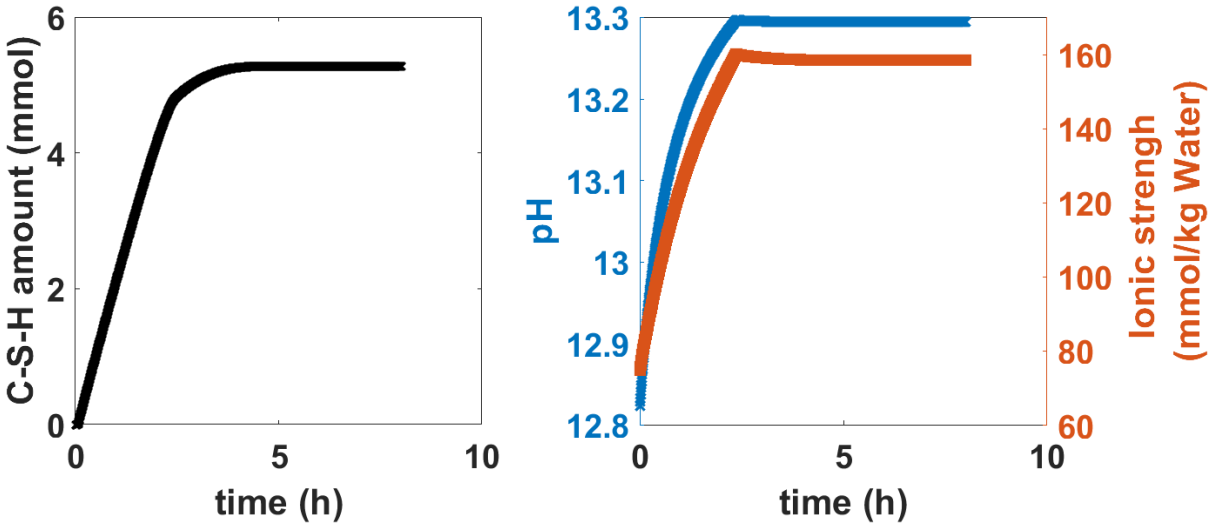


Figure 4.4.4 PBEM outputs with recalculated parameters for C-S-H, Ca:Si = 1.75, Q = 1.5 mL/min, (a)mmol C-S-H produced over time and (b) pH and ionic strength evolution over time

In the modelled experiment, calcium nitrate solution is in the batch reactor, and silicate solution with NaOH is pumped into the system at a constant rate. The calculated and regressed consumption of calcium is plotted in Figure 4.4.5 with silicon concentration in the reactor. Concentrations of sodium and nitrogen from $NO^{3-}$

from the calcium nitrate solution are also compared. At a rate of Q = 1.5 mL/min, addition of silicates stopped after 2.2 hours of reaction for a volume of 200 mL of solution.

At the high pHs for C-S-H Ca:Si = 1.75, $Ca^{2+}$ and $Ca(OH)^{+}$ are the most abundant species in solution, and silicate species, primarily $CaSiO_3$, peak in solution after addition of silicate species stops but is always the dominant silicate species.

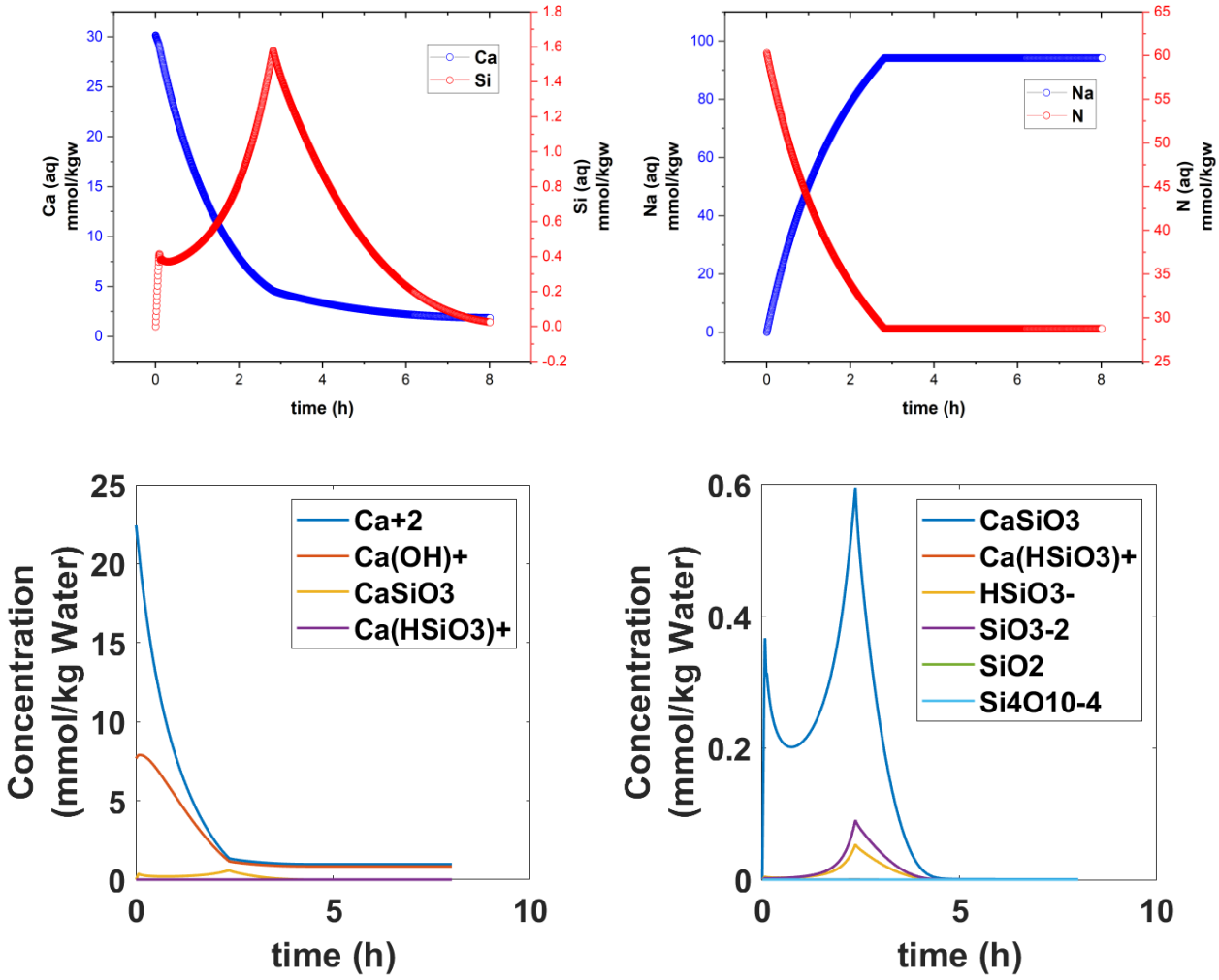


Figure 4.4.5 PBEM outputs with recalculated parameters for C-S-H, Ca:Si = 1.75, Q = 1.5 mL/min, (a) concentrations of aqueous calcium (blue) and silicon (red), (b) Concentrations of aqueous sodium (blue) and nitrogen (red), (c-d) Comparison of ionic calcium and silicate species in solution throughout precipitation process

Crystallite thickness, particle edge lengths, and critical nuclei sizes are plotted in Figure 4.4.6. Particle edge lengths and crystallite thicknesses are reliant on flowrate,

and higher sizes are expected at lower flows. Though accuracy of the calculations plotted are unknown, Andalibi et al. received crystallite thicknesses maximizing at 4nm for a flowrate of Q = 0.5 mL/min, and particle edge lengths up to 100nm. With the adjusted parameters and a flowrate of Q = 1.5 mL/min, crystallite thicknesses maximize at 0.8nm, and particle edge lengths reach 9nm which is smaller than expected, and suggesting that primary nucleation is dominating secondary nucleation under these conditions.

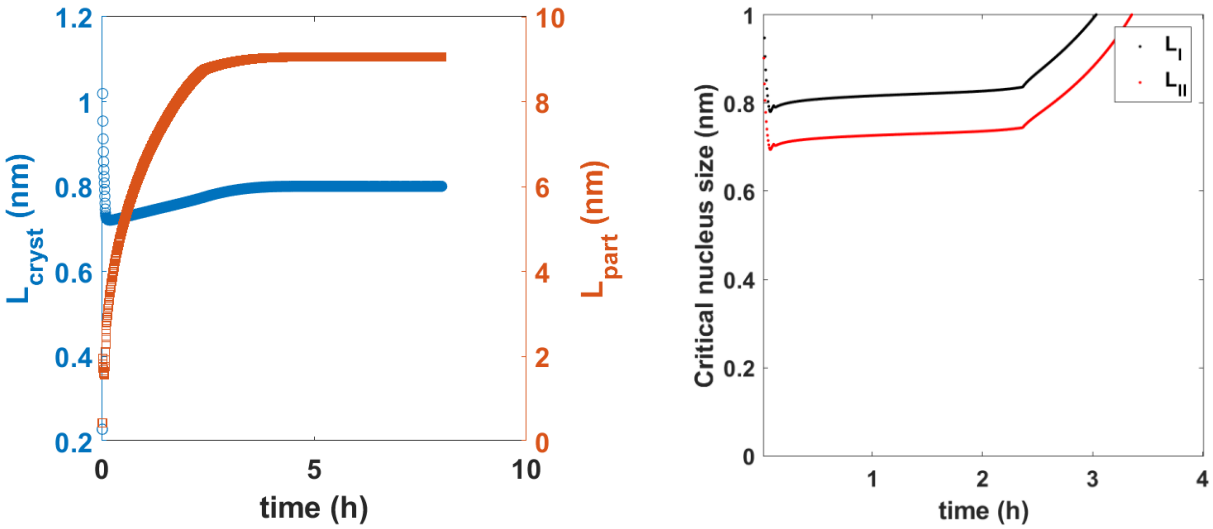


Figure 4.4.6 PBEM outputs with recalculated parameters (a) Comparison between crystallite thickness and particle edge lengths, (b) Comparison between critical nuclei sizes for primary ($L_I$) and secondary ($L_{II}$) nucleation events

Thicknesses of critical nuclei calculated with the adjusted parameters are at ~ 0.8nm for primary nucleation and ~ 0.7nm for secondary nucleation. In Figure 4.4.7, critical nuclei sizes, calculated with the Andalibi et al. parameters are plotted for Q = 1.5.

The critical nuclei sizes for C-S-H Ca:Si 1.25 to 2, calculated using the Andalibi et al. values for the “unknown” parameters are compared below, reported as 2.0-2.7nm and 1.7-2.7nm for primary and secondary nucleation, respectively. The critical nuclei sizes for Ca:Si of 2, 1.5, and 1.75 are comparable using the Andalibi et al. parameters, though do not follow the same functionality versus time. This could be explained by the delay in supersaturation which occurs with decreasing Ca:Si as

highlighted in Figure 4.4.1(a). Overall, the modified combined thermodynamic and population balance model is giving coherent results for these lower Ca molar ratios.

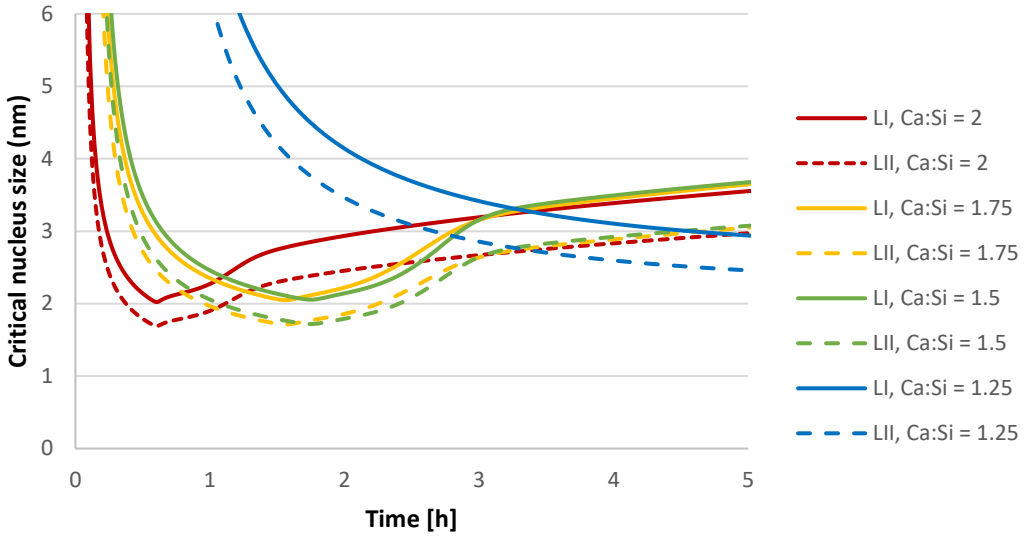


Figure 4.4.7 PBEM outputs with Andalibi et al. parameters for critical nuclei sizes for primary ($L_I$) full lines and secondary ($L_{II}$) dashed lines nucleation events for C-S-H Ca:Si 1.25, 1.5, 1.75, and 2[30], [31]

## 4.5 C-S-H + $ PBE

### 4.5.1 Sulfates and kinetics of cement and concrete

Sulfates are commonly found in cementitious mixtures, particularly as supplementary cementitious materials become more commonplace. Generally added by way of gypsum, $CaSO_4 * 2\ H_2O$, to control the setting time of cement so as to allow time for transportation, mixing, and placement, sulfates are necessary in the formulation to make high quality cements[3], [83]. In blended cements, the ‘filler effect’ is observed in which alite reacts at a faster rate due to supplemental materials in the place of clinker[82], [84]. The fast reaction of alite both increases the consumption of sulfates and the amount of sulfates required in the system, exhibiting the direct effect of sulfates on the kinetics of cement hydration[84]–[88].

Sulfates have also been observed to directly affect C-S-H, as adsorption on the surface of the hydrate has been observed and needle length has been observed to

increase in response to sulfate presence[83], [84], [89]–[91]. However, the direct effect of sulfates on the growth and nucleation of C-S-H are poorly understood.

In this section, the evolution of $Ca^{2+}$ during the precipitation of C-S-H + $ is monitored and compared to the precipitation of C-S-H alone. The concentrations used in this study: 0.022 Ca, 0.01 Si, and 0.0017 $ are based off of work by Berodier who characterized the $:Si molar ratio in Portland cement after 15 hours of hydration[92]. In this preliminary work, thermodynamic modelling is done to analyze the experimental setup, and the population balance model is applied to make first calculations on how growth rates, critical nuclei sizes, and supersaturation among other parameters change over time as C-S-H precipitates in the presence of sulfates.

### 4.5.2 Thermodynamic modelling of C-S-H + $ over precipitation

Sulfates were incorporated into C-S-H samples by adding $Na_2SO_4$ salt to $Na_2SiO_3$ + NaOH solution. For a solution containing 175mM of sulfates, thermodynamic modelling predicts $SO_4^{2-}$ to be the only species in solution at pHs above 4. The pHs of interest for this solution are at 12 and above, dependent on the desired Ca:Si molar ratio. Total amount of sulfur in solution is below the amount added at 150 mM, increasing after a 13.1 pH, suggesting the precipitation of an additional sulfur-containing species below this pH.

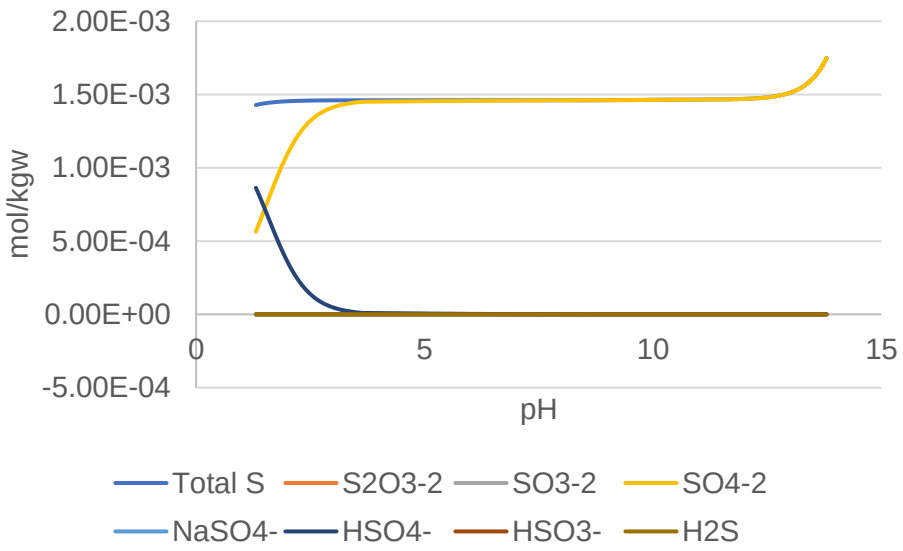

Figure 4.5.1 Aqueous speciation of sulfate species, 175mM $Na_2SO_4$ and 0.1 M $Na_2SiO_3$ and NaOH solution, titrated with $HNO_3$ to obtain pH profile

However, in analysis of the saturation indices only the amorphous silica phase, represented by ECSH1-SH, is above 1, and saturated though never supersaturated in solution, shown in Figure 4.5.2[93]. ECSH1-NaSH and ECSH2-NaSH, both represented by $NaOH_{2.5}*SiO_2*H_2O$, are undersaturated at the full range of pHs, and other sulfur-containing phases including $Na_2SO_4$ and $H_2S$ exhibited indices below 1.

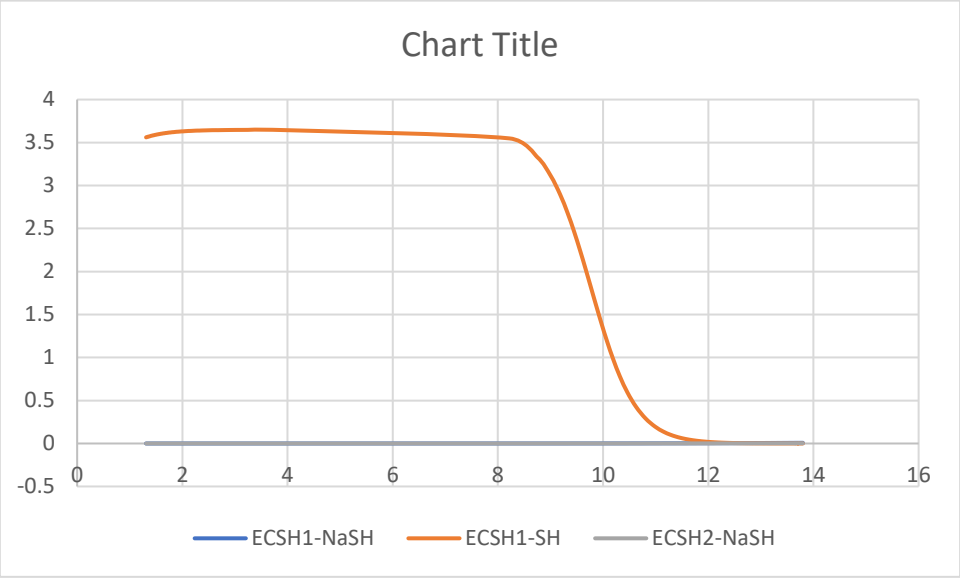


Figure 4.5.2 Saturation indices of species in 175mM $Na_2SO_4$ and 0.1 M $Na_2SiO_3$ and NaOH solution, titrated with $HNO_3$ to obtain pH profile

There may be sulfur-containing species unaccounted for, although experiments were continued in which sulfates were introduced in the silicate + NaOH solution at pHs above 10, at which analysis of saturation indices suggests no additional phases should form.

### 4.5.3 Recalculation of “unknown” parameters, C-S-H + $, Ca:Si = 1.75, Q = 1.5

Kinetic data of C-S-H + $ and C-S-H at Ca:Si molar ratios of 1.75 and a flowrate of ~1.5 mL/min were collected in Figure 4.5.3. The C-S-H sample started with 6.0mmol $Ca^{2+}$ in solution, and the C-S-H + $ sample began with 6.3mmol $Ca^{2+}$ in solution. Effort was made to have the same concentrations across the samples for

comparison purposes, and results are compared as a function of fraction $Ca^{2+}$ consumption.

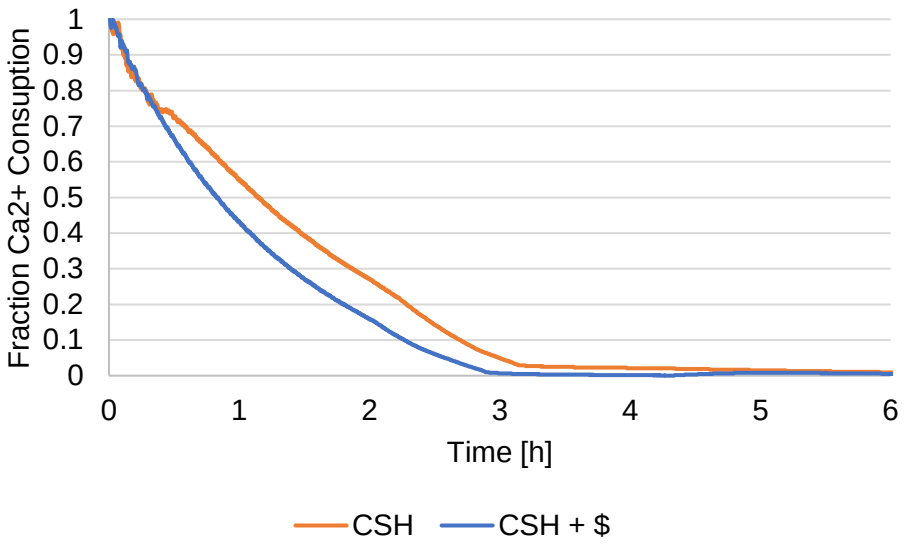


Figure 4.5.3 Fraction consumption of $Ca^{2+}$ during precipitation of C-S-H and C-S-H + $ in batch reactor

For a flowrate ~ 1.5 mL/min introduction of silicate solution into the reactor, C-S-H + $ appears to exhibit a slightly faster consumption of calcium throughout the precipitation process. The population balance model was used to calculate new values for interfacial tension, growth rate constant, cohesion energy, crystallite aspect ratio, and relative supersaturation power in the rate equation. The values are listed below in comparison to those calculated by Andalibi et al. in Table 4.5.1.

Table 4.5.1 Recalculated PBEM parameters for C-S-H + $, Ca:Si 1.75, Q = 1.5 mL/min

| | **C-S-H Ca:Si = 2**[30] | **C-S-H Ca :Si = 1.75** | **C-S-H + $ Ca :Si = 1.75** |
|---|---|---|---|
| Interfacial tension (mJ/m2) | 55.66 | 55.0 | 41.7 |
| Cohesion energy (mJ/m2) | 47.10 | 47.3 | 47.54 |
| Growth rate coefficient ($m^3/(g^2*mol*s)$) | 2.25e-9 | 1.00e-10 | 9.92e-8 |
| Kinetic order of growth | 1.80 | 1.68 | 1.35 |
| Edge length/thickness | 0.50 | 1.91 | 0.42 |

Results in Table 4.5.1 are based on two sets of collected kinetic data at Q = 1.5 mL/min. Interfacial tension is calculated as ~41 mJ/m$^2$, which is slightly lower than the values calculated by Andalibi et. al and by Briki et al. who predicted an interfacial tension of 100 mJ/m$^2$ by the Nielsen approach[76], [94]. However, the calculated values in this study are higher than the experimental estimations on C-S-H at 12 and 30 mJ/m$^2$ [95], [96]. The cohesion energies and edge length:thickness ratios are similar between the two C-S-H systems. Most notable is the increase in the growth rate coefficient upon the addition of sulfates.

Plotted in Figure 4.5.4, experimental data for C-S-H + $ is compared to the amount of free calcium predicted in the system before and after recalculation of parameters. The correlation between the experimental and calculated data is better after recalculating parameters for Ca:Si = 1.75, C-S-H samples, but not as close for the pure Ca:Si 1.75 C-S-H plotted in Figure 4.4.3.

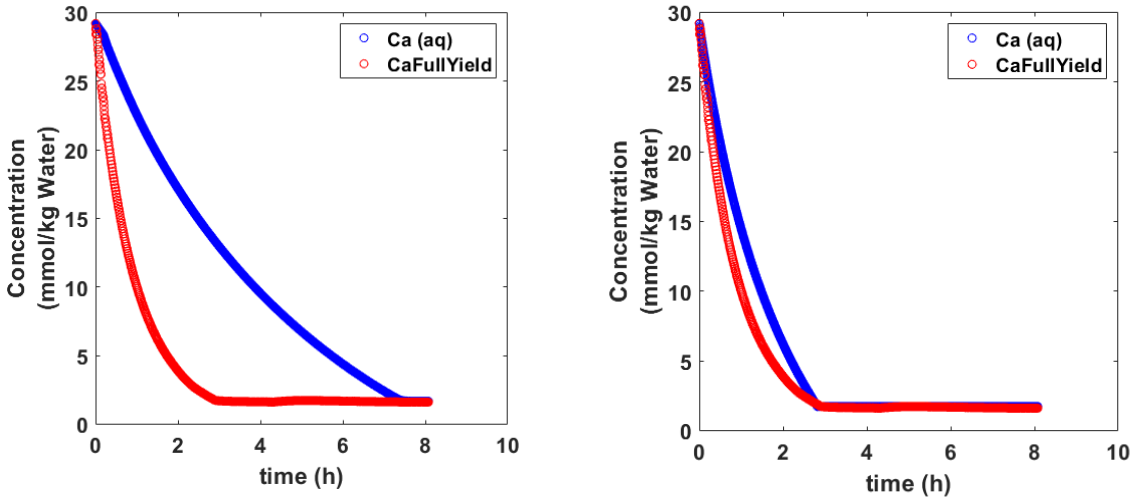


Figure 4.5.4 Comparison between experimental C-S-H + $, Ca:Si = 1.75, Q = 1.5 mL/min data and PBEM calculated $Ca^{2+}$ in system for (a) Andalibi et al. parameters[30] and (b) after recalculation of parameters.

However, some discrepancy is expected between the experimental and calculated parameters for two reasons. First, calculations on the supersaturation indices over

time indicate that portlandite is also supersaturated at the solution addition rate used for these experiments Figure 4.5.5. Also, although the C-S-H is supersaturated throughout the precipitation process, the rate declines rapidly over the first hour, and is lower than that of portlandite between 0.5 and 2.5 hours. The saturation index of portlandite decreases to below one after all silicate solution including NaOH and sulfates are added into the reactor.

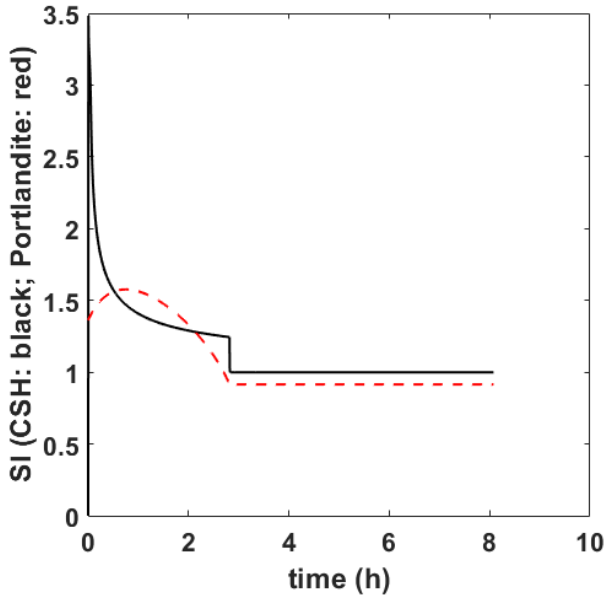


Figure 4.5.5 Comparison between saturation indices of C-S-H and portlandite for C-S-H + $ system, Ca:Si = 1.75, Q = 1.5 mL/min

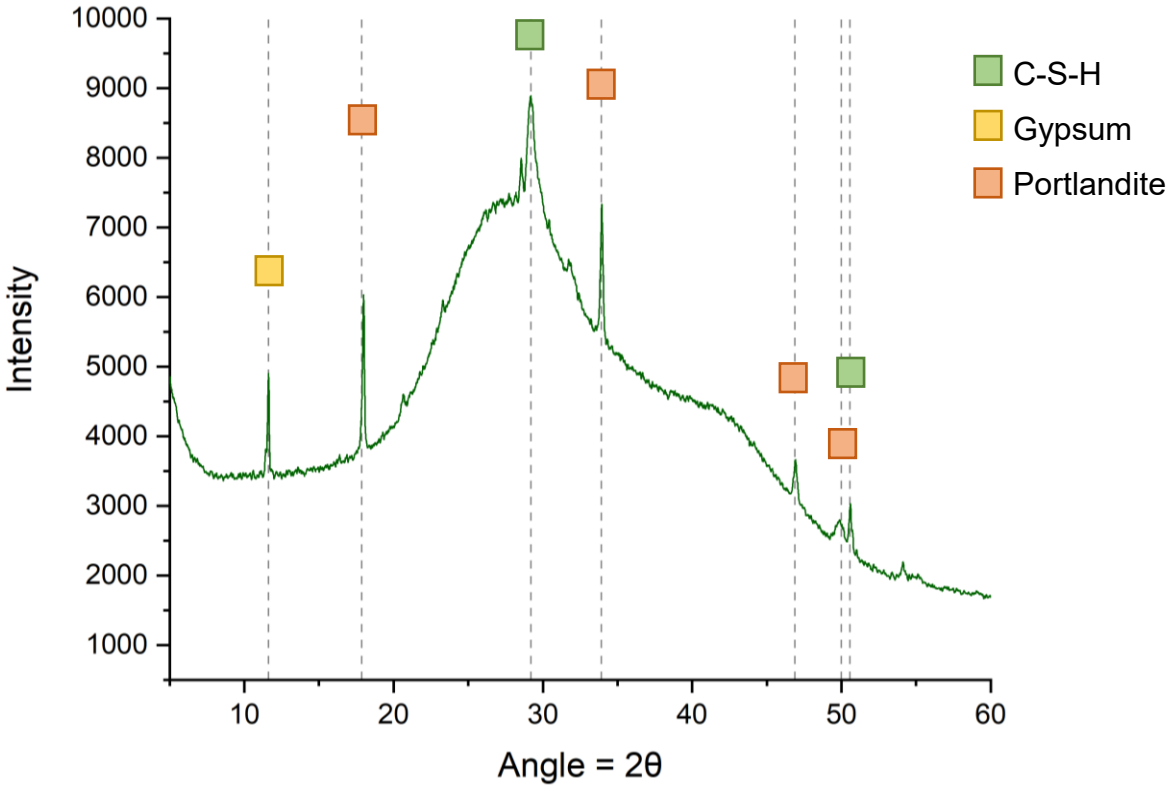


Figure 4.5.6 XRD of C-S-H + $ at Ca:Si = 175, 1.75M sulfate addition (10x over-sulfated)

Experimental data, from synthesis of C-S-H + $ at a Ca:Si of 1.5 and above also confirmed that portlandite forms in conjunction with C-S-H if sulfates are also present. Figure 4.5.6 displays an over-sulfated sample at a Ca:Si of 1.75, showing the presence of gypsum, portlandite, and C-S-H. As a result, two solids can be formed in this process, and the PBEM, as currently designed for pure-phase C-S-H, is designed to only account for the presence of a single, uniform and homogeneous solid. This explains the discrepancy between the measured and modelled calcium consumption of Figure 4.5.4(b).

Secondly, sulfates are known to adsorb on to the surface of C-S-H, and currently adsorption phenomena are unaccounted for in the thermodynamic package attached to the PBEM. Interfacial tension and cohesion energy are heavily reliant on surface interactions[78], [79]. Additionally, these parameters directly affect Figure 4.5.4 the activation free energies $\Delta G_{max\ I,II}$, and primary and secondary nucleation event variables $J_I$ and $J_{II}$, among other parameters.

The critical nuclei sizes for C-S-H, Ca:Si = 2, with the Andalibi et al. fitted parameters, and C-S-H + $,with the adjusted parameters, Ca:Si = 1.75 are compared below in Figure 4.5.7[30].

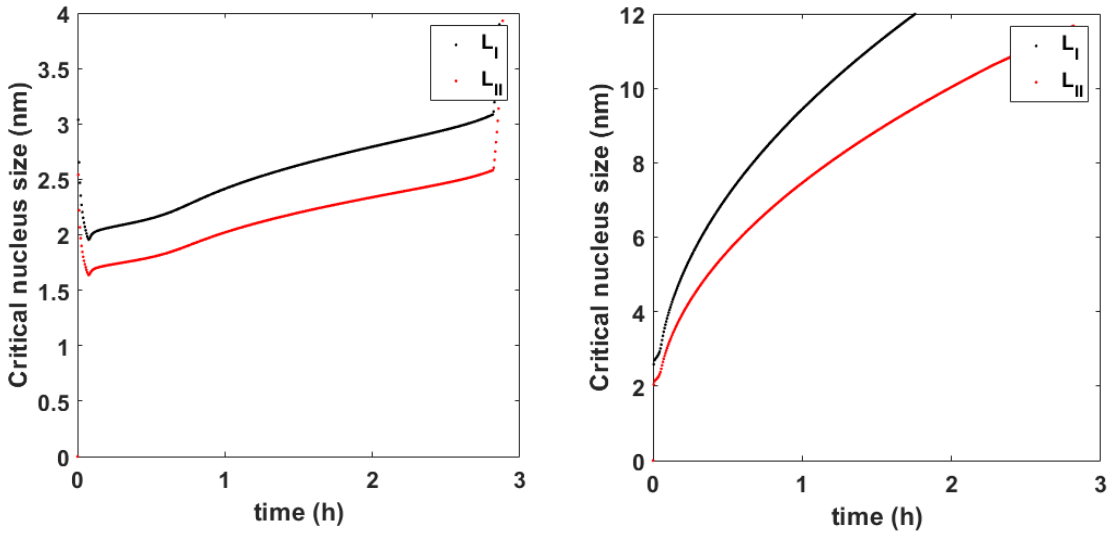


Figure 4.5.7 Comparison between critical nuclei sizes for primary and secondary events, calculated by PBEM for C-S-H Ca:Si = 2, and C-S-H + $ Ca:Si = 1.75, Q = 1.5 mL/min

A sharp increase in critical nucleus size is observed upon the addition of sulfates, which would correspond to a slowing of kinetics. Contrastingly, the recalculated growth rate coefficient with the addition of sulfates is ~50 times greater than the values calculated by Andalibi et al., and ~1000 times greater that the recalculated parameters for the pure-phase Ca:Si 1.75 sample[30].

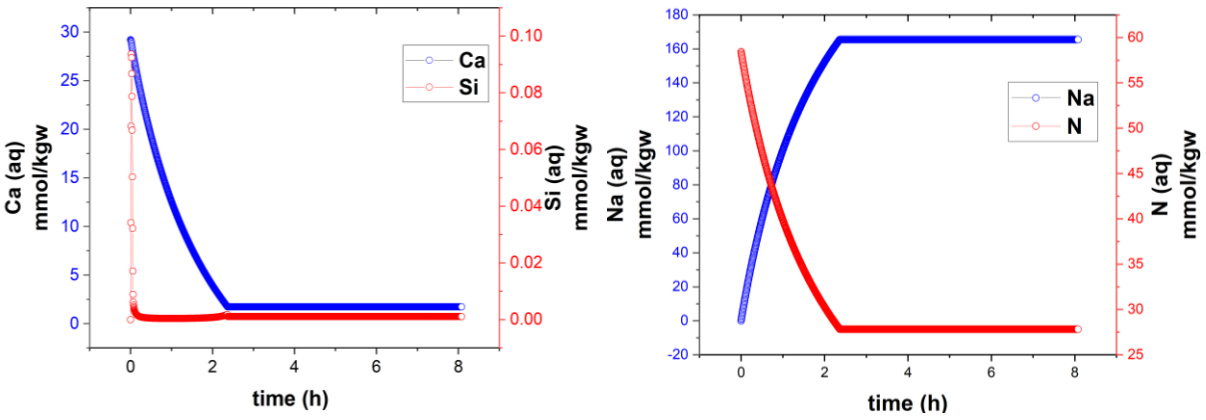


Figure 4.5.8 Concentrations of aqueous calcium, silicon, sodium, and nitrogen during precipitation of C-S-H + $, Ca:Si = 1.75, Q = 1.5

The concentration profiles for Ca, Si, Na, and N in solution are plotted in Figure 4.5.8. Though silicate solution is being added into the reactor, no aqueous silicon is measured throughout the precipitation process. Amount of C-S-H produced, pH, ionic strengths, crystallite thickness, and particle edge length are compared in Figure 4.5.9.

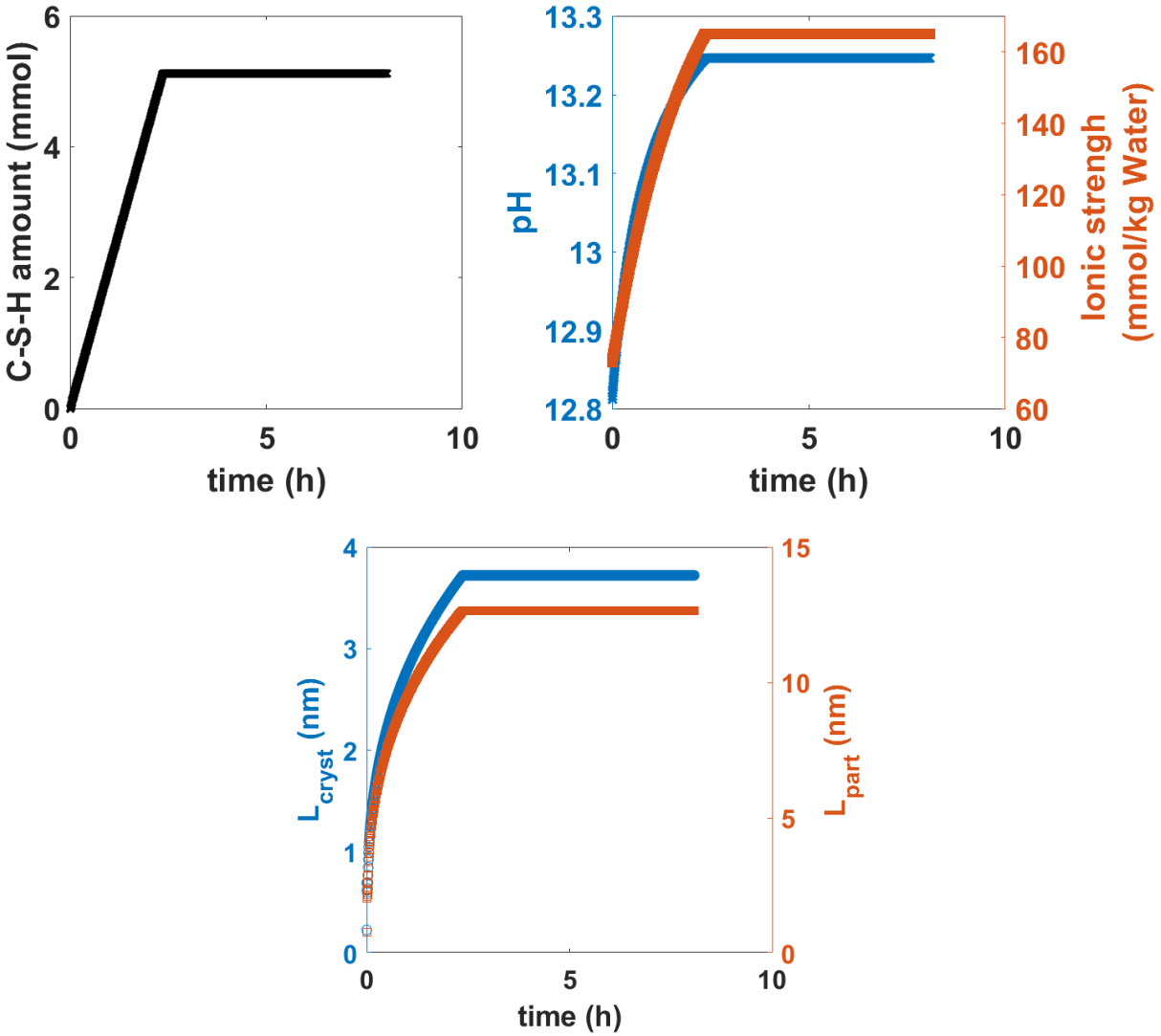


Figure 4.5.9 PBEM outputs for (a) C-S-H amount (b) pH and Ionic strength of solution, and (c) crystallite thickness, $L_{cryst}$, and particle edge length, $L_{part}$, for C-S-H + $, Ca:Si = 1.75, Q = 1.5 mL/min

The amount of C-S-H precipitated in addition to pH values and ionic strengths are as expected and given the recipe used. As observed in the pure-phase C-S-H with a Ca:Si = 1.75, lower particle edge lengths are predicted than expected, though the addition of sulfates results in a higher particle edge length than the recalculated, pure-phase C-S-H. It would be more expected to receive values ~100nm, as calculated by the work by Andalibi et al., or higher with the addition of sulfates[30], [83], [92]. The crystallite thickness $L_{cryst}$, is ~3.7nm after 3 hours of reaction, which is directly comparable to the values for C-S-H Ca:Si = 2[30].

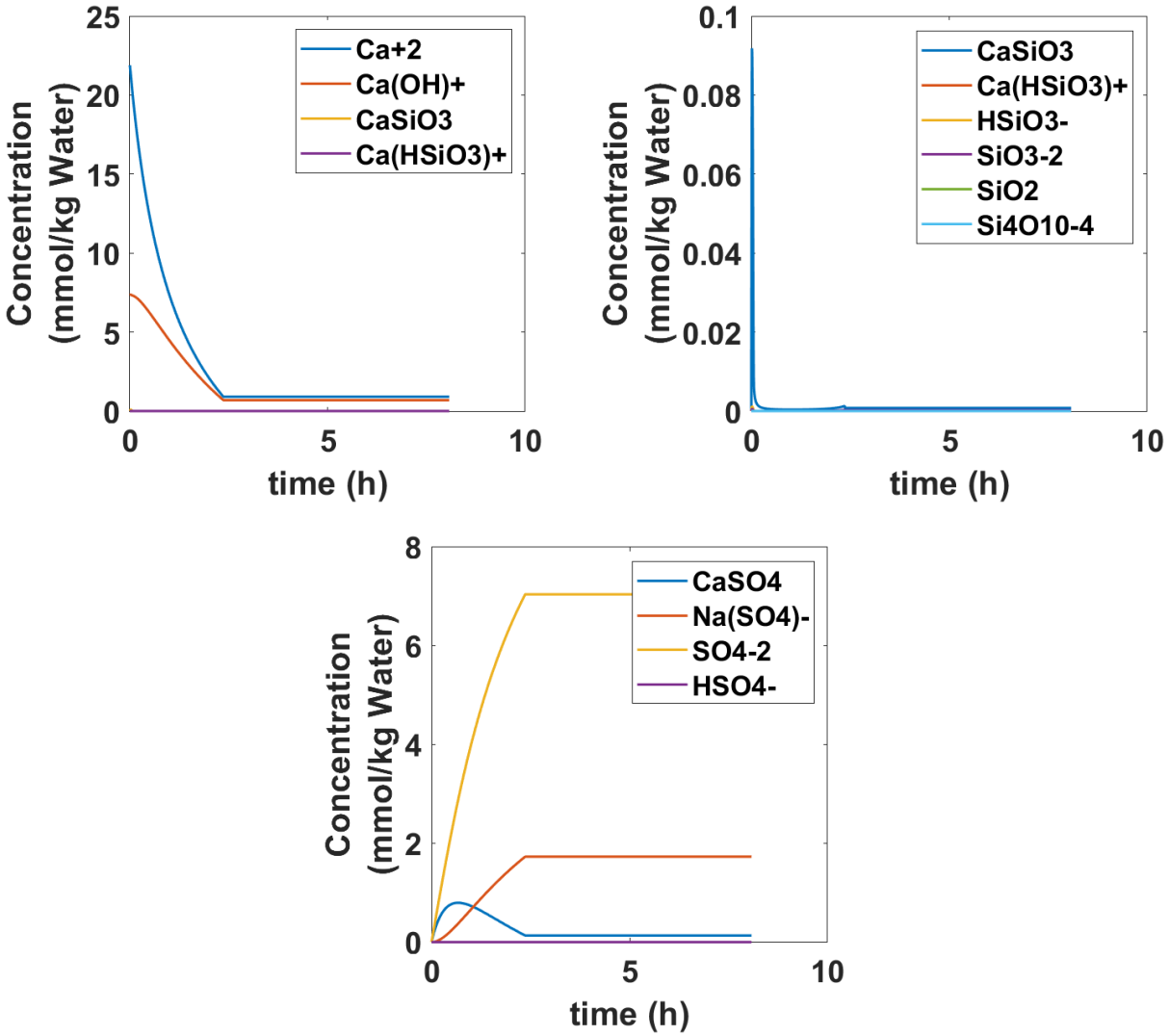


Figure 4.5.10 PBEM outputs comparing aqueous speciation of calcium, silicate, and sulfate species, C-S-H + $, Ca:Si = 1.75, Q = 1.5 mL/min

Aqueous speciation over time calculated by the population balance model shows primarily $Ca^{2+}$, $Ca(OH)^{+}$, $SO_4^{-2}$, and $Na(SO_4)^{-}$ in solution. As Figure 4.5.8 displayed very little or no silicate species in solution, similarly very low concentrations of silicates are measured in Figure 4.5.10. $CaSO_4$ concentration in solution increases as sulfates are added, though after an hour, and before all sulfates are added into the reactor, this concentration decreases.

In summary, the addition of sulfates is observed to modify consumption kinetics and the supersaturation of C-S-H and CH as a function of time. Further experiments investigating the precipitation products, perhaps cryo-EM methods, could prove useful in trying to understand how these changes manifest themselves in C-S-H

morphology. With the probability of 2-phases forming, the population balance model would have to be expanded to include 2 internal variables in order to take the simultaneous formation of C-S-H and CH. This could be done using the methods developed by Marchisio and Fox as they also used a moments-based method to solve the PBEM[71].

## 4.6 Scoping calculations on C-A-S-H PBE

### 4.6.1 Aluminates & kinetics of cement and concrete

In the production of cementitious materials, supplementary cementitious materials (SCMs) can be added to the mixture to decrease the $CO_2$ footprint of cement production. Many SCMs (e.g. calcined clays, slags, fly ash, etc.) are aluminum-rich, and the addition has been shown to affect the reactivity of cement, and consequently affect the dissolution of $C_3S$ and subsequent formation of C-S-H or C-A-S-H[86], [92], [97], [98]. In their work, Nicoleau et al. observed the delay in the acceleration phase in the hydration of alite resulting from inhibition at the surface of $C_3S$ due to the addition of aluminates[99]. And this inhibition to $C_3S$ was observed to decrease at pH values above 13 in work by Suraneni and Flatt[100]. Work by Quennoz and Scrivener suggested the poisoning of alite by aluminum presence, and the presence of aluminate hydrates reducing the hydration of $C_3S$ altogether[83]. Recent studies on C-A-S-H have provided insight on the atomic-level structure, but as the effect of aluminates on the hydration of $C_3S$ is not yet understood, the growth and nucleation of C-A-S-H alone has not been thoroughly investigated[18], [101].

In this section, a preliminary analysis of aluminates on the precipitation of C-S-H is made. Thermodynamic modelling is done to investigate the solutions in which aluminates are added. Additionally, $Ca^{2+}$ in solution is measured as C-A-S-H is precipitated and complications were encountered. Suggestions for ways to continue these experiments with higher success are discussed.

### 4.6.2 Solution modelling

In order to study the feasibility of the data collection experiment, solutions were studied by thermodynamic modelling to investigate both species in solutions and

saturation indices at different pH values for the “standard” reactant, 0.1-0.2M concentrations used to precipitate synthetic C-S-H. Figure 4.6.1 displays the dominant species in solution for pHs between 3 and 13.

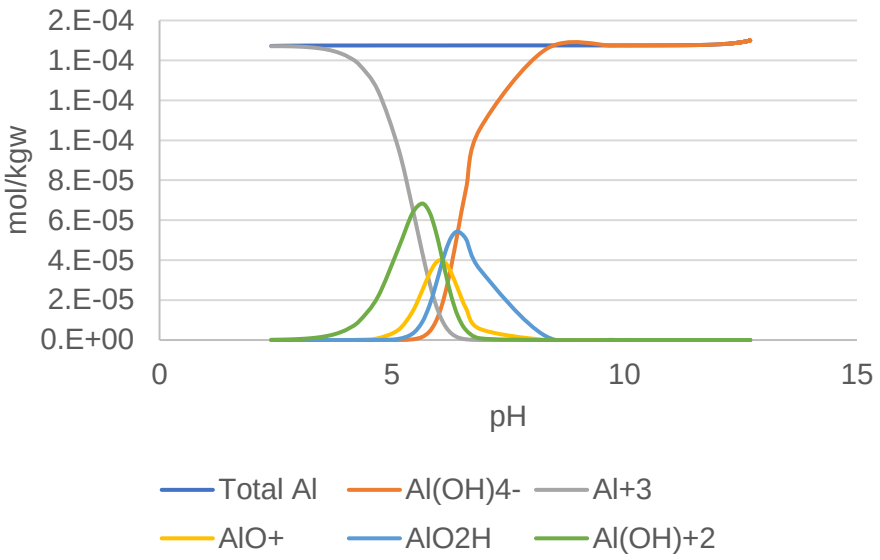


Figure 4.6.1 Concentration of 15mM $Al(NO_3)_3$ and 0.22M $Ca(NO_3)_2$ solution, titrated with $HNO_3$ to obtain pH profile

Calcium nitrate solution, at the concentrations used in the experiments diluted for data collection, has a pH ~ 9.7. At this point, thermodynamic modelling predicts primarily $Al(OH)^{4-}$ in solution.

Saturation indices are compared in Figure 4.6.2, displaying that in a solution of calcium nitrate and aluminum nitrate, at the pH of 9.7, Gibbsite and its polymorphs, bayerite and nordstrandite ($AlOH_{am}$ and $AlOH_{mic}$, respectively) are supersaturated with indices above 1.

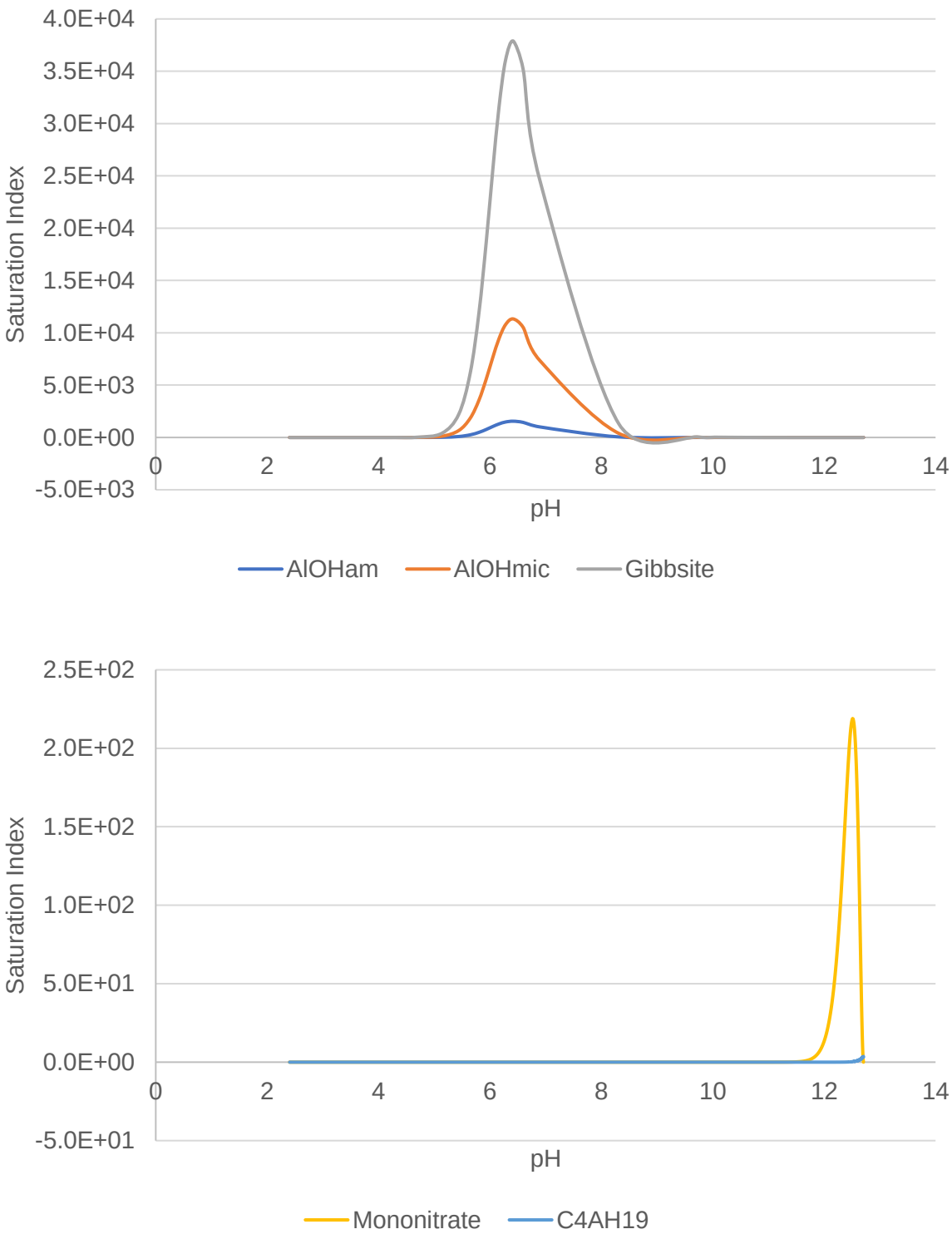


Figure 4.6.2 Saturation indices of aluminate species in 15mM $Al(NO_3)_3$ and 0.22M $Ca(NO_3)_2$ solution, titrated with $HNO_3$ to obtain pH profile

Between pHs ~10.5-11.7, no species are saturated in the media, and this would be a suitable pH interval for data collection on a non-diluted system, which exhibits a higher pH of calcium nitrate solution, at around 10.6. However, to obtain this pH in

the diluted system, NaOH, or another salt, would need to be added into the matrix. Unfortunately, increasing the pH would prematurely induce the formation of portlandite in solution.

The introduction of aluminum nitrate in the silicate solution was also studied to observe the species in solution, shown below in Figure 4.6.3. Sodium silicate solution, mixed with NaOH, initially starts at pH values above 12, depending on the desired Ca:Si. For all solutions with pH above 9, thermodynamic calculations predict primarily $Al(OH)^{4-}$ in solution after the addition of 15mM aluminates, as seen previously in the calcium nitrate solution. At pHs of ~12.3 and above, $AlSiO_5^{-3}$ is also predicted to be in solution.

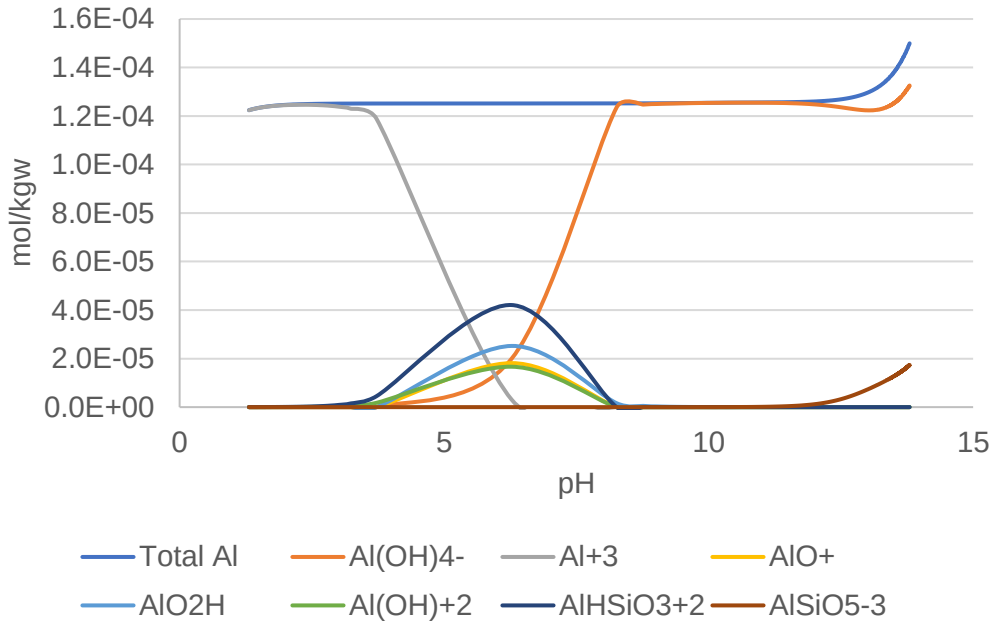


Figure 4.6.3 Concentration of aluminate species, 15mM $Al(NO_3)_3$ and 0.1M $Na_2SiO_3$ and NaOH solution, titrated with $HNO_3$ to obtain pH profile

Additionally, Figure 4.6.3, shows that not all aluminum is in solution until a pH of 13.8. This is further corroborated by analysis of the saturation indices, in Figure 4.6.4, showing the formation of considerably more species that are supersaturated and could form solids in the system. Analysis of the saturation indices, show that gibbsite, $AlOH_{am}$ and $AlOH_{mic}$ polymorphs, kaolinite, and natrolite ($Na_2Al_2Si_3O_{10} * 2 H_2O$) are also saturated to high pHs.

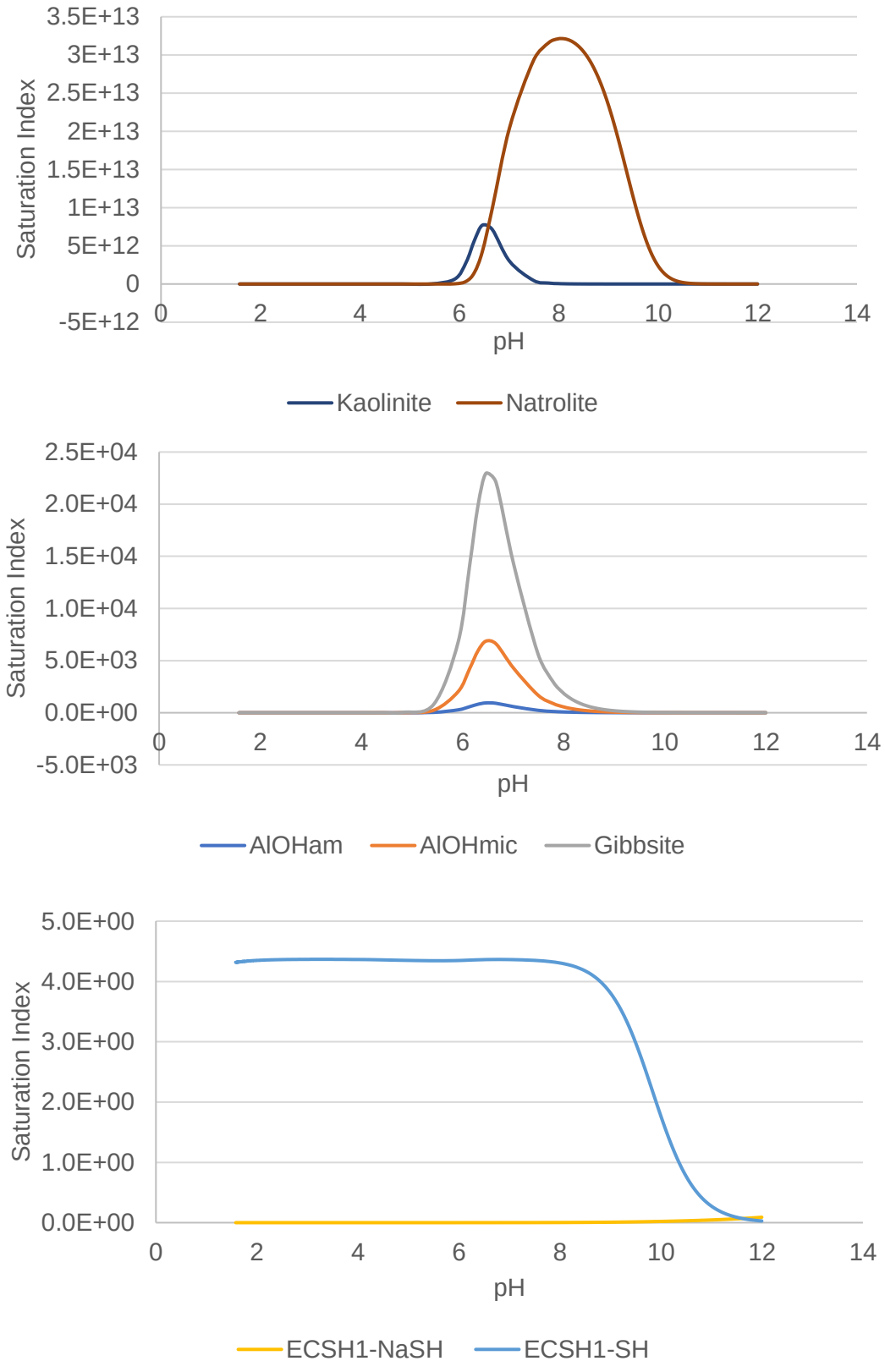


Figure 4.6.4 Saturation indices of aluminate species, 15mM $Al(NO_3)_3$ and 0.1M $Na_2SiO_3$ and NaOH solution, titrated with $HNO_3$ to obtain pH profile

However, after a pH of 12.5, thermodynamic modelling predicts no solids to be saturated in the solution. As a result, introducing aluminates into the solution may be possible via introduction in the silicate solution at pHs above 12.5, and this method would be reasonable for solutions to produce C-S-H at Ca:Si molar ratios of 1.5 and above. However, order of introduction would be expected to affect the precipitation of solids as NaOH should be added to the silicate solution before the aluminates to ensure that the introduction of aluminates is done at a high-enough pH.

### 4.6.3 Data collection involving aluminates

Experiments to precipitate C-A-S-H, Ca:Si = 1.6, with the dropwise precipitation method at a flowrate of 0.7 mL/min were done. 1.5mM of aluminates were added to the calcium nitrate solution the sample, and $Ca^{2+}$ concentration was measured throughout the reaction. Experiments were done at the dilutions described in section 4.2, however only at a 4x dilution, shown in Figure 4.6.5, was a $Ca^{2+}$ evolution over time obtained. At higher concentrations of both aluminates and calcium in the batch reactor, interference with the $Ca^{2+}$ electrode is observed.

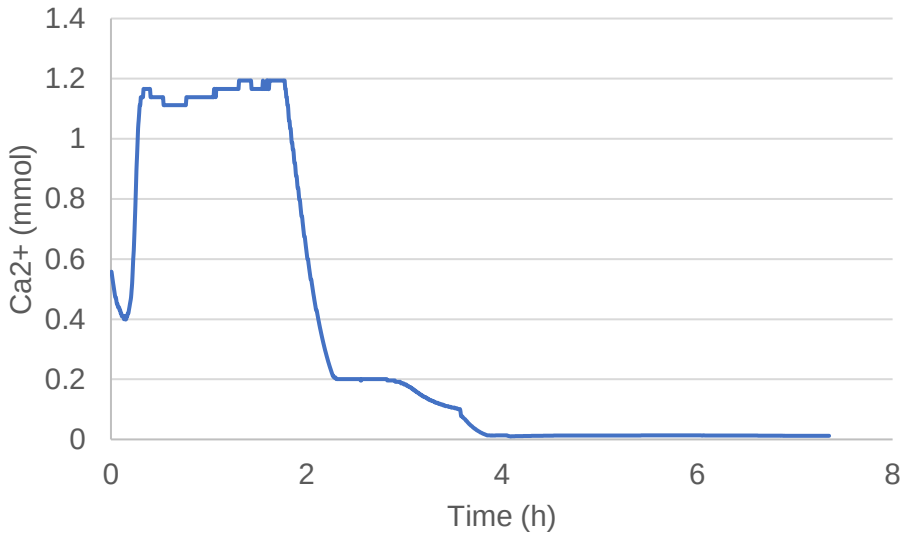


Figure 4.6.5 $Ca^{2+}$ evolution during precipitation of C-A-S-H with 1.5mM aluminates, Q = 0.7 mL/min, 4x dilution

Aluminum, which initially was in the reactor at the start of the experiment, and is at its highest concentration at the beginning of the experiment, shows inhibition in $Ca^{2+}$ measurement of the ion-selective electron. $Ca^{2+}$ concentration was expected to maximize ~ 5mmol, and around ~1.25mmol for this diluted experiment. Aluminates in calcium nitrate solution sat in the batch reactor for thirty minutes with the electrode as the required temperature was reached, and upon the start of the reaction, a concentration of 0.6 mmol $Ca^{2+}$ was measured. The electrode was wiped after 30 minutes reaction, and the $Ca^{2+}$ concentration was observed to increase, nearing the expected amount for this diluted system. However, a profile with small, discrete jumps in $Ca^{2+}$ is measured. After 2 hours of reaction, a concentration of 0.2mmol $Ca^{2+}$ is measured, and is observed to be consumed at a more constant rate until depletion.

### 4.6.4 Discussion

Results show certain limitations in both introducing aluminum into the C-S-H precipitation system and in collecting kinetic data with the $Ca^{2+}$ electrode. With care taken in order of introduction, introducing aluminates into the batch reactor in the silicate solution seems like a reasonable solution, particularly at high pH values. Calculations on solution speciation, in Figure 4.6.3, suggest that below a pH of 13.8, not all aluminum is in solution, and may be precipitated in the form of a N-A-S-H gel or possibly a hydrated sodium calcium aluminosilicate, though analysis on the saturation indices of solids included in the database suggest that there may be no saturated solid at pHs above 12.25. As a result, it may be best to introduce aluminates with possibly another salt than calcium nitrate. Sodium aluminate and aluminum silicate are other options for addition, though natrolite, a sodium-aluminum-silicate mineral, may continue to be present as thermodynamic modelling predicts supersaturation of natrolite at pHs of 13.3 and below. If data is collected on very high pH C-A-S-H, and aluminates are pumped into the reactor with the silicate solution, the risk of interference is significantly decreased as is the formation of a second phase before precipitation.

Introducing aluminates in the calcium nitrate solution seems like a less plausible option as the pHs of interest are higher than what is possible for the diluted data collection experiments, plotted in Figure 4.6.2. Another option is to introduce

aluminates in a separate solution, which can be done well under controlled experimental conditions and well synchronized flowrates, though the addition of a third solution would require more changes to the population balance model.

The second obstacle in collecting kinetic data with the C-A-S-H system is the effect of aluminum on the calcium electrode. The presence of aluminates in the solution matrix appears to block the measurement of $Ca^{2+}$ in solution as shown in Figure 4.6.5, and data was only able to be collected after 4x dilution of the already 10x diluted system. After two hours of reaction, a smooth curve for the consumption of $Ca^{2+}$ was collected, raising the possibility of successful data collection if aluminates are pumped into the reactor instead of initially being placed in the reactor. Additionally, if aluminates are added in the silicate + NaOH solution, a $Ca^{2+}$ consumption profile as collected in the kinetic data experiments used in the population balance model may still be attainable without too much additional dilution as the initial concentration of Al in the solution is zero.

To obtain kinetic data, it is also possible to collect $NO^{3-}$ concentration as a function of time, though in this case, $Al(NO_3)_3$ should not be used, so as to have only one source of nitrates and simplify the data collection. Turbidity, the measure of relative cloudiness in solution, may also inform on the nucleation of C-A-S-H.

## 4.7 Conclusions

In this chapter, the PBEM Matlab code of combined thermodynamic and population balance modelling was successfully modified for the analysis of synthetic C-S-H systems[30]. C-S-H with different Ca:Si can be modelled easily with the use of the simpler interface that was developed to cover the full range of Ca:Si ratios from 1 to 2. The validation of the approach, using experimental data, gave satisfactory results and highlighted further possible improvements, which are discussed below.

The population balance model was then used to investigate the effect of sulfate on precipitations on synthetic C-S-H. The collection of kinetic data was successful and showed changes in the precipitation kinetics. The main outcome of the addition of sulfates was the probable simultaneous precipitation of portlandite with the C-S-H. The kinetic parameters, as a consequence, may not be so accurate as the

population balance model was designed to follow one internal variable, and for 2 phases, a 2D population balance model will have to be incorporated. However, this modification of the saturation indices of C-S-H and portlandite (which never became supersaturated in the C-S-H system without sulfates), is very interesting as portlandite is always present in $C_3S$ and Portland cement hydration—showing how adding on extra component found in applied cements can eventually lead to clearer understanding of the nucleation and growth phenomena. The addition of aluminates created more challenging technical and theoretical situations that need further work to make better progress as highlighted below.

Naturally for such complex precipitation systems, there is much work left to do to obtain models for the growth and nucleation of C-S-H and systems at the full set of Ca:Si molar ratios with sulfates and aluminates. First, in order to collect good kinetic data, all solutions must be known and adjusted so that no additional phases form before the precipitation experiments begin. In preliminary experiments with C-A-S-H, thermodynamic modelling showed the precipitation of additional phases with $Al(NO_3)_3 * 9\ H_2O$ in both the calcium and silicate solutions. To continue this work, there may be options to add aluminates by way of different salts, though in many conditions, the formation of Natrolite seems to be common. Data collection with aluminates also proved to be difficult as there was adsorption of aluminum on the surface of the $Ca^{2+}$ ion selective electrode. Other options include trying a $NO^{3-}$ electrode in a solution where calcium nitrate is the only source of nitrates, working at high dilutions and pumping the aluminate-containing solution into the reactor, or collecting different types of data altogether like measuring turbidity.

Kinetic data was collected for C-S-H and C-S-H + $ at a Ca:Si of 1.75, and using the population balance equation model, inverse modelling was done to optimize parameters for both systems. Reasonable values for interfacial tension and cohesion energies were received, though given the reliance of these two parameters on surface interactions, the possibility of $Ca^{2+}$ adsorption on the surface of C-S-H, and the experimentally observed adsorption of sulfates, the accuracy of these values or the contribution of adsorption in these values is unknown[32], [80], [83].

In comparison to the kinetic growth rate constant of C-S-H at a Ca:Si of 2, the decrease in Ca:Si to 1.75 caused a 10x decrease in the growth rate constant to the

order of $10^{-10}$ $m^3/g^2$*mol*s while the addition of sulfates resulted in a growth rate constant on the order of $10^{-8}$ $m^3/g^2$*mol*s. Recalculated crystallite thicknesses for the pure-phase Ca:Si = 1.75 C-S-H were considerably lower than expected, the thicknesses below 1nm. With the addition of sulfates, this value rose to ~3.7nm which is consistent with the values calculated for the pure phase C-S-H at Ca:Si = 2[30]. Particle edge lengths for both recalculated systems at Ca:Si of 1.75 were much less than expected, maximizing at 13nm in C-S-H + $, and further investigation of these findings is needed.

Modelling additional C-S-H systems will require holistically advancements in surface thermodynamics of C-S-H as it pertains to both calcium and sulfate adsorption and expansions on the model to account for the precipitation or formation of more than one solid, namely portlandite. Before reaching this point however, good data collection must also be done in which temperatures, pump speeds, and cleaning must be well regulated. Also, solutions should be well controlled so as not to prematurely introduce an additional phase into the system. The population balance model allows for projections of the growth and nucleation of C-S-H for Ca:Si molar ratios of 1.5 and above, and with more data for the lower Ca:Si, it could very soon be useful for the full range of ratios.

# Chapter 5. Surface characteristics of synthetic C-S-H systems

C-S-H has a layered structure with a high surface area[81]. The interaction of the different species in pore solution with this high surface area can influence both transport and durability properties of cement and concrete. Previous work characterizing specific surface area, ion transport, and morphology and microstructure of C-S-H on a larger scale has shown large variability, creating many questions regarding the surface characteristics of C-S-H[102], [103]. In the past decade, great advancement has been made on compiling the bulk structure of C-S-H[18], [22]. However, comprehensive studies on the surface of C-S-H, accounting for its variability, has yet to be fully achieved. In this chapter, the measurement of zeta potentials with acoustophoresis of single-phase C-S-H, C-A-S-H, and C-S-H + $ is reported under different solution conditions to better understand the surface termination of synthetic C-S-H. The effects of sulfates and aluminates in addition to a full range of Ca:Si molar ratios from 1 to 2 are investigated and characterized with acoustophoresis and thermodynamic modelling.

## 5.1 Zeta potential of pure, single-phase C-S-H

### 5.1.1 Introduction

C-S-H, the main hydration phase of Portland Cement, has a disordered structure. Recent progress has given a better understanding of how the bulk structure of C-S-H changes in relation to the Ca:Si ratio, in particular the silicate chemical environment and Al incorporation from NMR spectroscopy and atomistic simulations[17], [18], [22]. More controlled experiments for a broader family of C-S-H structures are needed to find a similar understanding of the C-S-H surface, in particular at the high Ca:Si ratios which are found to average between 1.7 and 1.8 in early age ordinary Portland cement. The complexity of Portland cement-based systems, with 8 or more solid-solution interfaces at any given time during hydration makes the characterization of the C-S-H surface itself complicated. Recent advances in precipitation methods to reliably produce high ratio synthetic C-S-H, described in Chapter 3 and in the work by Kumar et al. allows this main hydration product to be studied in absence of the other phases found in cement[17], [32].

The atomic structure of C-S-H is analogous to that of a defective tobermorite, consisting of a double layer of Ca-O sheets between drierketten silicate chains which are separated by water-cation interlayers[14], [17]. Given the sheet-like structure of C-S-H on an atomistic scale and the resulting high specific surface area ranging between 200 to 300 $m^2/g$, surface interactions play a large role in understanding C-S-H from its nucleation and growth to adsorption and transport properties of cementitious materials[81], [104]. There has been a wide range of studies on the effect of the bulk composition of C-S-H, regarding alkali sorption, Ca:Si molar ratios, the uptake of sulfates and aluminates, and organic additives[12], [105]–[108]. However, no definitive model of the C-S-H surface has been determined[11], [18], [105].

Zeta potential, the focus of this work, is a measure of the electrical potential of charged particles in suspension at a small distance from the surface (the slipping plane). The slipping plane represents the layer between relatively static ions on the surface of a material and the ions mobile in the dispersion media. As a result, zeta potential measurements can be affected by surface charge, adsorption, and diffusion of different solution species present in cementitious systems[109], [110]. In previous work, measurements of zeta potential on C-S-H with Ca:Si ranging from 0.6 to 1.4 have shown negative charges at low Ca:Si, observed to increase by adding calcium, thus increasing the Ca:Si[53], [108], [111]. Potentials of up to +22 mV were measured in C-S-H with Ca:Si of 1.4 by Haas and Nonat, but no work has been done on C-S-H for high pure-phase Ca;Si >1.4[111]. In work by Harris et al., described in Chapter 3, high Ca:Si C-S-H samples, from 1.8 to 2 exhibited higher Ca:Si ratios than expected. Lower concentrations of calcium were measured in the supernatants than expected from thermodynamic modelling, leading to the hypothesis that there may be calcium adsorption on the surface at C-S-H, particularly at higher ratios[32].

The aim of this chapter is to analyze the effects of Ca:Si ratio, washing, and dispersion media on the zeta potential of synthetic C-S-H as it relates to understanding the termination and adsorption properties of the C-S-H surface. A full range of synthetic Ca:Si ranging from 1 to 2 is investigated in this study and characterized with acoustophoresis, solid and solution composition by ICP and XRD and thermodynamic modelling. In section 5.2, the effect of sulfates and aluminates on zeta potential, solution composition, and morphology is investigated.

### 5.1.2 Sample preparation and characterization

*C-S-H Synthesis*

C-S-H samples with Ca:Si molar ratios of 1, and 1.75 to be used in acoustophoresis and titration experiments were synthesized by dropwise precipitation used in the protocol described in Section 3.1[32].

Additional C-S-H samples with Ca:Si molar ratios from 1 to 2 were synthesized in a segmented flow tubular reactor (SFTR) as described in section 4.2.2.

All samples were washed with a 60 mL solution of 1:1 decarbonated water and ethanol.

*Acoustophoresis*

Zeta potential was measured with electroacoustics by the AcoustoSizer II supplied by Colloidal Dynamics, pH was also monitored. The equipment was calibrated with potassium tungosilicates (KSiW).

Before preparation, samples were either filtered without washing, or washed and filtered as described in section 3.1.7, in 60 mL of a 1:1, decarbonated water: ethanol solution.

To prepare samples for acoustophoresis, a suspension was created by adding 5 grams of filtered, wet C-S-H to 155 grams of dispersion media, either filtered reaction supernatant or 10mM NaOH solution. Suspensions were mixed for 15 minutes with a magnetic bar at 500 rpm, placed in an ultrasonic bath for 15 minutes, and allowed to mix at 500 rpm for another 15 minutes as the sample cooled to room temperature. Zeta potential measurements were taken immediately after mixing. All measurements were taken in triplicate for reproducibility. ICP measurements on supernatants from synthetic systems showed calcium concentrations in solution ranging from 2.6-7mm, 0.5-0.7mm of silicon, and 270-350mm of sodium, concentrations are given in Table 5.1.1[32]. Zeta potential measurements were also made on C-S-H samples dispersed in a 10mM NaOH solution.

Table 5.1.1 Inductively-Coupled Plasma Spectrometry measured concentrations for C-S-H Ca:Si 1.7-2.0, supernatant compositions for high Ca:Si samples

| Nominal Ca:Si | Ca:Si (ICP-OES) | Ca mmol/L | Si mmol/L | Na mmol/L |
|---|---|---|---|---|
| 1.7 | 1.79 | 2.64 | 0.59 | 289.7 |
| 1.8 | 1.88 | 4.89 | 0.66 | 272.7 |
| 1.9 | 2.05 | 5.06 | 0.59 | 347.1 |
| 2 | 2.3 | 6.98 | 0.58 | 340.2 |

*X-ray diffraction*

Samples characterized with X-ray diffraction were prepared as described in section 3.1.3.

*Inductively coupled plasma spectrometry*

Supernatants were characterized with ICP-OES, as described in section 3.1.3.

*Thermodynamic Modelling*

Thermodynamic modelling was done using both the Gibbs free energy minimization software, GEM-Selektor v.3, and PHREEQC Version 3[35], [37]. An expanded Cemdata-18 database was used including the CSHQ thermodynamic solid solution model, PSI-Nagra, redox-uncoupled gases from the PHREEQC database, and $NO^{3-}$ & $Na^{+}$ phases from the Lawrence Livermore National Laboratory (LLNL) database[31], [38]–[40].

### 5.1.3 Results & Discussion

*C-S-H dispersed in supernatant, comparison of Ca:Si*

Washed and unwashed samples with Ca:Si of 1.4, 1.75, and 2 were titrated after the initial zeta potential measurements with $HNO_3$ to dissolution around a pH of 10[46]. The results are plotted in Figure 5.1.1, and zeta potentials are compared at the similar pH values for each Ca:Si. At a molar ratio of 2, samples are compared at a pH of 12.80, at a ratio of 1.75 at pH 12.68, for pH of 12.10 at a Ca:Si of 1.4. Unwashed samples consistently exhibited slightly higher potentials, 1.48 mV higher for Ca:Si = 2, 2.91 mV higher for Ca:Si = 1.75, and 1.32 higher for Ca:Si = 1.4.

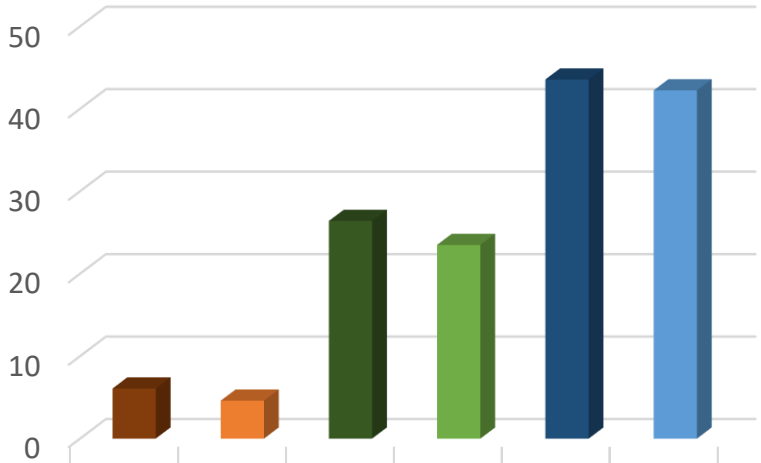


| | | | | | | |
|---|---|---|---|---|---|---|
| Zeta Potential (mV) | 6.08 | 4.6 | 26.4 | 23.49 | 43.55 | 42.23 |

Figure 5.1.1 Comparison between zeta potentials of 3.1 wt% C-S-H with Ca:Si = 2 (blue) at pH 12.80, 1.75 (green) at pH 12.69, and 1.4 (orange) at pH 12.10 for samples dispersed in reaction supernatant, unwashed (UW) and simple washed (W) in water and ethanol mix

In all cases, zeta potentials measured in this study never go below zero, possibly due to the presence of calcium and alkali in the dispersion media as shown in Table 5.1.1.

In comparison to previous zeta potential measurements by Barzgar et al. and Haas and Nonat made on synthetic C-S-H with Ca:Si <1.5, prepared by mixing CaO and silica fume, the increase in zeta potential with Ca:Si and pH is also observed[108], [111]. In this study, at a Ca:Si of 1.4, the zeta potential is positive at 4.6 mV when washed, but at the same Ca:Si, Barzgar et al. received negative potentials at pH values above 12.5 while Haas and Nonat measured potentials nearing 23 mV at a pH of 12.45, more comparable to the potentials of Ca:Si = 1.75 in this study.

Plotted in Figure 5.1.2 are the zeta potential measurements of washed synthetic C-S-H dispersed in filtered supernatant and titrated with nitric acid until precipitate dissolution. The zeta potential measurements of Haas and Nonat are also plotted for Ca:Si of 0.6 to 1.4, and exhibit the same trends of increasing potentials with increasing Ca:Si and pH.

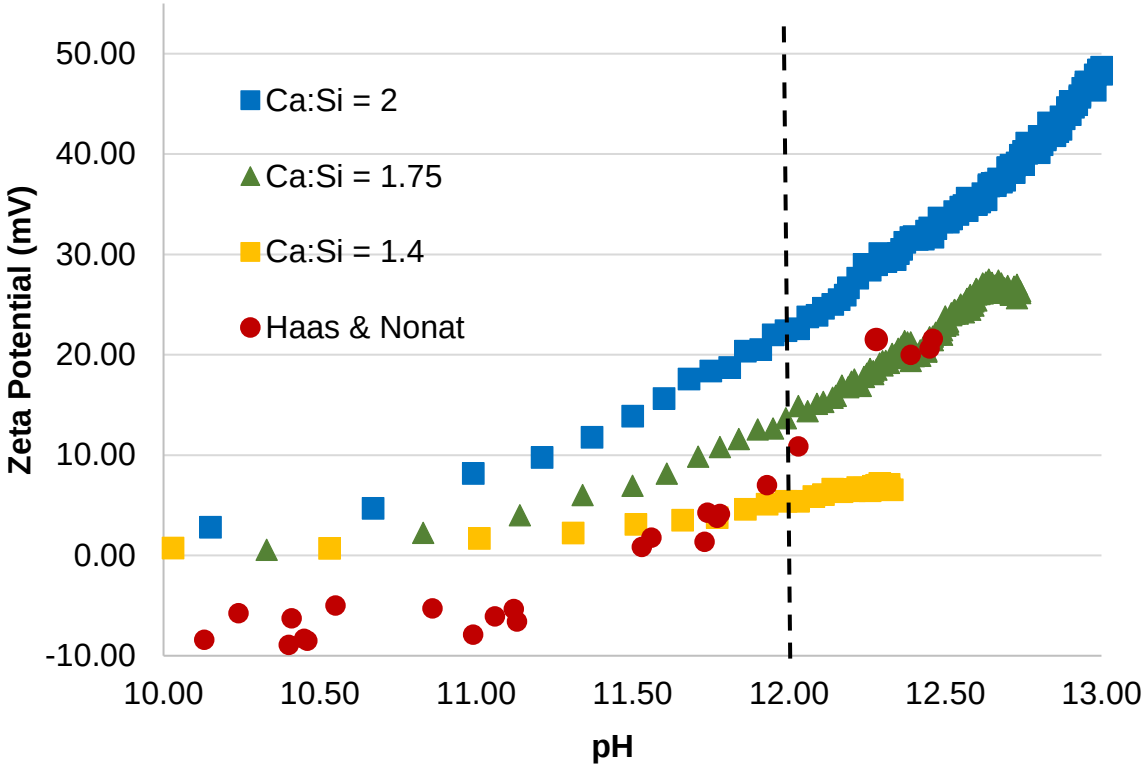


Figure 5.1.2 Comparison between zeta potentials of C-S-H with Ca:Si of 2 (blue), 1.75 (green), and 1.4 (yellow), 3.1wt% washed C-S-H dispersed in reaction supernatant and titrated with $HNO_3$ until C-S-H dissolution.

At a pH of 12, Figure 5.1.2 shows the average zeta potentials of 4.57, 13.70, and 22.76 for Ca:Si ratios of 1.4, 1.75, and 2, respectively. Experiments by Haas and Nonat exhibited zeta potentials of greater than 20 mV for C-S-H with Ca:Si up to 1.4—relatively high potentials for the ratio when compared to this study. However, the samples by Haas & Nonat were dispersed in a media with no alkali, and show only the effect of calcium concentration and pH on the zeta potential[111]. These variations between different studies show the sensitivity of the measured zeta potential to the dispersion media composition. The full details of the exact concentrations of the dispersion used in the Barzgar et al. and Haas and Nonat publications are not given. This makes quantitative comparison difficult, though general trends can be qualitatively interpreted.

Concentration values of calcium, silicon, and sodium in C-S-H supernatants measured by ICP-OES in Table 5.1.1 were used to calculate aqueous speciation at equilibrium for Ca:Si molar ratios of 1.7, 1.8, 1.9, and 2, plotted in Figure 5.1.3.

At equilibrium, thermodynamic modelling shows an increasing concentration of free $Ca^{2+}$ and $Ca(OH)^{+}$, $CaNO_3^{+}$, and $CaSiO_3$. At a Ca:Si of 2, we observe an increase of $NaHSiO_3$, $HSiO_3^{-}$, and $Ca(HSiO_3)^{+}$ species in solution to be compared with the trend of decrease observed as the Ca:Si increases from 1.7 to 1.9. The pH for all simulations was set at 13. Relatively, as the Ca:Si increases the relative amount of $Ca(OH)^{+}$ in solution in comparison to $Ca^{2+}$ increases as well.

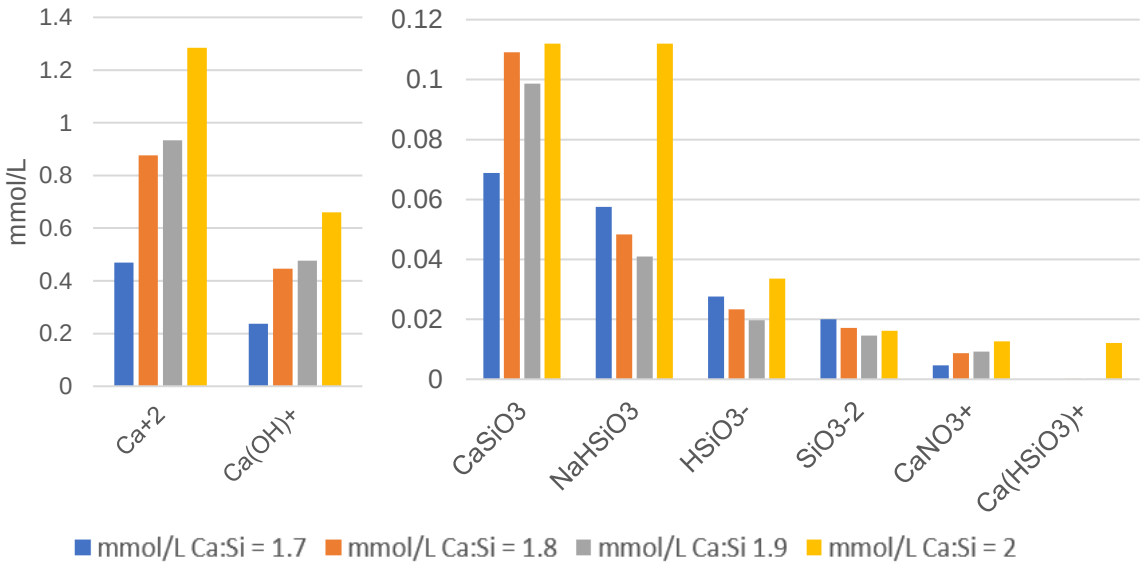


Figure 5.1.3 Aqueous speciation calculated by PhreeqC with Cemdata 18, C-S-HQ, and LLNL databases comparing synthetic C-S-H reaction supernatants for Ca:Si ratios of 1.7-2.0 at pH of 13

*C-S-H dispersed in 10mM NaOH, comparison of Ca:Si*

Zeta potential of C-S-H, Ca:Si from 1 to 1.75, dispersed in a 10mM NaOH solution is shown in Figure 14. In an alkali dispersion media with no additional calcium other than what may be on the surface, the potential remains positive and increases with the Ca:Si molar ratio, maximizing at 3.5 mV at a Ca:Si of 1.75, about four times lower than the potential of C-S-H at the same ratio dispersed in supernatant.

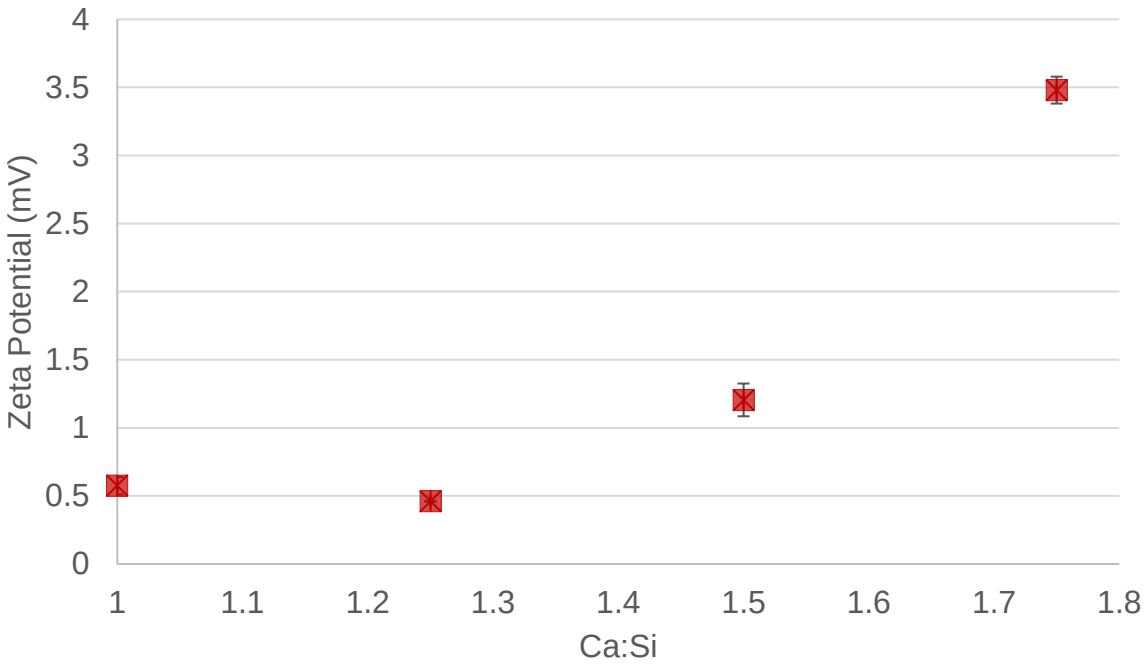


Figure 5.1.4 Zeta potential comparison of C-S-H, Ca:Si of 1, 1.25, 1.5, and 1.75, dispersed in 10mM NaOH (pH = 12). Error bars represent standard deviation in set of three measurements on the same sample.

Thermodynamic modelling with Cemdata 18.1 predicted that at equilibrium, 5.2mM of calcium should be in supernatant for synthetic C-S-H with a Ca:Si of 1.75, and a concentration of 22.30mM at Ca:Si = 2.

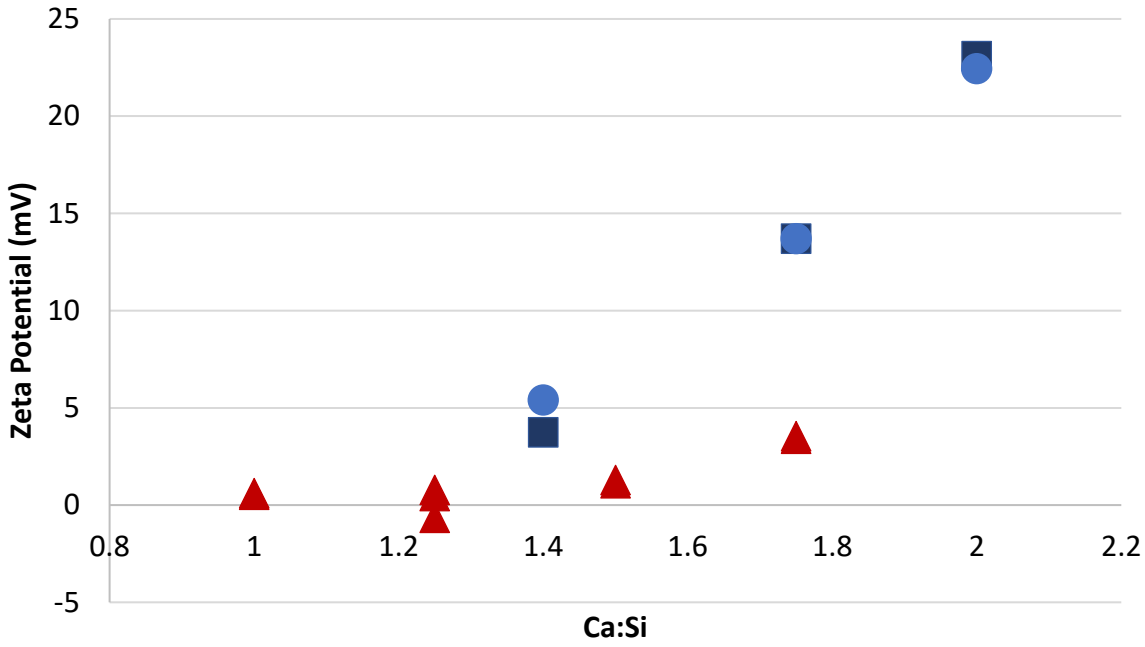


Figure 5.1.5 Comparison of Zeta Potentials of C-S-H dispersed in supernatant (blue), and in 10mM NaOH

Results for zeta potential measurements of samples washed and dispersed in filtered supernatant and in NaOH solution are plotted in Figure 5.1.5. In both cases, zeta potentials for synthethic C-S-H under these conditions is positive, suggesting a high affinity for positively charged ions to the surface. However, the stark potential difference between the two dispersion media suggests some desorption of ions from the surface of synthetic C-S-H when dispersed in NaOH.

*Calcium titration experiments*

To investigate the possibility of reversable adsorption on the surface of synthetic C-S-H, titration experiments were done with C-S-H at ratios of 1 and 1.75 after washing and dispersed in NaOH. Samples were then titrated with $Ca(NO_3)_2$ solution to 14mM and 45mM, respectively. In both cases, more than three times the amount of calcium in solution at equilibrium as calculated by thermodynamic modelling was added. For both experiments, there were 10 minutes between each addition of calcium to allow for equilibration. Additionally, the final titration measurements equilibrated for 15 hours before further zeta potential data collection. Samples were then re-filtered and re-dispersed into a 10mM NaOH solution, and then measured to see any change in zeta potential. Results are plotted in Figure 5.1.6 a-b.

In the case of Ca:Si = 1 C-S-H, the potential increased, and when re-filtered, and re-dispersed in 10mM NaOH, we observe a negative potential of -1.1 mV. In the case of C-S-H with a Ca:Si of 1.75, although more than 3 times the amount of calcium expected in solution from thermodynamic modelling is added, the sample reaches a maximum zeta potential of 9.54 mV, in comparison to the 13.70 mV of the C-S-H sample dispersed in supernatant. After the addition of calcium, and after an additional 15 hours of mixing, no significant change in zeta potential was measured, indicating that this lower zeta potential is not a kinetic effect but possibly change in relative surface concentration of $Ca^{2+}$ and $Na^{+}$ ions, as the calcium was only partially reversible in these conditions.

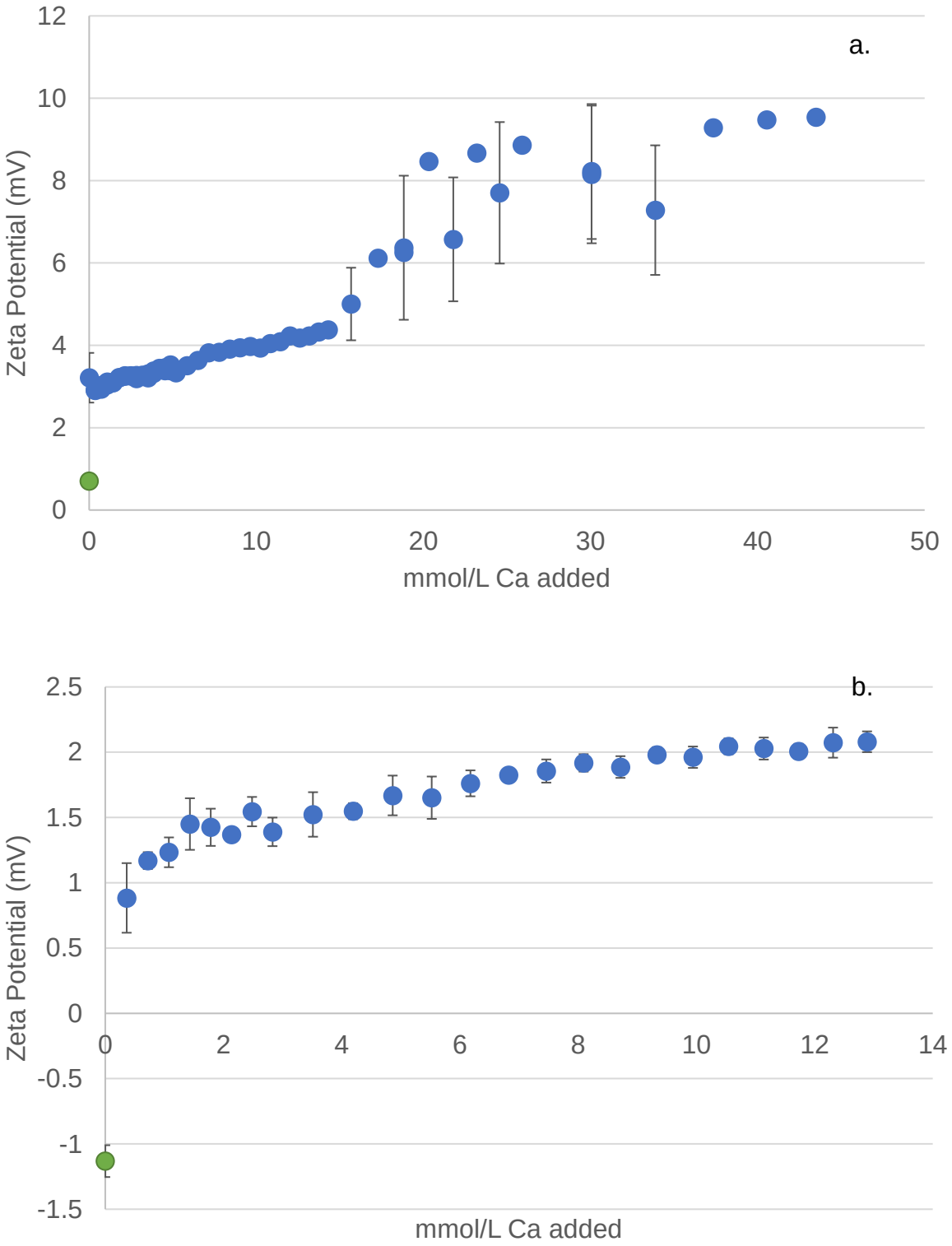


Figure 5.1.6 Synthetic C-S-H, nominal Ca:Si = 1 (a), and nominal Ca:Si = 1.75 (b), dispersed in pH 12 NaOH and titrated with $Ca(NO_3)_2$ solution (blue-cycle, C1); post-titration, sample re-filtered and re-dispersed into pH 12 NaOH (green-cycle, C2)

To check if there was any significant modification or decalcification of the C-S-H after these experiments, XRD data was collected on freeze dried samples. The XRD diffraction pattern of both titrated samples from Figure 5.1.6 are shown in Figure 5.1.7, with only a slight carbonation of Ca:Si = 1.75 C-S-H. Otherwise the C-S-H peaks align with both C-S-H from tobermorite and clinotobermorite phases. Clinotobermorite is structurally similar to tobermorite 11Å, with higher amounts of structural disorder[112]. Despite the slight carbonation, which is to be expected due to repeated handling, as discussed in Figure 3.1.7, C-S-H remains the main phase of the samples post titration and re-filtration.

Additionally, the titrated and re-filtrated Ca:Si 1 sample is the sole sample of this study to have a low-magnitude, negative zeta potential. As a result, it seems that the adding of calcium and subsequent re-dispersion into 10mM NaOH solution acted simultaneously as the most effective method to remove positively charged ions from the C-S-H surface, while simultaneously limiting the potentials from reaching the high magnitude zeta potentials observed on samples dispersed in supernatant.

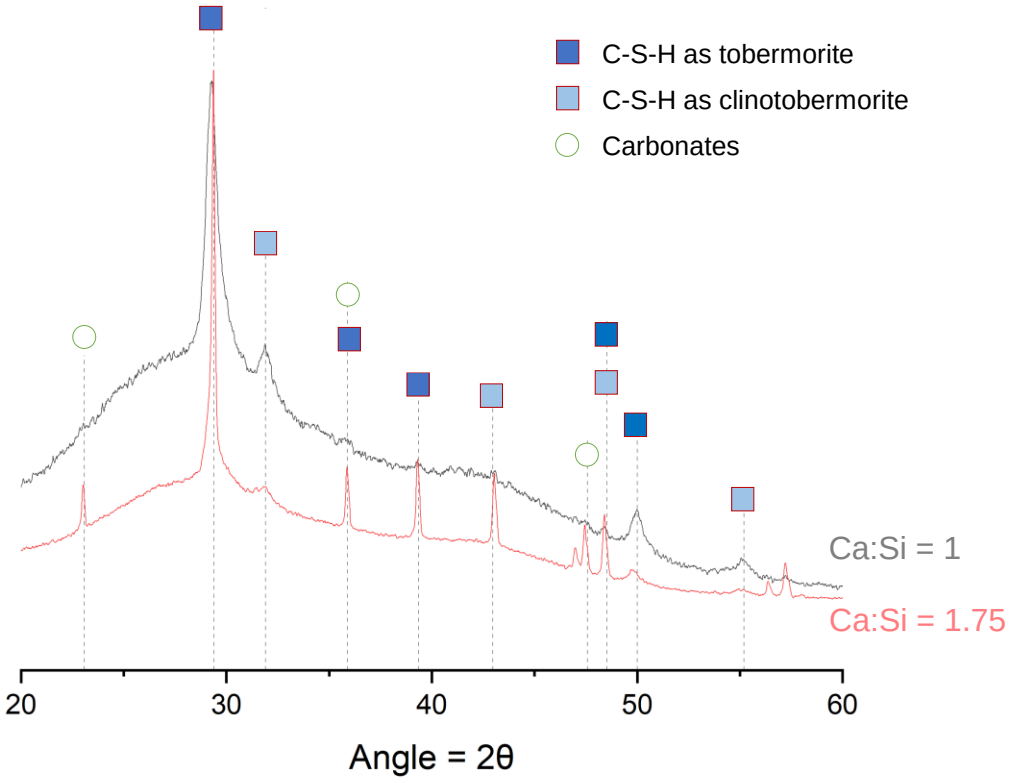


Figure 5.1.7 X-ray diffractogram of C-S-H with Ca:Si of 1 and 1.75 post dispersion in 10mM NaOH, titration with $Ca(NO_3)_2$, filtration, and re-dispersion in 10mM NaOH

*Adsorption of $Na^+$ and $Ca^{2+}$ on synthetic C-S-H surfaces*

After titration, and after re-filtration and re-dispersion into 10mM NaOH, two solutions per titration experiment were collected and measured by ICP-OES. With this data, the expected thermodynamic aqueous speciation was calculated, and results are given below in Table 5.1.2, including the measured pH values at which all speciation was also calculated to better understand the measured zeta potentials.

Table 5.1.2 Zeta potential measurements and ionic species in solution for Ca:Si = 1 and Ca:Si = 1.75 titration experiments after adding 12.8mM and 43.5mM of calcium to solution, respectively to C-S-H in cycle 1 (C1), and after re-filtration and re-dispersion into 10mM NaOH solution in cycle 2 (C2)

| | Ca:Si = 1, C1 | Ca:Si = 1, C2 | Ca:Si = 1.75, C1 | Ca:Si = 2, C2 |
|---|---|---|---|---|
| **pH** | 11.91 | 12.24 | 12.03 | 12.55 |
| **$ZP_{initial}$** | 0.9 mV | -1.1 mV | 3.5 mV | 0.7 mV |
| **$ZP_{final}$** | 2.1 mV | - | 9.5 mV | - |
| **$OH^-$** | 8.6e-03 | 1.9e-02 | 1.2e-02 | 3.9e-02 |
| **$Na^+$** | 4.9e-03 | 1.9e-02 | 1.5e-03 | 3.9e-02 |
| **$Ca^{2+}$** | 1.8e-03 | 1.2e-04 | 4.9e-03 | 7.8e-05 |
| **$Ca(OH)^+$** | 1.7e-04 | 2.3e-05 | 6.0e-04 | 2.7e-05 |

Comparison between C-S-H samples dispersed in supernatant, in 10mM NaOH solution, and in 10mM NaOH solution with added calcium displays the considerable difference and importance of dispersion media in addition to the effect of washing and order of exposure to sample surface. In the attempt to raise zeta potentials of samples dispersed in NaOH by titrating with calcium and exceeding the expected concentrations, we do not observe complete reversibility of $Ca^{2+}$ adsorption as the potentials plateau at less than the maximum potentials received in the experiments dispersed in supernatant alone—for a Ca:Si of 1.75 in supernatant, a potential of 13.7 was received at a pH of 12. ICP results for the samples titrated with calcium exhibit at first, 3 times the amount of calcium in solution, and then after re-filtration, and re-dispersion into 10mM NaOH, solution concentration results give 500 times the amount of $Na^+$ in solution when compared to $Ca^{2+}$.

But are these observations due to partial reversibility, or to the presence of $Na^+$ and simultaneous absence of $Ca^{2+}$? Haas and Nonat observed low Ca:Si C-S-H samples between nominal ratios of 0.8 and 1.6 raise from negative zeta potentials to 22 mV, comparable to the values observed in this study of Ca:Si = 1.75 sample suspended in supernatant. However, Haas and Nonat performed their experiments in alkali-free media, effectively removing any competition between $Na^+$ and $Ca^{2+}$ to the C-S-H surface.

When present, divalent ions have a higher propensity to be attracted to the surfaces; however monovalent ions can be competitive for the surface when considerably higher in concentration than the divalent counterpart[53], [113], [114].

This is not to conclusively say that $Na^+$ replaces $Ca^{2+}$ on the surface after treatment with excess calcium and filtration. Rather first, the effective removing of C-S-H from an environment in which the relative concentration of sodium is 100 times higher than that of calcium, washing, and re-dispersing in a divalent-free, sodium-rich media, in certain cases, 500 times greater in concentration than calcium, gives sodium an advantage to adsorb on the surface, and decreases the magnitude at which calcium can re-adsorb. This would consequently reduce the measured zeta potentials as observed.

*Approximation of effective surface charge densities*

To use the above zeta potentials to get an approximation of the surface charge density and thus a better idea of how C-S-H surfaces may be terminated under different conditions, further analysis was carried. To investigated further, full information on dispersion media and material dispersed is required for an accurate analysis and comparison of results. As a result, ICP data for all experiments were combined with the measured zeta potentials, pH values, and thermodynamic modelling to approximate ionic concentrations and thus effective surface charge densities.

The effective surface charge density is calculated using the Gouy-Chapman-Stern model in which in approximating charges at a surface, a nearly immobile layer of ions exists against the charged surface[115]. For this study in which we observe high ionic strengths, the distance between the surface and the slipping plane was approximated as the distance between the surface and the Debye length, represented by $\kappa^{-1}$, shown below in Equation 5.1 where $\epsilon_0$ is the dielectric constant, $\epsilon_r$ is vacuum permittivity, $k_B$ is the Boltzmann's number, T is absolute temperature, $N_A$ is Avogadro's number, e is elementary charge, and I is the ionic strength of the electrolyte.

$$\kappa^{-1} = \sqrt{\frac{\epsilon_0 \epsilon_r k_B T}{2 N_A e^2 I}} \qquad (5.1)$$

The Debye length, or the screening length represents the distance between ions affected by the surface of a particle and the bulk. At higher concentrations, the Debye length is lower, and can reasonably be taken as the slipping plane. In this study, the Debye length was predicted from ionic concentrations, calculated with thermodynamic modelling based on ICP results. The surface charge densities and Debye lengths calculated for the systems in this chapter were approximated for samples dispersed in supernatant and in 10mM NaOH solution, plotted below in Figure 5.1.8 and Figure 5.1.9, respectively.

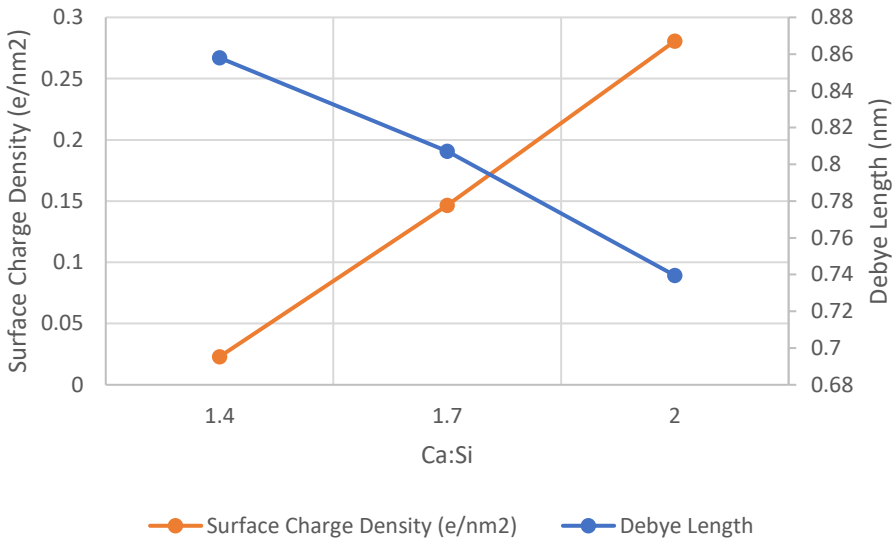


Figure 5.1.8 Surface charge density and Debye length of C-S-H, Ca:Si 1.4, 1.75, and 2.0 dispersed in supernatant at pH values of 12.1, 12.69, and 12.80, respectively

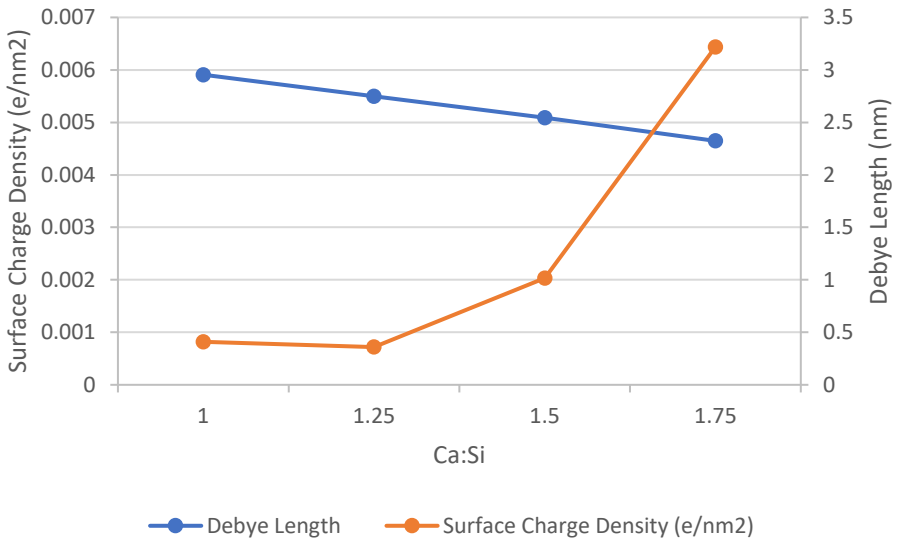


Figure 5.1.9 Surface charge density and Debye length of C-S-H, Ca:Si 1-1.75 dispersed in 10mM NaOH solution (pH = 12)

For both samples dispersed in supernatant and 10mM NaOH solution, as the Ca:Si increases, the ionic concentration of the dispersion medium increases as well. Correspondingly, the Debye length decreases with increasing ionic concentrations. Debye lengths for sample dispersed in supernatant range from 0.73 nm to 0.86 nm, and surface charge density values range from 2.2 x $10^{-2}$ to 2.8 x $10^{-1}$ elemental charge per $nm^2$, and increase with increasing Ca:Si molar ratio. Samples dispersed in 10mM NaOH exhibited lower ionic concentrations and higher Debye lengths ranging from 2.32 nm to 2.95 nm. Surface charge densities for these samples range from 8.2 x $10^{-4}$ to 6.4 x $10^{-3}$ elemental charge per $nm^2$. The plotted results and corresponding calculated ionic concentrations are calculated at the same pH value at which all zeta potential measurements were taken so as to match solution concentration ICP-OES measurements. For samples dispersed in supernatant, calculations for Ca:Si of 1.4, 1.75, and 2.0 solutions were done at pH values of 12.10, 12.69, and 12.80, respectively. Calculations for solutions dispersed in 10mM NaOH were done at pH values of 12.00.

### 5.1.4 Discussion

To best correlate measurements and compare zeta potentials to surface charge densities and potentials, full analysis of both the precipitates and dispersion media is necessary in addition to full details on sample treatment, which is often missing in publications. With synthetic C-S-H, results show that washing also plays a crucial role in determining the slipping plane potential, and given that a difference between washed and unwashed samples is consistently observed by acoustophoresis suggests the possibility of desorption of some positively charged ions from the surfaces of the samples during washing.

When dispersed in supernatant which has an increasing amount of calcium as the Ca:Si ratios increase, the potential is observed to increase, maximizing at nearly 50 mV. Synthetic C-S-H produced by the same methods and dispersed in NaOH with a pH of 12 also exhibited this increase of potential with Ca:Si; however, the potentials measured, in absence of the supernatant as the dispersion media, and at a lower pH than found in applied systems, are considerably lower (< 5 mV). Comparison of the potentials of C-S-H dispersed in supernatants and NaOH with a pH of 12 suggests at least a partial reversibility of calcium adsorption on the C-S-H sample.

To simulate this adsorption experimentally, C-S-H with ratios of 1 and 1.75 were titrated with $Ca(NO_3)_2$ solution. In both cases, 3 times the amount of calcium expected in the solution was added, and although the potential is observed to increase with increasing amount of calcium in solution, the zeta potential does not reach the potentials observed in the C-S-H dispersed in supernatants, suggesting that at the equilibrium times given for these experiments of 15 hours, the adsorption of calcium on the surface of these samples is only partially reversible. Comparison with data from Haas and Nonat rather suggests a probable effect of alkali presence on the C-S-H. The experiments presented here always had high alkali contents ( > 200 mM), and perhaps in absence of $Na^+$ as competitor at these high concentrations, calcium adsorption may very well be more reversible.

The titrated samples in Figure 5.1.8 and Figure 5.1.9 were filtered and re-dispersed and showed, in both cases, lower potentials, the potential of the nominal Ca:Si = 1 sample recorded at -1.1, the only negative potential observed in this study. XRD analysis confirmed both samples to be still solely C-S-H. These results also suggest that the re-dispersion into NaOH solution my effectively act as a wash, possibly removing $Ca^{2+}$ from the surface, leaving sites unterminated, or possibly partially replacing $Ca^{2+}$ with $Na^{+}$. These questions can be further explored by further experiments and washing C-S-H with the 1:1 decarbonated water: ethanol solution, and subsequently with calcium solutions at different concentrations to observe if an alkali-free, $Ca^{2+}$ solution will result in the same a full range of potentials from the lowly positive to the high magnitude potentials observed in the samples dispersed in filtered supernatant, as plotted in Figure 5.1.5.

Calculated effective charge densities, based on the Gouy-Chapman-Stern model, from the measured zeta potential values are lowly positive. In work that combined experimental analysis and Monte Carlo simulations, Labbez et al. observed a similar trend on the surface of Ca:Si = 0.66 ratio C-S-H[53]. Surface charge density increased at higher pH values and in the presence of divalent $Ca^{2+}$ ions over $Na^{+}$. In this section, samples dispersed in supernatant give surface charge densities that are two magnitudes higher than samples dispersed in 10mM NaOH. More work can be done to calculate the surface charge densities using different surface models in which the electrical double layer is approximated differently, namely the Grahame model which inner-sphere and outer-sphere adsorbed ions are described in which the outer-sphere plane is most similar to the Stern layer.

The surface of C-S-H is dynamic and like many other systems changes in response to its environments. It appears that not only can we increase the surface charge densities at will, but we can also remove ions or cause ions not originally present to adsorb. Positively or negatively terminated, our C-S-H samples display a high affinity for calcium and alkali, particularly at the Ca:Si molar ratios of 1.7 and above. The question still remains, what is at the surface of C-S-H? And given the thin, layered structure of the hydrate, what is the effect of Ca:Si molar ratio on surface termination? What surface termination occurs on fibrillar C-S-H versus nanoglobules or sheets?

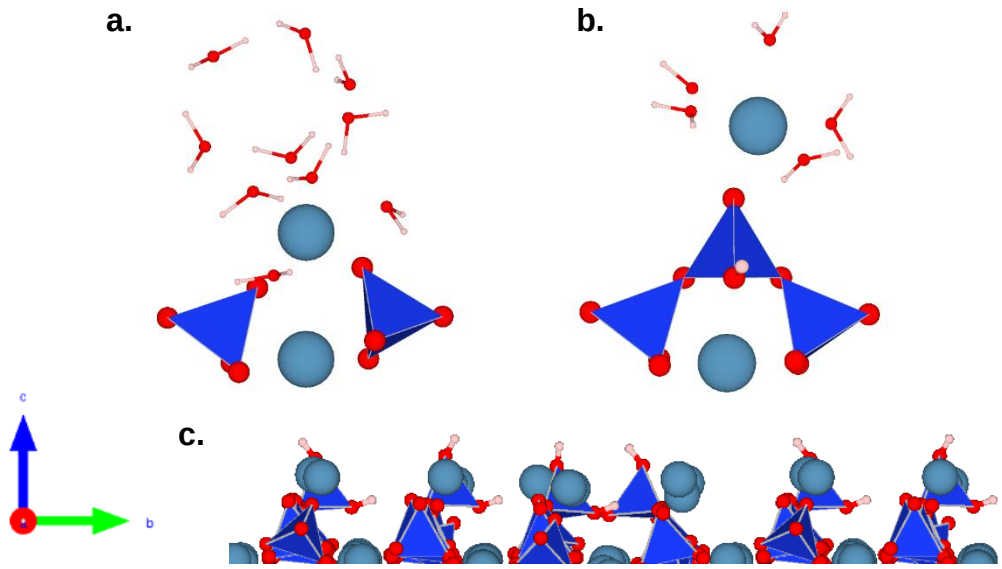


Figure 5.1.10 Atomistic simulations of the surface of C-S-H. (a) Ca in the bridging site coordinated to two oxygens in silicates & oxygens in $H_2O$ & lower main-layer calcium (b) Inner-sphere calcium adsorbed on $Q^{2b}$ bridging site (c) c-a plane in which main-chain calciums are coordinated to water or OH groups, prepared by Ziga Casar (EPFL)

In this section, potential at the slipping plane is studied—this most tangibly relates to surface termination, including adsorbed ions, rather than the physical surface of C-S-H alone. As a result, in order to understand the surface of C-S-H, atomic-scale simulations of the surface in addition to models of the electrical double layer, must be studied in combination with well documented zeta potential experiments[116]. The electrical double layer of C-S-H is likely complex—inner and outer layer adsorption is expected, and the washing experiments in Figure 5.1.1 suggest the possibility of even a second outer layer of adsorption in high $Ca^{2+}$ containing pore solution. Figure 5.1.10(b) displays inner-sphere calcium adsorbed to the surface of C-S-H. This complexity is even greater when considering the variation at different Ca:Si molar ratios and pH values. As a result, it is essential that experimental measurements include the dispersion solution and precipitate compositions, and all experimental conditions in order to best utilize thermodynamic modelling and determine ionic strength and speciation and thus be able to better interpret the zeta potential measurements.

### 5.1.5 Conclusions

In conclusion, zeta potential measurements were carried out on C-S-H with Ca:Si molar ratios ranging from 1 to 2. For each measurement, 3.15 wt% of precipitate was dispersed in either filtered supernatant or 10mM NaOH solution (pH = 12) and compared. Zeta potentials of samples dispersed in pH 12 NaOH were significantly lower than measured in samples dispersed in supernatant at the same pH. In Ca:Si 1.75 samples, potentials, dispersed in supernatant, exhibited a potential 10 mV higher than those in NaOH at a pH of 12, suggesting the desorption of the adsorbed ions ($Ca^{2+}$ and $Na^{+}$) on dispersions in NaOH.

This was further confirmed by experiments in which calcium was added to samples dispersed in NaOH solution. Three times the amount of calcium calculated by thermodynamic modelling of supernatants was added to C-S-H (Ca:Si = 1, 1.75) dispersed in NaOH. The Ca:Si 1.75 sample in supernatant had a potential of 13.7 mV while the potential of the sample dispersed in NaOH and titrated with calcium maximized at a potential of 9.5 mV. This suggests modification of the adsorption sites and/or C-S-H surface with this treatment history.

In conclusion, very careful characterization of the solid and dispersion medium with all handling details are essential for comparison with data from other studies.

The complexity of the C-S-H surface under these different conditions needs further zeta potential measurements under well controlled conditions. Full characterization also requires concurrent atomistic scale simulations to try and start accounting for the effect of Ca:Si ratios and a better understanding of how the predominant basal plane of the nanosheets of synthetic C-S-H are effectively terminated. These studies are currently underway in the SNF project (FNS: 200021_179076) at LMC(EPFL).

## 5.2 Synthesis of C-A-S-H and C-S-H + $ & surface analysis by acoustophoresis

The goal of studying synthetic C-S-H in isolation from other mineral phases in cement is to observe the separate effects of different additives and parameters. In this section, we focus on the addition of sulfates and aluminates on both solution species and zeta potential of precipitated synthetic C-S-H.

The effect of additives on zeta potential, ionic concentrations, and the resulting Debye lengths and surface charge densities of the resulting samples are investigated to better understand their surface properties.

### 5.2.1 Introduction

Aluminates and sulfates occur in cementitious systems for various reasons. To decrease the carbon footprint of Portland cement, supplementary cementitious materials or SCMs are often used to substitute the clinker in production. Often, these SCMs are aluminum-rich, and lead to the formation of more alumina-containing phases, making the cementitious system more complex[117]. In many cases, the addition of SCMs changes the reactivity of cement, directly affecting the formation of hydration products, which in effect, changes the setting of concrete[86], [92], [97], [98]. As a result, studying the main hydration products to determine how exactly they change in response to the presence of other elements or compounds is necessary.

The incorporation of aluminates in cement leads to the production of C-A-S-H, in which aluminates are in the structure of C-S-H with an Al:Si molar ratio normally less than 0.25[18], [20], [118]. Only recently has the bulk structure of C-S-H been understood at its full range of Ca:Si molar ratios; and this was used to determine the bulk structure of C-A-S-H again with the help of atomistic simulations combined with Si-NMR and Al-NMR experiments[18]. Notably, the recent findings by Kunhi Mohamed et al. predicted that aluminum can be present in C-S-H in four, five, or six-fold coordination. These include bridging sites, which, at high Ca:Si, means aluminates may take the place of calcium in C-S-H. Mohamed's study predicts that in high ratio C-A-S-H, calcium compensates the charge of the aluminum ion by moving to the interlayer[18]. By incorporating into the bridging sites, it is clear that aluminates can have an effect on the surface of C-S-H; however, the effect that this has on the surface charge, ionic speciation, and on a larger scale, morphology, have yet to be studied in detail.

Sulfates are often found in cements by way of gypsum, added to change the setting time of cement. Sulfate is commonly known to adsorb onto the surface of C-S-H during the accelerating period, which is the point at which initial setting occurs due to the growth of the hydration products, including C-S-H[83]. In newer cements like $LC^3$, sulfate is needed in higher amounts, further enhancing the reaction of alite, and adsorbing onto the surface of C-S-H[83], [84], [89]. In previous work, the addition of sulfates has been observed to increase the needle length of the hydration products, though understanding of how this affects both the bulk composition and the surface of C-S-H has not yet been achieved[90], [119]. Previous zeta potential measurements on ettringite and C-S-H show that sulfates clearly adsorb onto the surface of ettringite as the surface charge of ettringite is positive in alkaline solutions, but become negative in $SO_4^{2-}$ -containing pore solutions[120]. Currently, there are no studies which look to quantify the S:Ca molar ratio in C-S-H with adsorbed sulfates; however, in work by Berodier, the S:Ca ratio in Portland cement is stated as being between 0.08 and 0.1 at after 15 hours of hydration time[92].

This section serves to better understand how sulfates and aluminates affect the zeta potential and ionic speciation in the synthetic C-S-H system. Samples, produced in a segmented flow tubular reactor with Ca:Si values ranging from 1 to 2 are studied and characterized by acoustophoresis, inductively-coupled plasma spectrometry, transmission electron microscopy, and thermodynamic modelling to better understand how adding aluminates and sulfates changes the surface chemistry of synthetic C-S-H with the goal of bridging the gap between this model synthetic system to more applied systems.

## 5.2.2 Sample preparation & methodology

*Synthesis*

All samples analyzed in this study were produced by synthesis in a segmented flow tubular reactor, described in detail in Section 3.2.2.

175mM of sodium sulfate, $Na_2SO_4$, and 20mM aluminum nitrate nonahydrate, $Al(NO_3)_3$, supplied by Sigma-Aldrich, were added to the relevant samples based on the measurements of S:Ca in Portland cement and measured Al:Si in C-A-S-H[18], [20], [92]. Both materials are supplied by Sigma-Aldrich. The recipes used in this experiment are described in Table 5.2.1.

Table 5.2.1 Solution recipes for synthetic C-S-H in segmented flow tubular reactor at Ca:Si 1, 1.25, 1.5, and 1.75, and 2 for reactor volume of 400mL, silicate solution kept constant

| **Ca:Si** | **[Ca]** | **[Si]** | **10mM NaOH (mL)** |
|---|---|---|---|
| **1** | 0.055 M | 0.5 M | 2 mL |
| **1.25** | 0.065 M | 0.5 M | 4 mL |
| **1.5** | 0.080 M | 0.5 M | 12 mL |
| **1.75** | 0.095 M | 0.5 M | 15 mL |
| **2** | 0.110 M | 0.5 M | 20 mL |

Reactants were pumped into the reactor at a rate of 10 mL/min, reaction temperatures were maintained at 20℃, and the solutions were allowed to mix for 3 hours before collection. 30-40 grams were produced per sample and precipitates were washed with 60 mL of 1:1 pure water, ethanol mixture.

*Acoustophoresis*

Zeta potential was measured with electroacoustics by the AcoustoSizer II supplied by Colloidal Dynamics as described in Section 5.1.2.

*Thermodynamic Modelling*

Thermodynamic modelling was done as described in Section 5.1.2.

*Transmission Electron Microscopy*

To prepare a sample for TEM, 0.15 grams of filtered wet C-S-H, as described in Chapter 3, was dispersed in 20mL of isopropanol supplied by Reactolab S.A. The samples were placed into an ultrasonic bath for 15 minutes, and one drop of the dispersion was placed on a carbon film 300 mesh grid, supplied by Electron Microscopy Sciences. Sample on the grid is enclosed in a glass petri dish, and allowed to dry for 20 hours under a lamp.

The transmission electron microscope used for these studies is the Tecnai Osiris TEM, supplied with FEI. The microscope was operated at 200kV in the TEM mode for diffraction analysis.

## 5.2.3 Results and discussion

*Zeta Potential and Solution Analysis of Synthetic C-A-S-H*

The morphology of synthetic C-S-H, as seen in 0(a), can be described as foil-like, observed in samples produced both by the dropwise precipitation method described in Chapter 3 and the controlled hydration of $C_3S$[25], [32], [121], [122]. In the figure below, the morphologies of C-S-H and C-A-S-H are compared at a Ca:Si of 1.5. The C-S-H is possibly less ordered in comparison to the C-A-S-H sample, which appears to be more densely agglomerated.

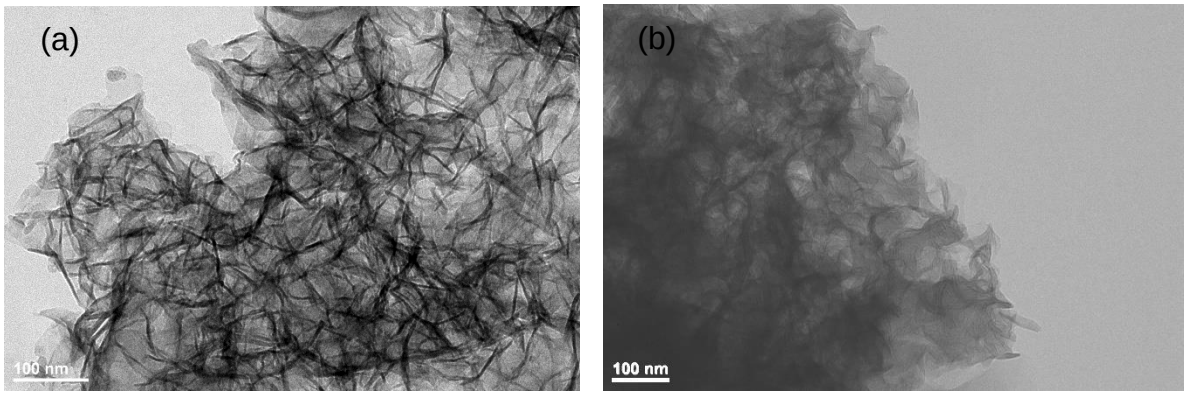


Figure 5.2.1 (a) TEM micrograph of synthetic C-S-H, Ca:Si = 1.5, (b) TEM micrograph of synthetic C-A-S-H, Ca:Si = 1.5, 20mM $Al(NO_3)_3$ addition

Figure 5.2.2 plots the zeta potential values measured from acoustophoresis of C-A-S-H and C-S-H with sulfates, or C-S-H + $, with Ca:Si ranging from 1 to 1.75, for 3.125 wt% solids dispersed in 10mM NaOH. These results are plotted with the results from C-S-H dispersed in NaOH solution from section 6.1. Results show a lowly positive charge at the slipping plane, except for one zeta potential measurement of -0.81 for a C-A-S-H sample at a Ca:Si of 1. As demonstrated in Section 6.1, under the investigated conditions, the zeta potential increases with increasing Ca:Si, and all measurements reported here are at the constant pH of 12.00. At a Ca:Si of 1.75, the zeta potential measurements of C-A-S-H are lower than that of C-S-H, averaging 2.34 mV  for C-A-S-H in comparison to the average of 3.51 mV for C-S-H. At other Ca:Si the zeta potentials are similar for all samples.

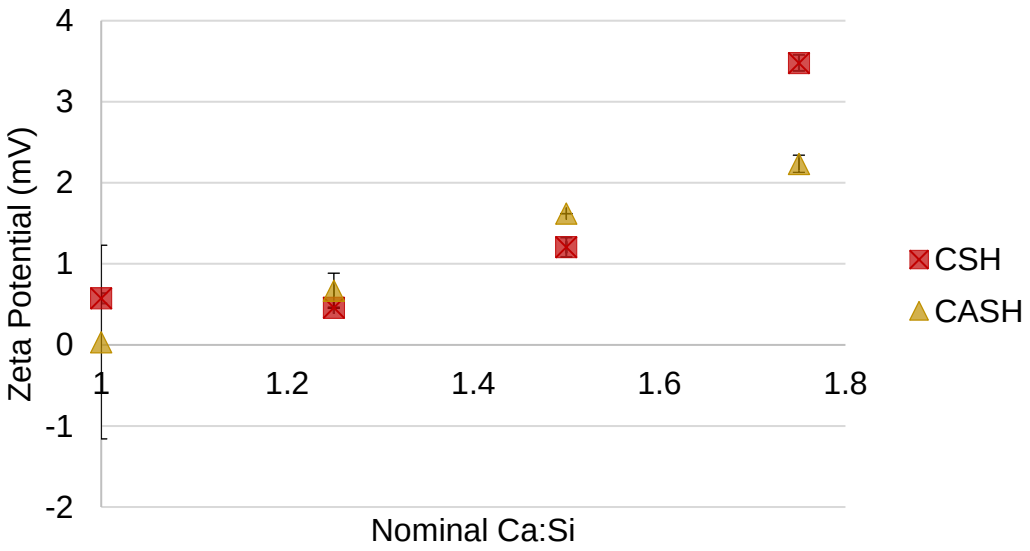

Figure 5.2.2 Zeta Potential (mV) of synthetic C-S-H (red) and C-A-S-H (yellow) at Ca:Si molar ratios ranging from 1 to 1.75, 3.125 wt% dispersed in 10mM NaOH. Error bars represent standard deviation in set of 3 measurements on the same sample.

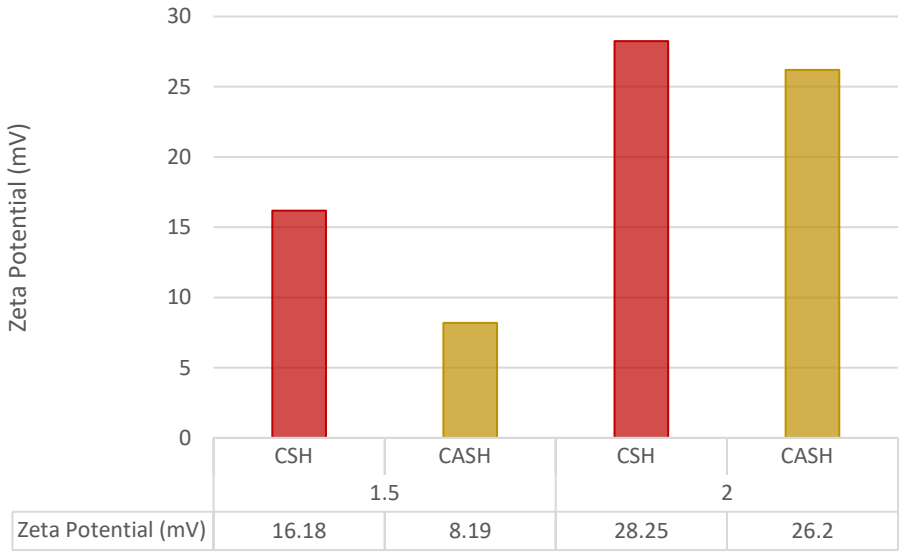


Figure 5.2.3 Zeta potential (mV) of synthetic C-S-H (red) and C-A-S-H (yellow) at Ca:Si molar ratios 1.5 and 2, 3.125 wt% dispersed in supernatant

Some samples of C-S-H and C-A-S-H were also dispersed in supernatant, and the results are plotted in Figure 5.2.3. The zeta potentials are significantly higher in the supernatant. As observed in the samples dispersed in NaOH, the potential increases with Ca:Si, and the measured potential of C-A-S-H is lower than that of C-S-H. Work by Kunhi Mohamed et al. shows that aluminates bond in the interlayers and bridging sites on the silicate chain of C-A-S-H, indicating that C-A-S-H may have less calcium on the surface than C-S-H if aluminates replace surface silicates. Additionally, it is also possible that the presence of aluminates in either the structure of C-A-S-H or in the solution modify the sites at which $Ca^{2+}$ would adsorb or has a smaller affinity for $Ca^{2+}$ than calcium itself as aluminates can replace silicate or calcium in the bridging sites[18].

C-A-S-H with Ca:Si of 1.5, and 1.6 were studied in more detail, and ICP measurements were used in combination with thermodynamic modelling to calculate the concentrations of ionic species in the dispersion media. Results are plotted below in Figure 5.2.4.

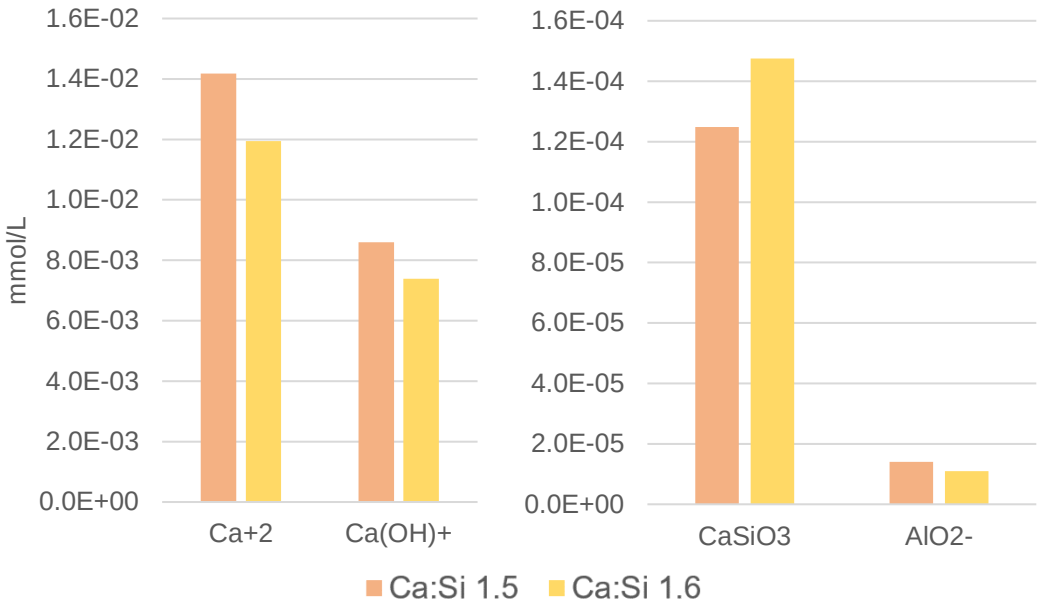


Figure 5.2.4 Results of thermodynamic modelling with PhreeqC, Cemdata18.1 database to see solution composition of C-A-S-H Ca:Si = 1.5 (orange), and Ca:Si = 1.6 (yellow) in samples, based on ICP-OES results

As the Ca:Si of the C-A-S-H samples increases, the $Ca^{2+}$ to $Ca(OH)^{+}$ ratio remains relatively steady, changing from 1.65 at a ratio of 1.5 to 1.62 at a ratio of 1.6, as the concentration of $Ca(OH)^{+}$ grows at a slightly faster rate than $Ca^{2+}$. In the 1.5 Ca:Si C-A-S-H sample, thermodynamic modelling gave 1.08 x $10^{-1}$ mol/L OH- species, and 7.06 x $10^{-2}$ mol/L $Na^{+}$ species, five times higher than the $Ca^{2+}$ concentration. In the 1.6 Ca:Si C-A-S-H sample, thermodynamic modelling gave 1.10 x $10^{-2}$ mol/L $OH^{-}$ species, and 7.85 x $10^{-2}$ mol/L $Na^{+}$ species, 6.5 times higher than the $Ca^{2+}$ concentration. As Ca:Si increases, thermodynamic modelling predicts an increase of $Ca^{2+}$ (~4mmol) in solution, this trend can be observed in Figure 3.1.10. However, in these experiments, as the Ca:Si increases from 1.5 to 1.6, calcium in solution decreases, suggesting that calcium is either adsorbed or somehow incorporated into C-S-H under these experimental conditions.

*Zeta Potential and Solution Analysis of Synthetic C-S-H + $*

In Figure 5.2.5 below, the morphologies of C-S-H and C-S-H + $ are compared at Ca:Si molar ratios 1.7 and 1.75, respectively. The C-S-H micrograph, like the slightly lower ratio sample seen in 0, are a poorly ordered agglomerates of thin nanofoils. With the addition of sulfates, the hydrate still exhibits a nanofoil morphology but the agglomerates appear to be oriented differently towards each other in such a way that the ends stick out, giving a hairy particle or sea urchin type morphology.

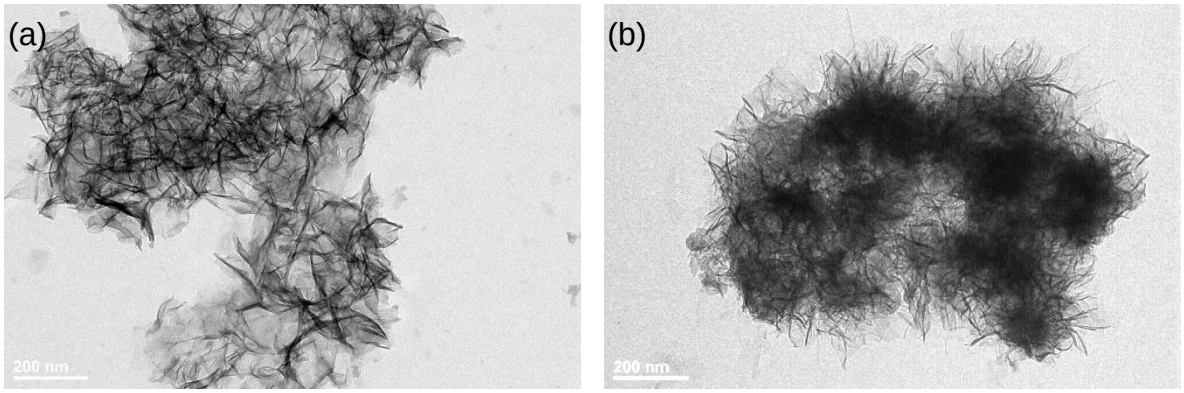


Figure 5.2.5 (a) TEM micrograph of C-S-H + $, Ca:Si = 1.7, (b) TEM micrograph of C-S-H + $, Ca:Si = 1.75, 175mM $Na_2SO_4$ addition

Zeta potential measurements for C-S-H + $ dispersed in 10mM NaOH in comparison to C-S-H are plotted in Figure 5.2.6. Similar to the C-S-H and C-A-S-H results, the potentials increase with increasing Ca:Si with similar potentials to C-S-H. As for the C-A-S-H sample, the zeta potential remains 1.5mV lower than the potential of C-S-H at Ca:Si = 1.75, at 1.84 mV for C-S-H + $ in comparison to the 3.51 mV of C-S-H.

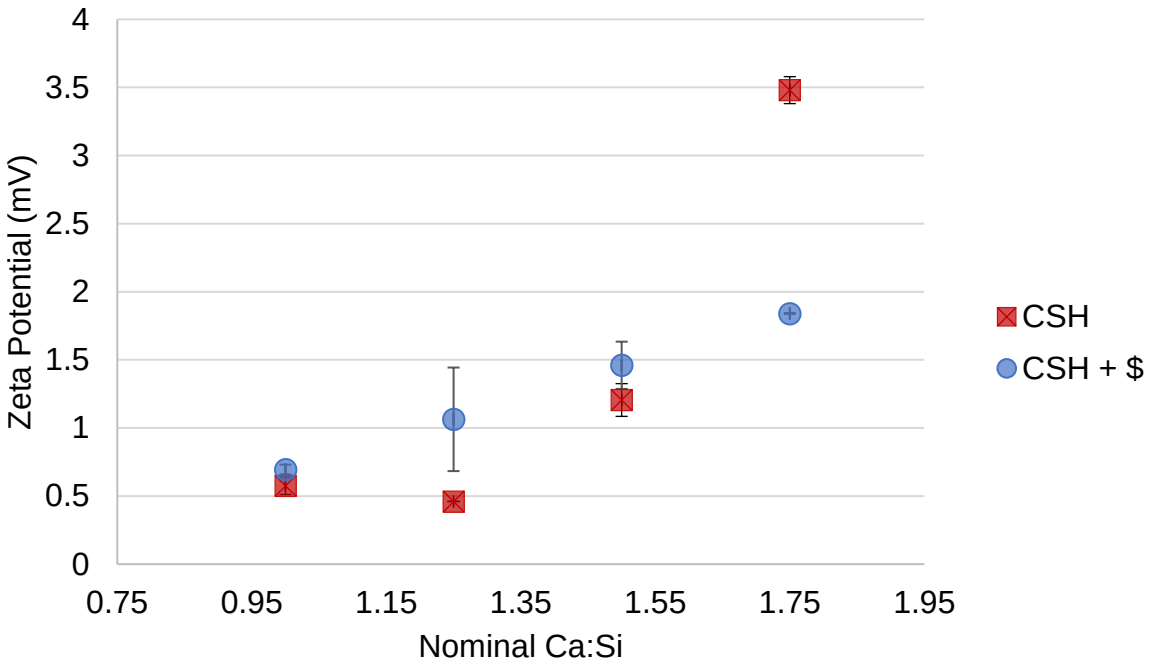


Figure 5.2.6 Zeta Potential (mV) of synthetic C-S-H (red) and C-S-H + $ (blue) at Ca:Si molar ratios ranging from 1 to 1.75, 3.125 wt% dispersed in 10mM NaOH. Error bars represent standard deviation in set of three measurements on the same sample.

The aqueous speciation in solutions of C-S-H + $ samples with Ca:Si of 1.7 and 1.8 dispersed in 10mM NaOH were analyzed in more detail using thermodynamic modelling of the supernatant based on ICP analysis. The speciation for these two different Ca:Si is plotted below in Figure 5.2.7.

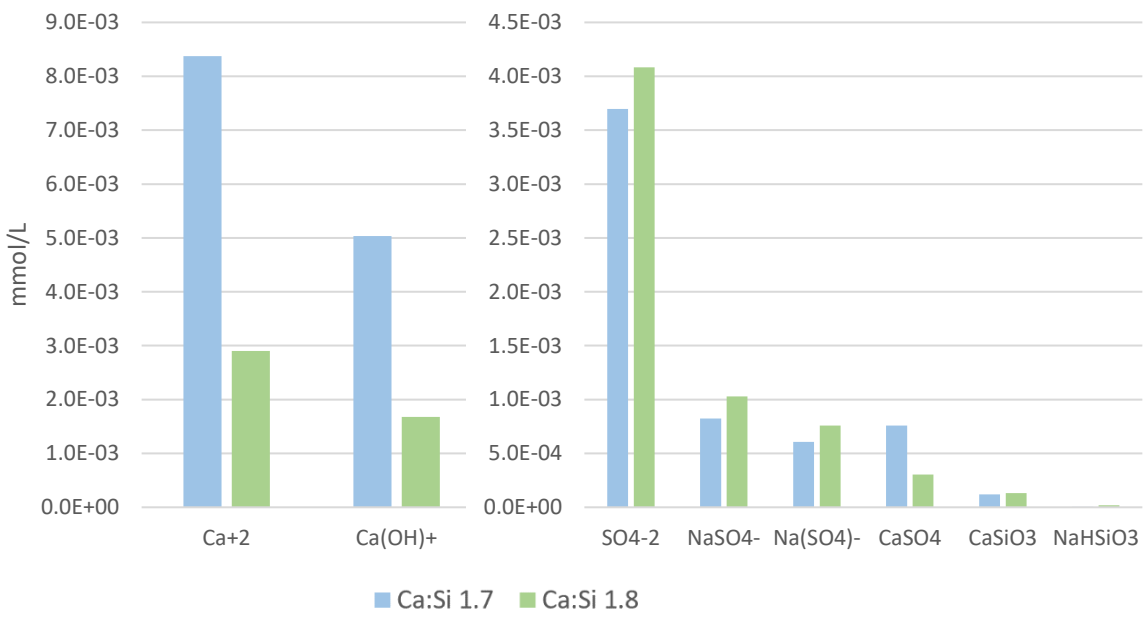


Figure 5.2.7 Thermodynamic modelling with PhreeqC, Cemdata18.1 database to see solution makeup of C-S-H + $ Ca:Si = 1.7 (blue), and Ca:Si = 1.8 (green) in samples, based on ICP-OES results

ICP results showed a $Ca^{2+}$ concentration 3 times higher in the Ca:Si = 1.7 sample compared to the 1.8 ratio sample. Thermodynamic modelling predicts that with an increasing Ca:Si, there is a decrease in free $Ca^{2+}$ and $Ca(OH)^{+}$ expected in solution at these conditions, and the ratio of $Ca^{2+}$ to $Ca(OH)^{+}$ increases from 1.66 to 1.73. $OH^{-}$ solution species concentration decreases from $1.08 \times 10^{-1}$ to $1.02 \times 10^{-1}$ mol/L with increasing Ca:Si. At the Ca:Si of 1.7, $Na^{+}$ solution concentration is $9.51 \times 10^{-2}$ mol/L, 11 times higher than the $Ca^{2+}$ solution. At a Ca:Si of 1.8, the $Na^{+}$ solution species concentration is $1.05 \times 10^{-1}$ mol/L, 36 times higher than the concentration of $Ca^{2+}$ in solution.

Precipitate analysis gave measured Ca:Si values of 2.0 and 1.99, respectively, plotted in Figure 5.2.8, higher than the nominal Ca:Si expected.

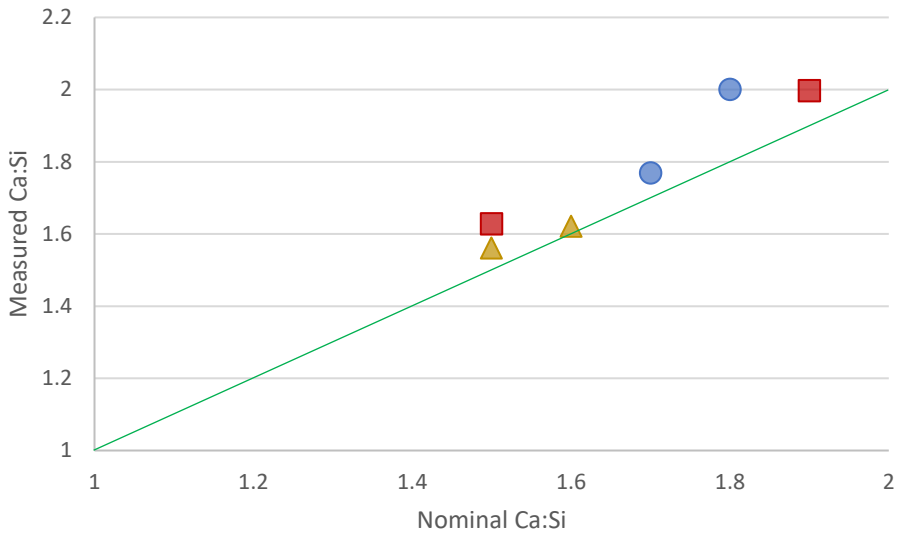


Figure 5.2.8 Comparison of composition of C-S-H (green), C-A-S-H (blue), and C-S-H +$ (yellow) samples Ca:Si, and Nominal Ca:Si trendline (green), measured by Inductively-Coupled Plasma Spectrometry (ICP-OES)

In observation of ICP measurements of C-S-H, C-A-S-H, and C-S-H + $ precipitates, nominal Ca:Si molar ratios with only a small overestimation of the Ca:Si ratio is observed in comparison to the very high Ca:Si observed on pure-phase C-S-H Section 3.1. ICP of C-S-H at high Ca:Si of 1.8 and above displayed ratios between 2.2 and 2.7. Figure 5.2.8 displays measured Ca:Si values of 2.0 ± 0.1 for nominal Ca:Si values of both 1.7 and 1.8.

Zeta potential measurements for both C-A-S-H and C-S-H + $ gave similar results to those observed in Section 5.1. As expected, potential increases with increasing Ca:Si, and the C-A-S-H samples, dispersed in supernatant exhibit both considerably higher potentials than those dispersed in 10mM NaOH solution, though lower than the potentials of C-S-H in supernatant.

For the samples dispersed in 10mM NaOH, the potentials of C-A-S-H and C-S-H + $ were mostly in line with those of C-S-H, though at a Ca:Si of 1.75, the zeta potential of C-A-S-H and C-S-H + $ are about 1.5 mV lower on average than that of C-S-H.

*Calculation of Ionic Concentrations & Debye Lengths*

ICP results were used to calculate the ionic concentrations and resulting Debye lengths for the C-A-S-H and C-S-H + $ samples in this study, listed below in Table 5.2.2.

Table 5.2.2 Ionic concentrations and Debye lengths calculated based on ICP-OES solution measurements and thermodynamic modelling

| Sample | Ionic concentration (mol/L) | Debye length (nm) |
|---|---|---|
| **C-A-S-H 1.5** | 0.122 | 0.863 |
| **C-A-S-H 1.6** | 0.122 | 0.863 |
| **C-S-H + $ 1.7** | 0.129 | 0.839 |
| **C-S-H + $ 1.8** | 0.119 | 0.873 |

For the C-A-S-H sample with Ca:Si of 1.5, a surface charge density can be calculated using zeta potentials plotted in Figure 5.2.3 for C-A-S-H dispersed in supernatant. At this potential, a surface charge density of 4.09 x $10^{-2}$ e/$nm^2$ is calculated using the Gouy-Chapman Stern model, assuming the slipping is at the Debye length, calculated to be less than 1nm for all samples.

## 5.2.4 Conclusions & future work

In this section, hydrates were studied with acoustophoresis, ICP-OES and TEM to better understand the effects of sulfates and aluminates on zeta potential, solution speciation and ionic concentration, and hydrate morphology. In C-A-S-H samples and C-S-H + $ samples dispersed in 10mM NaOH, the potential increases with increasing Ca:Si, plotted in Figure 5.2.2 and Figure 5.2.6. In both cases, however, at a Ca:Si of 1.75, the measured potentials are more than 1mV less than the potential of C-S-H, a notable difference with acoustophoresis measurements. C-A-S-H samples with Ca:Si of 1.5 and 2, dispersed in filtrated supernatant were observed to consistently have lower potentials than the C-S-H samples at the same Ca:Si molar ratios. Recent studies on the atomic-level structure of C-A-S-H predicted that aluminates bond in the bridging sites of silicate chains in C-S-H, possibly taking the place of calcium in high ratio C-S-H[18]. It is possible that the aluminate species in

the bridging site that may terminate the surface could also have a lower affinity for $Ca^{2+}$ adsorption, consequently reducing the measured zeta potential by reducing the surface charge density.

TEM micrographs of C-A-S-H display a possibly denser agglomerate in comparison to the thin, disordered nanofoil morphology of C-S-H at a Ca:Si of 1.5. A TEM micrograph of C-S-H + $ displays a more open and oriented agglomerate nanofoil morphology structure with the ends approaching a more of fibrillar structure.

To continue this work, and to better understand how the difference in solution speciation affects the surface termination of the hydrates, acoustophoresis measurements of C-A-S-H and C-S-H + $ dispersed in supernatant should be taken at a fuller range of Ca:Si molar ratios, in addition to ICP measurements of the filtered supernatants. Also, to see the effects of aluminates and sulfates on C-S-H alone, C-S-H dispersed in either NaOH or lime solution could be titrated with aluminate or sulfate solution, and eventually both to see if they can incorporate or adsorb on to certain sites at the C-S-H surface. In addition to these experimental approaches, molecular dynamic and metadynamic atomic scale simulations would help better interpret any experimental findings.

## 5.3 Conclusions

In this chapter, surface characteristics of synthetic C-S-H at the full range of Ca:Si molar ratios are measured by acoustophoresis and ICP-OES to investigate the effects of Ca:Si, washing, and dispersion media on zeta potential. In Section 5.1, the zeta potential of C-S-H increases with increasing Ca:Si in both filtered supernatant and in 10mM NaOH solution, as observed in previous studies[108], [111]. However, results exhibit a large difference between filtered supernatant and 10mM NaOH, plotted in Figure 5.1.5, suggesting the desorption of $Ca^{2+}$ in NaOH.

Titration experiments were carried out in which C-S-H with Ca:Si of 1 and 1.75 were dispersed in 10mM NaOH and titrated with calcium solution. These results showed a limited increase in zeta potential and indicate only a partial reversibility of $Ca^{2+}$ adsorption under these experimental conditions. In previous work by Haas and Nonat, C-S-H with Ca:Si of 1.4 was synthesized and dispersed in alkali-free

conditions and exhibited high potentials around 23 mV, comparable to the potentials of samples dispersed in filtered supernatants in this chapter. Though the samples investigated in this chapter were all produced in conditions containing alkali, the high potentials measured for samples dispersed in supernatant could be possibly replicated to the same magnitudes in a lime solution of increasing concentration rather than 10mM NaOH.

In Section 5.2, the separate effects of sulfates and aluminates on zeta potential, morphology, and ionic speciation of the synthetic C-S-H system were studied. Results showed the increase of zeta potential with Ca:Si, though at a Ca:Si of 1.75, both C-A-S-H and C-S-H + $ exhibited lower potentials than C-S-H. C-A-S-H, dispersed in supernatant, exhibited lower potentials than C-S-H at Ca:Si molar ratios of 1.5 and 2.

For accurate results on modelling surface charge densities for C-A-S-H & C-S-H + $, samples needed to be dispersed in well controlled media. In the experiments described above, 10mM NaOH is used. However, the relevance of working at a pH of 12 other than for comparison between samples challenges this choice. Other options include working with higher pH NaOH solution, or possibly working with lime water, which would allow one to modify both calcium concentration and pH, while avoiding the additional introduction of alkali to the system. Solution analyses should be completed on the samples, their supernatants, and the dispersion after an equilibrium has been reached to best predict the surface charges at all experimental points.

There is much work left to do to better understand the surface of C-S-H, and many unanswered questions. What reliance does the Ca:Si of C-S-H have on the calcium of the surface-terminated hydrate? Measurements of calcium and silicon in synthetic precipitates from Figure 3.1.9 exhibit Ca:Si molar ratios above 2.1, which is rarely observed. And so, the Ca:Si may not be wholly reliant on the terminated surface of C-S-H, but given the amount of surface area available on a thin nanofoil, and the high affinity for $Ca^{2+}$, it is a fair assumption that the adsorption of $Ca^{2+}$ becoming a potential-determining ion is a key feature. This is highlighted by the order of magnitude difference in zeta potentials measured in NaOH and in supernatant solution. The surface of C-S-H will not be fully modelled until an electrical double

layer model incorporating the surface terminations is developed. With the recent advancements in determining the bulk structures of C-S-H and C-A-S-H, and the advancements in the production of C-S-H at the full Ca:Si, the determination of the surface via atomistic simulations seems well within reach and will help interpret the changes in surface potentials as a function of solution composition[17], [18], [22], [32].

# Chapter 6. Heterogeneous substrates and synthetic C-S-H morphology

Ordinary Portland cement contains a wide range of phases and surfaces to react or be nucleated on. As blended cements are used more to decrease the emissions from Portland cement clinker, the importance of the effects of SCMs on C-S-H increases. Supplementary materials like slags, fly ash, and calcined clays have high aluminum contents, leading to the formation of C-A-S-H among other alumino-phases[86], [123]–[125]. Gypsum is commonly added to cements to control reactivity, leading to the observed adsorption of sulfates on the surfaces of C-S-H [83], [89], [126] Additionally, in blended cements, the effect of adding SCMs can sometimes increase the reaction of alite, consequently increasing sulfate adsorption and the amounts of sulfates required for the cement[84].

In applied cements, “foil-like”, and “fibrillar” C-S-H morphologies are often observed[17], [25], [127], [128]. Richardson observed foils in C-A-S-H at Ca:Si molar ratios at and below 1.5, and the increase of SCMs in the cement was deemed to cause this change from fibrils to foils[10]. Studies on synthetic C-S-H produced by dropwise precipitation exhibited nanoglobule structures at low Ca:Si, and nanofoils in ratios > 1.25; however fibrils in C-S-H produced without the presence of $C_3S$ are rarely observed, and there is poor understanding as to why fibrils or foils form[17].

In this chapter, aluminates, sulfates, and heterogeneous substrates are added to C-S-H to study the resulting effects on morphology and zeta potential. Additionally, the heterogeneous substrates used, calcite and quartz, are hydrated in silicate and calcium solutions respectively, and characterized by TEM analysis, XRD, and thermodynamic modelling.

## 6.1 Materials & methods

### 6.1.1 Transmission electron microscopy

To prepare a sample for TEM, 0.15 grams of filtered wet C-S-H, as described in Chapter 3, was dispersed in 20 mL of isopropanol supplied by Reactolab S.A. The samples were placed into an ultrasonic bath for 15 minutes, and 1-2 drops of the

dispersion was placed on a carbon film 300 mesh grid, supplied by Electron Microscopy Sciences. Sample on the grid was enclosed in a glass petri dish, and allowed to dry for 20 hours under a 30 W lamp, with no significant heat increase.

The transmission electron microscope used for these studies is the Tecnai Osiris TEM, supplied with FEI. The microscope was operated at 200kV in the TEM mode for diffraction analysis.

### 6.1.2 Acoustophoresis

Zeta potential measurements taken in this sample were conducted as described in 5.1.2. 5 gram samples of C-S-H, calcite, quartz, were dispersed in 155 mL of 10mM NaOH. Samples were allowed to mix for 30 minutes after dispersion preparation, and were placed in an ultrasonic bath for 30 minutes. All zeta potential measurements were made on an Acoustosizer II by Colloidal Dynamics.

### 6.1.3 Inductively-coupled plasma spectrometry

Samples of filtrated solutions and filtered supernatants after zeta potential measurements were studied by ICP-OES. All samples were prepared for analysis as described in 3.1.3.

### 6.1.4 Thermodynamic modelling

Thermodynamic modelling with GEMS, PhreeqC, and databases including Cemdata 18.1, PSI Nagra, and the LLNL database was done as described in 5.2.2[35], [37]–[40].

## 6.2 C-S-H, quartz & calcite

### 6.2.1 Introduction

C-S-H, the main hydration phase of Portland cement, composes 50-60% of hardened cement paste by volume. As a result, C-S-H is believed to be a chief contributor to early-age strength and largely responsible for many of the mechanical and transport properties of ordinary Portland cement[129].

Given the complexity of phases in Portland cement—8 to 10 phases are present at any time—the growth mechanisms of C-S-H and C-S-H-system hydrates are still unclear due to this complexity. In applied systems, the nucleation of C-S-H is effectively heterogeneous and heavily reliant on pore solutions, pH values, and available surface areas, leading to difficulties in measuring kinetics, solubilities, and other parameters during hydration.

In analysis of hydrated alite alone, the main anhydrous phase of Portland cement, C-S-H is observed to form two different morphologies: the inner product, grown on unreacted alite grains, and in the outer product which extends into the pore space[33]. Microscopy studies by Bazzoni on the hydration of $C_3S$ show the growth of C-S-H on both $C_3S$ and calcite, pictured in Figure 6.2.1, forming fibrils on both surfaces[127]. Bazzoni observed a more ordered or aligned outer product on the surface of limestone, thin and perpendicular to the limestone surface. On the surface of $C_3S$, Bazzoni observed a more disordered hydrate with random surface orientation and a gap between the unreacted $C_3S$ and C-S-H. In applied, yet simplified cementitious systems, C-S-H exhibits not only heterogenous nucleation but also various morphologies of formation[7], [127].

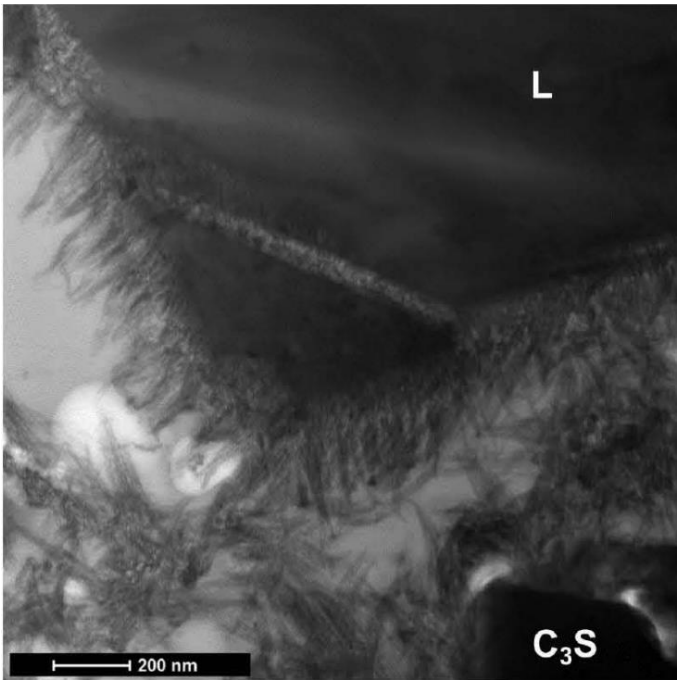


Figure 6.2.1 Bright field STEM image of 60% $C_3S$ – 40% limestone after 24h hydration. $C_3S$ for $C_3S$ grains, L for limestone[127]

C-S-H is also a product of belite ($C_2S$) hydration, and has been observed to grow on portlandite, quartz, and itself, exhibiting both secondary nucleation and aggregation[7]. Hence, the importance of heterogeneous nucleation on C-S-H formation in applied cements cannot be understated.

Synthetic C-S-H has provided distinct advantages in the community's advancement in understanding the main hydrate's structure, growth and nucleation, morphology, compressive strength, and solubility, among other parameters[17], [18], [27], [30], [130]. To better characterize the kinetics, thermodynamics, and even morphology of real systems, adding heterogeneous substrates is the required next-step in the use of synthetic C-S-H systems to unravel the complexities of the applied cement systems.

In work by Siramanont, the effects of calcite, quartz, and D-gluconate, a small molecule which acts as a retarder in cement production, were studied for their impact on hydrate kinetics, solution speciation, and synthetic C-S-H morphology[131]. Siramanont observed small amounts of nanofoil C-S-H growth on the surfaces of calcite and quartz at a pH of 13.5, and the presence of D-gluconate caused square or by-pyrimidal aggregation in C-S-H[131]. Kinetic experiments in which calcium concentration was measured as a function of time showed how possible $Ca^{2+}$ adsorption on the negative surface of quartz decreased the amount of free calcium in the precipitation process, and exhibited a very fast consumption of calcium after this short delay. The addition of calcite caused a higher initial amount of $Ca^{2+}$ in solution, though overall, the presence of calcite lowered the consumption of calcium throughout the precipitation process.

Currently, there are many questions regarding the morphology of C-S-H. Synthetic C-S-H, in work by Kumar et al. exhibited nanoglobule morphology in C-S-H samples produced at pHs less than 11.5, and nanofoils in pHs higher than 12[17]. However, in cement pastes or on hydrated $C_3S$, C-S-H has been noted for its fibrillar morphology. In work by Tajuelo et al., C-S-H synthesized by silica-lime reactions and by the controlled hydration of $C_3S$ was studied at Ca:Si molar ratios from 0.75 to 1.5. Both nanofoil and fibrillar morphologies were observed[25]. It was shown that the hydrated $C_3S$ samples produced more fibrillar C-S-H with an increase of CaO concentration ($Ca^{2+}$, > 20mM in solution). Currently, the C-S-H samples produced by

the dropwise precipitation method do not exhibit any fibrillar morphologies. This is true even at the highest Ca:Si molar ratios where thermodynamic modelling predicted $Ca^{2+}$ concentrations above this 20mM (Figure 3.1.10) value observed by Tajuelo et al. in Ca:Si molar ratios > 1.9[25], [32].

In this section, synthetic C-S-H produced by dropwise precipitation in addition to C-S-H grown in solution on the surfaces of calcite and quartz are studied. Samples are characterized by X-ray diffraction, thermogravimetric analysis, inductively-coupled plasma spectrometry, particle size dispersion, and TEM to better understand the effect of heterogeneous substrates on the C-S-H systems.

## 6.2.2 Experimental preparation

To grow C-S-H on the surface of quartz and calcite, two solutions were prepared as described below in Table 6.2.1. Samples were mixed at 300 rpm for 5 hours, then NaOH was added and mixed for an additional 48 hours. Small samples were taken at 3 hours, 24 hours, 1 week, and 1 month for TEM analyses and pH measurements. Calcite and quartz were supplied by Sigma Aldrich. The materials used by Siramanont were also used in these experiments[131].

Table 6.2.1 Experimental conditions of solutions in which C-S-H is grown on the surface of quartz and calcite. Where CQ is quartz in a calcium solution, SiCal is calcite in a silicate solution, and ref indicates reference sample.

| | **CQ_ref** | **SiCal_ref** |
|---|---|---|
| **Quartz** | 1 wt% | - |
| **Calcite** | - | 1 wt% |
| **NaOH** | 10 mL | 10 mL |
| **$Ca(NO_3)_2 * 4H_2O$** | 0.2M | - |
| **$Na_2SiO_3$** | - | 0.1M |

## 6.2.3 Pure C-S-H

As observed in other synthetic C-S-H studies, the samples produced in this chapter with the dropwise precipitation method exhibited disordered agglomerated nanofoil morphologies. In C-S-H samples with a Ca:Si nominal ratio of 1.75 and portlandite

presence due to slower mixing conditions (200 rpm) than described in section 3.1, no drastic changes in C-S-H morphology or ordering are observed, presented in Figure 6.2.3.

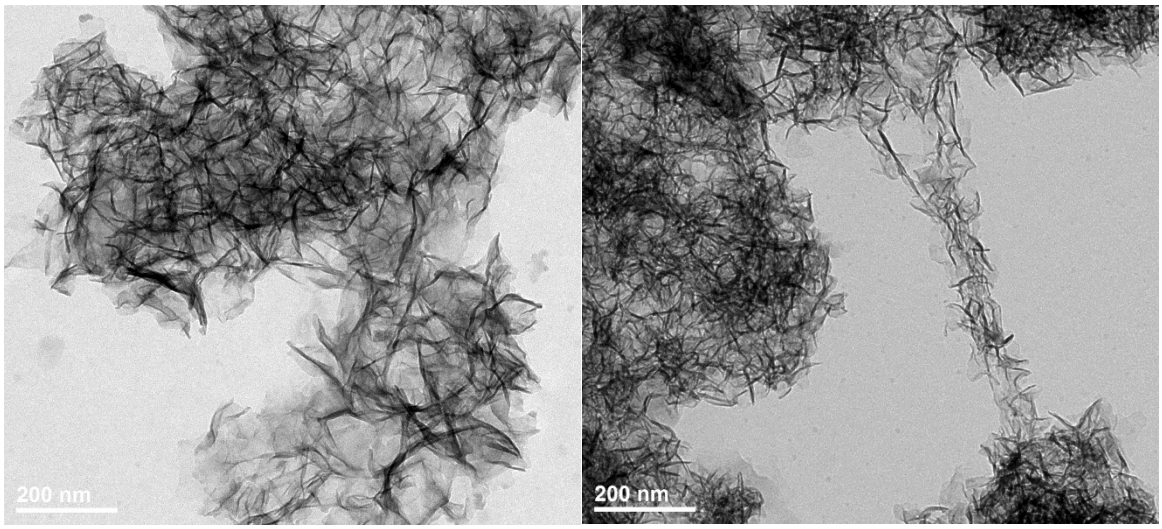


Figure 6.2.2 TEM image of C-S-H nominal Ca:Si = 1.7 produced by dropwise precipitation method

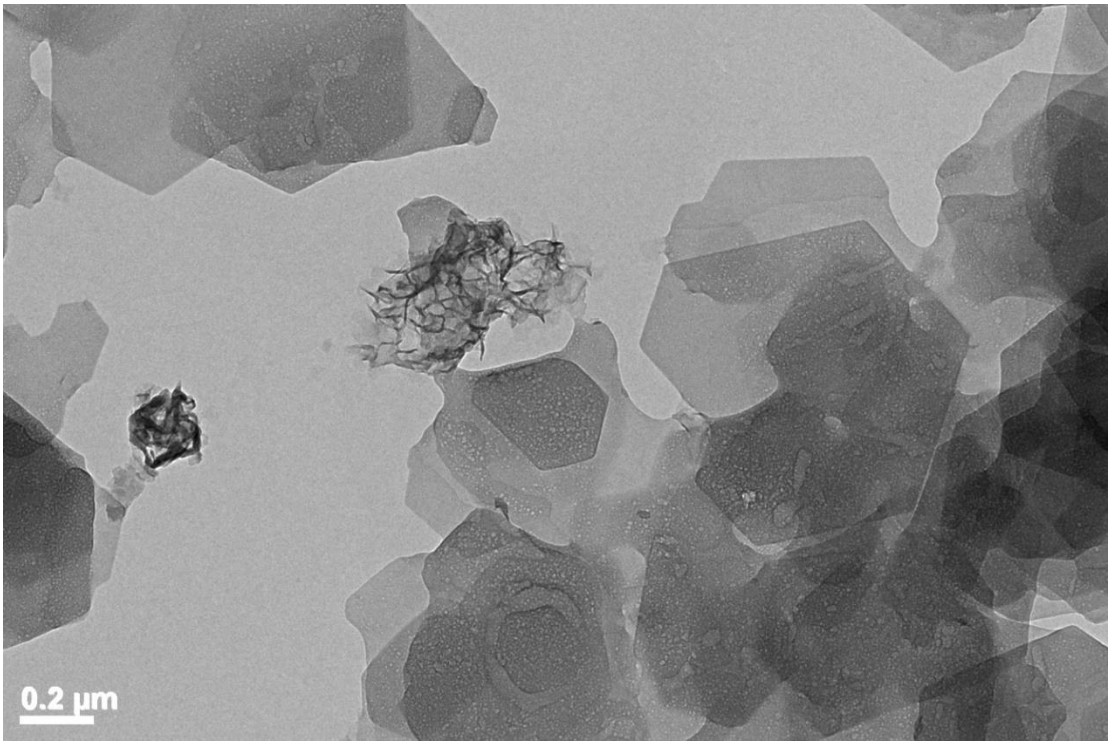


Figure 6.2.3 TEM image of portlandite and C-S-H, nominal Ca:Si = 1.75, produced by dropwise precipitation method, 200 rpm mixing

## 6.2.4 C-S-H & quartz

A TEM image of quartz before reaction is pictured in Figure 6.2.4. The quartz particle exhibits a smooth, irregular shape. Particle diameters, measured by laser diffraction ranged from 1 μm to 50 μm, averaging 15-20 μm, plotted in Appendix II.

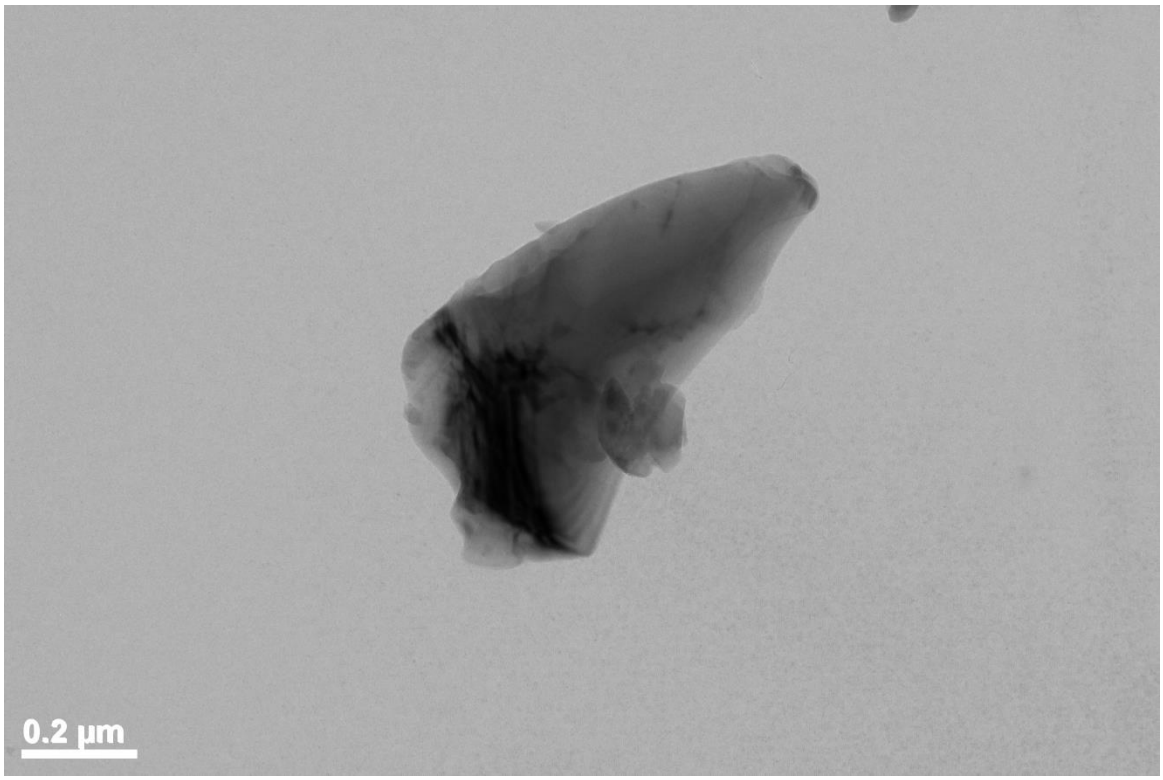


Figure 6.2.4 TEM micrograph of Quartz

Quartz was placed in a solution with calcium nitrate at a pH of 13.4. Very little change was observed in the quartz after 24 hours and 3 days. At 1 week, some erosion is observed at the surface of quartz, pictured in Figure 6.2.5, possibly due to dissolution of silicate into the calcium nitrate solution. In Figure 6.2.5b, small amounts of growth on the surface of quartz is observed. High amounts of portlandite, in platelet morphologies, were also observed in the sample. In similar work done by Siramanont, $Ca(OH)_2$ is also observed with quartz in a calcium nitrate solution at pH 13.5, and small amounts of C-S-H were observed as well after 8 hours in solution.

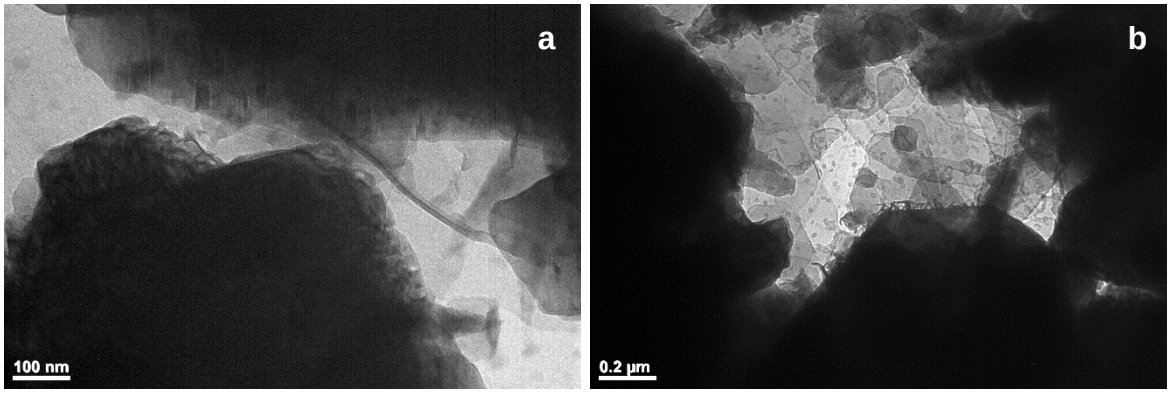


Figure 6.2.5 TEM image of quartz in $Ca(NO_3)_2$ solution, a) after 1 month, b) with portlandite presence

These results may be due to the additive effects of slow dissolution rate of quartz, and the immediate precipitation of $Ca(OH)_2$ upon the addition of NaOH to the solution. As a result, in order for C-S-H to form, both $Ca(OH)_2$ and quartz need to dissolve, which may be slower to occur upon the solution having both low concentrations of calcium and silicate. Results by Siramanont displayed both the formations of C-S-H and portlandite after only 24 hours in solution at a pH of 13.5. These samples, at 1 month suggest a higher preference for $Ca(OH)_2$ formation under these conditions.

### 6.2.5 C-S-H & calcite

A micrograph of calcite before reaction is pictured in Figure 6.2.6. The calcite particles appear to be relatively smooth and very irregular in shape with many 100nm irregularities on the surface. The particle diameters, measured by laser diffraction measurements of the calcite samples used in the following experiments range from 0.7 µm to 25 µm, averaging 7-8 µm, plotted in Appendix II.

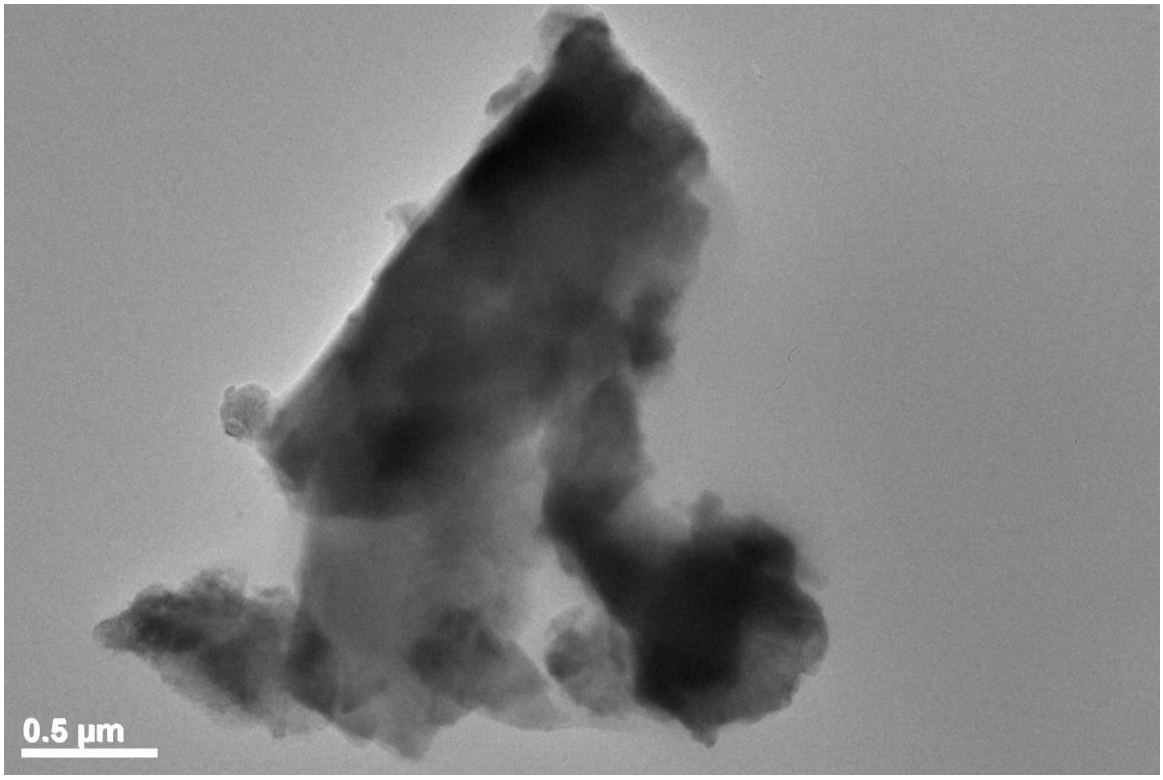


Figure 6.2.6 TEM image micrograph of calcite

Results from calcite placed in 0.1 M silicate solution are pictured below in Figure 6.2.7, showing the growth of C-S-H on the surface after 1 month in solution. Calcite grains are still visible throughout the sample, and C-S-H is present on both the surfaces of calcite and on the surface of C-S-H itself.

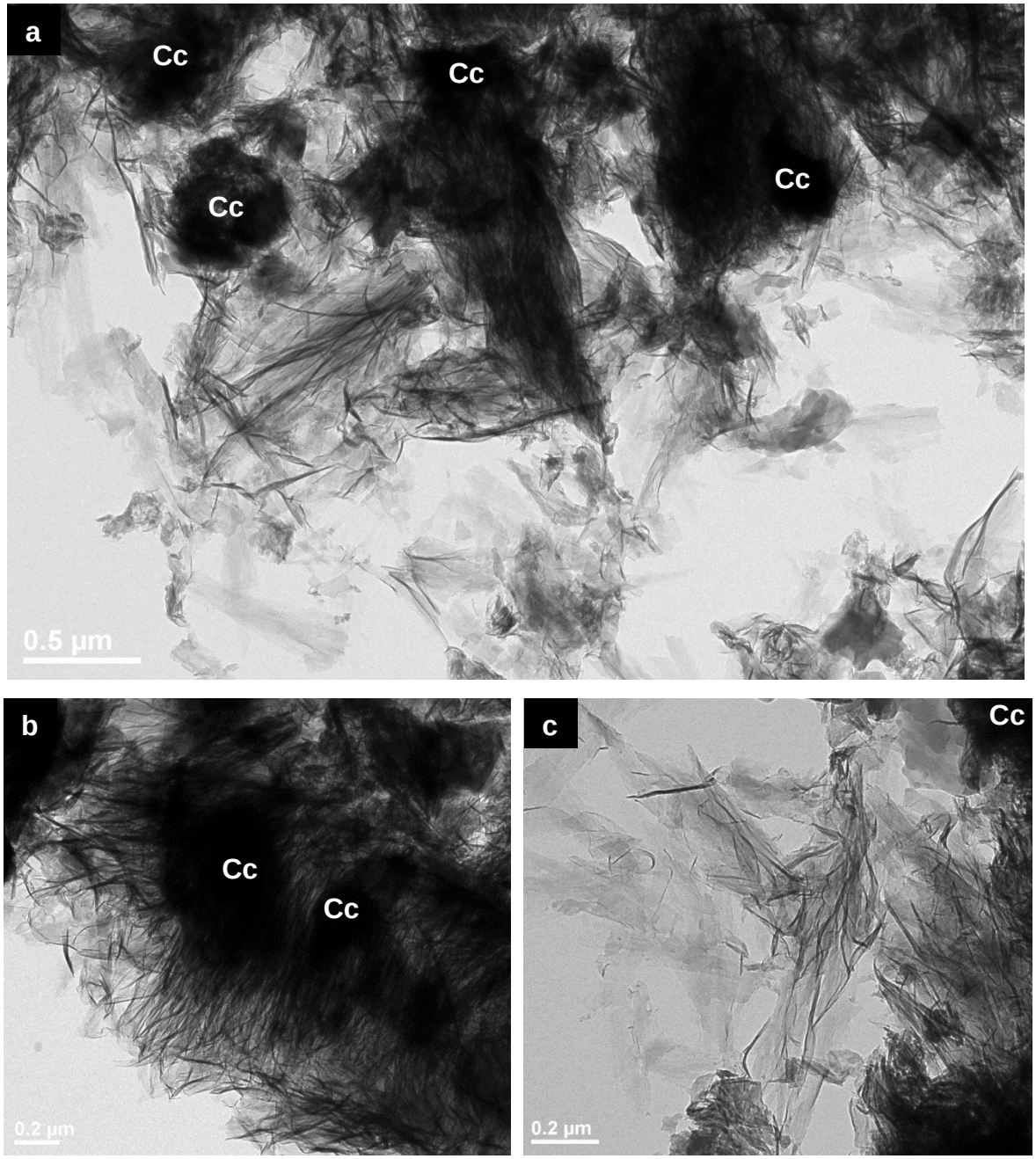


Figure 6.2.7 TEM of C-S-H grown on surface of calcite, 1 month. Calcite grains marked by, Cc.

In Figure 6.2.7a, the C-S-H exhibits a morphology somewhere between nanofoil and fibril, producing long ribbons between 750nm and 1 µm in length. Samples are ordered and perpendicular to the surface of the calcite grains in Figure 6.2.7b, and in Figure 6.2.7c, the C-S-H appears to be flat on the grid, exhibiting very thin ribbon-like structures, up to ~150nm in width. The C-S-H exhibits a thin, long sheet morphology, but seems more fibrillar at certain angles (~750-100nm). After 3 months, the pH was

measured at 13.49. Previous work by Siramanont investigated calcite in a silicate solution at a pH of 13.5 in which samples were taken at 3 and 8 hours, and the growth of C-S-H on the surface of calcite was observed, perpendicular to the surface (~250nm).

Thermodynamic modelling of the solution predicts that at equilibrium, there are 2.13 grams of C-S-H and 2.82 grams of calcite under these conditions. Solution species are given below in Figure 6.2.8.

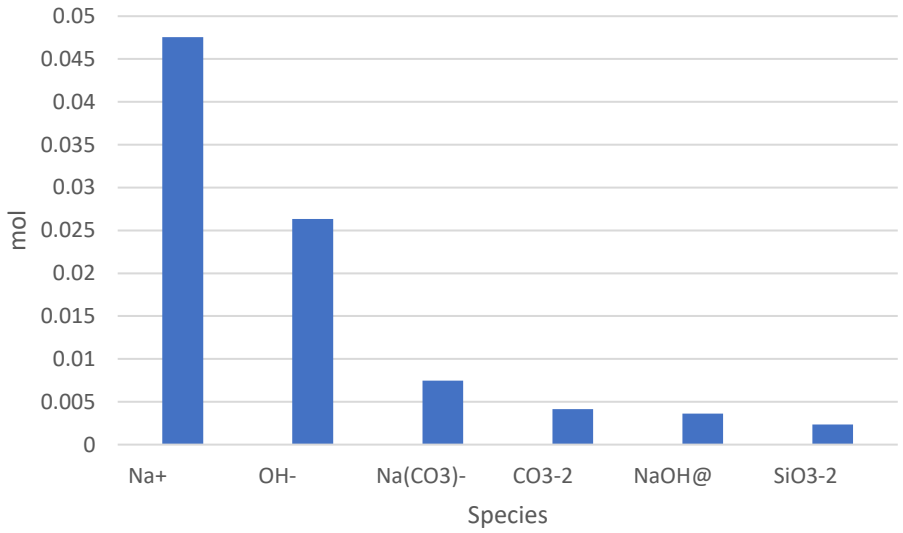


Figure 6.2.8 GEMS-calculated solution species for C-S-H grown from calcite in 0.1 M silicate solution, pH = 13.49

High amounts of free sodium and hydroxide are measured as NaOH is added to the solution to obtain the high pH. Sodium carbonate and free carbonate ions are also measured in solution. Small concentrations of free $Ca^{2+}$ and $CaOH^{+}$ in solution were calculated, both present in the order of $10^{-7}$ mol.

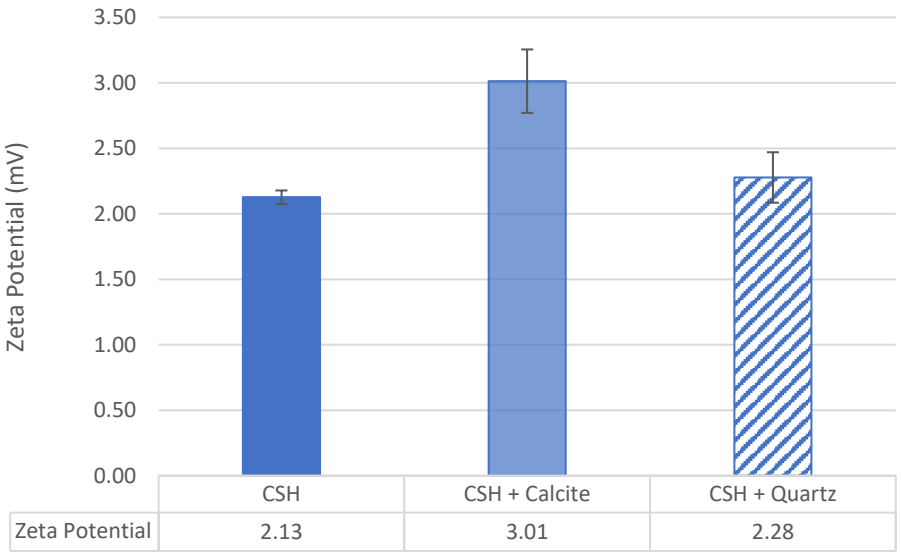


Figure 6.2.9 Zeta potentials of C-S-H produced with dropwise precipitation method, dispersed in 10mM NaOH, 3.125wt% dispersion, with 1wt% calcite and 1wt% quartz, Ca:Si = 1.6. Error bars represent standard deviation in set of six measurements.

Zeta potential measurements on C-S-H produced in the batch reactor with and without calcite and quartz are in Figure 6.2.9. Samples produced with additional amounts of calcite exhibit a higher potential. In these synthetic samples, small amounts of Ca and Si are measured in the filtrated supernatants, and so in the synthesis process, calcite dissolves to some degree, and there should be additional $Ca^{2+}$ in solution. ICP solution measurements should be taken on filtered supernatants to verify. The difference between C-S-H and C-S-H + quartz is likely not significant—though there probably is some dissolution of quartz, the addition of silicates to the solution at this small degree appears to have little to no effect on the surface termination.

## 6.2.6 Conclusions & future work

In this section, the effect of quartz and calcite on high Ca:Si C-S-H morphologies and solutions are studied. As observed in previous studies on synthetic C-S-H, the nanofoil morphology is primarily observed in samples with and without the formation of portlandite. Quartz, placed into a low-concentration, 0.2M calcium nitrate solution showed small amounts of C-S-H observed on the surface of quartz, as also seen in the similar experiments by Siramanont[131].

Thermodynamic modelling of the solution predicts the full dissolution of quartz and formation of C-S-H at equilibrium, though after 1 month, TEM images show still small amounts of C-S-H, undissolved quartz grains, and portlandite. As $Ca(OH)_2$ precipitates immediately upon the addition of NaOH into the solution and as there is no silicon in the solution at the start of the experiment. Additionally, there are very low amounts of calcium, which would effectively decrease the rate of dissolution for both $Ca(OH)_2$ and quartz, slowing the formation of C-S-H.

Calcite placed into a 0.1M silicate solution at a pH of 13.4 showed the formation of C-S-H after 1 month in solution. The hydrate exhibited an ordered fibrillar or ribbon-like morphology perpendicular to the surface of calcite, up to 1 μm in length. Calculations of solution species by GEMS shows high amounts of sodium and hydroxide species in addition to carbonate species. No calcium was observed in the solution.

Zeta potential measurements were taken of C-S-H produced in the batch reactor with either 1 wt% quartz or 1 wt% calcite added to the hydrate. Results showed little to no difference in potential upon the presence of quartz. However, the presence of calcite caused an increase in potential, possibly due to an increase of dissolved calcium in solution indicating higher amounts of adsorption/incorporation for this Ca:Si than observed in Chapter 5.

Calcite shows the very interesting effect of inducing the fibrillar morphology as seen in applied cementitious systems. The work done by Siramanont and in these experiments show the effects of heterogeneous substrates on changing the kinetics and morphologies of C-S-H. Though, to continue these works, kinetic experiments in which free calcium is measured as a function of time for systems with calcite in silicate solution and on the dissolution of $C_3S$ to better characterize dissolution rates. The dropwise precipitation method is done at high supersaturation of the C-S-H phase whereas in applied systems, the formation of C-S-H is dependent on dissolution rates[11], [132].

## 6.3 C-A-S-H, quartz & calcite

### 6.3.1 Introduction

To reduce the amount of $CO_2$ produced from cement production, supplementary cementitious materials, or SCMs, are blended with Portland cement. Many SCMs are aluminum-rich like fly ash or blast furnace slags. Upon reaction with Portland cement, the composition of C-S-H is changed as aluminates are incorporated into the structure. With addition of aluminates, the Ca:Si molar ratio decreases with higher amounts of aluminum[4], [86], [97]. SCMs have also shown to decrease reactivity of cement, consequently increasing the setting times of concrete. C-S-H and C-A-S-H occupy 50-60% volume of hydrated cement pastes, so any changes in properties or growth mechanisms upon the addition of aluminates, particularly given the high need for SCMs, are of great interest.

Many studies have been done on the incorporation of aluminum in C-S-H and the morphologies of C-A-S-H in alite pastes and blended cements. Avet et al. observed fibrillar C-A-S-H in $LC^3$ cements after 28 days of hydration on the surfaces of metakaolinite and ettringite, as did Rossen & Scrivener[123], [128], [133]. Studies on C-A-S-H alone, however, are limited. In recent work, the atomic-scale structure of C-A-S-H was modelled with the help of Al NMR experiments on synthetic hydrates produced by dropwise precipitation[18], [32]. However, the effect of aluminates on the morphology and kinetics on the hydrate alone have not yet been investigated, nor have the effects of heterogeneous substrates on synthetic C-S-H been studied.

In this section, aluminates were added to C-S-H samples produced by dropwise precipitation. Additionally, calcite and quartz were placed in silicate and calcium solutions in the presence of aluminates, respectively and studied by X-ray diffraction, TEM, STEM-EDX, acoustophoresis, and thermodynamic modelling for the effect of aluminates on morphology and solution species of synthetic C-A-S-H.

## 6.3.2 Experimental plan

*C-A-S-H sample preparation*

C-A-S-H samples were prepared as described in Section 3.1.5. Quartz and 0.1M sodium metasilicate solution were placed into the batch reactor. A solution of NaOH was added to the sodium and quartz solution to adjust the pH and to attain a final Ca:Si of 1.6. A solution of 0.22M calcium nitrate and aluminum nitrate, $Al(NO_3)_3$ was added dropwise into the batch reactor by a piston pump. The experiments are described below in Table 6.3.1. All samples were produced in batches of 200mL reactor volume.

Table 6.3.1 Experimental plan for C-A-S-H produced by the dropwise precipitation method with varying amounts of aluminates, and presence of quartz and calcite. Where Q indicates quartz, and Cal indicates calcite.

| | **C-A-S-H_Q** | **C-A-S-H_Cal** |
|---|---|---|
| **Quartz** | 1 wt% | |
| **Calcite** | | 1 wt% |
| **$Al(NO_3)_3$** | 10mM, 15mM, 20mM | 10mM, 15mM, 20mM |

*C-A-S-H growth in solution: Sample preparation*

To grow C-A-S-H on the surface of quartz and calcite, two 400mL solutions were prepared as described in Table 6.3.1. Samples including the substrate, aluminates, and either calcium or silicate solution, were mixed at 300 rpm for 5 hours before the addition of NaOH. After adding NaOH, the solutions were mixed for an additional 48 hours, and were sampled at 3 hours, 24 hours, 3 days, 1 week, and 1 month, and 3 months, for TEM analyses and pH measurements.

Table 6.3.2 Experimental plan for quartz and calcite solutions in calcium nitrate and sodium metasilicate solutions, respectively with varying amounts of aluminate addition at 13.4 pH. Where CQ is quartz in a calcium solution, SiCal is calcite in a silicate solution, and Al indicates presence of aluminum.

| | **CQ_Al** | **SiCal_Al** |
|---|---|---|
| **Quartz** | 1 wt% | - |
| **Calcite** | - | 1 wt% |
| **NaOH** | 10 mL | 10 mL |
| **$Ca(NO_3)_2$** | 0.2M | - |
| **$Na_2SiO_3$** | - | 0.1M |
| **$Al(NO_3)_3$** | 15mM | 15mM |

## 6.3.3 C-A-S-H & quartz

C-A-S-H, produced with 10-20mM of aluminates is pictured in Figure 6.3.1. As observed in previous C-A-S-H samples in section 5.2.3, the addition of aluminates produces dense agglomerates of nanofoils. At 20mM addition of aluminates in the samples, the right-most image displays agglomerated, more-ordered sheets and fewer sheets protruding from the agglomerate in comparison to the more dis-ordered nanofoils in the other images. A STEM-EDX analysis of C-A-S-H, in Figure 6.3.2 shows very homogeneous distributions of Ca, Si, O, and Al in the ordered C-A-S-H (Figure 6.3.1d) produced with 20mM aluminates.

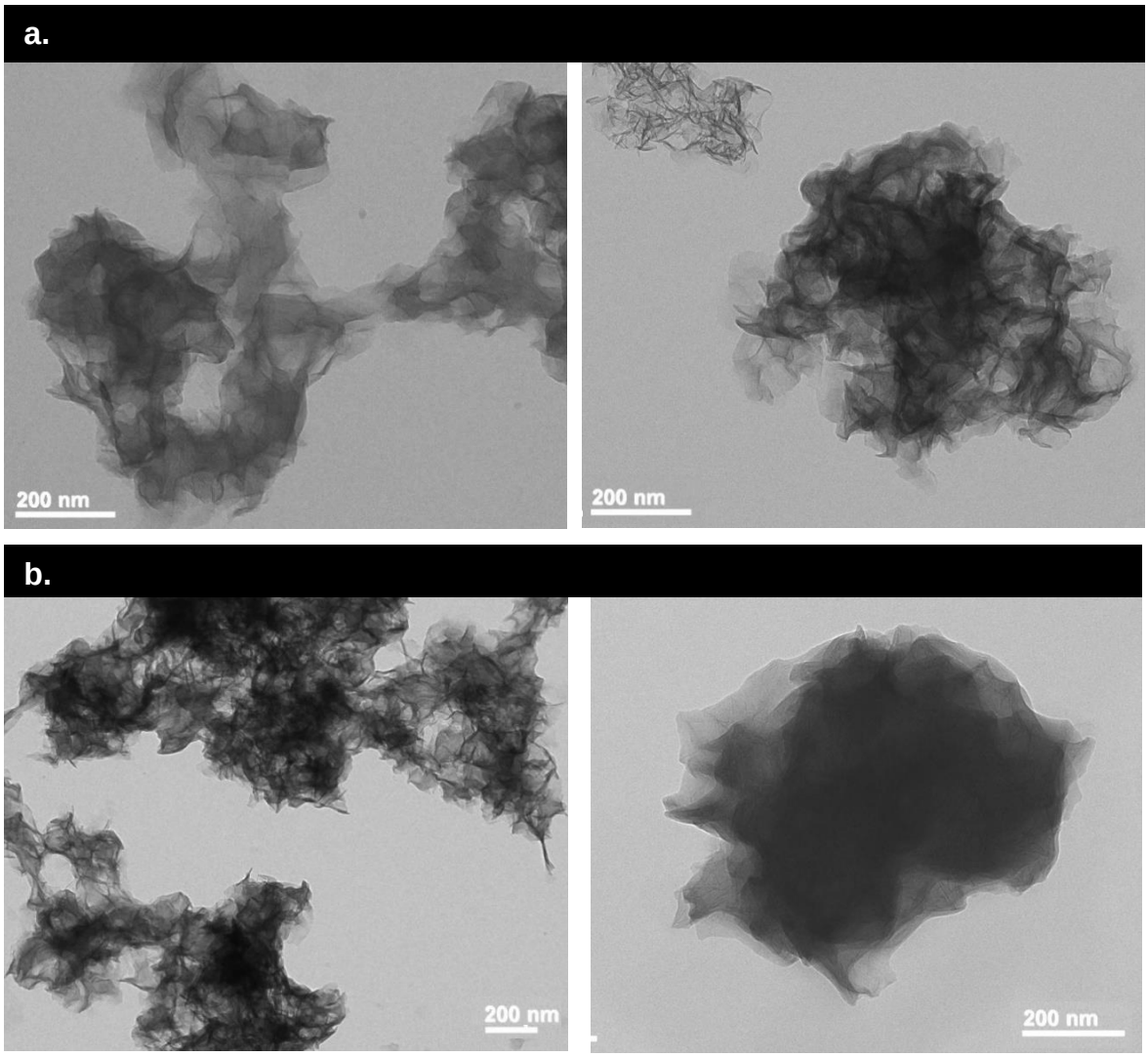


Figure 6.3.1 TEM micrographs of C-A-S-H produced in the presence of 1 wt% quartz with 10mM $Al(NO_3)_3$ in solution (a), and 20mM $Al(NO_3)_3$ (b), Ca:Si = 1.6

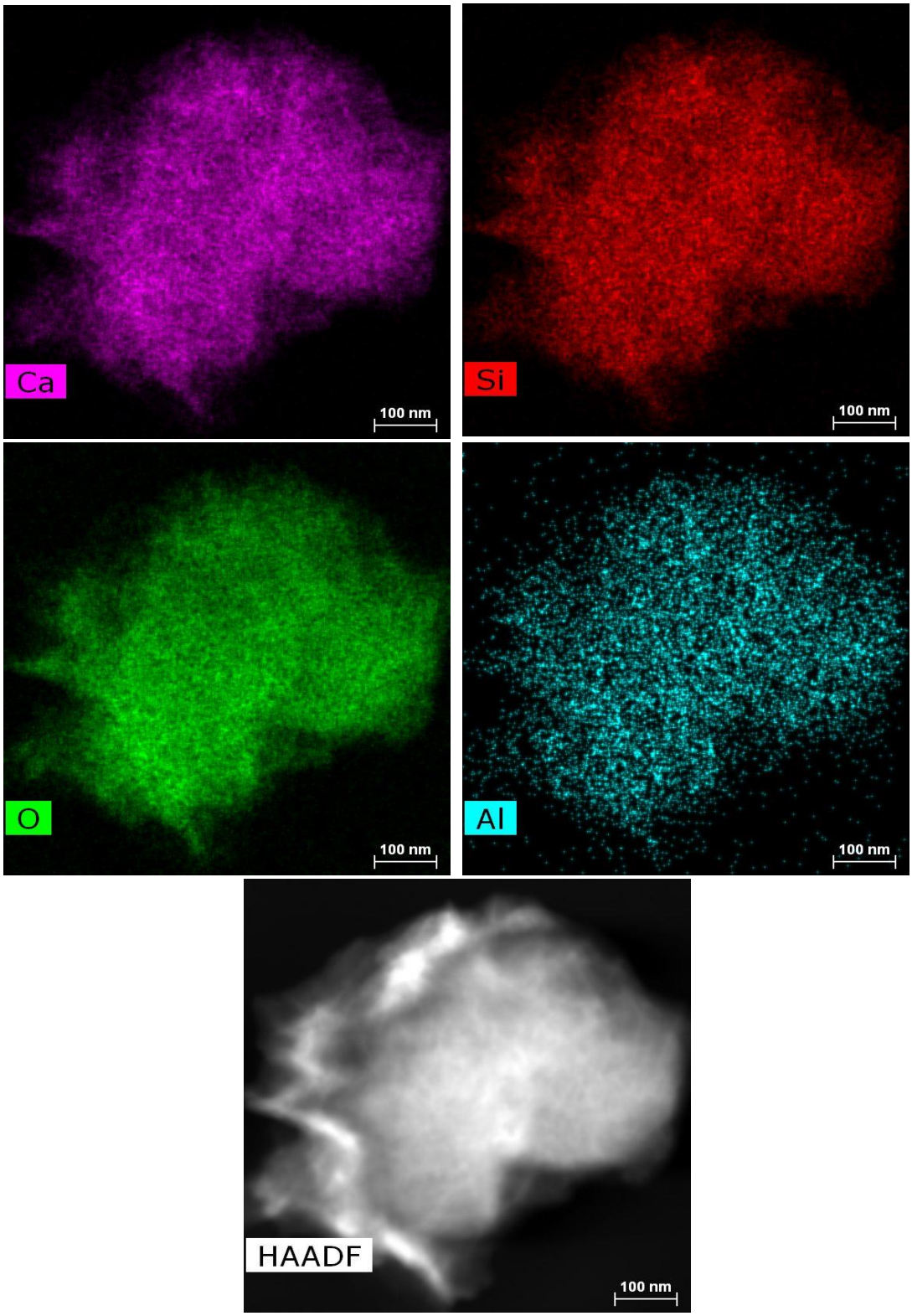


Figure 6.3.2 STEM-EDX micrographs of C-A-S-H produced in the presence of 1wt% quartz, 20mM $Al(NO_3)_3$, Ca:Si = 1.6

Quartz, hydrated in a 0.2M calcium nitrate solution with 15mM $Al(NO_3)_3$ at a pH of 13.4 is shown below in Figure 6.3.3. The TEM image shows small amounts of growth on the surface of quartz in a fibril and somewhat globular morphology. However, portlandite is also observed, the hexagonal platelets in the TEM image.

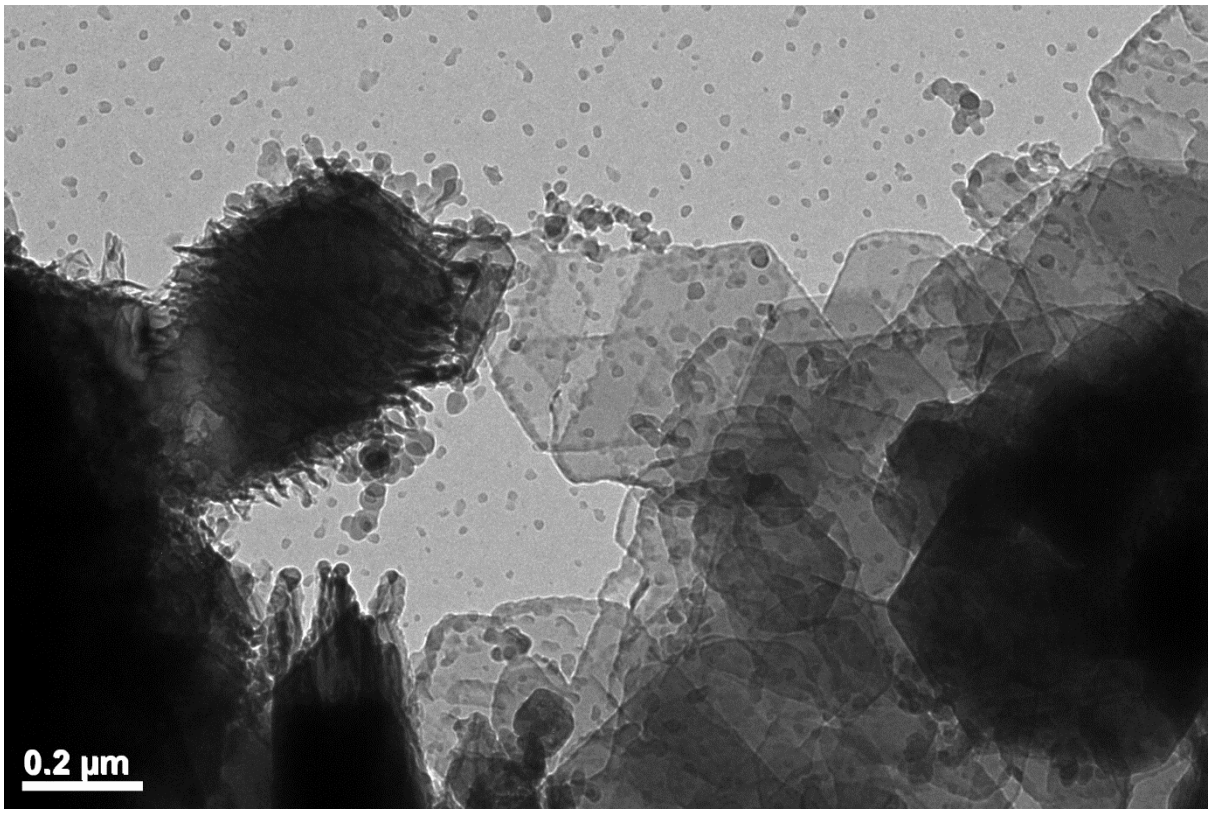


Figure 6.3.3 TEM image of quartz hydrated in calcium nitrate solution with 15mM $Al(NO_3)_3$, pH 13.4, 1 week

XRD analysis, in Figure 6.3.4 of quartz in silicate and aluminate solution confirms the presence of portlandite and quartz after three months. Additionally, XRD shows the presence of gibbsite or $Al(OH)_3$, and a calcium aluminum hydroxide phase, specifically margarite, $CaAl_2O_{10}(OH)_2$.

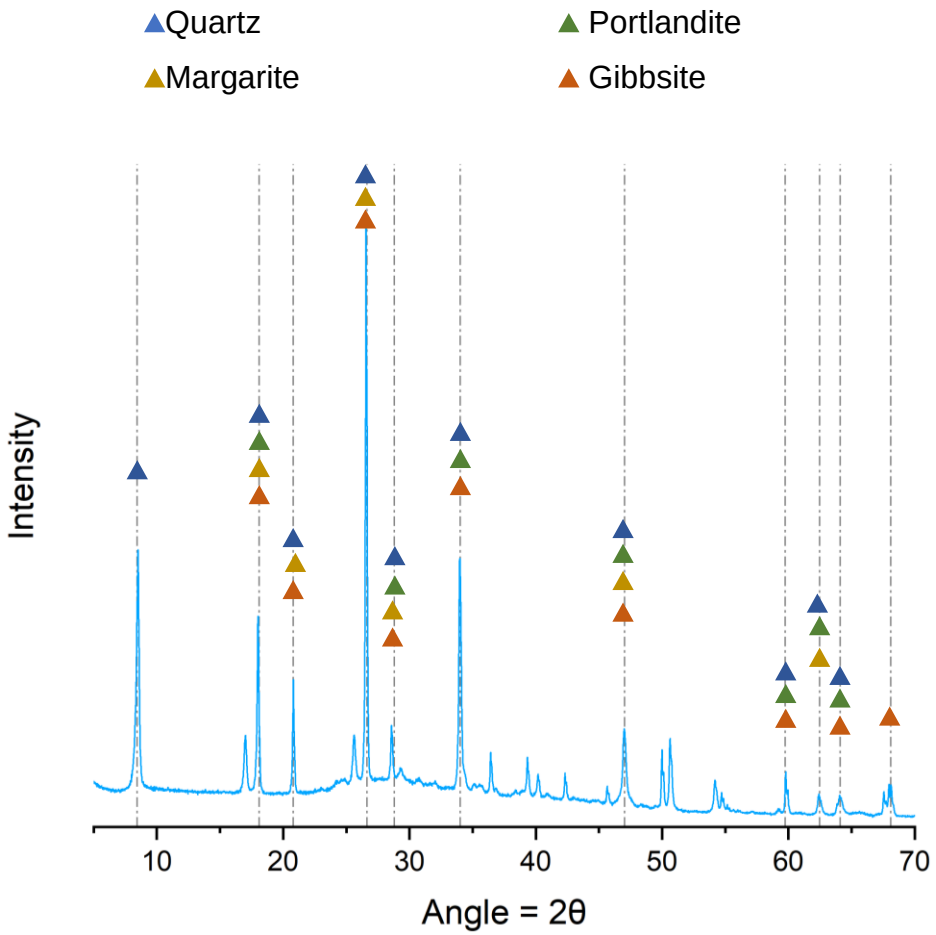


Figure 6.3.4 X-ray diffractogram of quartz hydrated in 0.2M calcium solution and 15mM $Al(NO_3)_3$, 3 months

Results show that with increasing concentrations of aluminum, ordering or layers in the sample may also increase in synthetic C-S-H samples. Samples precipitated in the presence of quartz exhibit similar morphologies as samples grown without it. For samples grown in solution, a fibrillar phase is observed to grow on the surface of quartz, possibly margarite or gibbsite as XRD does not observe the formation of a C-S-H hydrate. Additionally, as observed in the quartz samples in solution from section 6.2 and in the work by Siramanont, quartz shows a very slow dissolution.

### 6.3.4 C-A-S-H & calcite

Synthetic C-A-S-H with a 1.5 Ca:Si molar ratio was produced by the dropwise precipitation method in the presence of calcite with 10, 15, and 20mM of aluminates added to the batch reactor[17], [32]. In Figure 6.3.5, small agglomerates exhibit the nanofoil morphology and sheets appear to be slightly thicker agglomerates denser than C-S-H nanofoils in Figure 6.2.2. This denser agglomeration is better visualized in Figure 6.3.6, which shows C-A-S-H with 20mM aluminates added.

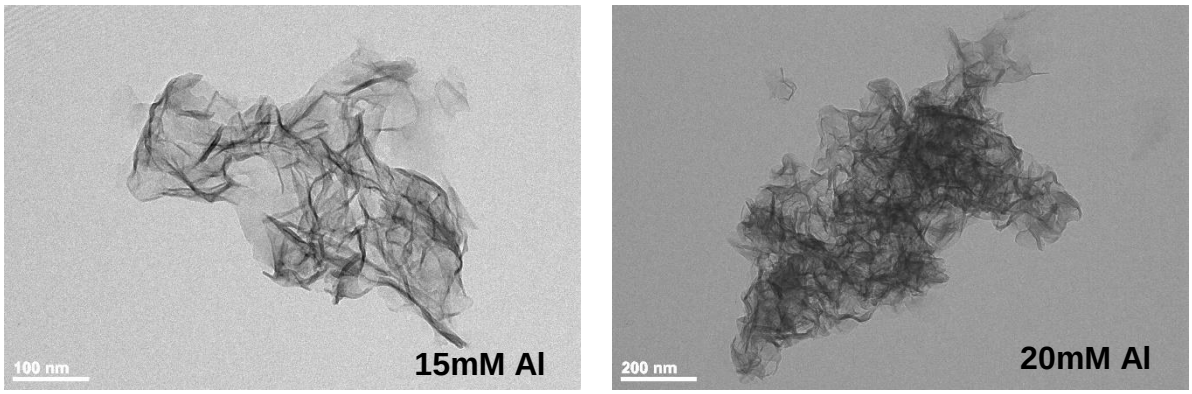


Figure 6.3.5 TEM micrographs of C-A-S-H produced by the dropwise precipitation method in the presence of 15 and 20mM $Al(NO_3)_3$, Ca:Si = 1.6

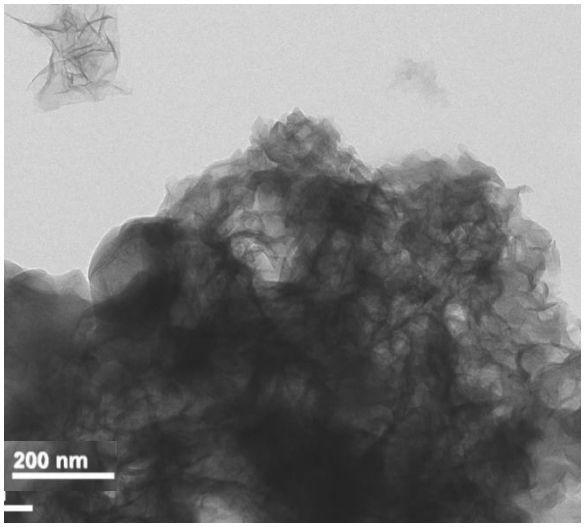


Figure 6.3.6 TEM micrograph of agglomerated C-A-S-H produced by the dropwise precipitation method in the presence of 20mM $Al(NO_3)_3$, Ca:Si = 1.6

Samples produced by placing calcite in a silicate solution in the presence of aluminates are pictured in Figure 6.3.7. After 3 days in solution, thick needle-like structures are observed in both solution and on the surface of calcite. Thermodynamic modelling calculations showed the formation of natrolite, $Na_2Al_2Si_3O_{10} * 2\ H_2O$ in the absence of calcium. Figure 6.3.7 displays the growth of natrolite on the surface of unreacted grains of calcite in solution with both silicate clusters and portlandite.

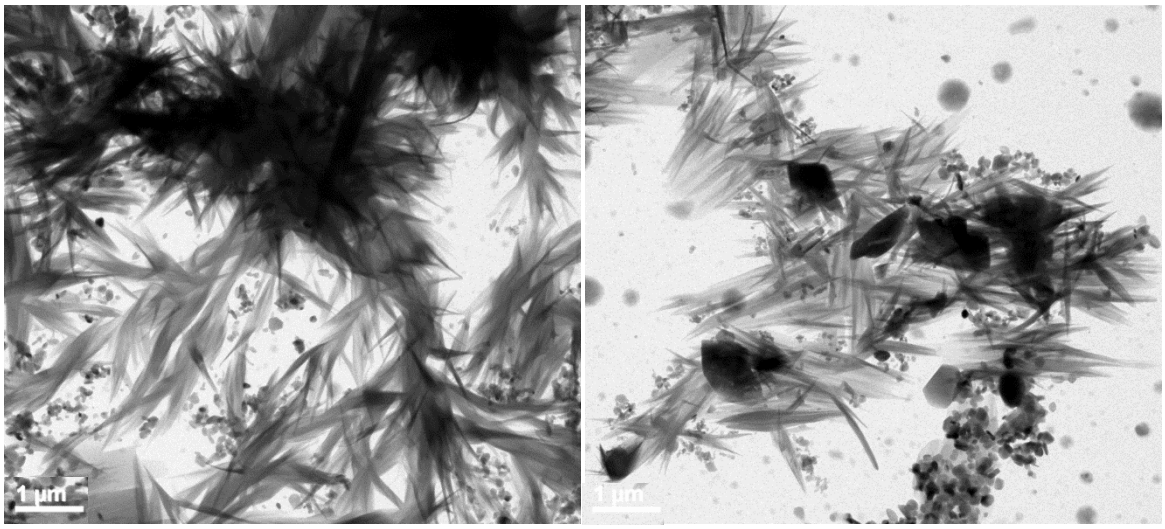


Figure 6.3.7 TEM micrograph of natrolite grown on the surface of calcite placed in 0.1 M silicate solution with presence of 15mM $Al(NO_3)_3$, pH = 13.4, 3 days

A TEM micrograph of the same sample is shown in Figure 6.3.8 after 1 week in solution. STEM-EDX analysis shows the presence of C-A-S-H in the needles in addition to clusters of silicate. The hydrate morphology in this sample is very comparable to the hydrated $C_3S$ and calcite samples by Bazzoni in Figure 6.2.1[127]. Natrolite, portlandite, and unreacted calcite are also found in this sample.

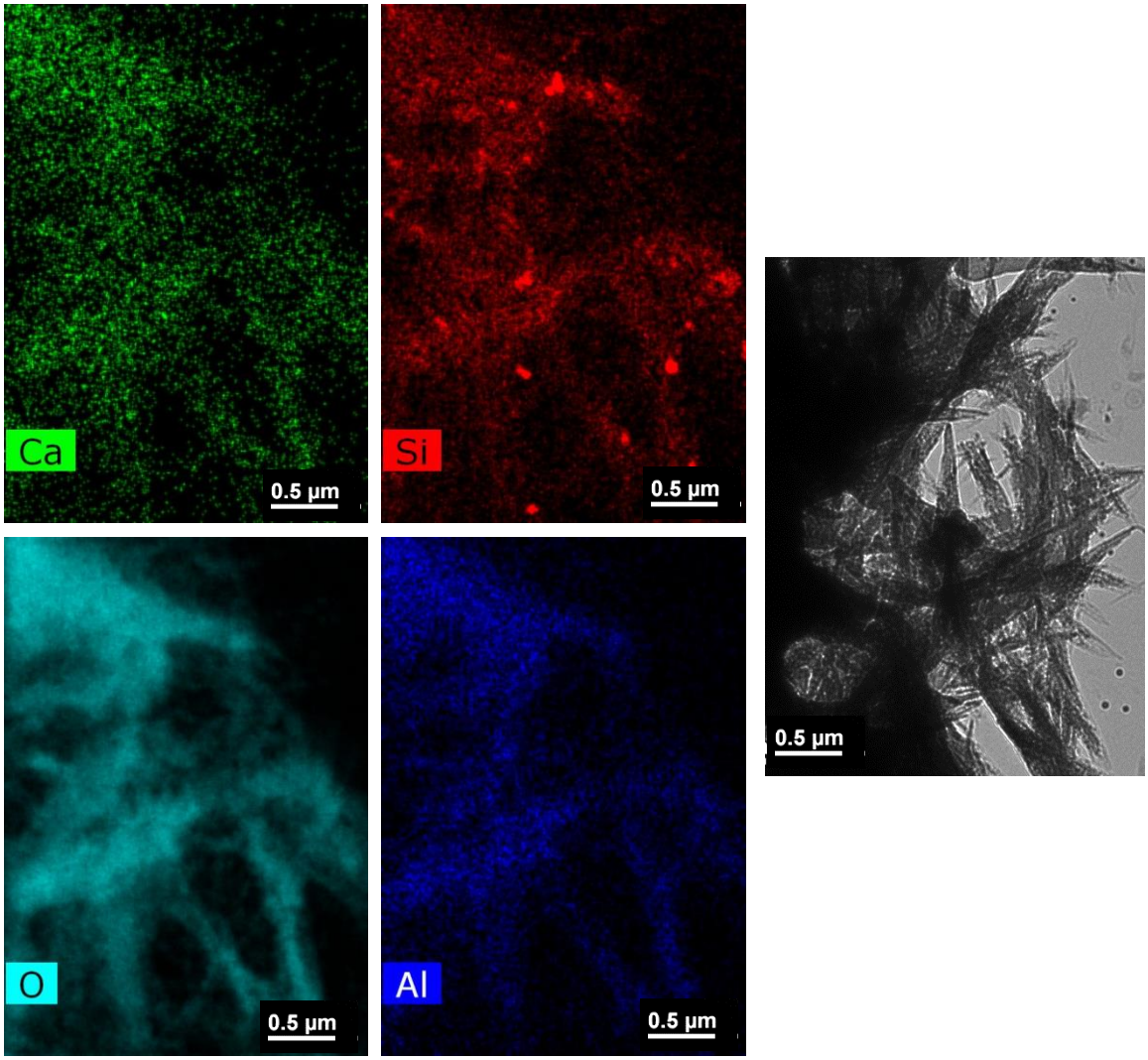


Figure 6.3.8 TEM and STEM-EDX micrographs of samples grown from calcite placed in 0.1 M silicate solution with presence of 15mM $Al(NO_3)_3$, 1 week

One-month samples are pictured in Figure 6.3.9 in TEM and STEM-EDX images. STEM-EDX shows Ca, Si, O, and Al homogeneously distributed throughout the sample. Two morphologies are observed, nanoglobules and a more compact structure. Low intensity of calcium is measured in comparison to silicon suggesting a low Ca:Si hydrate, particularly throughout the nanoglobule morphology suggesting it is C-A-S-H.

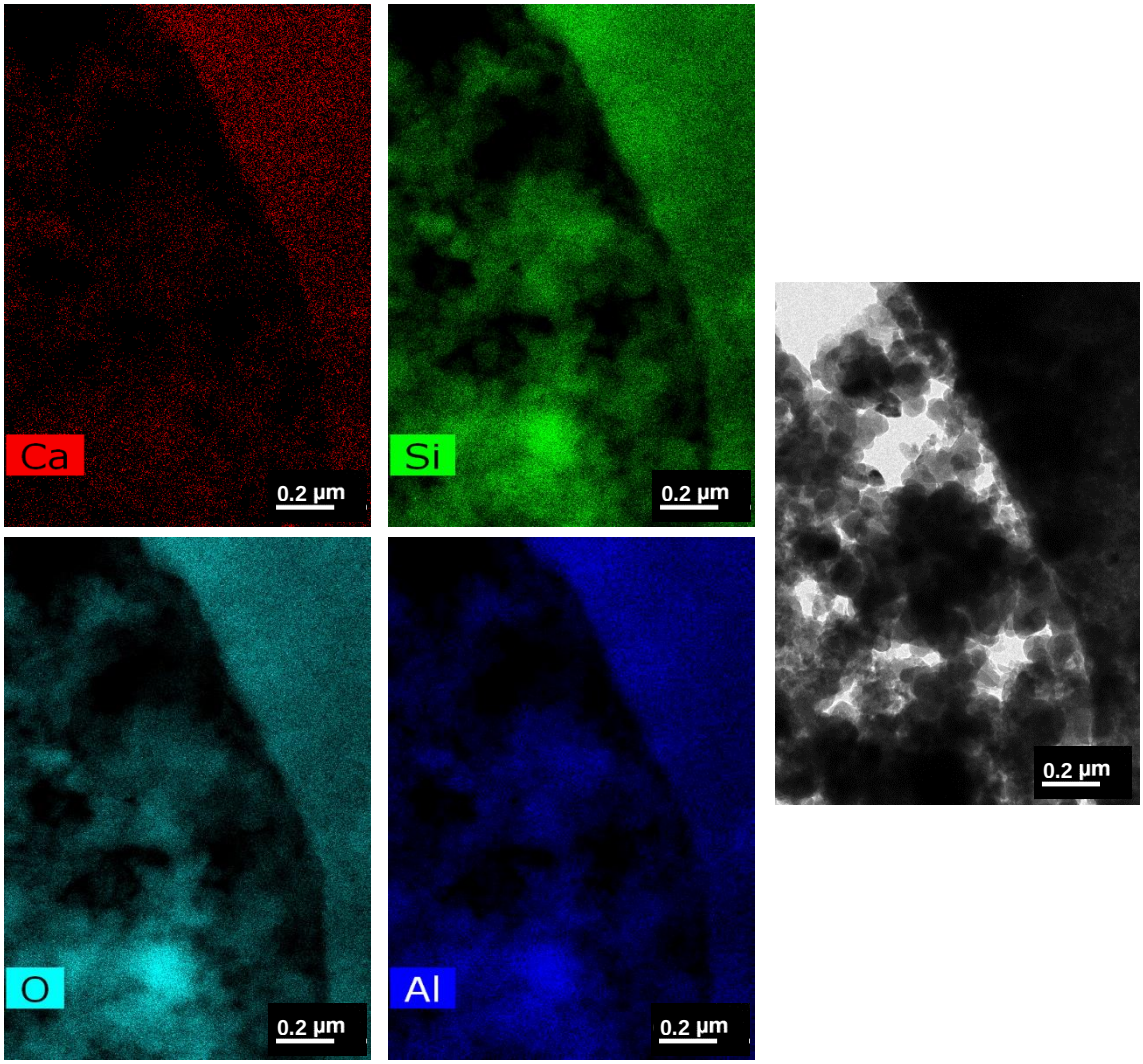


Figure 6.3.9 TEM and STEM-EDX micrographs of samples grown from calcite placed in 0.1M silicate solution with presence of 15mM $Al(NO_3)_3$, 1 month

Three-month samples are pictured in Figure 6.3.10, and exhibit a dense, disordered nanofoil structure more similar to the C-A-S-H samples observed in Figure 6.3.6. No fibrillar or needle-like morphologies were observed.

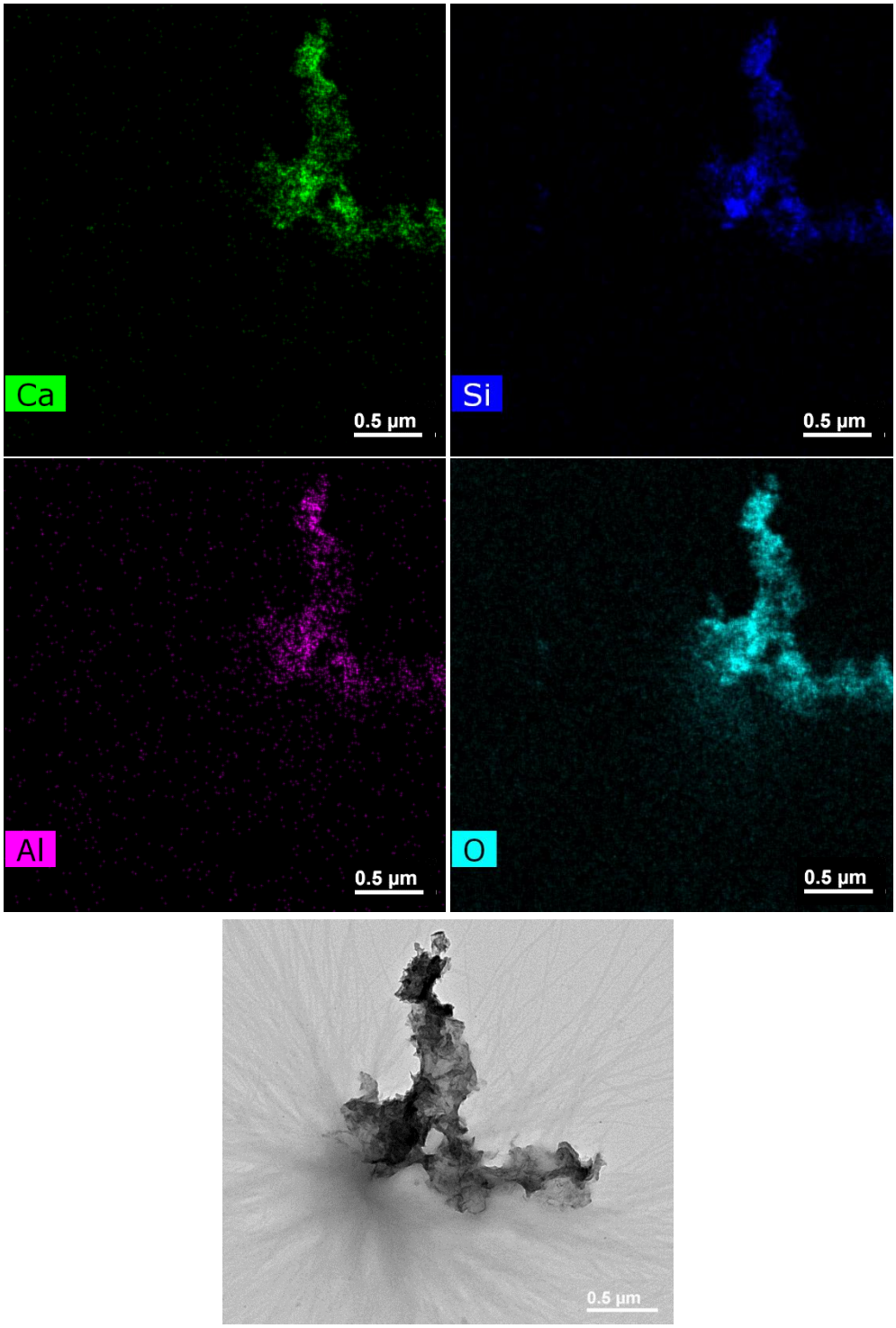


Figure 6.3.10 TEM and STEM-EDX Micrographs of samples grown from calcite in 0.1 M silicate solution with presence of 15mM $Al(NO_3)_3$ solution, pH = 13, 3 months

An x-ray diffractogram of the 3 month sample exhibits peaks for both C-S-H (or C-A-S-H) and calcite. Additionally, Al-tobermorite is detected, $Ca_5Si_5Al(OH)O_{17}$ * 5

$H_2O$[134]–[136]. This phase has higher amounts of water and comparable amounts of aluminates as found in C-A-S-H phases. This could be a result of the method of formation and the high excess of water in solution.

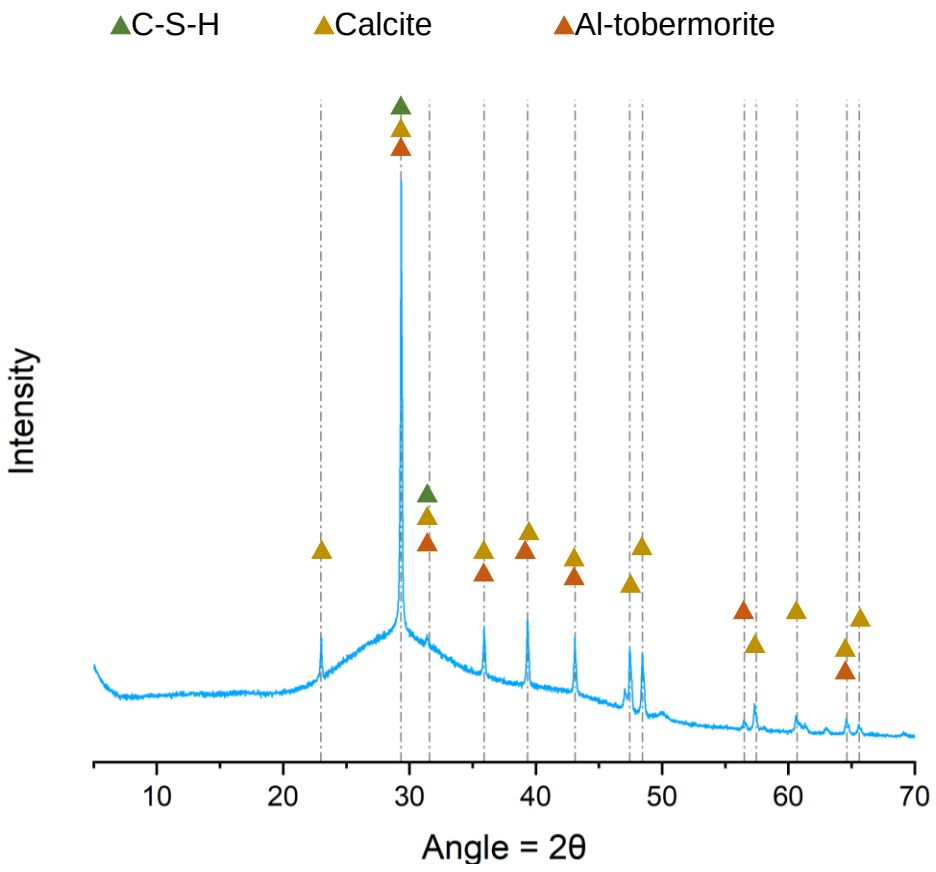


Figure 6.3.11 X-ray diffractogram of calcite hydrated in 0.1M silicate solution and 15mM $Al(NO_3)_3$, 3 months

Thermodynamic modelling of the solution at the final measured pH of 13.43 gives 2.1 grams of natrolite and 3.9 grams of calcite although both XRD and TEM show the presence of C-S-H as well. Calculated solution species are presented in Figure 6.3.12. Calculations predict little free $Ca^{2+}$ and $CaOH^{+}$ in solution, both present in the order of $10^{-6}$ mol.

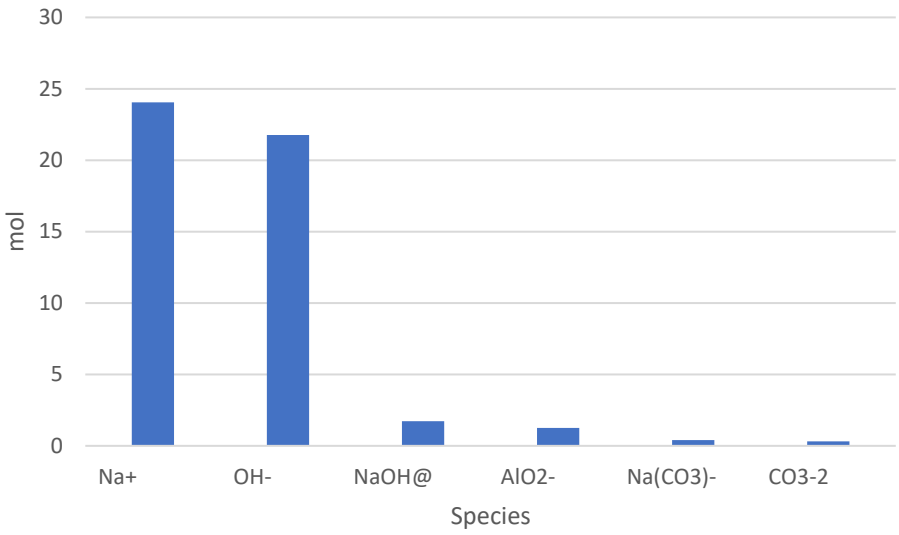


Figure 6.3.12 GEMS-calculated equilibrium solution species for C-A-S-H grown from calcite in 0.1M silicate solution, pH = 13.43

In Figure 6.3.13, masses of natrolite, calcite, portlandite, and C-S-H, calculated by thermodynamic modelling for a solution of calcite in 0.1M silicate solution, were plotted as a function of CaO addition in the sample. Thermodynamic modelling predicts that at equilibrium, with increased calcium in solution, the amount of natrolite formed decreases, and C-S-H goes up. After 2 grams of addition, the formation of portlandite also begins to increase linearly. In future experiments, supplementing a certain amount of calcium in the solution may aid preferential formation of C-S-H. However, in comparing the STEM-EDX results, the transition from samples at 3 days to 1 week shows both that calcite steadily dissolves and also that calcium has a propensity to incorporate itself into the natrolite structure. Although thermodynamic modelling predicts the presence of the natrolite phase over C-S-H under the solution conditions at equilibrium, results show that as the calcium dissolves into the solution, natrolite quantity decreases, C-S-H forms, and eventually portlandite forms with excess calcium. Calcium both incorporates and eventually changes the structure of the phase grown on the surface of the calcite, becoming nanoglobules after a month, and then changing into a nanofoil-like structure after three months.

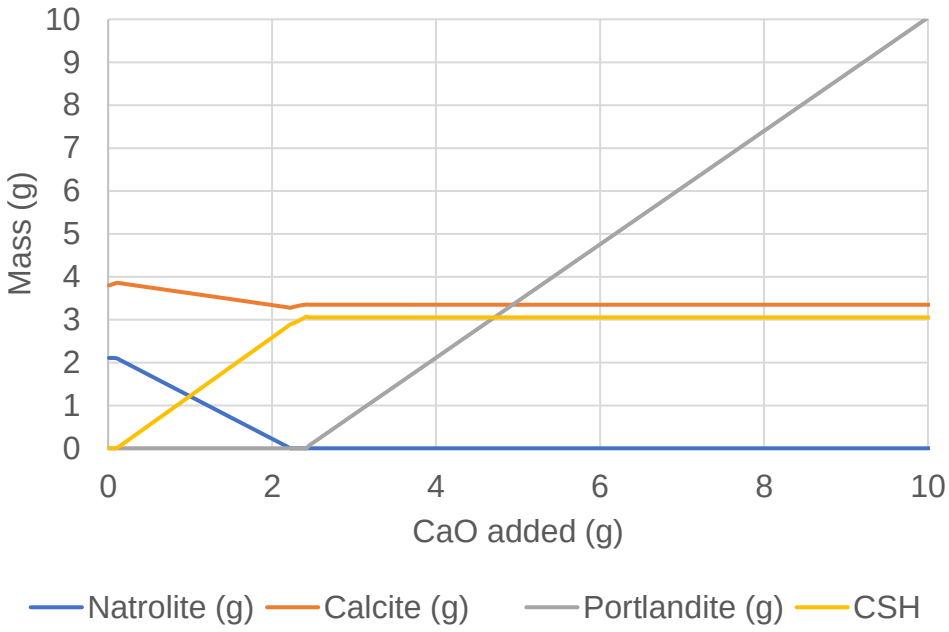


Figure 6.3.13 GEMS-calculated masses of present phases at equilibrium for calcite in 0.1M silicate solution at 13.4 pH

Zeta potential measurements of C-A-S-H produced in the batch reactor with calcite and quartz (samples visualized in Figure 6.3.6) are compared below in Figure 6.3.14. Both the addition of calcite and quartz causes an increase in the measured potential. However, in the case of C-S-H under these same conditions, the potential of C-A-S-H + quartz is observed to make a more notable increase in potential while the calcite on C-A-S-H causes little change. Aluminates, as shown by recent work, has been predicted to be on the bridging sites of silicate chains, effectively incorporating into the C-A-S-H structure, and so change in zeta potential could be expected proportional to the aluminates incorporated in the sample[18].

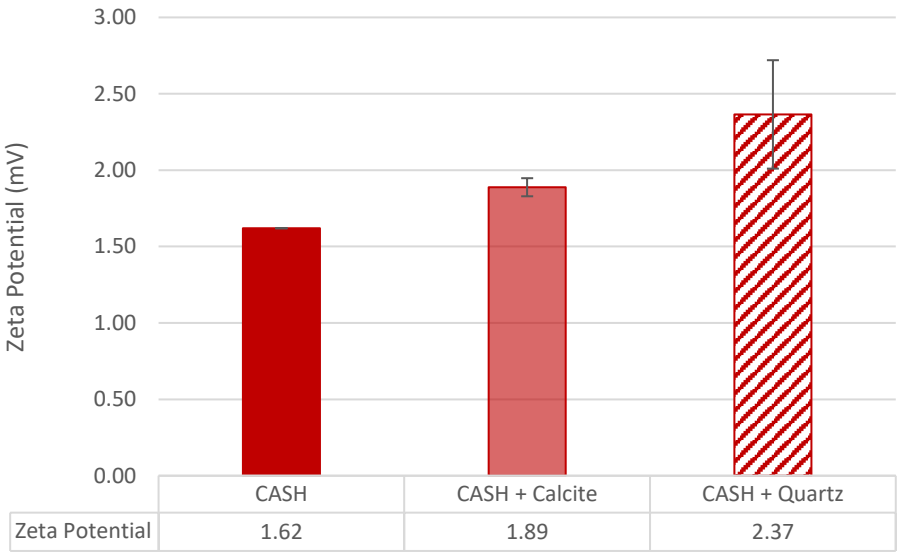


Figure 6.3.14 Zeta potentials of C-A-S-H produced with dropwise precipitation method, dispersed in 10mM NaOH, 3.125 wt% dispersion, with 1 wt% calcite and 1 wt% quartz, Ca:Si = 1.6

The inclusion of aluminates into the structure of C-S-H seems to decrease the propensity for calcium adsorption as C-S-H and calcite samples exhibited a greater increase in potential. This change in potential between C-A-S-H and C-S-H was also observed in section 5.2.3 where C-A-S-H exhibited lower potentials than C-S-H when dispersed in both 10mM NaOH and filtered supernatant. There is no solution composition analysis after zeta potential was taken for these samples, and this should be taken in the future to fully analyze the results.

## 6.3.5 Conclusions

In this section C-A-S-H morphology in the presence of quartz and calcite is studied. For C-A-S-H samples synthesized by dropwise precipitation, increasing amounts of aluminates caused denser nanofoil morphologies than observed in C-S-H alone with the presence of calcite and quartz.

Samples of quartz placed in calcite and aluminate solution showed small amounts of fibrillar hydrate growth on the surface of quartz and high amounts of portlandite in solution. Over a period of 3 months, very little change was observed in the sample, and x-ray diffractograms show the presence of calcium aluminum hydrate hydroxide, aluminum hydroxide, portlandite, and quartz.

Samples of calcite placed into a silicate and aluminate solution showed the precipitation of natrolite, in a sharp needle-like morphology on the surface of calcite after 3 days in solution. After 1 week, STEM-EDX results showed the distribution of Ca, Si, O, and Al in the needles, and after 1 month, the morphology appeared to have changed into a nanoglobule structure. At three months, the structure of C-A-S-H resembled the disordered, dense nanofoils as observed in the samples produced by the dropwise precipitation method. After three months, x-ray diffraction showed the presence of C-S-H, calcium aluminum hydroxide hydrate, and calcite. Thermodynamic modelling of the solution at equilibrium with additional CaO added showed that without any additional calcium in the solution, natrolite is expected to form. This particularly applies with early samples taken up to 3 days in which calcite is not dissolved enough to provide free calcium into the solution. Under the solution conditions, thermodynamic calculations do not predict the formation of C-S-H or C-A-S-H, although hydrates were observed in the sample in TEM and XRD. In work by Kumar et al., nanoglobules were observed in Ca:Si molar ratios of 1, and above 1.25, nanofoils were observed[17]. Other studies also showed this metastability of C-S-H morphology, primarily dependent on solution composition and the presence of polycarboxylate ether superplasticizers[137]–[140]. In future work, pH values should be taken during intermediate steps in sampling, as it is possible that in these TEM images, the transformation between different phases of C-A-S-H will be observed.

Zeta potential measurements showed increasing potentials in C-A-S-H produced with quartz and calcite. Calcite had little effect on the potential of C-A-S-H, unlike the increase in potential observed with C-S-H and calcite, suggesting that the inclusion of aluminates decreases either the dissolution of calcite, or has a lower chance to bind to free calcium. In samples of C-A-S-H and quartz samples showed an increase in potential over C-A-S-H alone, though it’s difficult to conclude on these observations as no solution data was taken for these dispersions.

## 6.4 C-S-H + $, quartz, & calcite

### 6.4.1 Introduction

Sulfates play an important role in the production of cement and concrete. Gypsum, $CaSO_4 * 2\ H_2O$ is often added in small amounts to cement to retard setting times[3], [83]. This allows there to be more time for transporting, mixing, and installing the concrete. Gypsum has been shown to interact with both C-S-H and alite during the acceleration period[82], [83], [91]. Also, in certain blended cements, the addition of SCMs gives an effect called the “filler effect” in which the reaction of alite is accelerated, affecting the rate at which sulfate is consumed, and increasing the amount of sulfate needed in the cement mixture[84]–[88]. As a result, with the advancements in sustainable cement, it is increasingly important to understand the effect of sulfates on C-S-H.

In work by Zunino, the needle length of C-S-H grown on the surface $C_3S$ with 3% gypsum was observed to increase on average by ~100nm from 200-250nm in the first 8 hours of hydration [141]. Additionally, Zunino measured a higher heat release, indicating reactivity, due to the presence of sulfates. With the addition of gypsum, spikes of C-S-H grew more densely on the surface of $C_3S$, perpendicular to the surface of the unreacted grain. Mota et al. showed that sulfate modifies the growth of C-S-H in studies that investigated the effects both of alkali and sulfate on alite[142]. Hydrated alite samples with NaOH and gypsum exhibited a more foil-like morphology while the samples with $Na_2SO_4$ grew more fibrillar-like C-S-H, similar to that observed on plain alite.

However, there is little work done characterizing sulfates on C-S-H alone, which may be necessary to pinpoint the difference between nanoglobule, nanofoil, and fibrillar C-S-H. In this section, C-S-H with the addition of sulfates by $Na_2SO_4$ are studied for the effect on morphology, as well as in the presence of quartz and calcite. Based on measurements taken by Berodier, 175mM of sulfates are added to the investigated samples[92]. Samples are characterized by TEM, XRD, acoustophoresis, and thermodynamic modelling.

## 6.4.2 Experimental plan

*C-S-H sample preparation*

C-S-H +$ samples were prepared as described in Section 3.1.5. Sodium metasilicate and sodium sulfate solution were mixed with calcium nitrate and NaOH to obtain a Ca:Si = 1.6 sample during C-S-H precipitation. Quartz, when added was included in the silicate solution while calcite was included in the calcium solution. The experiments are summarized in Table 6.4.1. All samples were produced in batches of 200 mL reactor volume.

Table 6.4.1 Experimental plan for C-S-H + $ produced by the dropwise precipitation method. Q indicates quartz, and Cal indicates calcite.

| | **C-S-H$_Q** | **C-S-H$_Cal** |
|---|---|---|
| **Quartz** | 1 wt% | |
| **Calcite** | | 1 wt% |
| **$Na_2SO_4$** | 150mm, 175mM, 200mm | 150mm, 175mM, 200mm |

*C-S-H + $ grown in solution sample preparation*

To grow C-S-H + $ on heterogeneous substrates, quartz or calcite was placed in a calcium or silicate solution, respectively, with $Na_2SO_4$. Solutions were mixed for 5 hours at 300 rpm before the addition of NaOH to bring the pH to 13.4. Afterwards, solutions were mixed for an additional 48 hours. Samples were taken at 3 hours, 1 day, 3 days, 1 week, 1 month, and 3 months. The experimental plan is summarized in Table 6.4.2.

Table 6.4.2 Experimental plan for quartz and calcite solutions in calcium nitrate and sodium metasilicate solutions, respectively with varying amounts of sulfate addition at 13.4 pH. Where CQ is quartz in a calcium solution, SiCal is calcite in a silicate solution, and $ indicates presence of sulfates.

| | **CQ_$** | **SiCal_$** |
|---|---|---|
| **Quartz** | 1 wt% | - |
| **Calcite** | - | 1 wt% |
| **NaOH** | 10 mL | 10 mL |
| **$Ca(NO_3)_2$** | 0.2M | - |
| **$Na_2SiO_3$** | - | 0.1M |
| **$Na_2SO_4$** | 175mM | 175mM |

## 6.4.3 C-S-H + $ quartz

C-S-H + $ was produced in the presence of quartz by the dropwise precipitation method. TEM images are presented below in Figure 6.4.1, exhibiting possibly ordered aggregation. STEM-EDX analysis of the same sample in Figure 6.4.2 shows homogeneous distributions of Ca, Si, O, and S in certain portions of the sample in addition to clusters of silicates and a sulfur-oxide or sodium sulfate phase. This type of aggregation was not reported for C-A-S-H in section 6.3.3, though density of sample does appear to be higher like the C-A-S-H samples, particularly in comparison to other C-S-H + $ samples, seen in Figure 5.2.5.

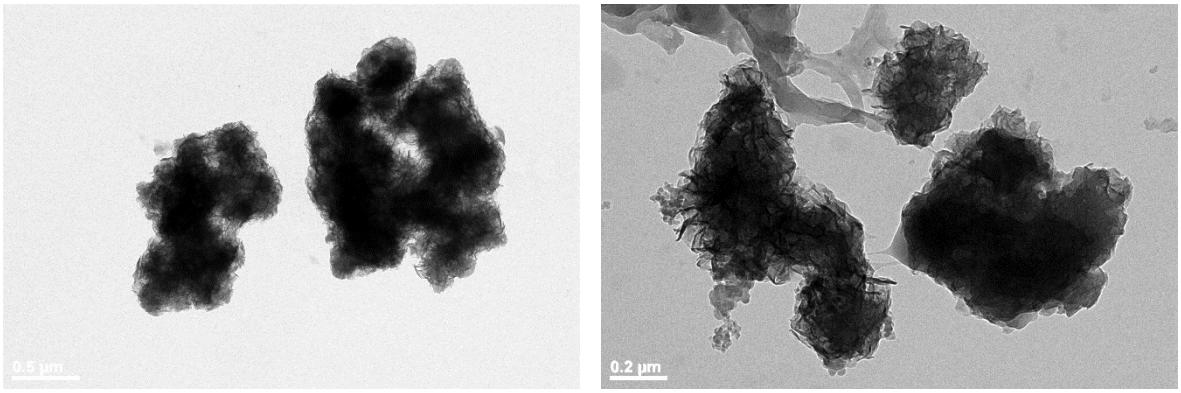

Figure 6.4.1 TEM image of C-S-H + $ and 1 wt% quartz, 175mM sulfates, Ca:Si = 1.6, produced by dropwise precipitation method

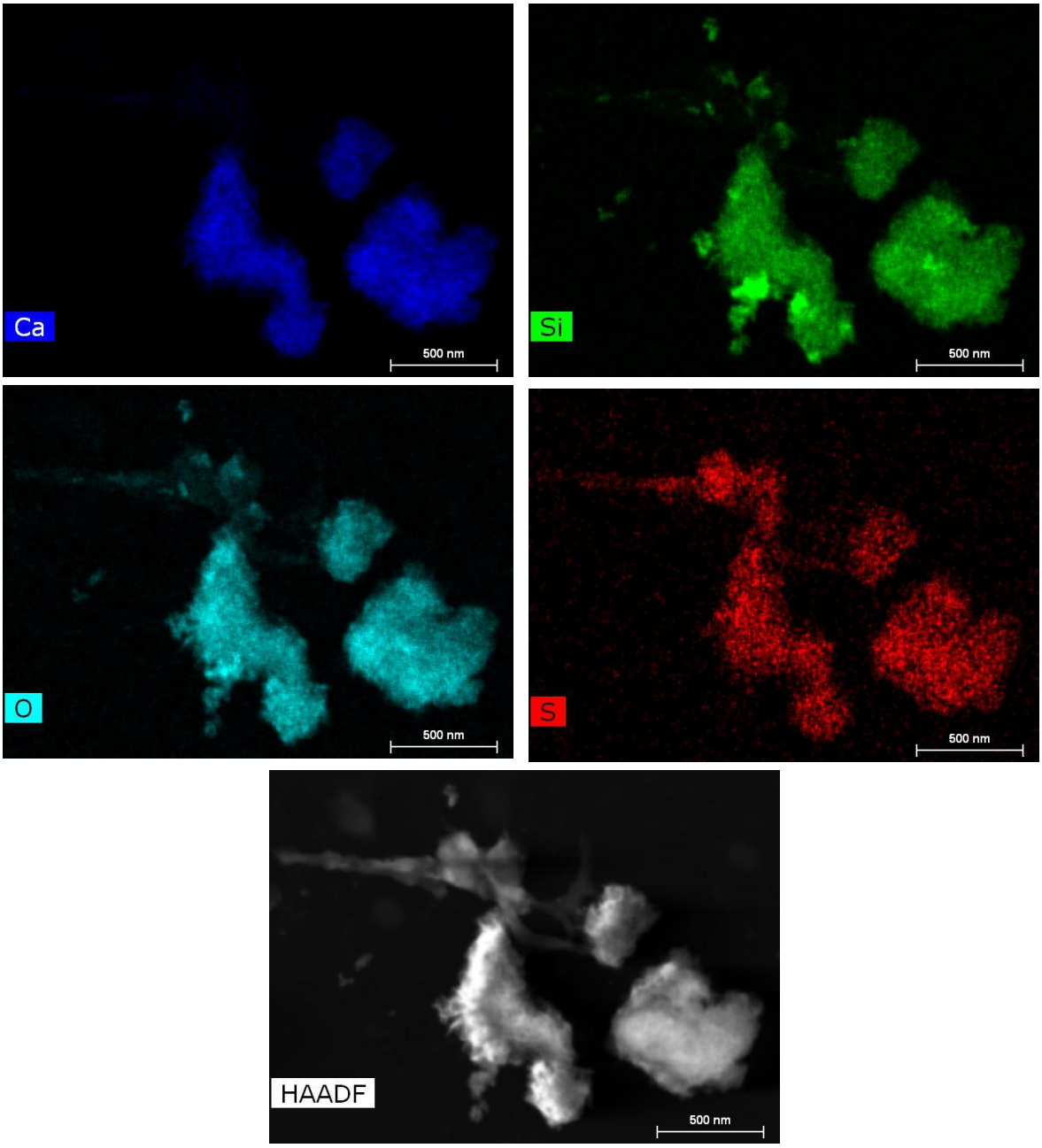


Figure 6.4.2 STEM-EDX elemental images of C-S-H + $ and 1 wt% quartz, Ca:Si = 1.6, produced by dropwise precipitation method

Quartz placed in 13.4 pH calcium nitrate solution with sulfates is shown below in Figure 6.4.3. As observed in previous experiments to grow C-S-H and C-A-S-H on the surface of quartz, very small amounts of quartz appear to be dissolved or reacted

in the solution. The TEM shows rough edges on quartz and small amounts of hydrate growth after three days in solution.

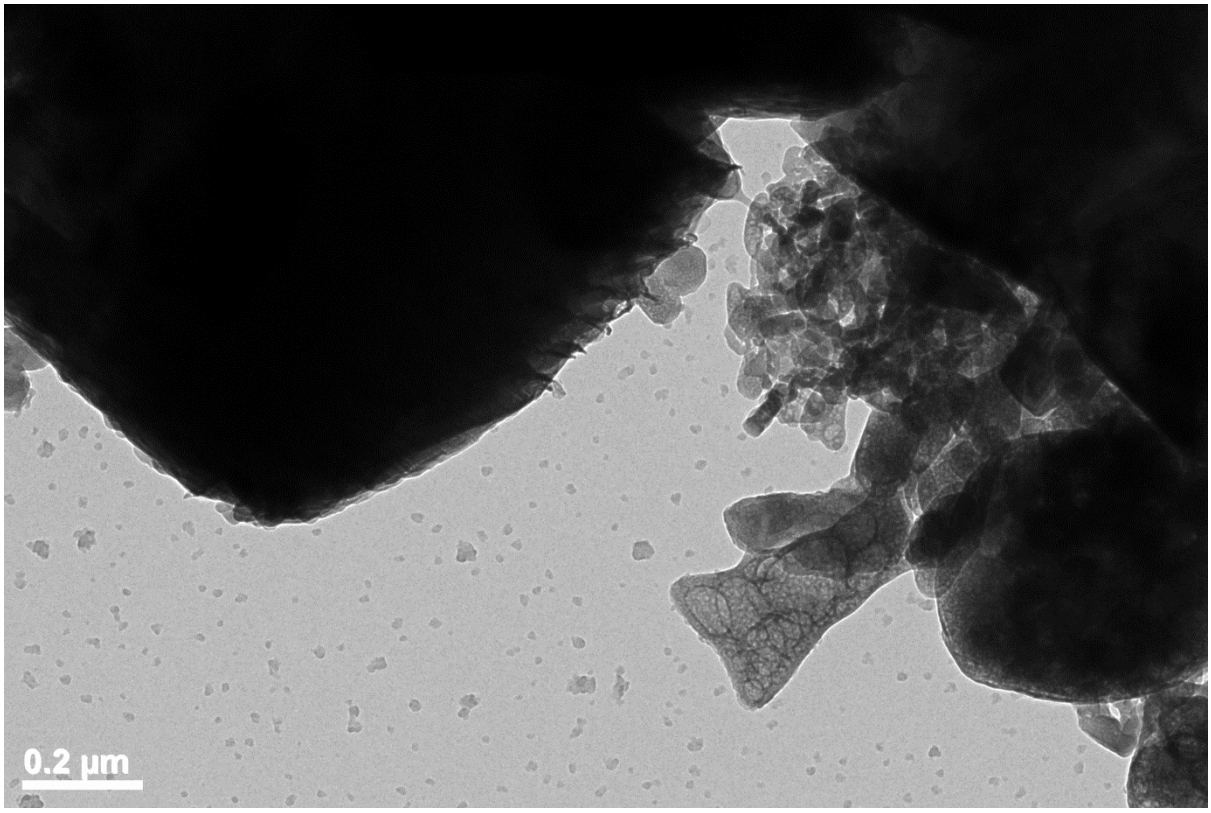


Figure 6.4.3 TEM image of quartz hydrated in calcium nitrate solution with 175mM $Na_2SO_4$, pH 13.4, 3 days

XRD analysis of the same sample after 3 months in solution shows the presence of calcium sulfate hydrate, portlandite, silicon dioxide, calcium silicate hydroxide, and calcite.

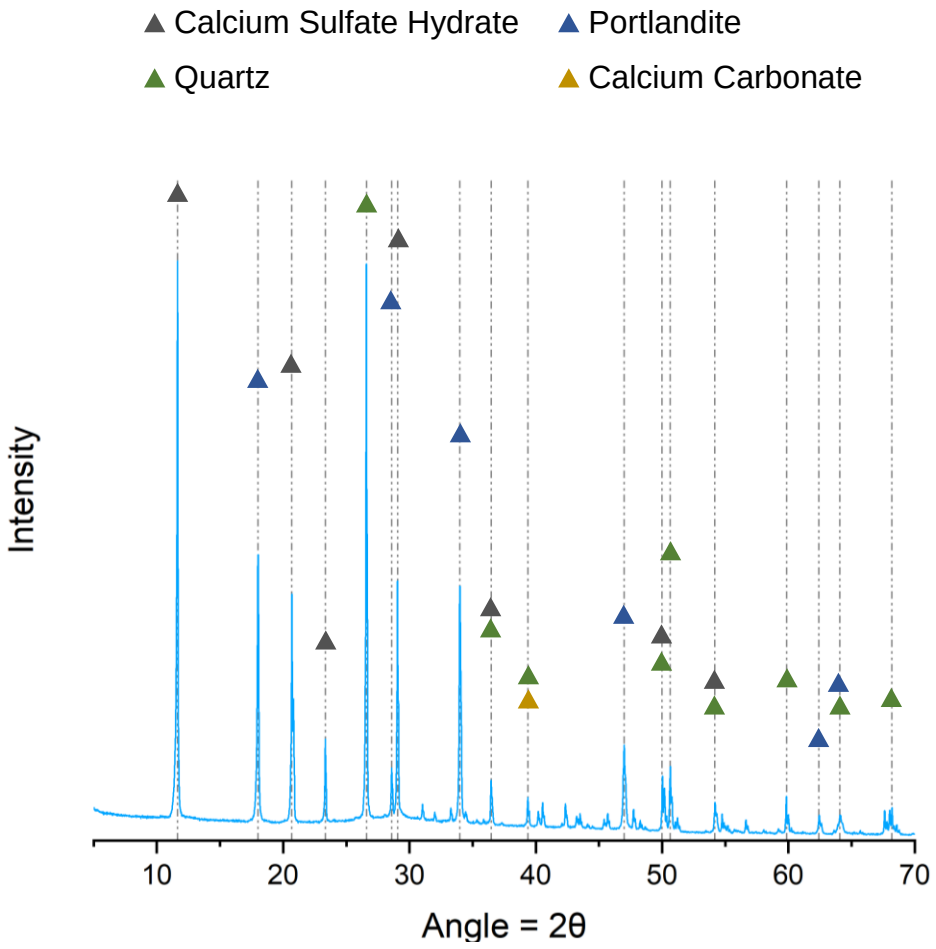


Figure 6.4.4 Diffractogram of quartz hydrated in 0.2M calcium solution and 175mM sulfates, 3 months

In this study, C-S-H + $ is precipitated in the presence of quartz, showing a more ordered agglomeration to samples without quartz, and exhibiting a homogeneous distribution of Ca, Si, and S throughout the sample. TEM results and XRD analysis confirm the presence of hydrate on the surface of the quartz particle, though as observed in the C-A-S-H and C-S-H experiments, quartz dissolves slowly under these conditions and growth on the surface is limited. In all cases, XRD shows the formation of $Ca(OH)_2$.

## 6.4.4 C-S-H + $ & calcite

C-S-H + $ with a Ca:Si of 1.6 was produced in the presence of calcite by dropwise precipitation. TEM micrographs are shown below in Figure 6.4.5. The C-S-H + $ shows a thin, nanofoil morphology, as observed in Figure 5.2.5.

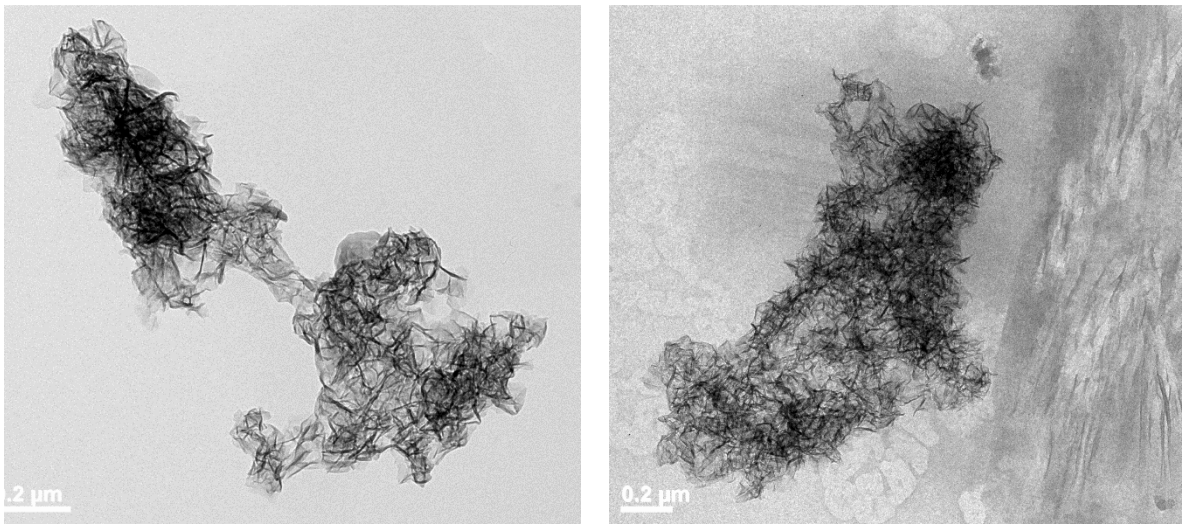


Figure 6.4.5 TEM micrographs of C-S-H + $, Ca:Si = 1.6, 175mM sulfates, produced with 1 wt% quartz

STEM-EDX elemental analysis of the same sample showed homogeneous distribution of Ca, Si, and O in the C-S-H samples with a low intensity of sulfur. Additionally, unreacted sulfates from $Na_2SO_4$ solution are also observed in the sample.

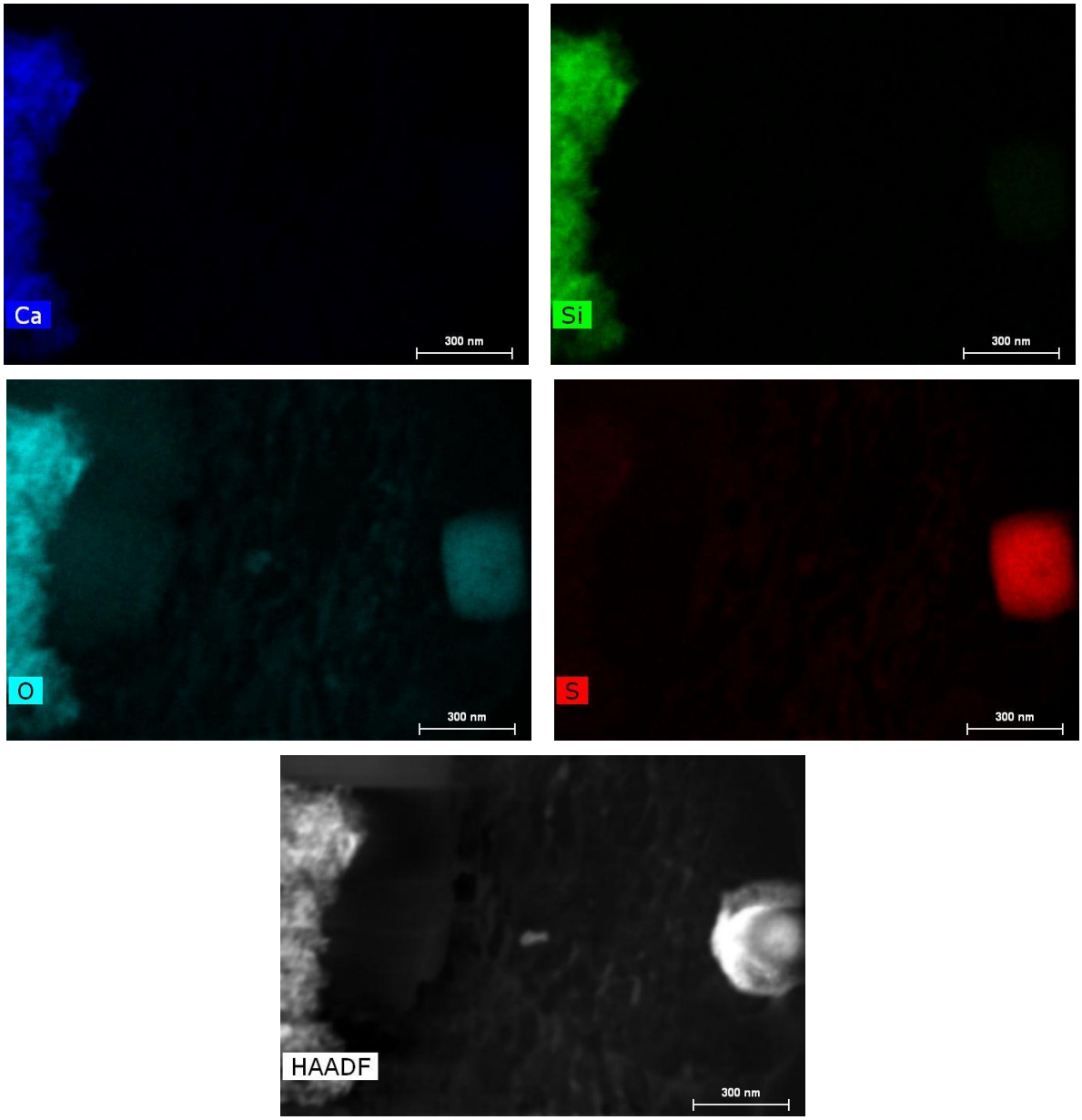


Figure 6.4.6 STEM-EDX images of C-S-H + $, Ca:Si = 1.6, 175mM sulfates, produced with 1 wt% calcite

Calcite was placed in a 0.1 M silicate solution at a pH of 13.4. After 3 days in solution, TEM shows the formation of both sheet and fibrillar C-S-H on the surface of calcite in addition to silicate and sulfate clusters. Fibrils and thin sheets are observed in Figure 6.4.7(a), exhibiting widths up to 400nm, without taking any perceived folding into account. Also, with the addition of sulfates, very long fibrils are observed between 750nm to 2 μm in Figure 6.4.7(b) and Figure 6.4.7(c).

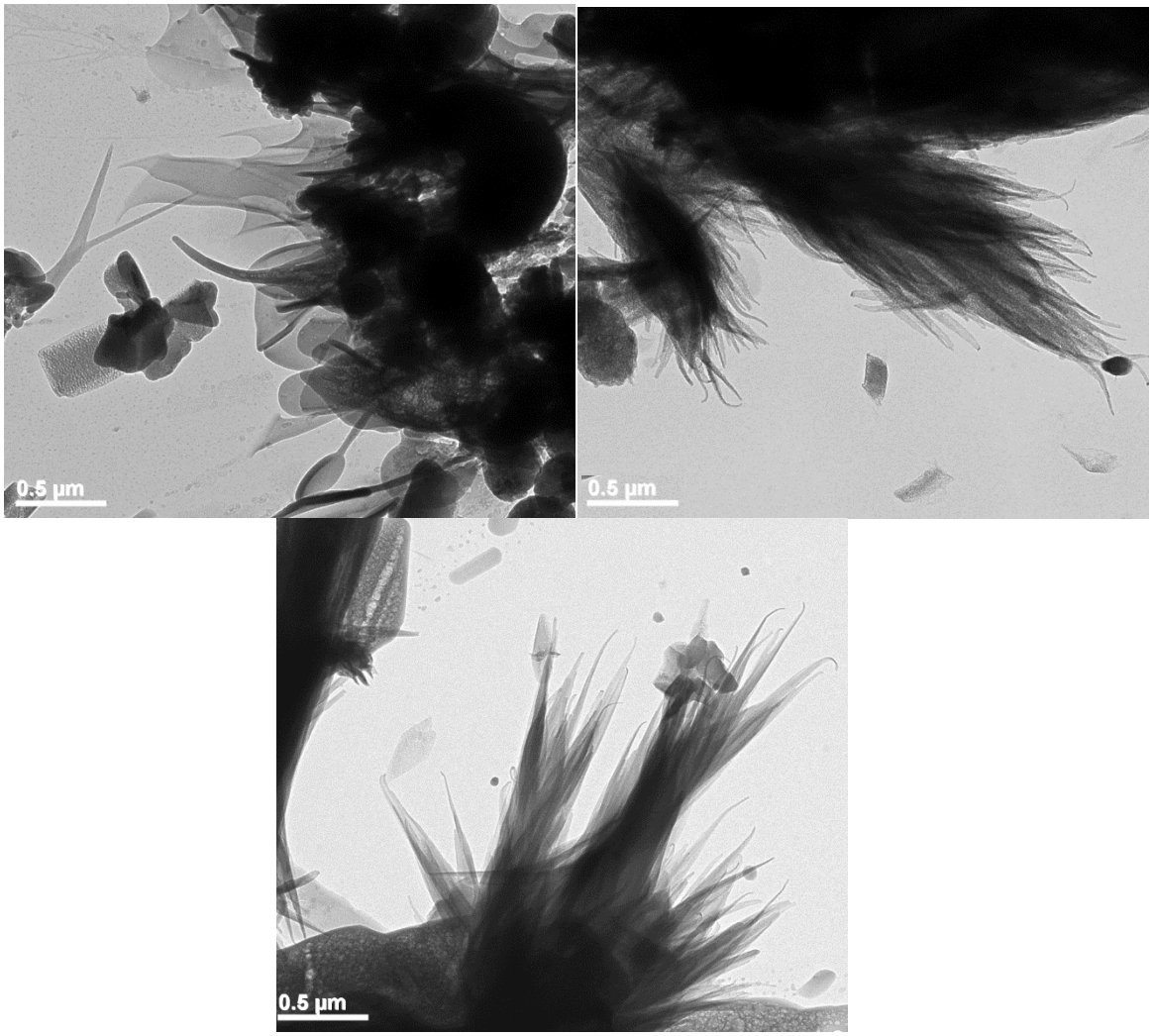


Figure 6.4.7 TEM image of calcite in 0.1 M silicate solution and 175mM $Na_2SO_4$ at 13.4 pH, 3 days

After a week in solution, TEM images show the continued growth of both C-S-H and portlandite. Figure 6.4.8 shows disordered C-S-H fibrils on the surface of calcite. Portlandite is also observed on the ends of C-S-H.

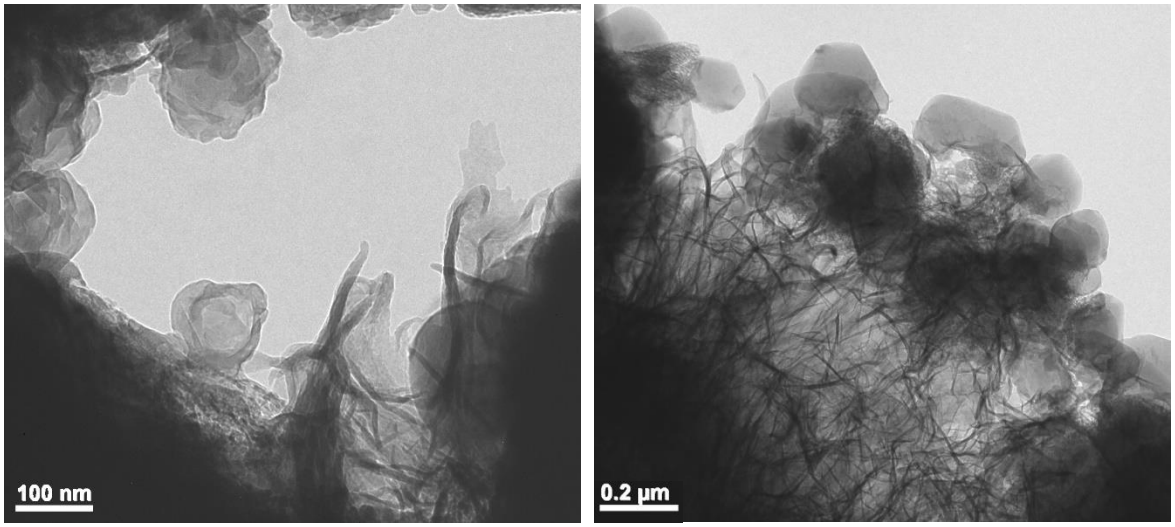


Figure 6.4.8 TEM image of calcite in 0.1M silicate solution and 175mM $Na_2SO_4$ at 13.4 pH, 1 week

After three months, C-S-H + $ samples grown from calcite, exhibited long, ribbon-like morphologies, shown in Figure 6.4.9. Ribbons and fibrils exhibit widths ~200nm and lengths of more than 2 µm. STEM-EDX of the same sample is presented in Figure 6.4.10, showing homogeneous distribution of Ca, Si, O, in addition to light amounts of sulfates which would only be adsorbed on the sample.

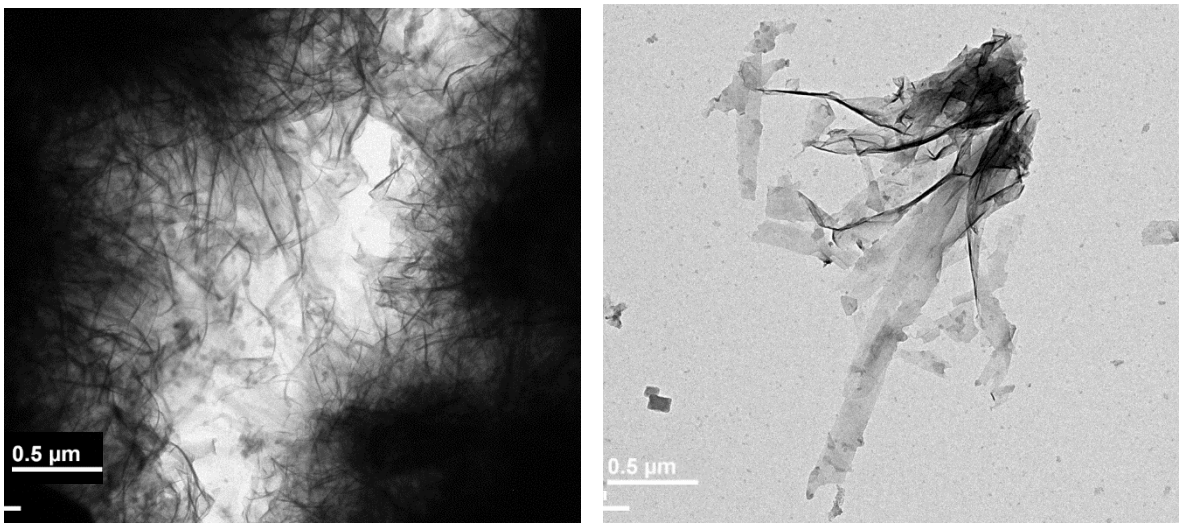


Figure 6.4.9 TEM image of C-S-H grown from calcite in 0.1 silicate solution and 175mM $Na_2SO_4$, 13.4 pH, 3 months

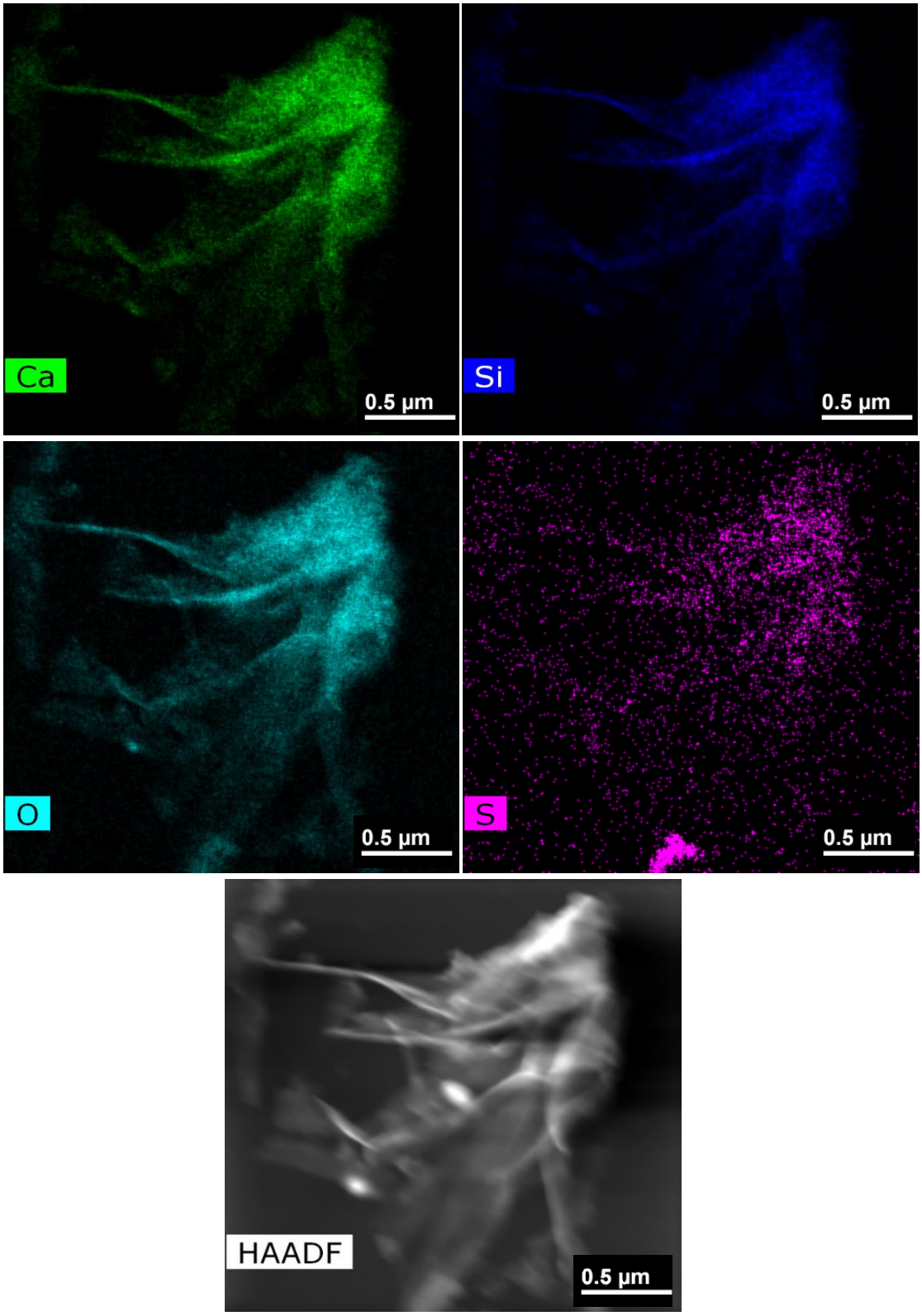


Figure 6.4.10 STEM-EDX elemental images of calcite in 0.1 M silicate solution and 175mM $Na_2SO_4$ at 13.4 pH, 3 months

The observations in this section are consistent with the work by Mota et al. in which hydrated alite was investigated in the presence of NaOH, gypsum, NaOH + gypsum, and $Na_2SO_4$[142]. The latter induced an aggregated, fibrillar structure on the surface of alite, while samples with just NaOH exhibited more of a foil-like structure. This suggests that firstly, the foil-like structure that is observed in synthetic C-S-H systems could be caused by the use of alkali or perhaps just NaOH. To further test this hypothesis, synthetic C-S-H samples produced with KOH rather than NaOH could be studied under the microscope. Secondly, these results show that neither alite nor sulfates are necessary to achieve fibrillar C-S-H. In section 6.2.5, fibrillar C-S-H without the presence of sulfates was formed on the surface of calcite and in the presence of NaOH.

XRD analysis of the sample showed the presence of C-S-H, calcite, calcium sulfate, and thaumasite in the sample after three months.

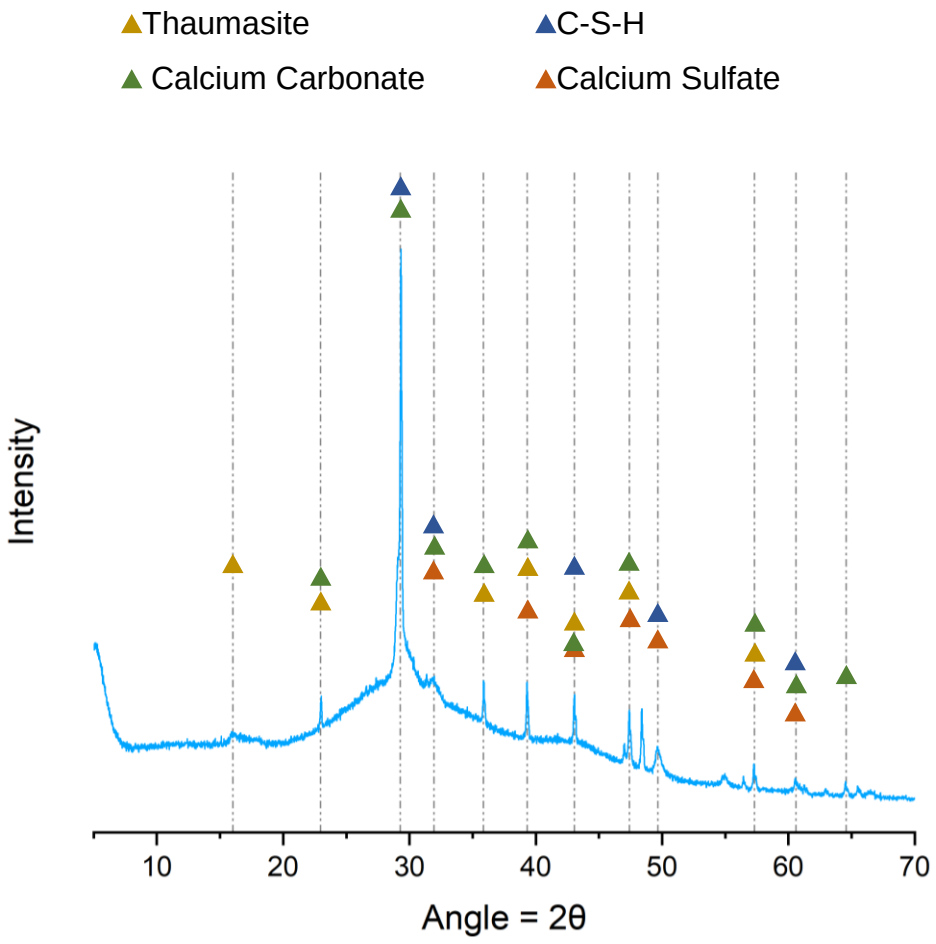


Figure 6.4.11 X-ray diffractogram of calcite after hydration in 0.1M silicate solution and 175 mM $Na_2SO_4$ at 13.4 pH, 3 months

Thermodynamic modelling of the solution at the final measured pH of 13.43 predicts 2.18 grams of C-S-H and 3.0 grams of calcite at equilibrium. Calculated solution species are presented in Figure 6.4.12. Results show high concentrations of free $Na^+$ and $OH^-$ in solution in addition to carbonate ions. Calculations predict little free $Ca^{2+}$ and $CaOH^+$ in solution, both present in the order of $10^{-7}$ mol.

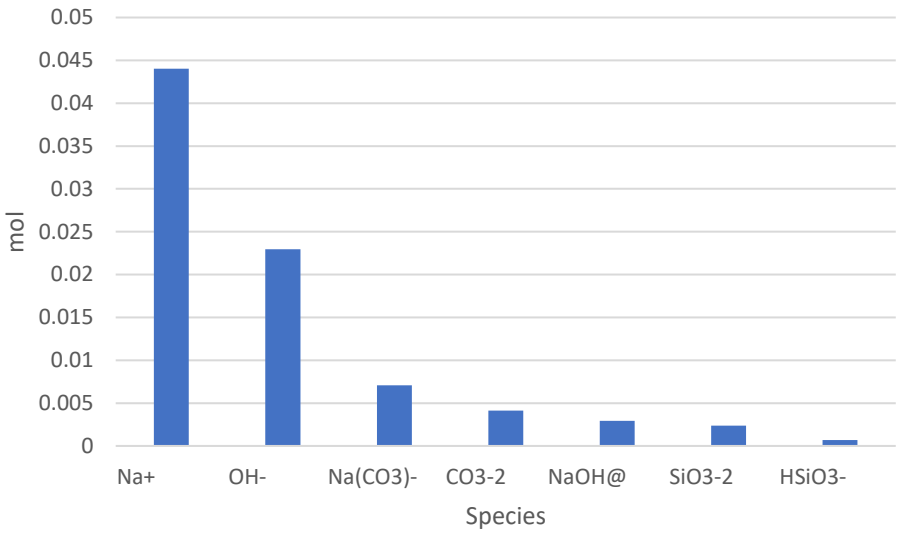


Figure 6.4.12 GEMS-calculated solution species for C-S-H + $ grown from calcite in 0.1 M silicate solution, pH = 13.43

Zeta potential measurements on C-S-H synthesized in the presence of sulfates, calcite, and quartz are plotted in Figure 6.4.13. There is little to no change between C-S-H + $ alone and in the sample with calcite. However, the presence of quartz shows an increase of more than 1 mV, exhibiting similar potentials to those observed with C-A-S-H + quartz. Sulfates are known to adsorb onto the surface of C-S-H, possibly decreasing the potential. However, in order to fully analyze these results, solution concentration data should be measured and species in solution should be calculated.

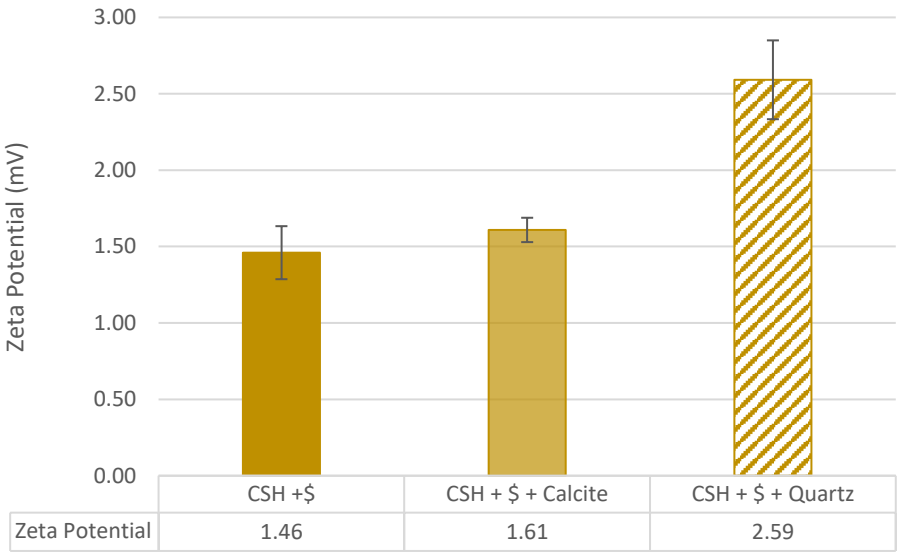


Figure 6.4.13 Zeta potentials of C-S-H + $ produced with dropwise precipitation method, dispersed in 10mM NaOH, 3.125 wt% dispersion, with 1 wt% calcite and 1 wt% quartz, Ca:Si = 1.6. Error bars refer to standard deviation among six measurements of the same sample.

## 6.4.5 Conclusions

In this study, sulfates and heterogeneous substrates are investigated for their effect on C-S-H morphology. C-S-H + $ synthesized in the presence of quartz exhibited disordered nanofoils possibly in a more ordered aggregated structure. Additionally, nanofoils appear to be denser, also observed in C-A-S-H samples in section 6.3. Quartz was placed into a calcium solution with sulfates and exhibited small amounts of hydrate growth on the surface of the substrate. XRD analysis confirmed the presence of a C-S-H phase with sulfates in addition to quartz, carbonation, and portlandite after 3 months.

C-S-H + $ synthesized by dropwise precipitation in the presence of calcite exhibited the frequently observed thin disordered nanofoil morphology. Samples of calcite placed in silicate solution formed long fibrils on the surface of calcite up to 2 μm in length after 3 days. After a week in solution, the fibrils in the sample became denser as more calcite was available in the solution for C-S-H to form. Portlandite was also observed on the ends of the C-S-H fibrils. Finally, after three months in solution, the C-S-H + $ samples showed nanoribbons, some longer than 2 μm in length, and

~200nm in width. X-ray diffractograms confirmed the presence of C-S-H, calcite, and calcium sulfate phases.

Zeta potential measurements of C-S-H + $ with calcite and quartz exhibited little to no change in potential upon synthesis in the presence of calcite. However, the addition of quartz caused a 1 mV (30%) increase of potential.

## 6.5 Conclusions & future work

To summarize, C-S-H with aluminates and sulfates were synthesized by dropwise precipitation in the presence of quartz and calcite as substrates. C-A-S-H samples exhibited little change with the addition of quartz, however with increasing aluminate concentrations, the nanofoils appeared denser in structure. This trend is also observed in C-A-S-H synthesized in the presence of calcite. C-S-H + $ samples exhibited denser morphologies than samples synthesized without quartz, additionally, these hydrates appeared to exhibit a more ordered aggregation. C-S-H + $ samples produced in the presence of calcite showed little difference to the samples with no substrates.

C-S-H, C-A-S-H, and C-S-H + $ showed very small amounts of growth on the surface of quartz, and portlandite was observed on the samples as well. Effectively and immediately, in preparation of this solution $Ca(OH)_2$ is precipitated before quartz can dissolve. With the slow dissolution of quartz, Si is not readily available to drive the formation of C-S-H. From a thermodynamic perspective, the immediate precipitation of portlandite reduces calcium in in solution, which may also slow the dissolution of quartz. After 3 months, the experiment to grow C-A-S-H on the surface of quartz exhibited no hydrate phases in x-ray diffraction, while C-S-H + $ showed the formation of calcium sulfate hydrate.

Calcite, placed in a silicate and aluminum solution showed the precipitation of natrolite after 3 days in solution. Similar to the experiments with quartz in solution, without calcite dissolved, natrolite, a sodium-aluminum-silicate phase, is supersaturated under these conditions and forms upon preparation of the solution. However, after 1 week, the needle-morphologies of natrolite show the presence of calcium in STEM-EDX analysis. After 1 month, the sample exhibited a nanoglobule

structure, and finally after 3 months, the sample exhibited dense nanofoils. Though not necessarily representative of cementitious systems, these experiments showed transformation between morphologies, which is also observed in synthetic C-S-H as the Ca:Si increases from 1 to 1.25[17]. As a result, full characterization of the intermediate points of this experiment—taking pH measurements and solution samples for ICP analysis—would be helpful in better understanding the reason for nanoglobules over nanofoils.

Finally, C-S-H and C-S-H + $ was grown on the surface of calcite, and both samples exhibited fibrillar, and nanoribbon morphologies. C-S-H on the surface of calcite exhibited lengths up to 1 μm, and with the addition of sulfates, lengths of more than 2 μm were observed. In the quest to determine the cause for fibrillar C-S-H, the work in this chapter in combination with studies done by Mota et al. and Zunino show that fibrillar C-S-H is not caused by the presence of aluminates or sulfates. Additionally, Mota et al. suggests that NaOH on alite causes the morphology of hydrates to be more foil-like—this could help explain the morphologies observed in most synthetic C-S-H samples as NaOH is used in high concentration to control Ca:Si. However, all samples in this chapter were produced with the use of NaOH, and the investigation in section 6.2 suggests that NaOH without the presence of $Na_2SO_4$ does not inhibit the fibrillar morphology from forming.

In future work, a method should be developed to achieve high-quality SEM images of C-S-H and C-A-S-H, which proves to be challenging due to interaction between the beam and the sample in addition to coatings being too thick. However, with SEM images, studies can better compare between synthetic C-S-H and the C-S-H on hydrated alite and $C_3S$. Specific surface area measurements of the substrates should also be taken.  Additionally, kinetic data collection over durations longer than 24 hours would help quantify the availability of $Ca^{2+}$ upon the dissolution of calcite and $C_3S$.

In summary, it is very possible that the formation of synthetic fibrillar C-S-H relies on the presence of a substrate, particularly a calcium-containing substrate. It is also very possible that the kinetics of hydrating calcium containing substrate is necessary to form the morphologies observed on the surfaces of alite grains.

# Chapter 7. Summary of the thesis

## 7.1 Final conclusions

The overarching goal of this thesis is to give insight and detailed characterization of synthetic C-S-H, C-A-S-H, and C-S-H + $. Growth, nucleation, composition, structure, and morphology changes in the main hydration product were investigated in response to controlled variations in experimental parameters. This thesis is organized into four different parts to examine single-phase C-S-H and related systems, produced by dropwise precipitation in batch and segmented flow tubular reactors[17], [34].

To begin the thesis, a reproducible method to precipitate high Ca:Si C-S-H was described in Section 3.1 based on the dropwise precipitation method[32]. In this chapter, focus was placed on the mixing requirements to maintain supersaturation of the C-S-H phase whereas portlandite remained undersaturated throughout the entirety of the precipitation process. Population balance modelling of the synthetic C-S-H system consistently predicted the supersaturation of C-S-H and undersaturation of portlandite at all Ca:Si molar ratios, assuming a well-controlled, well mixed system (Section 4.4). In comparing the targeted Ca:Si molar ratios, predicted by thermodynamic modelling, to the ratios measured by ICP-OES and XRF, strong correlation was observed until Ca:Si ratios of 1.8 and above, where higher amounts of calcium were measured on precipitates and similarly less calcium was observed in the supernatants than expected from thermodynamic modelling.

In response, surface properties of C-S-H at different Ca:Si ratios were investigated by acoustophoresis measurements to determine zeta potential at the slipping plane as described in Section 5.1. Results showed that with increasing Ca:Si molar ratio of samples, the zeta potential rises for samples dispersed both in reaction supernatant and 10mM NaOH. However, samples dispersed in supernatants reached considerably higher potentials than those dispersed in NaOH solution. At a pH of 12, C-S-H with Ca:Si of 1.75 exhibited a 13.7 mV potential in supernatant, compared with the 3.41 mV in 10mM NaOH solution. As the pH increases, a supernatant-dispersed sample at a pH of 12.69 gave zeta potentials of 23 mV . The reversibility of calcium adsorption at the surface of C-S-H was also investigated as washed

samples were dispersed in NaOH solution and titrated with calcium. Calcium was found to re-adsorb onto the hydrates; however, only partially. In work by Haas & Nonat, alkali-free Ca:Si = 1.4 C-S-H samples exhibited zeta potentials comparable to the Ca:Si 1.75 samples dispersed in supernatant, indicating that the high concentration of alkali in our systems dispersed in NaOH may limit the reversibility of $Ca^{2+}$ adsorption[111].

Zeta potentials of synthetic C-A-S-H and C-S-H + $ dispersed in 10mM NaOH were comparable to those of C-S-H, are discussed in Section 5.2. At a Ca:Si of 1.75, potentials of samples including aluminates and sulfates were consistently more than 30% less than the zeta potential measured for pure C-S-H. Adsorption of sulfates and the possible incorporation of aluminates into the bridging sites of C-S-H, taking the place of calcium, may help explain the reduced zeta potentials. However, a fuller set of both zeta potential and ICP-OES measurements must be taken to further support such hypotheses.

In Chapter 4, the population balance model was expanded to allow the use of different thermodynamic databases depending on the C-S-H system under investigations. Additionally, calculations were made to compare the supersaturation ratios of C-S-H and portlandite over time throughout the precipitation process, showing that C-S-H remains consistently supersaturated while portlandite remains undersaturated for all Ca:Si between 1 and 2. This was demonstrated experimentally in chapter 3 where pure phase C-S-H was produced at all Ca:Si ratios between 1 and 2. C-S-H and C-S-H + $ at a Ca:Si of 1.75 were further analyzed by the population balance model to see how growth and nucleation changed in comparison to the pure phase Ca:Si = 2 system, previously studied by Andalibi et al[30]. The model parameters were adjusted based on collected experimental kinetic data. Slower kinetic growth rates were measured in the pure phase Ca:Si = 1.75, while the addition of sulfates resulted in a kinetic growth rate 10x higher in magnitude. However, as the population balance model doesn't currently include surface interactions, namely for the adsorption of $Ca^{2+}$ and sulfates, more work needs to be done before conclusions can be made on the mechanisms behind these observed changes. Additionally, the PBEM of C-S-H with the presence of sulfates commonly predicted the formation of portlandite in conjunction with C-S-H, and so in future

work, the population balance model will need to account for more than one solid to better model the sulfate-doped system.

C-S-H undergoes heterogeneous nucleation in applied systems. As a result, studies described in Chapter 6, C-S-H, C-A-S-H, and C-S-H + $ were grown on the surfaces of quartz and calcite in continuation of previous work done by Siramanont[131]. Without the presence of additional substrates, C-S-H, C-A-S-H, and C-S-H + $ all exhibited nanofoil morphologies. More densely agglomerated structures were observed for C-A-S-H samples, and C-S-H + $ exhibited an agglomeration in which the ends stuck out, perpendicular to the surface. Quartz, as a heterogeneous substrate, exhibited a slow dissolution rate, although hydrate was observed to grow the surfaces of the substrate in small quantities. The presence of quartz exhibited possibly ordered aggregation in C-S-H + $ system, which was not observed in C-S-H or C-A-S-H samples. C-S-H and C-S-H + $ samples grown on calcite exhibited fibrillar morphologies more commonly observed in applied cementitious materials with lengths up to 1 μm and 2 μm, respectively.

Calcite placed in a silicate solution with aluminates exhibited C-A-S-H growth after three months in solution. However, these samples showed phase transformations as natrolite, a sodium-aluminum-silicate needle-like mineral formed initially at the surface of calcite. Over the next months, calcium was observed to incorporate into the natrolite needles first, nanoglobules with Ca, Si, O, and Al formed, and finally a dense nanofoil C-A-S-H formed, corroborated by XRD measurements, displaying the transitive properties of C-S-H morphology as solution conditions change as observed by other groups in the literature[137], [139].

The effects of relative humidity and Ca:Si on interlayer spacing and free water in synthetic C-S-H samples as reported in Section 3.2. Samples exhibited a small increase in interlayer spacing with relative humidity. Between samples produced by precipitation in a batch reactor and in the segmented flow tubular reactor (SFTR), higher spacings were observed in the SFTR, ranging up to 13.9Å for a Ca:Si = 1.5, comparable to the 14Å tobermorite, which has often served as the base for the atomistic C-S-H structure[17], [18]. No trends between Ca:Si and interlayer distance were observed as often suggested in the literature. This suggests that drying

conditions could be playing a significant role and perhaps influencing the interlayer spacing more than is recognized in the literature.

Much work is left to do in order to fully understand C-S-H. This thesis focuses on a simplified system in which small changes to the main hydration product are made in an effort to better understand the structure, composition, nucleation, growth, and effect of sulfates, and aluminates on C-S-H. With better understanding of the simplified C-S-H system, the effect of SCMs, sulfates, and other additives on Portland cement can be better understood with the goal of optimizing sustainability of cements in the future.

## 7.2 Future perspectives

As industrialization continues to rise and as Portland cement and its derivatives are used at higher rates, the synthetic C-S-H system paves a promising pathway to understand and control how slight changes to cement may change the main hydration phase. Synthetic C-S-H, particularly at high Ca:Si molar ratios, gives the opportunity to investigate the effect of individual parameters on the main hydration phase. And there is a plethora of avenues to follow in order to fully understand C-S-H, only a few of which were studied in this thesis.

Pore solution has been observed to have a large effect on C-S-H structure and morphology among other parameters. In this thesis, an extensive study was done on the effect of solutions on zeta potential and surface charge density, and this work is planned to be continued by atomistic-level modelling of the C-S-H surface in order to understand the surface terminations of C-S-H in addition to the electrical double layer and the surface itself. This work is currently underway in collaboration with Mr. Ziga Casar (EPFL) who is studying the surfaces of C-S-H at an atomistic-level as it pertains to water and calcium at the surface of C-S-H. Simplified experiments in which solution data and zeta potential measurements are taken on the synthetic C-S-H system can be done for other pertinent ions including $Cl^-$, $Zn^{2+}$, and $Mg^{2+}$. This will allow the validation of the atomistic modelling and allow them to be used to create links between C-S-H structure, surface properties, and eventually transport properties of great importance for the durability and consequently sustainability of blended cements.

With the insights gained from Chapter 4 on collecting kinetic data and using the population balance equation model, work can be continued on modelling the growth and nucleation of C-S-H. The first line of work falls on compiling a surface complexation model for C-S-H. This would allow better understanding of the work already done with the population balance equation model and facilitate further uses of the model as different variations of C-S-H are studied. The next steps will require adjusting the mass balances built into the model so as to account for both surfaces, via surface complexation models, and the presence of more than one solid. Finally, data collection for C-A-S-H should be done in the future. At current, the most promising route is to pump aluminum silicate and sodium silicate solution into calcium solution in the reactor—minimizing the chance for aluminum interference on the electrode. Thermodynamic modelling also shows that at pH values > 13.3 natrolite is undersaturated, and so high ratio C-A-S-H could be studied with this method.

The introduction of heterogeneous substrates provides an intriguing new line of questions as fibrillar C-S-H and C-S-H + $ was consistently obtained at pHs > 13.3. As this work is continued, CryoTEM and tomography experiments would help determine the exact morphologies obtained in both separated and aggregated particles. Additionally, producing fibrillar C-S-H on the surface of calcite, and adding different admixtures or elements under the microscope may aid with understanding the individual effects of certain ions on morphology, structure, and also kinetics of formation of the main hydration phase, C-S-H.

# References

[1] IEA, “Tracking cement 2020,” 2020. https://www.iea.org/reports/tracking-cement-2020 (accessed May 24, 2022).

[2] T. Czigler, S. Reiter, P. Schulze, and K. Somers, “Laying the foundation for zero-carbon cement,” 2020. [Online]. Available: https://www.mckinsey.com/industries/chemicals/our-insights/laying-the-foundation-for-zero-carbon-cement

[3] H. F. W. Taylor, Cement chemistry. Thomas Telford Publishing, 1997. doi: 10.1680/cc.25929.

[4] B. Lothenbach, K. Scrivener, and R. D. Hooton, “Supplementary cementitious materials,” Cem. Concr. Res., vol. 41, no. 12, pp. 1244–1256, Dec. 2011, doi: 10.1016/j.cemconres.2010.12.001.

[5] R. T. Kreh, Masonry Skills. Cengage Learning, 2014. [Online]. Available: https://books.google.ch/books?id=4Vw8AwAAQBAJ

[6] J. Bensted, “Hydration of Portland cement,” in Advances in Cement Technology, Elsevier, 1983, pp. 307–347. doi:10.1016/b978-0-08-028670-9.50015-6.

[7] K. L. Scrivener and A. Nonat, “Hydration of cementitious materials, present and future,” Cem. Concr. Res., vol. 41, no. 7, pp. 651–665, Jul. 2011, doi: 10.1016/j.cemconres.2011.03.026.

[8] “Hydration of Portland cement,” in Structure and performance of cements, CRC Press, 2002, pp. 75–131. doi: 10.1201/9781482295016-9.

[9] P. Juilland, E. Gallucci, R. Flatt, and K. Scrivener, “Dissolution theory applied to the induction period in alite hydration,” Cem. Concr. Res., vol. 40, no. 6, pp. 831–844, Jun. 2010, doi: 10.1016/j.cemconres.2010.01.012.

[10] I. G. Richardson, “The nature of C-S-H in hardened cements,” Cem. Concr. Res., vol. 29, no. 8, pp. 1131–1147, Aug. 1999, doi: 10.1016/s0008-8846(99)00168-4.

[11] B. Lothenbach and A. Nonat, “Calcium-silicate-hydrates: Solid and liquid phase composition,” Cem. Concr. Res., vol. 78, pp. 57–70, Dec. 2015, doi: 10.1016/j.cemconres.2015.03.019.

[12] E. L’Hôpital, B. Lothenbach, D. A. Kulik, and K. Scrivener, “Influence of calcium to silica ratio on aluminum uptake in calcium-silicate-hydrate,” Cem. Concr. Res., vol. 85, pp. 111–121, Jul. 2016, doi: 10.1016/j.cemconres.2016.01.014.

[13] K. Fujii and W. Kondo, “Heterogeneous equilibrium of calcium-silicate-hydrate in water at 30C,” J. Chem. Soc., Dalt. Trans., no. 2, pp. 645–651, 1981, doi: 10.1039/dt9810000645.

[14] X. Cong and R. J. Kirkpatrick, “$^{29}$Si MAS NMR study of the structure of calcium-silicate-hydrate,” Adv. Cem. Based Mater., 2002, doi: 10.1016/s1065-7355(96)90046-2.

[15] A. C. A. Muller, K. L. Scrivener, A. M. Gajewicz, and P. J. McDonald, “Densification of C-S-H Measured by $^{1}$H NMR relaxometry,” J. Phys. Chem. C, vol. 117, no. 1, pp. 403–412, Dec. 2012, doi: 10.1021/jp3102964.

[16] J. J. Beaudoin, V. S. Ramachandran, and R. F. Feldman, “Interaction of chloride and C-S-H,” Cem. Concr. Res., vol. 20, no. 6, pp. 875–883, Nov. 1990, doi: 10.1016/0008-8846(90)90049-4.

[17] A. Kumar et al., “The atomic-level structure of cementitious calcium-silicate-hydrate,” J. Phys. Chem. C, vol. 121, no. 32, pp. 17188–17196, Jul. 2017, doi: 10.1021/acs.jpcc.7b02439.

[18] A. K. Mohamed et al., “The atomic-level structure of cementitious calcium aluminate silicate hydrate,” J. Am. Chem. Soc., vol. 142, no. 25, pp. 11060–11071, May 2020, doi: 10.1021/jacs.0c02988.

[19] F. Brunet, P. Bertani, T. Charpentier, A. Nonat, and J. Virlet, “Application of $^{29}$Si homonuclear and $^{1}$H- $^{29}$Si heteronuclear NMR correlation to structural studies of calcium-silicate-hydrates,” J. Phys. Chem. B, vol. 108, no. 40, pp. 15494–15502, Sep. 2004, doi: 10.1021/jp031174g.

[20] A. Nonat, “The structure and stoichiometry of C-S-H,” Cem. Concr. Res., vol. 34, no. 9, pp. 1521–1528, Sep. 2004, doi: 10.1016/j.cemconres.2004.04.035.

[21] S. Galmarini, “Atomistic simulation of cementitious systems,” Ecole Polytechnique Federale de Lausanne, 2013. doi: 10.5075/epfl-thesis-5754.

[22] A. K. Mohamed, S. C. Parker, P. Bowen, and S. Galmarini, “An atomistic building block description of C-S-H - Towards a realistic C-S-H model,” Cem. Concr. Res., vol. 107, pp. 221–235, May 2018, doi: 10.1016/j.cemconres.2018.01.007.

[23] J. J. Chen, J. J. Thomas, H. F. W. Taylor, and H. M. Jennings, “Solubility and structure of calcium-silicate-hydrate,” Cem. Concr. Res., vol. 34, no. 9, pp. 1499–1519, Sep. 2004, doi: 10.1016/j.cemconres.2004.04.034.

[24] I. G. Richardson, “Model structures for C-(A)-S-H(I),” Acta Crystallogr. Sect. B Struct. Sci. Cryst. Eng. Mater., vol. 70, no. 6, pp. 903–923, Nov. 2014, doi: 10.1107/s2052520614021982.

[25] E. T. Rodriguez, I. G. Richardson, L. Black, E. Boehm-Courjault, A. Nonat, and J. Skibsted, “Composition, silicate anion structure and morphology of calcium-silicate-hydrates (C-S-H) synthesized by silica-lime reaction and by controlled hydration of tricalcium silicate ($C_3S$),” Adv. Appl. Ceram., vol. 114, no. 7, pp. 362–371, Oct. 2015, doi: 10.1179/1743676115y.0000000038.

[26] E. Gallucci, X. Zhang, and K. L. Scrivener, “Effect of temperature on the microstructure of calcium-silicate-hydrate (C-S-H),” Cem. Concr. Res., vol. 53, pp. 185–195, Nov. 2013, doi: 10.1016/j.cemconres.2013.06.008.

[27] W. Kunther, S. Ferreiro, and J. Skibsted, “Influence of the Ca/Si ratio on the compressive strength of cementitious calcium-silicate-hydrate binders,” J. Mater. Chem. A, vol. 5, no. 33, pp. 17401–17412, 2017, doi: 10.1039/c7ta06104h.

[28] S.-J. Ding, M.-Y. Shie, and C.-Y. Wang, “Novel fast-setting calcium silicate bone cements with high bioactivity and enhanced osteogenesis in vitro,” J. Mater. Chem., vol. 19, no. 8, p. 1183, 2009, doi: 10.1039/b819033j.

[29] M. M. Abdalla, C. Y. K. Lung, P. Neelakantan, and J. P. Matinlinna, “A novel, doped calcium silicate bioceramic synthesized by sol-gel method: Investigation of setting time and biological properties,” J. Biomed. Mater. Res. Part B Appl. Biomater., vol. 108, no. 1, pp. 56–66, Mar. 2019, doi: 10.1002/jbm.b.34365.

[30] M. R. Andalibi et al., “On the mesoscale mechanism of synthetic calcium-silicate-hydrate precipitation: a population balance modeling approach,” J. Mater. Chem. A, vol. 6, no. 2, pp. 363–373, 2018, doi: 10.1039/c7ta08784e.

[31] M. R. Andalibi, P. Bowen, A. Carino, and A. Testino, “Global uncertainty-sensitivity analysis on mechanistic kinetic models: From model assessment to theory-driven design of nanoparticles,” Comput. & Chem. Eng., vol. 140, p. 106971, Sep. 2020, doi: 10.1016/j.compchemeng.2020.106971.

[32] M. Harris, G. Simpson, K. Scrivener, and P. Bowen, “A method for the reliable and reproducible precipitation of phase pure high Ca/Si ratio (>1.5) synthetic calcium-silicate-hydrates (C-S-H),” Cem. Concr. Res., vol. 151, p. 106623, Jan. 2022, doi: 10.1016/j.cemconres.2021.106623.

[33] A. Ouzia and K. Scrivener, “The needle model: A new model for the main hydration peak of alite,” Cem. Concr. Res., vol. 115, pp. 339–360, Jan. 2019, doi: 10.1016/j.cemconres.2018.08.005.

[34] A. Aimable, T. Strachowski, E. Wolska, W. Lojkowski, and P. Bowen, “Comparison of two innovative precipitation systems for ZnO and Al-doped ZnO nanoparticle synthesis,” Process. Appl. Ceram., vol. 4, no. 3, pp. 107–114, 2010, doi: 10.2298/pac1003107a.

[35] D. A. Kulik et al., “GEM-Selektor geochemical modeling package: revised algorithm and GEMS3K numerical kernel for coupled simulation codes,” Comput. Geosci., Aug. 2012, doi: 10.1007/s10596-012-9310-6.

[36] T. Wagner, D. A. Kulik, F. F. Hingerl, and S. V Dmytrieva, “GEM-Selektor geochemical modeling package: TSolMod library and data interface for multicomponent phase models,” Can. Mineral., vol. 50, no. 5, pp. 1173–1195, Oct. 2012, doi: 10.3749/canmin.50.5.1173.

[37] D. L. Parkhurst and C. A. J. Appelo, “Description of input and examples for PHREEQC version 3: a computer program for speciation, batch-reaction, one-dimensional transport, and inverse geochemical calculations.” US Geological Survey, 2013. doi: 10.3133/tm6a43.

[38] B. Lothenbach et al., “Cemdata18: A chemical thermodynamic database for hydrated Portland cements and alkali-activated materials,” Cem. Concr. Res., vol. 115, pp. 472–506, Jan. 2019, doi: 10.1016/j.cemconres.2018.04.018.

[39] W. Hummel, U. Berner, E. Curti, F. J. Pearson, and T. Thoenen, “Nagra/PSI chemical thermodynamic data base 01/01,” Radiochim. Acta, vol. 90, no. 9–11, pp. 805–813, Sep. 2002, doi: 10.1524/ract.2002.90.9-11_2002.805.

[40] “Lawrence Livermore National Laboratory (LNLL) Open Data Initiative,” 2020. doi: https://doi.org/10.6075/J0HD7T2Q.

[41] “Ion-Selective Electrode,” Mettler Toledo. https://www.mt.com/int/en/home/products/Laboratory_Analytics_Browse/pH-meter/sensor/ion-selective-electrode.html (accessed May 13, 2022).

[42] A. M. Neville, “Properties of concrete,” 2011, Accessed: Jun. 08, 2022. [Online]. Available: https://books.google.com/books/about/Properties_of_Concrete.html?id=vsztgAEACAAJ

[43] M. A. SAGHIRI et al., “Calcium silicate-based cements and functional impacts of various constituents,” Dent. Mater. J., vol. 36, no. 1, pp. 8–18, 2017, doi: 10.4012/dmj.2015-425.

[44] C.-C. Chen, C.-C. Ho, C.-H. D. Chen, and S.-J. Ding, “Physicochemical Properties of calcium silicate cements for endodontic treatment,” J. Endod., vol. 35, no. 9, pp. 1288–1291, Sep. 2009, doi: 10.1016/j.joen.2009.05.036.

[45] Z.-Q. Wu and J. F. Young, “The hydration of tricalcium silicate in the presence of colloidal silica,” J. Mater. Sci., vol. 19, no. 11, pp. 3477–3486, Nov. 1984, doi: 10.1007/bf02396922.

[46] P. S. Roller and G. Ervin, “The system calcium oxide-silica-water at 30°.The association of silicate ion in dilute alkaline solution,” J. Am. Chem. Soc., vol. 62, no. 3, pp. 461–471, Mar. 1940, doi: 10.1021/ja01860a001.

[47] S. A. Greenberg and T. N. Chang, “Investigation of the colloidal hydrated calcium silicates. II. Solubility relationships in the calcium oxide-silica-water system at 25°,” J. Phys. Chem., vol. 69, no. 1, pp. 182–188, Jan. 1965, doi: 10.1021/j100885a027.

[48] J. E. Rossen, B. Lothenbach, and K. L. Scrivener, “Composition of C-S-H in pastes with increasing levels of silica fume addition,” Cem. Concr. Res., vol. 75, pp. 14–22, Sep. 2015, doi: 10.1016/j.cemconres.2015.04.016.

[49] G. L. Kalousek, “Studies of portions of the quaternary system soda-lime-silica-water at 25 degrees C,” J. Res. Natl. Bur. Stand. (1934)., vol. 32, no. 6, p. 285, Jun. 1944, doi: 10.6028/jres.032.015.

[50] I. G. Lodeiro, A. Fernández-Jimenez, A. Palomo, and D. E. Macphee, “Effect on fresh C-S-H gels of the simultaneous addition of alkali and aluminium,” Cem. Concr. Res., vol. 40, no. 1, pp. 27–32, Jan. 2010, doi: 10.1016/j.cemconres.2009.08.004.

[51] R. Snellings, “X-ray powder diffraction applied to cement,” A Pract. Guid. to Microstruct. Anal. Cem. Mater., pp. 126–195, Jan. 2018, doi: 10.1201/B19074-4.

[52] B. Lothenbach, P. Durdziński, and K. De Weerdt, “Thermogravimetric analysis,” A Pract. Guid. to Microstruct. Anal. Cem. Mater., pp. 177–211, Jan. 2016, doi: 10.1201/B19074-6.

[53] C. Labbez, B. Jönsson, I. Pochard, A. Nonat, and B. Cabane, “Surface charge density and electrokinetic potential of highly charged minerals: Experiments and Monte Carlo simulations on calcium-silicate-hydrate,” J. Phys. Chem. B, vol. 110, no. 18, pp. 9219–9230, Apr. 2006, doi: 10.1021/jp057096+.

[54] F. Baillon, F. Espitalier, C. Cogné, R. Peczalski, and O. Louisnard, “Crystallization and freezing processes assisted by power ultrasound,” in Power Ultrasonics, Elsevier, 2015, pp. 845–874. doi: 10.1016/b978-1-78242-028-6.00028-4.

[55] G. Geng, R. J. Myers, M. J. A. Qomi, and P. J. M. Monteiro, “Densification of the interlayer spacing governs the nanomechanical properties of calcium-silicate-hydrate,” Sci. Rep., vol. 7, no. 1, Sep. 2017, doi: 10.1038/s41598-017-11146-8.

[56] R. Shahsavari, M. J. Buehler, R. J.-M. Pellenq, and F.-J. Ulm, “First-principles study of elastic constants and interlayer interactions of complex hydrated oxides: case study of tobermorite and jennite,” J. Am. Ceram. Soc., vol. 92, no. 10, pp. 2323–2330, Oct. 2009, doi: 10.1111/j.1551-2916.2009.03199.x.

[57] J. E. Oh, S. M. Clark, H.-R. Wenk, and P. J. M. Monteiro, “Experimental determination of bulk modulus of 14Å tobermorite using high pressure synchrotron

X-ray diffraction," Cem. Concr. Res., vol. 42, no. 2, pp. 397–403, Feb. 2012, doi: 10.1016/j.cemconres.2011.11.004.

[58] G. Renaudin, J. Russias, F. Leroux, F. Frizon, and C. Cau-dit-Coumes, "Structural characterization of C-S-H and C-A-S-H samples-Part I: Long-range order investigated by Rietveld analyses," J. Solid State Chem., vol. 182, no. 12, pp. 3312–3319, Dec. 2009, doi: 10.1016/j.jssc.2009.09.026.

[59] H. F. W. Taylor, "Relationships between calcium silicates and clay minerals," Clay Miner., vol. 3, no. 16, pp. 98–111, 1956, doi: 10.1180/claymin.1956.003.16.06.

[60] D. Sugiyama, "Chemical alteration of calcium-silicate-hydrate (C-S-H) in sodium chloride solution," Cem. Concr. Res., vol. 38, no. 11, pp. 1270–1275, Nov. 2008, doi: 10.1016/j.cemconres.2008.06.002.

[61] K. Garbev, G. Beuchle, M. Bornefeld, L. Black, and P. Stemmermann, "Cell dimensions and composition of nanocrystalline calcium-silicate-hydrate solid solutions. Part 1: Synchrotron-based X-ray diffraction," J. Am. Ceram. Soc., vol. 91, no. 9, pp. 3005–3014, Sep. 2008, doi: 10.1111/j.1551-2916.2008.02484.x.

[62] I. Maruyama, T. Ohkubo, T. Haji, and R. Kurihara, "Dynamic microstructural evolution of hardened cement paste during first drying monitored by 1H NMR relaxometry," Cem. Concr. Res., vol. 122, pp. 107–117, Aug. 2019, doi: 10.1016/j.cemconres.2019.04.017.

[63] C. Roosz et al., "Distribution of water in synthetic calcium-silicate-hydrates," Langmuir, vol. 32, no. 27, pp. 6794–6805, Jun. 2016, doi: 10.1021/acs.langmuir.6b00878.

[64] J. J. Thomas et al., "Modeling and simulation of cement hydration kinetics and microstructure development," Cem. Concr. Res., vol. 41, no. 12, pp. 1257–1278, Dec. 2011, doi: 10.1016/j.cemconres.2010.10.004.

[65] J. Frenkel, “A general theory of heterophase fluctuations and pretransition phenomena,” J. Chem. Phys., vol. 7, no. 7, pp. 538–547, Jul. 1939, doi: 10.1063/1.1750484.

[66] M. Volmer and A. Weber, “Keimbildung in übersättigten Gebilden,” Zeitschrift für Phys. Chemie, vol. 119U, no. 1, pp. 277–301, Jan. 1926, doi: 10.1515/zpch-1926-11927.

[67] S. Karthika, T. K. Radhakrishnan, and P. Kalaichelvi, “A review of classical and nonclassical nucleation theories,” Cryst. Growth & Des., vol. 16, no. 11, pp. 6663–6681, Oct. 2016, doi: 10.1021/acs.cgd.6b00794.

[68] A. Carino, A. Testino, M. R. Andalibi, F. Pilger, P. Bowen, and C. Ludwig, “Thermodynamic-kinetic precipitation modeling. A case study: The amorphous calcium carbonate (ACC) precipitation pathway unraveled,” Cryst. Growth & Des., vol. 17, no. 4, pp. 2006–2015, Mar. 2017, doi: 10.1021/acs.cgd.7b00006.

[69] S. Rigopoulos, “Population balance modelling of polydispersed particles in reactive flows,” Prog. Energy Combust. Sci., vol. 36, no. 4, pp. 412–443, Aug. 2010, doi: 10.1016/j.pecs.2009.12.001.

[70] A. Testino, V. Buscaglia, M. T. Buscaglia, M. Viviani, and P. Nanni, “Kinetic modeling of aqueous and hydrothermal synthesis of barium titanate ($BaTiO_3$),” Chem. Mater., vol. 17, no. 21, pp. 5346–5356, Sep. 2005, doi: 10.1021/cm051119f.

[71] D. L. Marchisio and R. O. Fox, Computational models for polydisperse particulate and multiphase systems. Cambridge University Press, 2009. doi: 10.1017/cbo9781139016599.

[72] J. C. Wheeler, “Modified moments and Gaussian quadratures,” Rocky Mt. J. Math., vol. 4, no. 2, Jun. 1974, doi: 10.1216/rmj-1974-4-2-287.

[73] R. A. Sack and A. F. Donovan, “An algorithm for Gaussian quadrature given modified moments,” Numer. Math., vol. 18, no. 5, pp. 465–478, Oct. 1971, doi: 10.1007/bf01406683.

[74] R. G. Gordon, “Error bounds in equilibrium statistical mechanics,” J. Math. Phys., vol. 9, no. 5, pp. 655–663, May 1968, doi: 10.1063/1.1664624.

[75] A. Lewis, M. M. Seckler, H. Kramer, and G. van Rosmalen, Industrial crystallization. Cambridge University Press, 2015. doi: 10.1017/cbo9781107280427.

[76] A. E. Nielsen, “Electrolyte crystal growth mechanisms,” J. Cryst. Growth, vol. 67, no. 2, pp. 289–310, Jul. 1984, doi: 10.1016/0022-0248(84)90189-1.

[77] D. Kashchiev, “Nucleation theorem,” in Nucleation, Elsevier, 2000, pp. 58–69. doi: 10.1016/b978-075064682-6/50006-8.

[78] R. J.-M. Pellenq, N. Lequeux, and H. van Damme, “Engineering the bonding scheme in C-S-H: The iono-covalent framework,” Cem. Concr. Res., vol. 38, no. 2, pp. 159–174, Feb. 2008, doi: 10.1016/j.cemconres.2007.09.026.

[79] B. Jönsson, A. Nonat, C. Labbez, B. Cabane, and H. Wennerström, “Controlling the cohesion of cement paste,” Langmuir, vol. 21, no. 20, pp. 9211–9221, Sep. 2005, doi: 10.1021/la051048z.

[80] B. Jönsson, H. Wennerström, A. Nonat, and B. Cabane, “Onset of cohesion in cement paste,” Langmuir, vol. 20, no. 16, pp. 6702–6709, Jun. 2004, doi: 10.1021/la0498760.

[81] H. M. Jennings, “A model for the microstructure of calcium-silicate-hydrate in cement paste,” Cem. Concr. Res., vol. 30, no. 1, pp. 101–116, Jan. 2000, doi: 10.1016/s0008-8846(99)00209-4.

[82] E. Berodier and K. Scrivener, “Understanding the filler effect on the nucleation and growth of C-S-H,” J. Am. Ceram. Soc., vol. 97, no. 12, pp. 3764–3773, Aug. 2014, doi: 10.1111/jace.13177.

[83] A. Quennoz and K. L. Scrivener, “Interactions between alite and $C_3A$-gypsum hydrations in model cements,” Cem. Concr. Res., vol. 44, pp. 46–54, Feb. 2013, doi: 10.1016/j.cemconres.2012.10.018.

[84] F. Zunino and K. Scrivener, “The influence of the filler effect on the sulfate requirement of blended cements,” Cem. Concr. Res., vol. 126, p. 105918, Dec. 2019, doi: 10.1016/j.cemconres.2019.105918.

[85] K. Scrivener et al., “Impacting factors and properties of limestone calcined clay cements ($LC^3$),” Green Mater., vol. 7, no. 1, pp. 3–14, Mar. 2019, doi: 10.1680/jgrma.18.00029.

[86] M. Antoni, J. Rossen, F. Martirena, and K. Scrivener, “Cement substitution by a combination of metakaolin and limestone,” Cem. Concr. Res., vol. 42, no. 12, pp. 1579–1589, Dec. 2012, doi: 10.1016/j.cemconres.2012.09.006.

[87] I. De la Varga, J. Castro, D. P. Bentz, F. Zunino, and J. Weiss, “Evaluating the hydration of high volume fly ash mixtures using chemically inert fillers,” Constr. Build. Mater., vol. 161, pp. 221–228, Feb. 2018, doi: 10.1016/j.conbuildmat.2017.11.132.

[88] M. D. Niemuth, L. Barcelo, and J. Weiss, “Effect of fly ash on optimum sulfate levels measured using heat and strength at early sges,” Adv. Civ. Eng. Mater., vol. 1, no. 1, p. 20120012, Nov. 2012, doi: 10.1520/acem20120012.

[89] H. P. S. G. (Editor); L. M. (Editor); P. K. (Editor) Barbarulo Rémi; Peycelon, “Experimental study and modelling of sulfate sorption on calcium-silicate-hydrates,” Annales de chimie (Paris. 1914). 2003.

[90] R. S. Gollop and H. F. W. Taylor, “Microstructural and microanalytical studies of sulfate attack. I. Ordinary Portland cement paste,” Cem. Concr. Res., vol. 22, no. 6, pp. 1027–1038, Nov. 1992, doi: 10.1016/0008-8846(92)90033-r.

[91] E. Gallucci, P. Mathur, and K. Scrivener, “Microstructural development of early age hydration shells around cement grains,” Cem. Concr. Res., vol. 40, no. 1, pp. 4–13, Jan. 2010, doi: 10.1016/j.cemconres.2009.09.015.

[92] E. Berodier and K. Scrivener, “Evolution of pore structure in blended systems,” Cem. Concr. Res., vol. 73, pp. 25–35, Jul. 2015, doi: 10.1016/j.cemconres.2015.02.025.

[93] R. J. Myers, S. A. Bernal, and J. L. Provis, “A thermodynamic model for C-(N-)A-S-H gel: CNASH-ss. Derivation and validation,” Cem. Concr. Res., vol. 66, pp. 27–47, Dec. 2014, doi: 10.1016/j.cemconres.2014.07.005.

[94] Y. Briki, F. Avet, M. Zajac, P. Bowen, M. Ben Haha, and K. Scrivener, “Understanding of the factors slowing down metakaolin reaction in limestone calcined clay cement ($LC^3$) at late ages,” Cem. Concr. Res., vol. 146, p. 106477, Aug. 2021, doi: 10.1016/j.cemconres.2021.106477.

[95] E. Ntafalias and P. G. Koutsoukos, “Spontaneous precipitation of calcium-silicate-hydrate in aqueous solutions,” Cryst. Res. Technol., vol. 45, no. 1, pp. 39–47, Jan. 2010, doi: 10.1002/crat.200900538.

[96] S. Garrault-Gauffinet and A. Nonat, “Experimental investigation of calcium-silicate-hydrate (C-S-H) nucleation,” J. Cryst. Growth, vol. 200, no. 3–4, pp. 565–574, Apr. 1999, doi: 10.1016/s0022-0248(99)00051-2.

[97] C. Targan, A. Olgun, Y. Erdogan, and V. Sevinc, “Effects of supplementary cementing materials on the properties of cement and concrete,” Cem. Concr. Res., vol. 32, no. 10, pp. 1551–1558, Oct. 2002, doi: 10.1016/s0008-8846(02)00831-1.

[98] A. Schöler, B. Lothenbach, F. Winnefeld, M. Ben Haha, M. Zajac, and H.-M. Ludwig, “Early hydration of SCM-blended Portland cements: A pore solution and isothermal calorimetry study,” Cem. Concr. Res., vol. 93, pp. 71–82, Mar. 2017, doi: 10.1016/j.cemconres.2016.11.013.

[99] L. Nicoleau, E. Schreiner, and A. Nonat, “Ion-specific effects influencing the dissolution of tricalcium silicate,” Cem. Concr. Res., vol. 59, pp. 118–138, May 2014, doi: 10.1016/j.cemconres.2014.02.006.

[100] P. Suraneni and R. J. Flatt, “Use of micro-reactors to obtain new insights into the factors influencing tricalcium silicate dissolution,” Cem. Concr. Res., vol. 78, pp. 208–215, Dec. 2015, doi: 10.1016/j.cemconres.2015.07.011.

[101] E. Pustovgar et al., “Influence of aluminates on the hydration kinetics of tricalcium silicate,” Cem. Concr. Res., vol. 100, pp. 245–262, Oct. 2017, doi: 10.1016/j.cemconres.2017.06.006.

[102] Y. Yang, R. A. Patel, S. V Churakov, N. I. Prasianakis, G. Kosakowski, and M. Wang, “Multiscale modeling of ion diffusion in cement paste: electrical double layer effects,” Cem. Concr. Compos., vol. 96, pp. 55–65, Feb. 2019, doi: 10.1016/j.cemconcomp.2018.11.008.

[103] T. Zhang and O. E. Gjørv, “Diffusion behavior of chloride ions in concrete,” Cem. Concr. Res., vol. 26, no. 6, pp. 907–917, Jun. 1996, doi: 10.1016/0008-8846(96)00069-5.

[104] J. J. Thomas, H. M. Jennings, and A. J. Allen, “The Surface Area of Hardened Cement Paste as Measured by Various Techniques,” Concr. Sci. Eng., vol. 1, pp. 45–64, 1999.

[105] G. Plusquellec and A. Nonat, “Interactions between calcium-silicate-hydrate (C-S-H) and calcium chloride, bromide and nitrate,” Cem. Concr. Res., vol. 90, pp. 89–96, Dec. 2016, doi: 10.1016/j.cemconres.2016.08.002.

[106] T. T. H. Bach et al., “Retention of alkali ions by hydrated low-pH cements: Mechanism and $Na^+/K^+$ selectivity,” Cem. Concr. Res., vol. 51, pp. 14–21, Sep. 2013, doi: 10.1016/j.cemconres.2013.04.010.

[107] C. Nalet and A. Nonat, “Ionic complexation and adsorption of small organic molecules on calcium-silicate-hydrate: Relation with their retarding effect on the hydration of $C_3S$,” Cem. Concr. Res., vol. 89, pp. 97–108, Nov. 2016, doi: 10.1016/j.cemconres.2016.08.012.

[108] S. Barzgar, B. Lothenbach, M. Tarik, A. Di Giacomo, and C. Ludwig, “The effect of sodium hydroxide on Al uptake by calcium-silicate-hydrates (C-S-H),” J. Colloid Interface Sci., vol. 572, pp. 246–256, Jul. 2020, doi: 10.1016/j.jcis.2020.03.057.

[109] R. F. Giese, W. Wu, and C. J. van Oss, “Surface and electrokinetic properties of clays and other mineral particles, untreated and treated with organic or inorganic cations,” J. Dispers. Sci. Technol., vol. 17, no. 5, pp. 527–547, Jan. 1996, doi: 10.1080/01932699608943521.

[110] M. James, R. J. Hunter, and R. W. O’Brien, “Effect of particle size distribution and aggregation on electroacoustic measurements of .zeta. potential,” Langmuir, vol. 8, no. 2, pp. 420–423, Feb. 1992, doi: 10.1021/la00038a017.

[111] J. Haas and A. Nonat, “From C-S-H to C-A-S-H: Experimental study and thermodynamic modelling,” Cem. Concr. Res., vol. 68, pp. 124–138, Feb. 2015, doi: 10.1016/j.cemconres.2014.10.020.

[112] S. Merlino, E. Bonaccorsi, and T. Armbruster, “The real structures of clinotobermorite and tobermorite 9 Å: OD character, polytypes, and structural relationships,” Eur. J. Mineral., vol. 12, no. 2, pp. 411–429, Mar. 2000, doi: 10.1127/0935-1221/2000/0012-0411.

[113] M. Porus, C. Labbez, P. Maroni, and M. Borkovec, “Adsorption of monovalent and divalent cations on planar water-silica interfaces studied by optical reflectivity

and Monte Carlo simulations," J. Chem. Phys., vol. 135, no. 6, p. 64701, Aug. 2011, doi: 10.1063/1.3622858.

[114] T. Hiemstra and W. H. Van Riemsdijk, "On the relationship between charge distribution, surface hydration, and the structure of the interface of metal hydroxides," J. Colloid Interface Sci., vol. 301, no. 1, pp. 1–18, Sep. 2006, doi: 10.1016/j.jcis.2006.05.008.

[115] P. Hiemenz and R. Rajagopalan, "Principles of colloid and surface chemistry", Third Edition, Revised and Expanded, 3rd Edition," p. 672.

[116] I. Androniuk, C. Landesman, P. Henocq, and A. G. Kalinichev, "Adsorption of gluconate and uranyl on C-S-H phases: Combination of wet chemistry experiments and molecular dynamics simulations for the binary systems," Phys. Chem. Earth, Parts A/B/C, vol. 99, pp. 194–203, Jun. 2017, doi: 10.1016/j.pce.2017.05.005.

[117] B. Lothenbach, L. Pelletier-Chaignat, and F. Winnefeld, "Stability in the system $CaO-Al_2O_3-H_2O$," Cem. Concr. Res., vol. 42, no. 12, pp. 1621–1634, Dec. 2012, doi: 10.1016/j.cemconres.2012.09.002.

[118] A. J. Allen, J. J. Thomas, and H. M. Jennings, "Composition and density of nanoscale calcium-silicate-hydrate in cement," 2007, doi: 10.1038/nmat1871.

[119] E. Gallucci and K. Scrivener, "Crystallisation of calcium hydroxide in early age model and ordinary cementitious systems," Cem. Concr. Res., vol. 37, no. 4, pp. 492–501, Apr. 2007, doi: 10.1016/j.cemconres.2007.01.001.

[120] A. Zingg et al., "The microstructure of dispersed and non-dispersed fresh cement pastes --New insight by cryo-microscopy," Cem. Concr. Res., vol. 38, no. 4, pp. 522–529, Apr. 2008, doi: 10.1016/j.cemconres.2007.11.007.

[121] M. Collepardi and B. Marchese, "Morphology and surface properties of hydrated tricalcium silicate pastes," Cem. Concr. Res., vol. 2, no. 1, pp. 57–65, Jan. 1972, doi: 10.1016/0008-8846(72)90023-3.

[122] H. M. Jennings, B. J. Dalgleish, and P. L. Pratt, “Morphological development of hydrating tricalcium silicate as examined by electron microscopy techniques,” J. Am. Ceram. Soc., vol. 64, no. 10, pp. 567–572, Oct. 1981, doi: 10.1111/j.1151-2916.1981.tb10219.x.

[123] J. E. Rossen and K. L. Scrivener, “Optimization of SEM-EDS to determine the C-A-S-H composition in matured cement paste samples,” Mater. Charact., vol. 123, pp. 294–306, Jan. 2017, doi: 10.1016/j.matchar.2016.11.041.

[124] P. Durdziński, M. Ben Haha, M. Zajac, and K. L. Scrivener, “Phase assemblage of composite cements,” Cem. Concr. Res., vol. 99, pp. 172–182, Sep. 2017, doi: 10.1016/j.cemconres.2017.05.009.

[125] F. Deschner et al., “Hydration of Portland cement with high replacement by siliceous fly ash,” Cem. Concr. Res., vol. 42, no. 10, pp. 1389–1400, Oct. 2012, doi: 10.1016/j.cemconres.2012.06.009.

[126] F. Zunino and K. L. Scrivener, “Influence of kaolinite content, limestone particle size and mixture design on early-age properties of limestone calcined clay cements ($LC^3$),” in RILEM Bookseries, Springer Singapore, 2020, pp. 331–337. doi: 10.1007/978-981-15-2806-4_39.

[127] A. Bazzoni, “Study of early hydration mechanisms of cement by means of electron microscopy,” 2014, doi: 10.5075/EPFL-THESIS-6296.

[128] F. Avet, E. Boehm-Courjault, and K. Scrivener, “Investigation of C-A-S-H composition, morphology and density in Limestone Calcined Clay Cement ($LC^3$),” Cem. Concr. Res., vol. 115, pp. 70–79, Jan. 2019, doi: 10.1016/j.cemconres.2018.10.011.

[129] L. Nicoleau and M. A. Bertolim, “Analytical model for the alite ($C_3S$) dissolution topography,” J. Am. Ceram. Soc., vol. 99, no. 3, pp. 773–786, May 2015, doi: 10.1111/jace.13647.

[130] J. J. Thomas, J. J. Chen, A. J. Allen, and H. M. Jennings, “Effects of decalcification on the microstructure and surface area of cement and tricalcium silicate pastes,” Cem. Concr. Res., vol. 34, no. 12, pp. 2297–2307, Dec. 2004, doi: 10.1016/j.cemconres.2004.04.007.

[131] J. Siramanont, “Effect of ions and admixtures on the growth of synthetic calcium-silicate-hydrate (C-S-H),” 2018, doi: 10.5075/EPFL-THESIS-9007.

[132] F. Bellmann and G. W. Scherer, “Analysis of C-S-H growth rates in supersaturated conditions,” Cem. Concr. Res., vol. 103, pp. 236–244, Jan. 2018, doi: 10.1016/j.cemconres.2017.05.007.

[133] J. E. Rossen, “Composition and morphology of C-A-S-H in pastes of alite and cement blended with supplementary cementitious materials,” 2014, doi: 10.5075/EPFL-THESIS-6294.

[134] Takahashi, “Al-tobermorite,” Priv. Commun., 1967.

[135] M. D. Jackson et al., “Phillipsite and Al-tobermorite mineral cements produced through low-temperature water-rock reactions in Roman marine concrete,” Am. Mineral., vol. 102, no. 7, pp. 1435–1450, Jul. 2017, doi: 10.2138/AM-2017-5993CCBY.

[136] M. D. Jackson et al., “Unlocking the secrets of Al-tobermorite in Roman seawater concrete,” Am. Mineral., vol. 98, no. 10, pp. 1669–1687, Oct. 2013, doi: 10.2138/AM.2013.4484.

[137] N. Krautwurst et al., “Two-step nucleation process of calcium-silicate-hydrate, the nanobrick of cement,” Chem. Mater., vol. 30, no. 9, pp. 2895–2904, Apr. 2018, doi: 10.1021/acs.chemmater.7b04245.

[138] V. Kanchanason and J. Plank, “Role of pH on the structure, composition and morphology of C-S-H–PCE nanocomposites and their effect on early strength

development of Portland cement," Cem. Concr. Res., vol. 102, pp. 90–98, Dec. 2017, doi: 10.1016/j.cemconres.2017.09.002.

[139] M. Schönlein and J. Plank, "A TEM study on the very early crystallization of C-S-H in the presence of polycarboxylate superplasticizers: Transformation from initial C-S-H globules to nanofoils," Cem. Concr. Res., vol. 106, pp. 33–39, Apr. 2018, doi: 10.1016/j.cemconres.2018.01.017.

[140] D. Gebauer, H. Cölfen, A. Verch, and M. Antonietti, "The multiple roles of additives in $CaCO_3$ crystallization: A quantitative case study," Adv. Mater., vol. 21, no. 4, pp. 435–439, Jan. 2009, doi: 10.1002/adma.200801614.

[141] F. A. Zunino Sommariva, "Limestone calcined clay cements ($LC^3$): raw material processing, sulfate balance and hydration kinetics," 2020, doi: 10.5075/EPFL-THESIS-8173.

[142] B. Mota, T. Matschei, and K. Scrivener, "The influence of sodium salts and gypsum on alite hydration," Cem. Concr. Res., vol. 75, pp. 53–65, Sep. 2015, doi: 10.1016/j.cemconres.2015.04.015.

# Chapter 8. Appendix

## Appendix I. Thermodynamic modelling inputs

To make thermodynamic calculations using GEMS on the synthetic system, the following settings were used. Databases applied include the PSI-Nagra database, and Cemdata18.1 with the CSHQ model chosen.

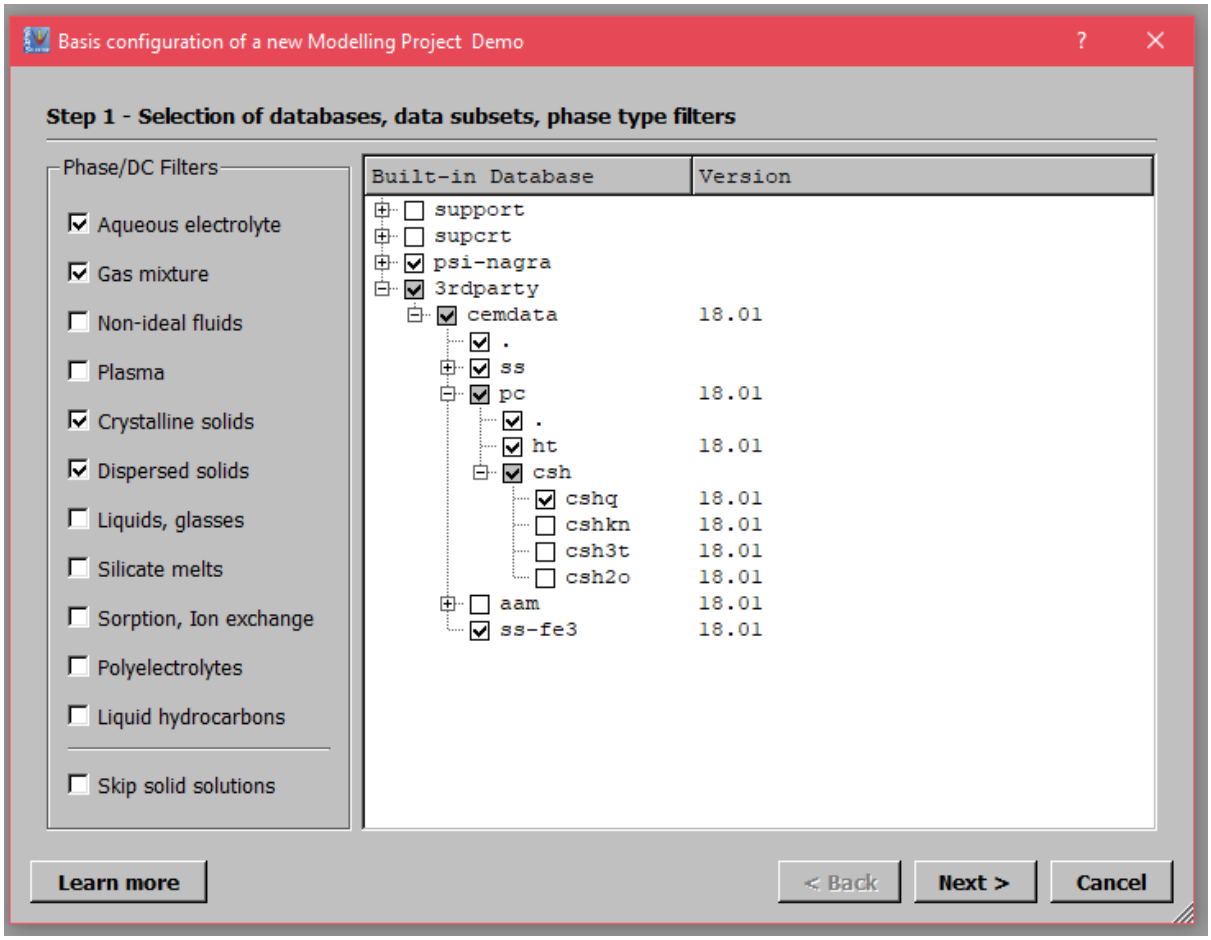

The elements chosen for the system are as follows:

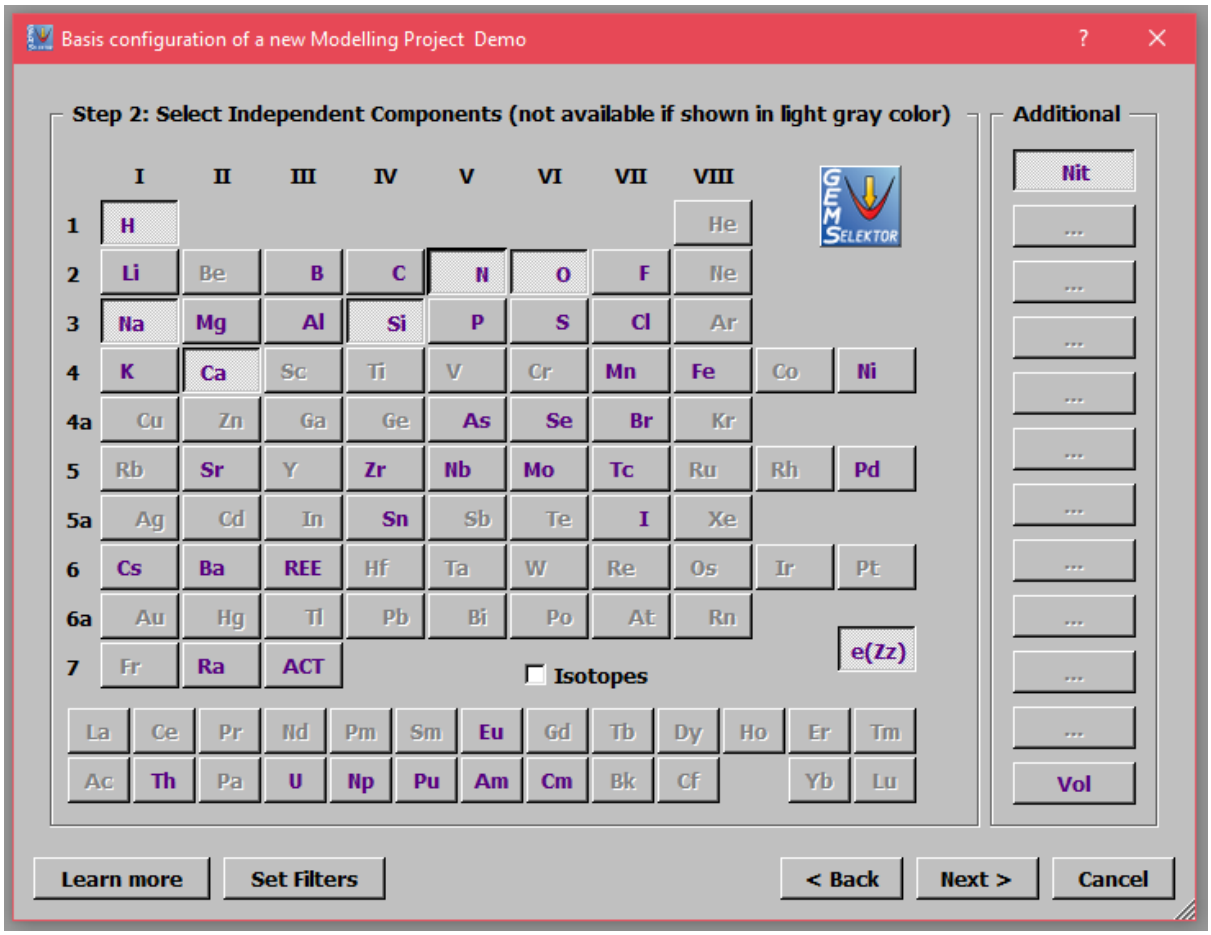


Nitrogen (Nit) on the far, upper right of the interface, is included in the base configuration step to model purging of the system. Reactive nitrogen is also included to incorporate calcium nitrate. Elements for sulfates, aluminates, and carbonates should also be added in this step if needed.

The model used to calculate the aqueous phase is based on NaOH, as NaOH is used to make synthetic C-S-H as described in Chapter 3. The setup is as follows:

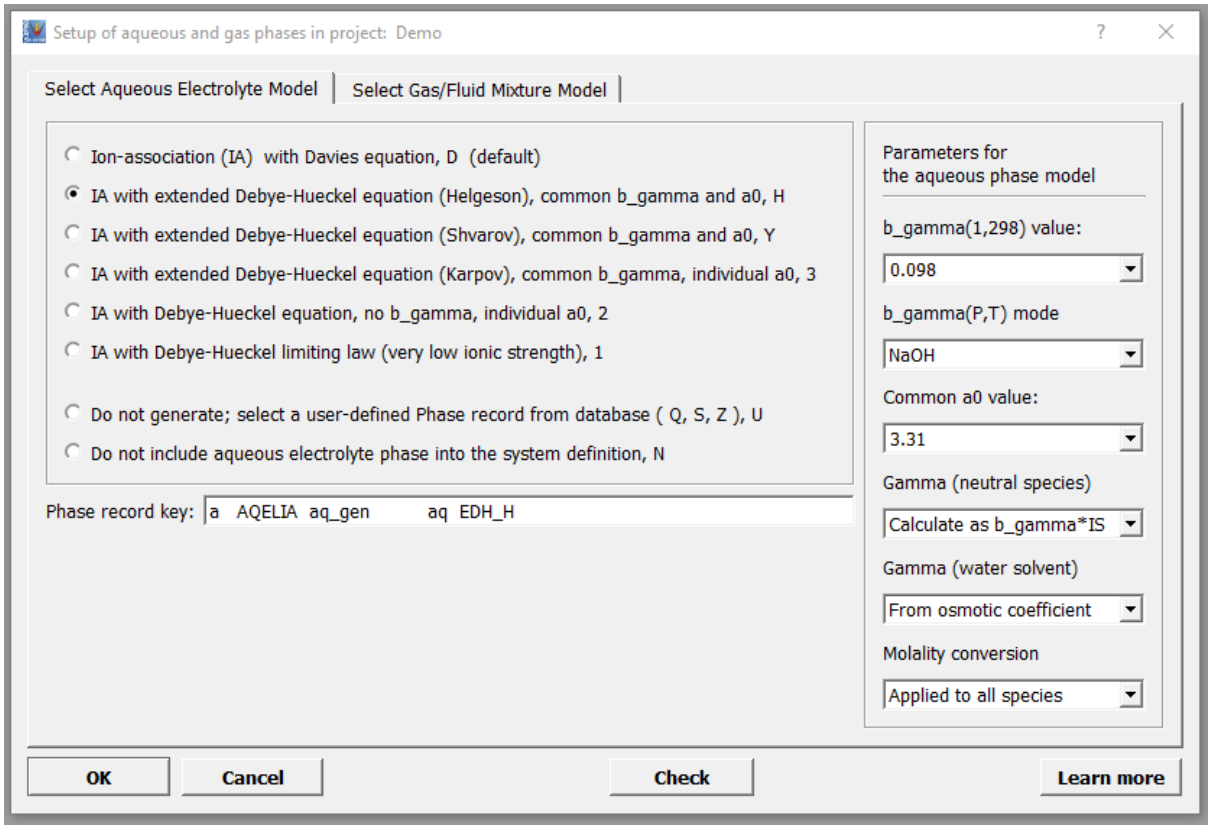

The following recipe composition objects were chosen to define the initial recipe, the values can be altered as needed, depending on the starting concentration. Starting units can also be changed as needed.

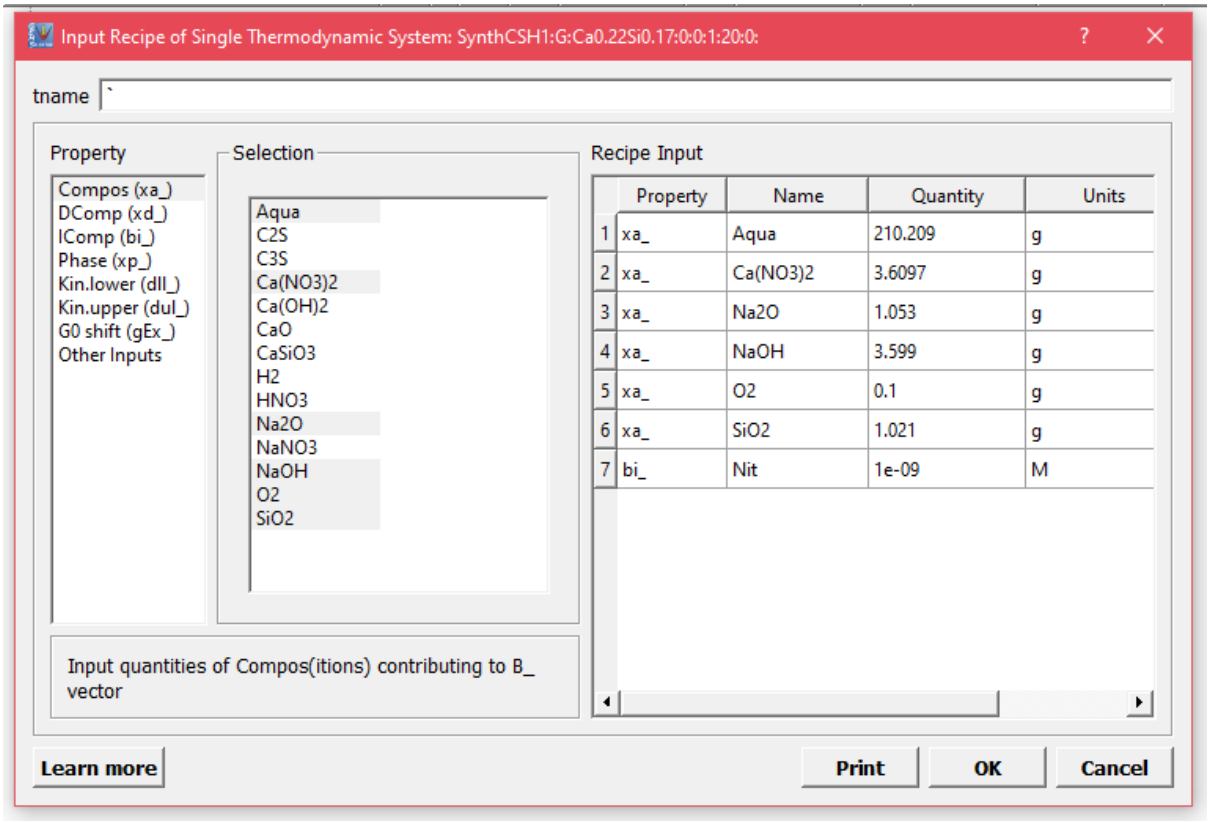

Finally, a demo process calculation is pictured below. In his calculation, the starting concentrations of Ca:Si are 0,.22M: 0.1M. The input for recipe composition objects is represented by $x_a$, is in grams. The starting amount of NaOH is placed at 0.01 g, and the system increases the amount of NaOH, calculating equilibrium with each incremental addition of NaOH. The pH and Ca:Si increase as a result.

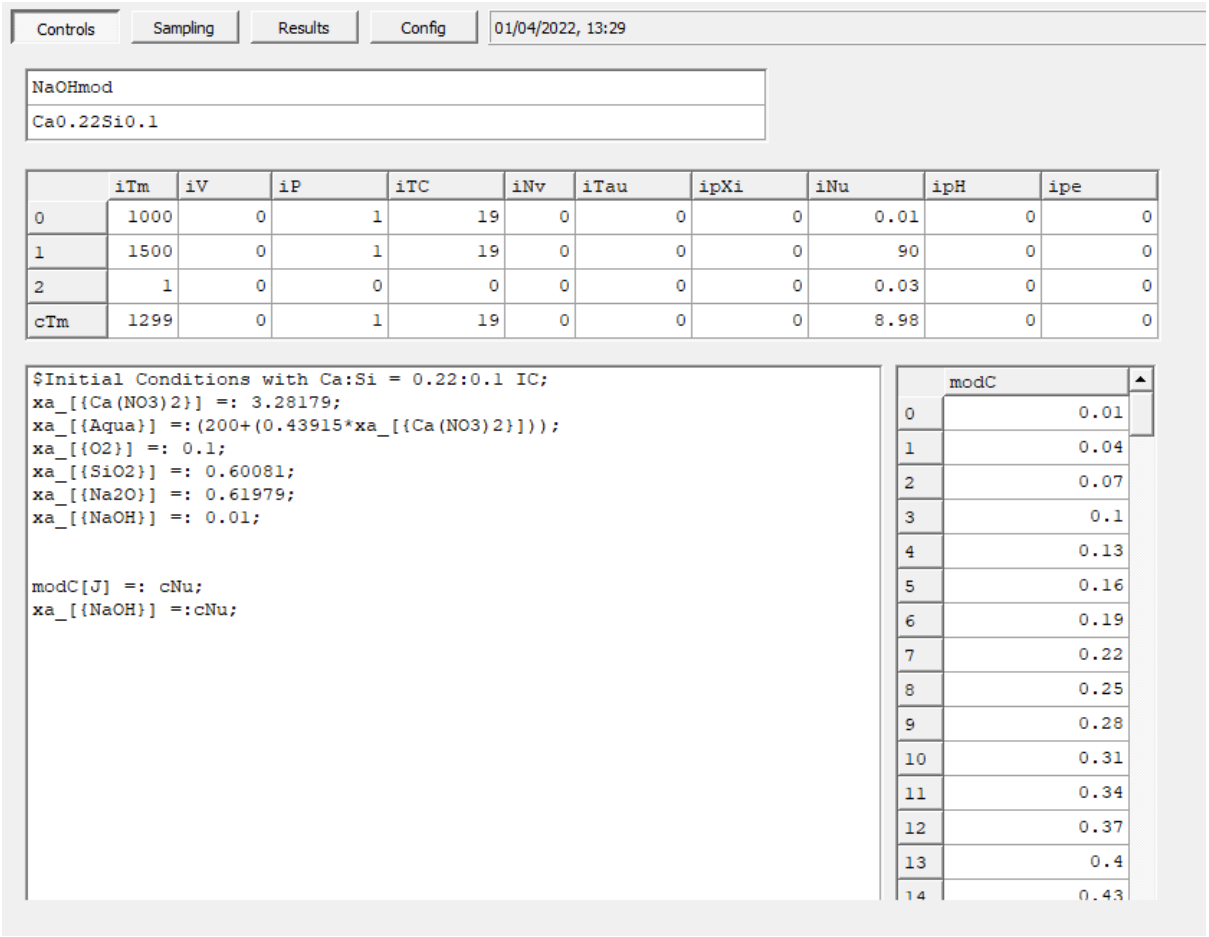


| | iTm | iV | iP | iTC | iNv | iTau | ipXi | iNu | ipH | ipe |
|---|---|---|---|---|---|---|---|---|---|---|
| 0 | 1000 | 0 | 1 | 19 | 0 | 0 | 0 | 0.01 | 0 | 0 |
| 1 | 1500 | 0 | 1 | 19 | 0 | 0 | 0 | 90 | 0 | 0 |
| 2 | 1 | 0 | 0 | 0 | 0 | 0 | 0 | 0.03 | 0 | 0 |
| cTm | 1299 | 0 | 1 | 19 | 0 | 0 | 0 | 8.98 | 0 | 0 |

| | modC |
|---|---|
| 0 | 0.01 |
| 1 | 0.04 |
| 2 | 0.07 |
| 3 | 0.1 |
| 4 | 0.13 |
| 5 | 0.16 |
| 6 | 0.19 |
| 7 | 0.22 |
| 8 | 0.25 |
| 9 | 0.28 |
| 10 | 0.31 |
| 11 | 0.34 |
| 12 | 0.37 |
| 13 | 0.4 |
| 14 | 0.43 |

# Appendix II. Laser diffraction

Particle size distribution (PSD) was measured by laser diffractometry. 250 mg of powder were mixed with 50ml of isopropanol (refractive index 1.378). Solutions were mixed with an ultrasonic horn for 15 minutes. Then samples were mixed with a magnetic stirrer during experimental sampling. Measurements were taken with the Malvern Mastersizer laser diffractomer, while stirring at 2300 rpm. To calculate the PSD, 1.529/0.001 and 1.572/0.001 were used as the refractive index/extinction coefficient of quartz and calcite, respectively.

Particle size diffraction measurements of quartz and calcite in isopropanol gave the following dispersion results:

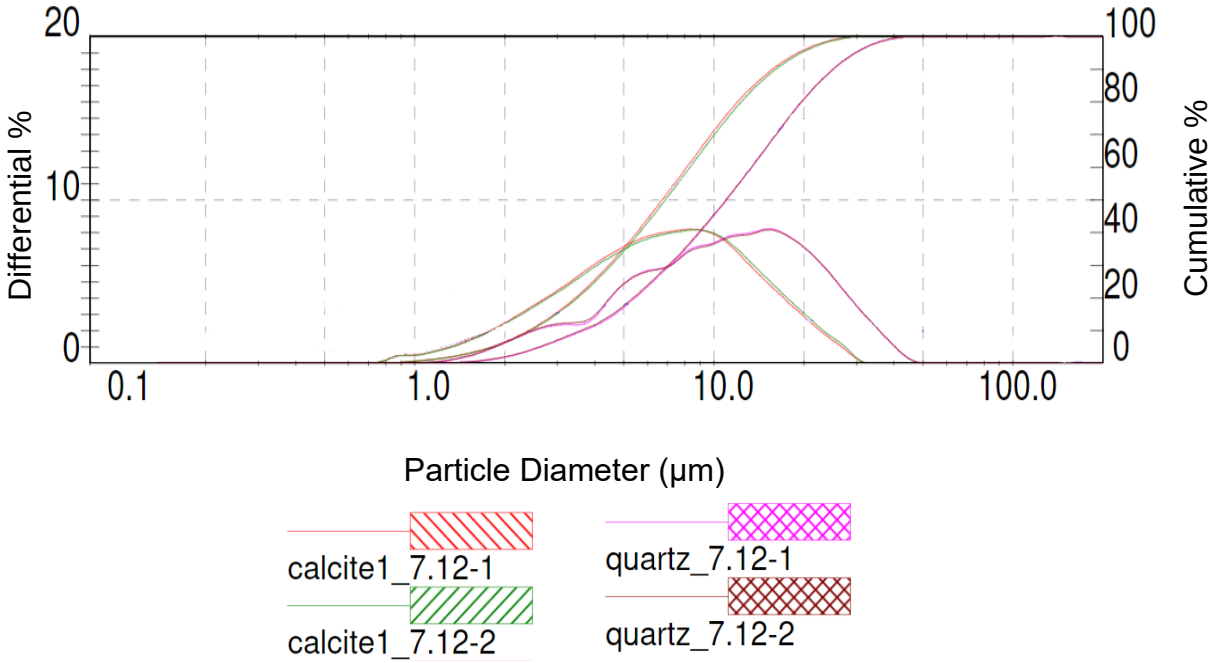


# Appendix III. Repository

Full sets of TEM images and expanded population balance model code can be found in the repository, link below.

https://drive.google.com/drive/folders/1HEhASjvBbuRMRnvB6QTbVsvDMRvtu1sl?usp=sharing